Photobiomodulation Laser in Retinal Degeneration

A thesis submitted in fulfilment of the requirements for the degree of Master of Philosophy (Ophthalmology) at the University of Adelaide.

Jack Zi Jie Ao

Discipline of Ophthalmology and Visual Sciences

School of Medicine

Faculty of Health Science

Table of Contents

Abstract

Photoreceptors are specialized neurons that form the first-order of the visual pathway. The retina displays prodigious energy demands which have been largely attributed to significant aerobic glycolysis by photoreceptors. Retinal degenerative diseases such as Retinitis Pigmentosa (RP), Age-related Macular Degeneration and Diabetic Retinopathy which involve the degeneration of photoreceptors are thought to involve a pathophysiological component of cellular energy deficiency. Hence, therapies addressing this component to conserve neurons, termed bioenergetic neuroprotection may be viable options to combat these diseases. RP is a collection of heterogeneous hereditary retinal dystrophies that are marked by genetic rod mutations leading to rod loss followed by secondary cone loss. There has been speculation behind the mechanisms of cone loss although more recently a bioenergetic dysfunction has been proposed. There is currently no viable treatment for RP although preventing cone loss would be a clinically significant therapeutic outcome and medical breakthrough.

Photobiomodulation (PBM) which refers to irradiation of tissue with 630-1000nm light, is known to increase cellular energy, decrease oxidative stress and inflammation. Hence, PBM would be a novel bioenergetics neuroprotective therapy for retinal degenerative disease including RP. Past studies have examined light-emitting diode (LED) based PBM on retina however there is concern of scattering and filtering of incoherent light. Moreover, there is no consensus on optimal treatment parameters. Therefore, the overarching aims of my thesis were to 1) investigate safe and optimal dosages of PBM laser in normal rat retinae and 2) examine the neuroprotective efficacy of PBM laser in a

retinal degeneration rodent model. The first experiment assessed the safety of PBM laser at irradiance doses 25, 100, 500 mW/cm^2 and at a duration 90 seconds in pigmented and albino rats. Structural and functional parameters were measured through electro-retinogram, spectral domain optical coherence tomography, fluorescein angiography and histological evaluation. PBM laser was safe at low and medium irradiance doses however there was occasional focal structural damage only in pigmented rats exposed to 500 mW/cm^2 irradiance. There were otherwise no functional changes and albino rats were unaffected. The findings in this study helped decide suitable irradiance dosages for the subsequent study. The second experiment examined the neuroprotection efficacy of PBM laser in the rd1 mice, a rapidly progressive autosomal RP rodent model. Mice were lasered twice weekly until P90 before their retinae were examined for cone survival through immunofluorescent staining. Cone function was examined through optokinetic assessment. We found significant cone neuroprotection in treated eyes that was supported by significant preservation of visual function. The current body of work should motivate further studies to explore the neuroprotective mechanisms of PBM and provide the basis for clinical translation.

Declaration

I certify that this work contains no material which has been accepted for the award of any other degree or diploma in my name, in any university or other tertiary institution and, to the best of my knowledge and belief, contains no material previously published or written by another person, except where due reference has been made in the text. In addition, I certify that no part of this work will, in the future, be used in a submission in my name, for any other degree or diploma in any university or other tertiary institution without the prior approval of the University of Adelaide and where applicable, any partner institution responsible for the joint-award of this degree. I give permission for the digital version of my thesis to be made available on the web, via the University's digital research repository, the Library Search and also through web search engines, unless permission has been granted by the University to restrict access for a period of time. I acknowledge the support I have received for my research through the provision of an Australian Government Research Training Program Scholarship.

Jack Zi Jie Ao

May 2019

Acknowledgements

The work contained within this thesis was supported by the NHMRC and the Australian Government Research Training Program Stipend Scholarship.

I would firstly like to thank my supervisor Professor Robert Casson for graciously accepting me as a Masters student at his laboratory. His optimism, enthusiasm and encouraging advice helped sculpted my interest in ophthalmic research not only during my candidature but for my future career. I want to also thank my co-supervisors Dr. John Wood and Dr. Glyn Chidlow for teaching me the ropes of how to conduct good basic science research, for their encouraging advice and constructive feedback. I have gained a deeper appreciation for research as a result.

My appreciation also goes to Teresa Mammone, Sergi Kozirev and Mark Daymon for orientating me around the lab, providing helpful advice and technical assistance.

I want to express my thanks to Dr. Weng Onn Chan and Dr. David Sia for encouraging me to pursue a career in ophthalmology.

I also want to thank Dr. Daniel Narayan, Dr. Paul Sia and Dr. Yiani Harpas for their mentoring and teaching me a lot of about not only being a good researcher but how to be a good clinician as well.

I want to thank my parents, Patrick and Lisa as well as my brothers Erik and Mark for their support throughout my study.

Most importantly, I want to show my deep appreciation for my partner, Judy for her unwavering support and patience during my candidature.

Presentations:

- *"Selective inhibition of calpain- 2 protects retinal ganglion cells and their function in retinal ischaemic-reperfusion injury"* **Best Paper** Plenary session at RANZCO 2018 National Congress 19th November 2018 at Adelaide, SA
- *"Neuroprotection efficacy of laser-delivered photobiomodulation in a severe mouse model of retinitis pigmentosa"* Poster session **ORIA Top Presentations** at RANZCO 2018 National Congress 19th November 2018 at Adelaide, SA
- *"Evaluation of the safety of laser-delivered Photobiomodulation and its neuroprotection efficacy in a mouse model of Retinitis Pigmentosa"* Poster presentation at International ARVO 2018 Annual Meeting 29th April 2018 at Hawaii, Honululu, USA
- *"A safety study of Photobiomodulatory Near-Infrared Laser"* Poster presentation at RANZCO 2017 National Congress 31st October 2017 at Perth, WA
- *"Bioenergetic Neuroprotection of Photoreceptors"*- Oral presentation at the Inaugural National Flinders Eye and Vision Collaboration Day 22nd September 2017 at Flinders Medical Centre, SA
- *"Photobiomodulatory Near-Infrared Laser: Is it safe?"* Poster presentation at 11th Annual Florey Postgraduate Research Conference 20th September 2017 at National Wine Center, SA

Relevant Publication:

- **Ao J**, Wood JPM, Chidlow G, Gillies MC, Casson RJ *"The Role of Retinal Pigment Epithelium in Age-related Macular Degeneration and Photobiomodulation as a potential therapy?"*-Clinical & Experimental Ophthalmology- 2018 Aug;46(6):670-686.PMID: 29205705

Awards and scholarships attained during candidature (2017-2018):

- **Australian Government Research Training Program Stipend Scholarship (formerly known as Australian Postgraduate Awards) 2017-18** Awarded by Australian Government
- **Walter and Dorothy Duncan Trust Grant 2017** to cover travel to RANZCO 2017 National Congress (Perth, WA). Awarded by University of Adelaide
- **Quintiles IMS Poster Prize 2017**- 11th Annual Florey Postgraduate Research Conference. Awarded by University of Adelaide
- **Dr. Roneal Naidu Memorial Prize 2017** In recognition of outstanding postgraduate research with clinical impact in a surgical discipline. Awarded by University of Adelaide
- **Avant Doctors-in-Training Research Scholarship 2018-2019** Awarded by Avant
- **John Parr Trophy 2018-** Best Paper Prize in RANZCO 2018 National Congress (Adelaide, SA). Awarded by RANZCO

1. Introduction

1.1 Structure of the Retina

The vertebrate retina is a light-sensitive tissue located at the posterior portion of the interior of the eye. It is predominantly a neuronal tissue, and the neural region comprises two synaptic layers alternating between three cellular layers.

Structurally, there are generally recognized to be ten clearly identifiable layers of the retina (Figure 1.1). Starting from the most interior portion of this tissue, the layers are as follows:

1. Inner limiting membrane (ILM), which is a basement membrane layer formed from astrocytes and the end feet of Müller cells.
2. Nerve fibre layer (NFL) containing retinal ganglion cell axons.
3. Ganglion cell layer (GCL) comprising of retinal ganglion cell bodies and displaced amacrine cells.
4. Inner plexiform layer (IPL) which is a dense fibrillar zone composed of dendrites of ganglion, bipolar, horizontal and amacrine cells, and their synaptic inter-connections.
5. Inner nuclear layer (INL) encompassing cell bodies of bipolar, horizontal and amacrine cells as well as of Muller glial cells.
6. Outer plexiform layer (OPL) containing synapses between photoreceptors, bipolar cells and horizontal cells.
7. Outer nuclear layer (ONL) which is mainly comprised of photoreceptor cell bodies.

8. External limiting membrane (ELM) which separates the inner segment from the cell body of photoreceptors and which is made up of tight junctions between these cells and Muller cells.
9. Photoreceptor segment layer which comprises the inner segments (IS) and outer segments (OS) of rod and cone photoreceptors.
10. Retinal pigment epithelium (RPE) which is a monolayer of cuboidal cells that is adjacent to the choriocapillaris and which forms the outer blood retinal barrier.

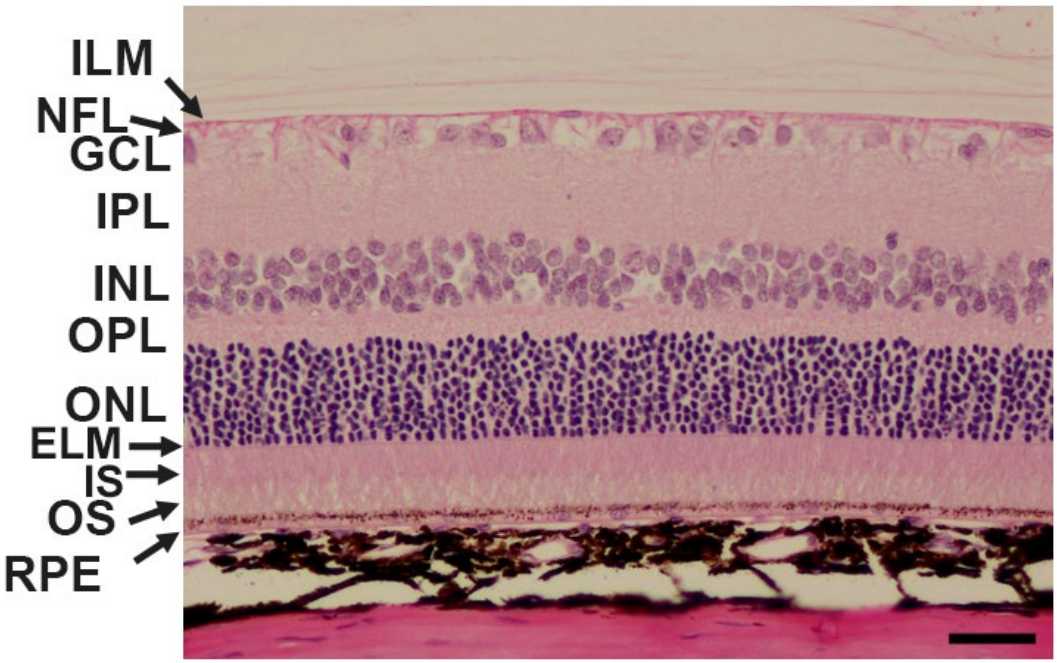

Figure 1.1: Light micrograph of a normal rat retinal section, stained with haematoxylin and eosin. ILM, inner limiting membrane; NFL, nerve fiber layer; GCL, ganglion cell layer; IPL, inner plexiform layer; INL, inner nuclear layer; OPL, outer plexiform layer; ONL, outer nuclear layer; ELM, external limiting membrane; IS, inner segment; OS, outer segment; RPE, Retinal pigment epithelium. **Scale bar 30 µm.**

1.2 Photoreceptors

Photoreceptors are specialized retinal neurons that contribute to the initial steps in vision by converting light into electrical signals to be interpreted by the brain: a process known as phototransduction. There are three types of photoreceptors in the vertebrate retina: rods, cones (known as the "classical photoreceptors") and the intrinsically photo-sensitive retinal ganglion cells.

In human and non-human primates, rods comprise 95% of the classical photoreceptors and are located throughout the retina, except in the fovea and the blind-spot, but are concentrated in the periphery. In mice retinae, rods comprise of 97% of photoreceptors. These cells are responsible for mediating dim (scotopic) vision, and are sensitive to a single light photon. Cones on the other hand, which comprise the remaining 5% of the classical photoreceptors, are less sensitive to light, and are densely packed in the rod-free area of the retina known as the fovea. They are responsible for bright-light (photopic) and colour vision. Intrinsically photo-sensitive retinal ganglion cells are a diverse collection of cells that contain the pigment melanopsin and are responsible for conveying ambient signals to higher brain centres.[1,2] For the purposes of this thesis the term photoreceptor will refer only to the classical photoreceptors.

1.2.1 Structure of photoreceptors

General overview

Structurally, photoreceptors have an elongated shape and are compartmentally organized into an outer segment (OS), inner segment (IS), cell body and synaptic region (Figure

1.2). The OS possesses photo-sensitive pigments that facilitate photon absorption and subsequent conversion to electrical signals to be interpreted by the brain, a process known as phototransduction.

The inner segments contain the majority of the organelles including the endoplasmic reticulum, Golgi complex and mitochondria. Many ion channels are also present, on the plasma membrane, here. Separating the OS and IS is a cylindrical structure composed of doublet microtubules called the connecting cilium which may facilitate protein transport between the segments. The cell body holds the photoreceptor nucleus and is continuous with the inner segment (IS). The synaptic region comprises synaptic vesicles and ribbon synapses that connect to bipolar and horizontal cells at the outer plexiform layer (OPL).

Rods and cones have notable architectural differences in the OS which may explain differences in their sensitivity and ability to respond to varying light intensities.

Rod OS structure

Rods have more elongated OS compared to cones, with the typical mammalian rod OS having a diameter of 1.2-2.0 μm and a length of 20-34 μm.[3] [2,4,5]. Electron microscopy of the rod OS reveals stacks of disk membranes that are discontinuous with the plasma membrane unlike the cone OS, which are formed as membrane invaginations. Within the disk membranes are abundant photo-sensitive units, based on the protein, rhodopsin, which absorb photons as part of the phototransduction cascade.[6] Rhodopsin is composed of the chromophore 11-cis-retinal (Vitamin A derivative) and a light sensitive opsin subtype called scotopsin. Other prominent phototransduction proteins are the trimeric G-

protein, transducin, made up of α, β and γ subunits, and phosphodiesterase (PDE6) which consists of the two sub-units PDE6A and PDE6B as well as two identical inhibitory sub-units of PDE6G. Within the rod OS plasma membrane is the cyclic nucleotide gated (CNG) channel consisting of three CNGA1 and one CNGB1 subunits. The CNG channel forms a complex with the Na^+–Ca^{2+}–K^+ exchanger (NCKX1 or SLC24A1) on the OS plasma membrane and plays a vital role in hyperpolarization during phototransduction.[7] Gene mutations related to phototransduction membrane proteins commonly result in retinal diseases. Mutations in the genes encoding arrestin, rhodopsin kinase or NCKX1 cause congenital stationary night blindness (CSNB) whilst gene mutations affecting rhodopsin, CNGA1, CNGB1, PDE6A or PD6B result in Retinitis Pigmentosa. [7]

Cone OS structure

Cones have shorter OS than rods, with a typical length of 13 μm and diameter of 1.2 μm. The cone OS initially form evaginations that gradually develop into a series of discs which are continuous with the OS plasma membrane, tapering to form a cone-like shape.[8] Similar to rods, the disk membranes house photopigments consisting of 11-cis-retinal and light sensitive cone opsins called photopsins. In the primate retina, there are classically three classes of photopsins: S (OPN1SW), M (OPN1MW) and L (OPN1LW) with maximum absorbance within the visible spectrum wavelengths of 420-440 nm, 530-545 nm and 558-565 nm respectively.[9] There are differences in the composition of PDE6 and the CNG channel between rods and cones. The cone PDE6 is composed of two identical catalytic sub-units of PDE6C and two identical inhibitory sub-units of

PDE6H.[10] The cone CNG channel comprises two NGA3 subunits and two CNGB3 subunits.[11]

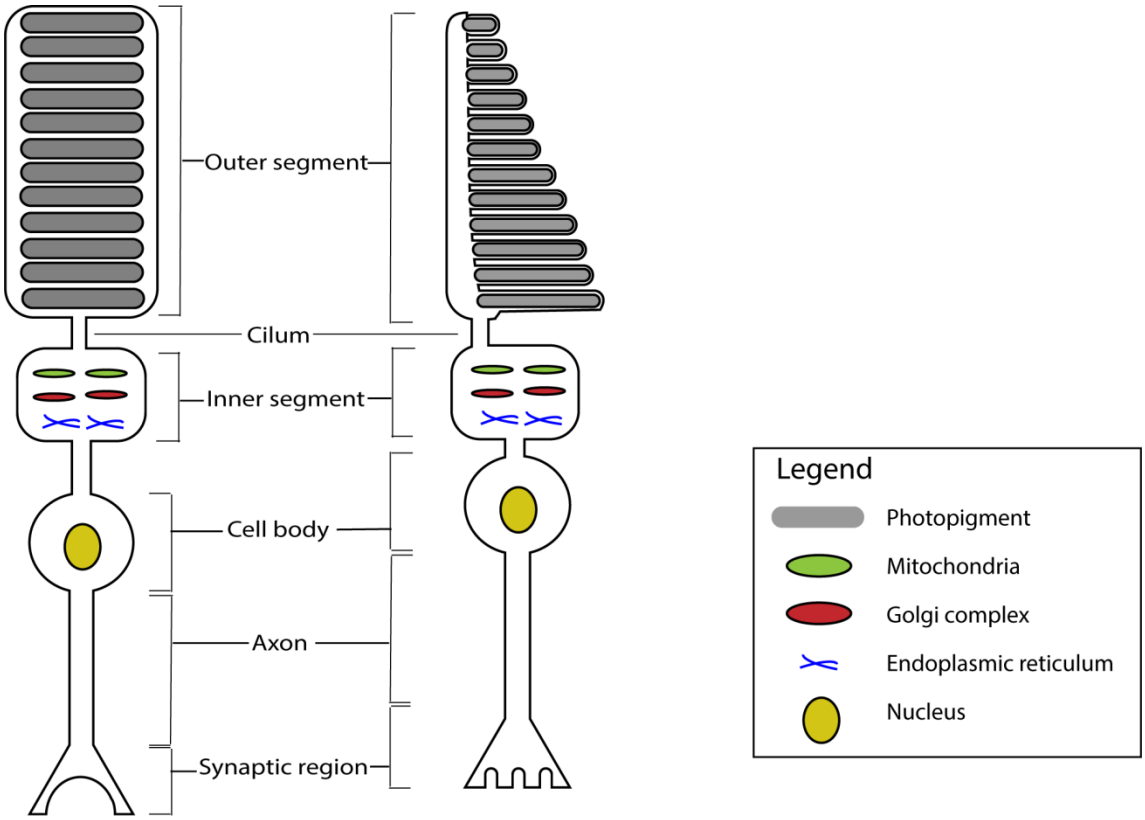

***Figure 1.2**: Schematic diagram showing the generalized structure of both rod and cone photoreceptors. These cells are structurally similar and include an outer segment, connecting cilium, cell body, axon and synaptic region. The outer segment is made up of stacked disks of photopigments. The cilium is made up of a ring of doublet microtubules that forms a bridge between the outer and inner segment. The inner segment is composed of several organelles including the mitochondria, Golgi complex and endoplasmic reticulum. The cell body houses the photoreceptor nucleus. The axon comprises nerve fibers that lead to the synaptic region which contains synaptic vesicles and ribbon synapses that connect to bipolar and horizontal cells at the outer plexiform layer.*

1.2.3 Phototransduction cascade

The steps of the phototransduction cascade are similar in cones and rods. Upon exposure to light, the photopigment component 11-cis-retinal is photoisomerized to the all-trans-retinal isomer which results in conformational change of the bound opsin. This causes the active opsin to bind to transducin, resulting in catalytic exchange of guanosine diphosphate (GDP) for guanosine triphosphate (GTP) on the α sub-unit of transducin. This leads to the α-subunit of transducin to dissociate from its bound βγ subunits, thereby activating PDE6 which hydrolyses cyclic guanosine monophosphate (cGMP). The decrease in cGMP causes the closure of CNG channels, reduced cation influx and subsequent hyperpolarization. When the cell is in its hyperpolarized state, voltage-gated calcium channels close, culminating in decreased release of the neurotransmitter, glutamate, at the synaptic region.

The resetting of the photoreceptor cell back to its dark-state occurs through a similarly discrete sequence of steps. In rods, activated rhodopsin becomes phosphorylated by enzymes such as G-protein coupled receptor kinase, protein kinase C or rhodopsin kinase, before being deactivated by binding to arrestin.[12] The renewal of rhodopsin requires conversion of all-trans-retinal to 11-cis retinal which occurs in the visual cycle (outlined in the section below). Hydrolysis of GTP on the sub-unit of transducin results in PDE6 returning to its previous state. Activation of guanylate cyclase through guanylate-cyclase-activating proteins (GCAPs) results in restoration of cGMP levels.[13] This triggers the re-opening of CNG channels and the renewal of the photoreceptor to its dark, partially depolarized state. Whilst in this state, the influx of Na^+ and Ca^{2+} through the photoreceptors is known as dark current.

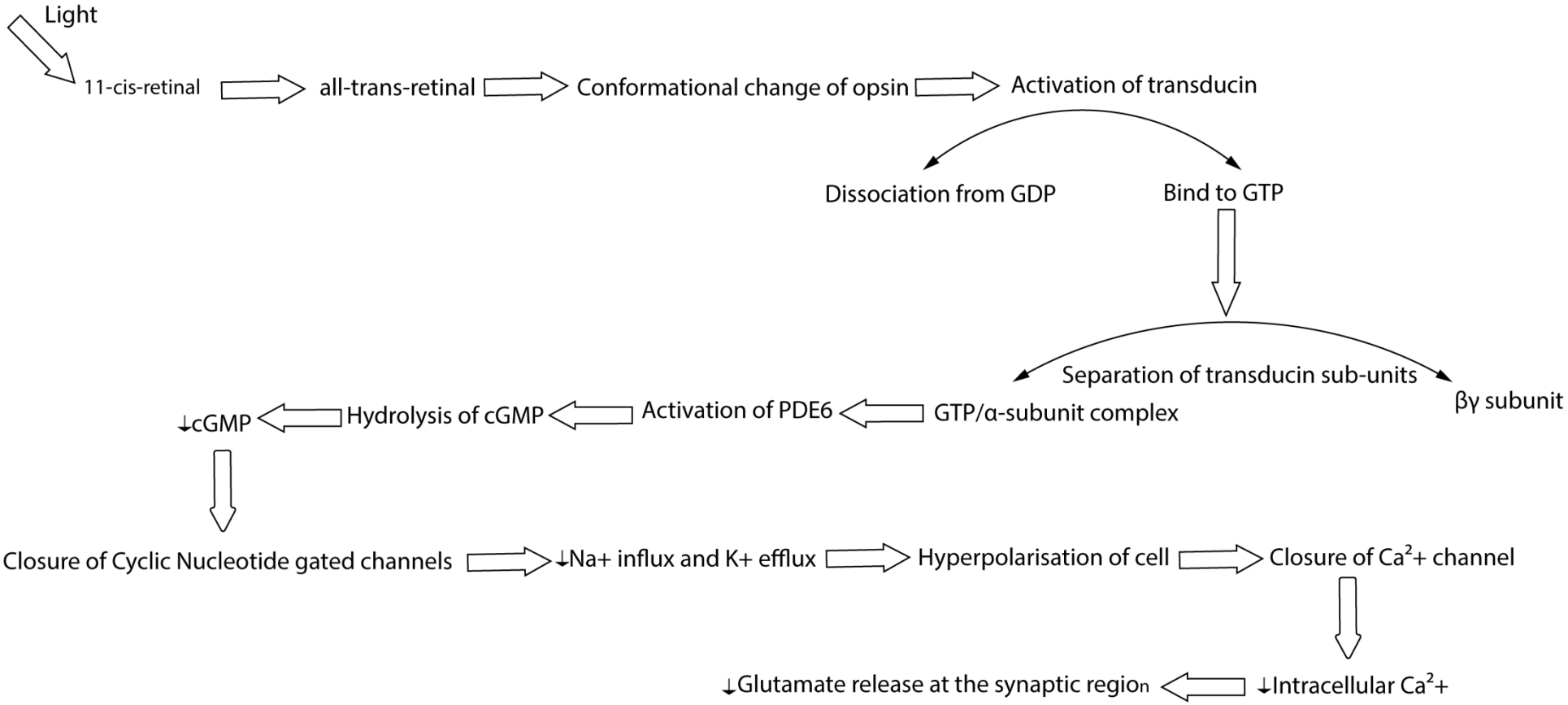

Figure 1.3: Phototransduction cascade: Light causes photoisomerization of 11-cis retinal to all-trans-retinal. This results in a conformational change of opsin and activation of transducin. The activated transducin then separates into the βγ subunit and GTP/α-subunit complex, the latter resulting in activation of PDE6 and hydrolysis of cGMP. The drop in cGMP results in closure of Cyclic Nucleotide gated channels and subsequent decreased sodium influx and potassium efflux. The cell membrane becomes hyperpolarized, resulting in closure of calcium channels. The decrease in intracellular calcium leads to decreased glutamate release at the synaptic region.

1.2.4 Visual cycle

The visual cycle is the process by which 11-cis-retinal is regenerated from all-trans-retinal. Following light exposure, all-trans-retinal is converted into all-trans-retinol by retinal dehydrogenase in the OS before being transported to the RPE by interstitial retinol-binding protein 3 (RBP3) .[14,15] All-trans-retinol can also originate from the blood circulation, carried by serum retinol binding protein, before entering the RPE cell basolaterally through the STRA6 (Stimulated by retinoic acid 6) protein.[16,17] Whilst in the RPE, all-trans-retinol is bound to cellular retinol binding protein and esterified to all-trans-retinyl-ester in the presence of the catalyst lecithin retinol acyl transferase. All-trans-retinyl-ester undergoes isomerization via the action of the enzyme retinoid isomerohydrolase (RPE65) to produce 11-cis-retinol which is subsequently converted by 11-cis-retinol dehydrogenase to produce 11-cis-retinal. 11-cis-retinal is then transported by RBP3 to the OS where it combines with opsin to reform rhodopsin or cone opsin. The cycle is repeated following light exposure whereby the resulting all-trans-retinal is reconverted to its all-trans-retinol and cycled back to the RPE for reisomerization and oxidation.[16 18] The comparatively faster regeneration rate of cone pigment has lead to the postulation of an alternative cone visual cycle separate from the RPE involving Müller cells.[19] In vitro experiments of cultured chicken Müller cells demonstrate isomerization of all-trans-retinol to 11-cis-retinol which enact as a source for cone photopigment.[20] Later experiments by Mata et al.[21] reported the presence of all-trans retinol isomerase, 11-cis-retinyl-ester synthase and 11-cis-retinol dehydrogenase in cone-rich ground squirrel and chicken retinae that support the existence of a cone visual cycle revolving around Müller cells. More recently, there has been data to support a

cone visual cycle in human and primate retinae.[19] However, the exact mechanisms of the cone visual cycle are still poorly understood and remain a topic of research interest.

1.2.5 Energy metabolism

Photoreceptors are known to be highly metabolically active cells that constitute a significant portion of the retina's energy consumption. The generation of adenosine trisphosphate (ATP), the essential form of intracellular energy transport in all lifeforms, is achieved through two pathways: glycolysis and oxidative phosphorylation. The major energy substrate in both pathways is glucose which is generally catabolised to pyruvate, where it enters the Krebs cycle to facilitate oxidative phosphorylation, in the presence of oxygen. When oxygen is scarce, pyruvate is shunted away from oxidative phosphorylation and is converted to lactate by the enzyme lactate dehydrogenase. Lactate derived from Müller cells has been identified as a possible energy substrate for photoreceptors; however, there is evidence that glucose is the preferred energy substrate when adequately available.[22,23] Other bioenergy-related mediators known to be utilized or metabolised by photoreceptors include phosphocreatine and amino acids.[24] Oxidative phosphorylation in the mitochondria is much more efficient than glycolysis, yielding up to 36 ATP molecules compared to 2 ATP molecules generated in glycolysis. Interestingly, the isolated retina produces abundant lactate despite the presence of oxygen, and displays similar metabolic characteristics to cancer cells - a phenomenon known as the Warburg effect or aerobic glycolysis.[25] One postulation for this observation is that aerobic glycolysis allows for the production of metabolic intermediates for biosynthesis especially in the retina where there is immense turnover

of the photoreceptor outer segment.[26,27] Noell et al.[28] demonstrated that inhibition of glycolysis by iodoacetate resulted in decreased retinal and rod cell function measured by decreased electrical amplitudes on the electroretinogram (ERG). Additionally, Graymore observed a decrease of glycolysis by more than 50% in dystrophic rat retinae lacking photoreceptors compared to normal rat retinae.[29,30] Moreover, Chertov demonstrated that glucose withdrawal leads to mitochondrial failure, ATP depletion and subsequent photoreceptor cell death in isolated mouse retinae.[31]

The amount of energy utilized by the photoreceptor is dependent on the degree of light exposure. Greater energy is required in the dark to maintain ionic gradients, particularly, the pumping out excess Na^+ via the Na^+/K^+ ATPase pump in the inner segment, creating the so-called "dark current". In bright-light conditions, the outer segment uses energy mainly for phototransduction and light adaptation, with remaining energy used for the production, recycling and transportation of photopigments and neurotransmitters.[24] In mouse rods, it is estimated that $1x10^8$ molecules of ATP are used per second in the dark whilst only less than a quarter of this amount is utilized in light.[32]

In darkness, the ATP expenditure of cones and rods is similar due to their analogous voltage-dependence and amplitude of the dark current. In bright light, cones have significantly greater ATP expenditure than rods, however, for several reasons: the turnover of transducin is at least twice as great; Na^+ influx through cGMP-gated channels does not reduce more than half; higher depolarization rate in cones; and greater rhodopsin kinase activity.[10,32]

Comparatively, oxygen concentration and lactate formation in the inner retina remains consistent in light and dark, suggesting the inner retina's metabolism is not influenced by differences in lighting conditions.[33]

Energy deficiency has been attributed as a cause of degeneration of photoreceptors in inherited diseases including Retinitis Pigmentosa[34,35] as well as acquired diseases such as age-related macular degeneration[36,37], diabetic retinopathy [38] and central retinal artery/vein occlusion[39,40]. A form of intervention known as bioenergetic neuroprotection could specifically address this metabolic issue, thereby potentially preserving photoreceptors or slowing down their degeneration.

1.3 Bioenergetic neuroprotection

In the broadest sense, neuroprotection refers to the relative preservation of neurons following an insult. In a bioenergetic-based approach, neuroprotection aims to preserve damaged or threatened neurons by increasing the availability of the energy supply.[41] The neuroprotective benefit of several bioenergetic agents has been observed in several animal models of neurological and ophthalmic diseases. Creatine, which may provide protection by metabolic energy buffering, has been found to be neuroprotective in Parkinson's disease[42], Huntington's disease[43-45], Amytrophic Lateral Sclerosis[46], cerebral ischaemia[47] and traumatic brain injury[47,48]. Nicotinamide, a precursor to nicotinamide adenine dinucleotide phosphate, has been successful in protecting against phototoxic[49] and ischaemic retinal injury[50] as well as cerebral excitotoxic injury as induced by the ionotropic glutamate receptor agonist, N-methyl-D-aspartate[51]. Moreover, ubiquinone has also found to be neuroprotective in Huntington's disease, Parkinson's disease and glaucoma through anti-oxidative and mitochondrial protective

mechanisms.[52-55] Research from our laboratory has demonstrated the neuroprotective effect of short-term hyperglycaemia and intraocular glucose delivery in animal models of ischaemic retinal injury[56,57] and experimental glaucoma[58]. In the clinical setting, topical[59] and subconjunctival[60] glucose delivery resulted in temporary recovery of contrast sensitivity in patients with severe primary open angle glaucoma. More recently, N-acetyl-cysteine amide has been observed to have a protective effect in animal models of traumatic brain injury by maintaining mitochondrial function.[61,62]

Despite these promising results, the success of these bioenergetic agents in the clinical setting has been mostly limited and inconclusive.[63-65]

1.4 Retinitis Pigmentosa

Retinitis Pigmentosa (RP) is a group of hereditary retinal diseases that is characterized by the initial degeneration of rods followed by the subsequent loss of cones. It is one of the leading causes of inherited blindness, affecting 1 in 4000 with an estimated 1.5 million individuals affected globally.[66,67] The main mutations that result in RP involve the dysfunction of rod-specific proteins including rhodopsin in the phototransduction cascade. There are at least 50 genes currently known to cause non-syndromic RP with nearly 3100 mutations being reported in these genes. Syndromic forms of RP including Usher syndrome and Bardet-Biedl syndrome account for over 1200 pathogenic mutations.[68] RP can be inherited in an autosomal-recessive (50-60%), autosomal dominant (30-40%) or X-linked pattern (5-15%) with non-mendelian digenic or mitochondrial inheritance accounting for only a minority of cases.[69]

1.4.1 Clinical presentation of RP

The onset of symptoms is variable with some patients being asymptomatic until mid-adulthood whilst others display symptoms in early childhood. Typically, the earliest manifestation is night blindness and difficulty with dark adaptation during adolescence. Patients may fail to recognize night blindness as most night activities are adequately lit to allow for compensation by cone-mediated vision. Patients may often present with vision loss after involvement of cone degeneration. Symptoms progress to involve loss of mid-peripheral vision which extends to far peripheral vision, creating a tunnel visual defect. Eventually, the central visual field becomes affected. Visual acuity can remain relatively normal in advanced RP with a remnant island of central vision. Up to 90% cone loss at the fovea may occur before there is a visual acuity reduction.[70] On fundus examination, there are classically intra-retinal "bony spicule" pigmentary changes, severe arteriolar narrowing and a "waxy pallor" appearance of the optic disk. Electro-retinograms (ERG) which record electrical response of the retina to light stimulus, initially demonstrate reduced scotopic and combined amplitudes before affecting photopic responses, signifying cone loss.[71] Eventually, in late stage RP, the ERG response may be eliminated. Automated visual field testing reveals mid-peripheral visual loss that expands peripherally and centrally until central vision becomes compromised.

1.4.2 Pathophysiology

Rod degeneration

Due to the heterogeneity of RP, the precise mechanism of rod degeneration is unclear

and may vary depending on the affected gene. Generally, genetic mutations in RP lead to dysfunctional rod proteins or altered phototransduction pathways which trigger rod degeneration. Mutations in genes encoding for rhodopsin results in autosomal dominant RP and is the basis for the transgenic rodent model P23H rat.[72] In these rats, rhodopsin accumulates high molecular weight oligomeric species within the cytoplasm predisposing to subsequent destruction by the ubiquitin-dependent proteasome system.[73] Genes affecting the rod OS structural proteins, rod outer segment 1 and peripherin 2, cause a variant of autosomal dominant RP.[74] Rod degeneration in one form of autosomal recessive RP results from altered PDE6b activity, which leads to elevated levels of cGMP.[75] Retinal degeneration mouse models of RP which feature this mutation, display high cGMP levels that precede photoreceptor and inner retinal degeneration.[76] Similarly, several in vitro studies have linked elevated cGMP to photoreceptor degeneration.[76-78] The use of PDE6 inhibitors or cGMP analogues in human retinal explants lead to rod inner segment and cone structural changes with the combination virtually destroying all rods.[79] Iodoacetate, a potent inhibitor of PDE6 results in raised cGMP and subsequent photoreceptor degeneration.[80]

Cone degeneration

Cones degenerate secondary to rod loss in RP. Analysis of RP patients with 18 different rhodopsin mutations revealed cone OS function remained normal until rod OS loss exceeded 75%, with the topography of cone loss strongly correlated to rod loss.[81] The earliest event of cone degeneration is the deformation and loss of the cone OS.[82] The

mechanism of secondary cone degeneration in RP is still unresolved yet there are several theories to explain the phenomenon.

One explanation is the gap-junction mediated "bystander effect" which postulates that rod-derived products such as glutamate and apoptosis-promoting factors are released following rod cell death and propagate to cones via gap junctions, causing the death of these cells too.[83] The "bystander effect" has been observed in cultures[84-86] as well as in rodent models of transient cerebral ischaemia[87]. In a study examining the effects of a transgene encoding normal rds/peripherin integrated into the X-chromosome in male and female rds-/- mutant retinas, Kedzierski et al.[88] showed significant photoreceptor loss in both transgene-expressing and non-expressing retinal patches. The authors suggested that rod-derived toxin release from neighbouring cells was the cause of transgene-expressing photoreceptor death. More recently, this theory has been disputed by Kranz et al.[82] who showed that mice deficient for the rod-cone coupling protein connexin36 did not show any delay or prevention of cone loss. Rod-derived toxin release would also be expected to affect nearby cells such as bipolar cells, however, these cells do not undergo widespread death following photoreceptor loss.[89]

Another theory for secondary cone degeneration in RP is the role of microglial activation. The initiating event of rod death triggers the activation of microglial cells which migrate to the outer retinal and sub-retinal layers.[90,91] Microglial cells release pro-inflammatory cytokines, nitric oxide, tumour necrosis factor α, reactive oxygen species, excitatory amino acids, proteases and arachidonic acid derivatives which trigger cone death.[92,93] Elevation of activated microglial cells have been identified in RP patients.[92] Upregulation of Toll-like receptor 4 as well as monocyte chemoattractant protein-1 and

CC Chemokine receptor 2 interaction has been linked to microglial activation in retinal degeneration mice models.[94,95] Conversely, microglial activation may be modulated by the interaction between CXC3C chemokine receptor on microglial cells and its ligand CX3CL1 expressed by neurons either as a membrane bound or secreted ligand.[96,97] In culture, retina-derived glial cells appear to release heat-inactivated, soluble molecules that induce apoptosis of photoreceptor cells.[98] An essential flaw with the "bystander effect" and microglial activation theories is that neither can suitably explain the ongoing cone degeneration which occurs long after the destruction of all rods nor the fact that other cell types remain unaffected.

Oxidative stress is an alternative mechanism to explain cone death in RP. Oxidative stress occurs when there is an imbalance between the generation of reactive oxygen species (ROS) and the cell's antioxidant defence system. ROS production comes from various physiological biochemical processes including mitochondrial respiration, photochemical and enzymatic reactions, or from exposure to UV light, ionizing radiation, or heavy metal ions.[99] Under physiological conditions within the retina, ROS derive via the high consumption of oxygen and are therefore produced mainly in mitochondria. Low levels of ROS provide physiological benefit by facilitating redox signaling pathways, cellular proliferation and gene expression. However, ROS are generally highly unstable and can interact with lipid, proteins and DNA to cause cell dysfunction and death, especially when present at elevated levels.

One of the precipitating factors for oxidative stress is the elevated level of oxygen in the outer retina following rod loss.[100] Rods, which constitute 95% of the photoreceptor population, consume most of the oxygen in the retina. Without rods, cones exposed to

hyperoxia undergo progressive oxidative damage and die. Cones in the mid-peripheral retina are lowest in density and are therefore highly predisposed to hyperoxia and subsequent oxidative damage resulting in the archetypal scotopic visual field defect described previously.[101] Degeneration begins to affect other less dense regions, gradually progressing to higher cone densities, correlating closely to the pattern of visual loss in RP. Eventually, cones at the fovea are eliminated, causing complete blindness. Animal models of RP display biomarkers of oxidative damage such as acrolein and 4-hydroxynonenal-adducts.[102,103]

Oxidative stress in RP has been linked to excess superoxide generation from activated nicotinamide adenine dinucleotide phosphate (NADPH) oxidase in cones.[104] Superoxide may lead to further ROS production or can directly affect surrounding cell structures. Cones contain abundant mitochondria, making them particularly susceptible to oxidative stress. Mitochondrial damage may lead to further ROS production, ultimately overwhelming the cone's intrinsic antioxidant system.

While excess ROS production has been linked to oxidative stress in RP, lower antioxidant levels have also been implicated. A study of RP patients revealed lower activity of the extracellular antioxidant enzyme, superoxide dismutase (SOD), in their aqueous humour as well as upregulated lipid peroxidation products in their blood.[105] Moreover, RP patients have been identified to have lower intraocular levels of the reduced antioxidant form of glutathione yet elevated levels of its oxidized form.[106]

An additional argument for oxidative stress as a cause of cone degeneration is that antioxidant supplementation appears to preserve cone survival and ERG function in

mouse models of RP.[103,107] . There is also evidence that oral antioxidant N-acetylcysteine and its precursor N-acetylcysteine provide significant cone protection.[101,108,109] Similarly, upregulation of SOD gene expression leads to substantial cone protection and preserved visual function in mice with RP.[110,111]

Another explanation as to why secondary cone loss occurs in RP is that rods secrete trophic factors essential to cone survival. In rod-deficient retinas co-cultured with rod-rich retinal tissue, cone loss was significantly attenuated, suggesting the presence of diffusible trophic factors.[112] One such factor isolated from cone-rich chicken embryos has been identified as rod-derived cone viability factor (RdCVF).[113] Two isoforms of this factor have been identified: the short isoform of RdCVF expresses cone protective activity whilst the long isoform RdCVF-L does not. Retinal explants transfected with RdCVF expressed a higher number of cones than control retinas.[113] When RdCVF was removed from the medium through immunodepletion, cone protection became noticeably absent. In RP mouse models, RdCVF expression decreases during rod degeneration marking the onset of cone loss. Injection of exogenous RdCVF in autosomal dominant RP rats resulted in notable preservation of cones and their function as demonstrated by ERG.[114] Similarly, upregulation of RdCVF gene expression in mouse models of rod-cone dystrophy improved ERG cone function and delayed cone loss.[115] RdCVF may also play a role in combating retinal oxidative stress.[116] A second trophic factor, RdCVF 2 and, more specifically, its short isoform variant, has been identified to have potential cone protection ability however its efficacy remains unexplored.[117,118]

1.4.3 A potential bioenergetic mechanism of cone degeneration in RP

More recently, evidence has emerged of a bioenergetic component in the mechanism of cone death in RP. The discovery of an RdCVF receptor, Basigin-1 (BSG-1), expressed in cone inner segments has provided a potential mechanism for RdCVF to stimulate cone survival through aerobic glycolysis.[35] Aı¨t-Ali et al. revealed that BSG-1 itself binds to glucose transporter 1 (GLUT1) and this interaction increases glucose uptake to cones in the presence of RdCVF. The intracellular ATP concentration was also markedly elevated in RdCVF-treated cone cultures supplemented with glucose compared to negative control. Hence, rod loss would precipitate in RdCVF shortage and aerobic glycolysis compromise in cones. Subsequent energy failure would inevitably lead to cone death. The activation of the mammalian target of rapamycin (mTOR) signalling pathway has been attributed to cone preservation in RP.[34,119] The mTOR signaling pathway is responsible for the regulation of cell growth, metabolism, proliferation and energy status.[120] The mTOR protein is a serine-threonine kinase that is divided into two complexes: mTOR complex 1 (mTORC1) and mTOR complex 2 (mTORC2). Activation of mTORC1 in retinal degeneration mouse models led to enhanced glucose utilization and retention in addition to maintenance of NADPH levels, which further prevented caspase activation and apoptosis.[119] As a result, cone survival was significantly prolonged suggesting that a metabolic disturbance may play a role in secondary cone loss. With energy deficiency as a possible component of cone degeneration in RP, a bioenergetic based intervention could therefore conceivably be utilized to provide cone neuroprotection.

Therapies for RP

Currently, RP is an incurable condition. Vitamin A is the only treatment with demonstrable benefit in preserving electroretinographic cone function in RP patients.[121] Research on potential therapeutic modalities for RP currently include gene therapy[122,123], photoreceptor transplantations[124,125] and interventions targeting biochemical pathways[126].

1.4.4 An overview of relevant animal models to study RP

The use of animal models provides an essential foundation to study RP disease mechanisms and potential therapies. Rodent models are commonly used because of their cost-effectiveness and the availability of techniques for genetic manipulation (particularly in the case of mice). The Royal College Surgeons (RCS) rat displays retinal degeneration similar to RP caused by a genetic defect in the proto-oncogene tyrosine-protein kinase MER protein (MerTK) resulting in accumulation of debris in the outer retina from impaired RPE phagocytosis of rod OS. RCS rats display degeneration beginning at postnatal day (P)15-20 and becoming complete by around P60. On the other hand, the P23H rat is a commonly used animal model for autosomal dominant RP. The primary genetic defect in this model is the substitution of histidine for proline at codon 23 in the rhodopsin gene. The resulting abnormal rhodopsin impairs rod function and subsequently triggers rod degeneration as early as P10, rapidly followed by secondary cone loss [127]. By P180, most rods are depleted except for those in the periphery. Rod and cone degeneration occurs in a ring-like fashion, with degenerated retinal areas increasing in size and number between P90 and P180.[128]

The retinal degeneration-slow (*rds*) mouse is another model of RP that displays early onset retinal degeneration by P7 that slowly progresses. The ONL starts to degenerate by P14 and is completely obliterated within 12 months, with ERG readings becoming absent at this time.[129] The genetic defect in the *rds* mouse is the insertion of foreign DNA into an exon of peripherin 2, resulting in the failure to develop rod OS.

The retinal degeneration 10 (rd10) mouse is a model of autosomal recessive RP. Sequence analysis reveals a missense mutation in exon 13 of PDE6B. At 4 weeks, rd10 mice display retinal degeneration with sclerotic vessels. The ERG declines as early as P18 before becoming non-existent at P60.[129,130]

Arguably, the most well-known rodent model of autosomal recessive RP is the retinal degeneration 1 (rd1) mouse. The genetic defect in the rd1 mouse was established by murine viral insert and a second nonsense mutation in Exon 7 of the gene encoding for PDE6b. This defect results in cGMP accumulation which triggers photoreceptor degeneration.[131] Rd1 mice are characterized by early onset severe retinal degeneration with rod loss beginning at P8-10 and completing by P21.[76,132] By P21-28, the ONL progressively thins until there is only a single layer of cones that degenerate more gradually. The ERG signal is maximal at P14-15 and is comparable to age-matched normal mice but quickly declines, becoming undetectable at P21. Total loss of image-forming vision occurs by P40 and degeneration of most cones occurs by P100. [76]

1.5 Photobiomodulation

Photobiomodulation (PBM) or Red-Near Infrared (R-NIR) light therapy refers to the non-invasive irradiation of tissue with light in the far-red to near-infrared light spectrum

(630-1000 nm) with delivery methods varying from laser sources to light emitting diode (LED) devices.[133] The study of the therapeutic properties of light in the far red and near infrared range of the spectrum (630 – 1000 nm) began in the 1960s when it was serendipitously observed that the recently invented ruby laser enhanced wound healing in rats. Over the ensuing decades the field of PBM has broadened to include treatment of a range of conditions. Despite a level of underlying skepticism of PBM due to the broad range of its purported applications, an increasing number of reports from well-respected groups mean that support for this treatment is increasing. Pertinently, more recently, focus has turned to the potential beneficial effects of PBM as a treatment for blinding retinal diseases. Positive effects for PBM have been demonstrated in various retinal disease animal models including those for light-induced retinal degeneration[134-136], age-related macular degeneration (AMD)[137], retinitis pigmentosa[138], diabetic retinopathy[139] and retinopathy of prematurity[140,141] as evidenced by improved ERG , decreased inflammatory markers and diminished cell loss.

In terms of the clinic, there are some reports that state that PBM has yielded positive results in patients with AMD[142,143], diabetic retinopathy[144], amblyopia[145] and Retinitis Pigmentosa[146], as reflected in improvements in visual acuity and decreases in visual field loss. However, these clinical studies range from interventional case series to a single case report and therefore evidence surrounding the clinical efficacy of PBM remains unclear. Thus, it is still a matter of debate as to whether PBM really has any positive effects against retinal diseases. Nevertheless the mechanism of PBM and its relative safety should motivate more robust clinical studies.

1.5.1 Mechanisms of Photobiomodulation

Photobiomodulation targets Cytochrome C oxidase and unbinds nitric oxide

The mitochondrially-bound electron transport complex component, cytochrome C oxidase (COX), represents the primary photo-acceptor in biological systems for red/infrared light. As a source of red/near infrared light, therefore, PBM necessarily targets COX, and thus, must affect electron transfer in the reduction of oxygen during mitochondrial respiration. This would increase both the mitochondrial membrane potential (MMP) and the synthesis of ATP (Figure 1.4). Ultimately, this triggers and enhances cellular repair processes and metabolism in photoreceptors, choroid cells and the retinal pigment epithelium.[142] Evidence of COX as the primary target for PBM was confirmed by Eells who reported this treatment improved rat retinal function following methanol intoxication which is known to inhibit cytochrome oxidase activity.[147] PBM treatment of primary cultured neurones has also been shown to reverse the effect of tetrodotoxin by upregulating COX activity.[148]

Desmettre *et al*.[149] found that PBM laser therapy to the choroid induced increased expression of heat shock proteins, which are known to stimulate cellular metabolism and prevent premature cell death.

Another potential mechanism of PBM is the photo-dissociation of nitric oxide (NO) from COX as demonstrated by Karu *et a*l.[150]. NO is non-convalently bound to COX via its heme iron and copper binding centres, competing with oxygen and thereby preventing mitochondrial respiration. Hence, NO dissociation from COX would restore

mitochondrial oxygen consumption, therefore increasing energy production and boosting cellular metabolic processes.[133]

Activation of downstream retro-signalling pathways

In vitro experiments have reported that PBM therapy increases phagocytosis and lysosomal activity, both of which assist in reducing inflammation and enhancing repair of the retina.[151] These processes result from PBM triggering downstream signaling cascades via changing cellular levels of ATP, cAMP, NO, ROS and Ca^{2+} and eventual altered gene expression, promoting anti-inflammatory processes, enhancement of anti-oxidants defences and down-regulation of apoptosis as well as cell migration and proliferation.[152]

Protein synthesis

PBM has been demonstrated to increase protein expression in maturing epithelial cells in addition to collagen I production in human gingivial fibroblasts.[153,154] Irradiation with 660nm light also led to increased expression of collagen IV in skeletal muscles of injured rats. Similarly, osteoblasts showed elevated production of bone matrix proteins osteoglycin and mimecan following PBM.[155]

Anti-inflammation

PBM has been observed to decrease inflammation by inhibiting expression of prostaglandin E2, cyclooxygenase 1 and 2 mRNA expression in human fibroblast cells.[156] The proposed mechanism was through modulation of the pro-inflammatory nuclear factor-kappa B signaling pathway. Moreover, PBM has been reported to decrease the pro-inflammatory mediators TNF-α, IL-1β, IL-6, IL-8, IL-10 and inducible

Nitric Oxide (iNOS) in animal models of arthritis, wound healing, inflammatory lung disease and auto-immune encephalomyelitis. [156-162] Downregulation of the complement system by PBM has also been reported in retinal degenerative diseases.[163,164]

Modulation of oxidative stress

It is possible that the action of PBM on COX, and therefore the electron transport chain, influences mitochondrial ROS production in healthy cells. However, PBM is known to decrease ROS production and therefore provide an anti-oxidative effect during oxidative stress.[165] In culture, PBM has been observed to protect rat neural cells against oxidative injury and enhance neurite outgrowth.[166] Decreased signatures of oxidative stress including protein carbonyls and thiobarbituric acid reactive species as well as increased expression of the anti-oxidant enzymes SOD, glutathione perioxidase and catalase were reported following PBM, in diverse animal models including skeletal muscle injury, diabetes-impaired wound healing and inflammatory pain.[167-169]

Anti-apoptosis

Prevention of apoptosis is another notable reported effect of PBM. For example, PBM partially prevented caspase-mediated apoptosis of cultured cortical neurons exposed to potassium cyanide.[170] Furthermore, in an animal model of experimental autoimmune encephalitis, PBM stimulated the up-regulation of the apoptosis-preventative *bcl-2* gene, which resulted in decreased neuron death within the spinal cord.[162]. A similar effect was observed in skeletal muscles of aged rats after PBM irradiation.[171] Moreover, PBM treatment following experimental traumatic brain injury resulted in significant downregulation of the pro-apoptotic protein, Bax, in addition to a mild elevation in Bcl-2 expression.[172]

Cell migration and proliferation

PBM is also known to promote wound healing by stimulating cell proliferation and migration. For example, red light irradiation enhanced proliferation and maturation of keratinocytes and this was associated with enhanced expression of the cell division driver, Cyclin D1.[153] Likewise, human fibroblasts subjected to hyperglycaemia to simulate diabetes, and then exposed to PBM had an increased rate healing via proliferation and differentiation. This was associated with expression of epidermal growth factor and the "Janus kinase/Signal transducer and activators of transcription" (JAK/STAT) signalling pathway.[173] Furthermore, of some interest, PBM stimulated proliferation, migration, differentiation and viability elevation in stem cells.[174-176] This implies that since stem cell therapy is limited by the slow proliferation rate of undifferentiated cells, PBM may enhance clinical applications of this treatment modality.

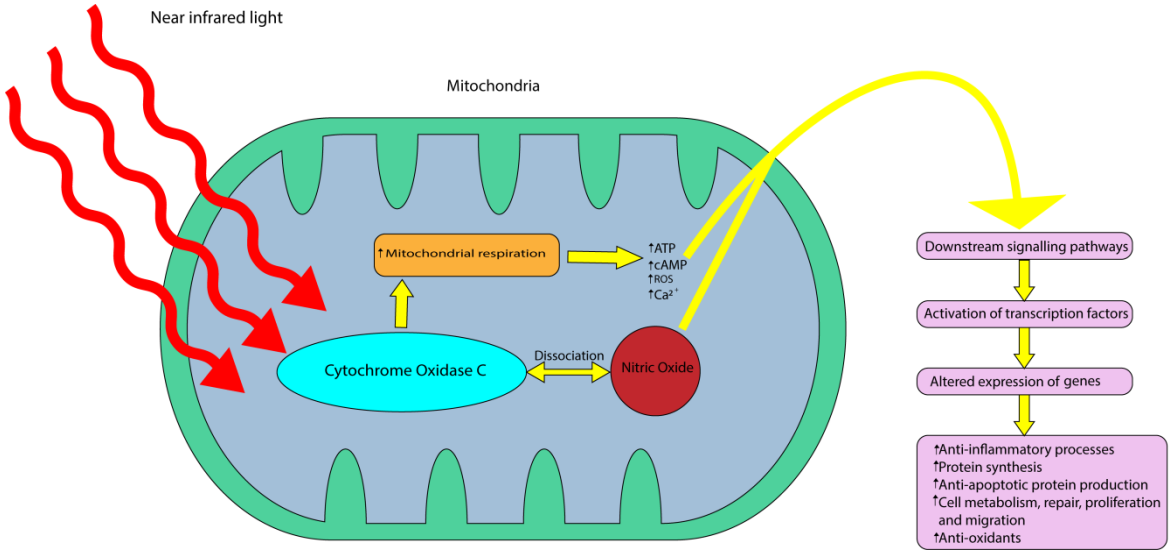

Figure 1.4: Schematic diagram of the proposed mechanisms of PBM. Near infrared light within wavelengths 630-1000 nm targets the mitochondrial enzyme Cytochrome C Oxidase resulting in 1) direct stimulation of mitochondrial respiration and 2) dissociation of nitric oxide which indirectly increases mitochondrial respiration. These processes result in elevation of ATP, cAMP, reactive oxygen species and intracellular calcium which impact downstream signalling pathways to increase anti-inflammatory processes, protein synthesis, anti-apoptotic protein production, cellular repair/metabolism/proliferation/migration and cellular anti-oxidant defences.

1.5.2 Treatment Parameters

The dosage values of PBM treatments vary widely between studies. Lack of consistency is compounded by the fact that dose values can be expressed in terms of either irradiance levels or fluence. Irradiance or power density corresponds to the power received by a surface per unit area and is expressed as mW/cm^2. Fluence, also known as energy density, refers to the energy received by a surface per unit area and is thus conveyed as J/cm^2. Care must be taken when comparing different studies to interconvert data from fluence to irradiance, as appropriate (see Figure 1.5). The fluence range typically used is 1-20 J/cm^2 while irradiance can vary greatly depending on the light source, spot size and purpose of therapy. Irradiances of 5-50 mW/cm^2 are typically used for stimulation and healing with much higher irradiances used for analgesia and nerve inhibition.[177] The frequency of treatment sessions can also vary with only a single session being needed for pain relief while chronic degenerative conditions can require ongoing frequent and multiple sessions.[177-179]

The wavelength typically used in PBM is 670 nm although there have been a few studies that have compared the efficacy of different wavelengths. Wong-Riley et al.[148] reported the most effective wavelengths for preventing neuronal death from COX

inhibition were 670 nm and 830 nm, corresponding with maximal absorption spectra of COX. Giacci et al.[180] noted 670 nm was more effective than 830 nm light in preserving visual function in a rat model of optic nerve transection. Interestingly, Giacci et al.[180] also reported 670 nm but not 830nm light significantly reduced photoreceptor apoptosis in light-induced retinal degeneration despite the greater measured tissue penetrance of the latter wavelength. In the same study, neither 670nm nor 830nm light were effective in treating spinal cord injuries or traumatic brain injuries of rats. The authors concluded that the efficacy of the wavelength varied depending on the nature of the tissue and severity of injury.

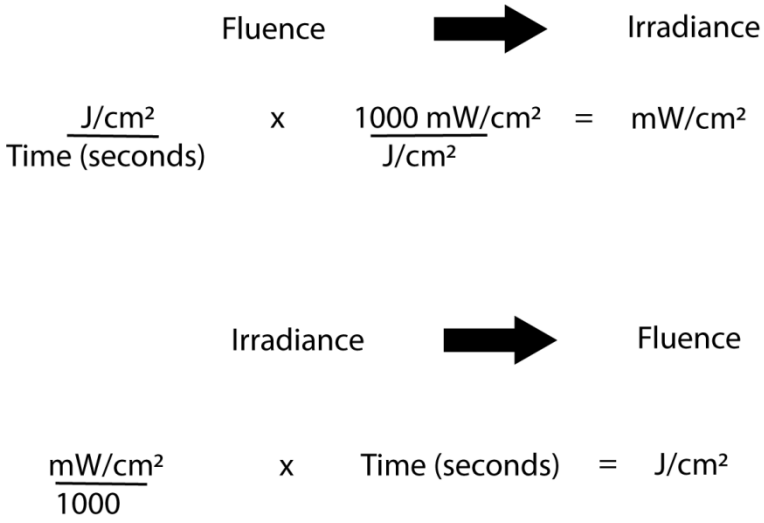

Figure 1.5: Interconversion of fluence and irradiance values.

1.5.3 Laser VS LED PBM

Previous studies have examined PBM delivered through either laser or LED.[181] Laser is an acronym for "light amplification by stimulated emission of radiation". Lasers use stimulated emission of electromagnetic radiation to produce a monochromatic coherent beam of light. On the other hand, LEDs are light sources that rely on the passage of electrical currents through semiconductor materials to release photons and subsequent light. Laser delivered PBM was long considered to be superior to LED-induced PBM due to their theoretically potential higher power densities and penetrance. However more recently, LED-delivered PBM has been increasingly preferred due to its safety, ease of use, ability to irradiate large areas and cost-effectiveness. Some comparative studies have suggested no difference in effectiveness between laser- and LED-delivered PBM however the majority of these studies have only examined wound healing.[181-184] In consideration of tissues such as the retina which are of limited size and exist within an enclosed structure, laser PBM may be more beneficial due to less scattering. However, the comparative effectiveness between laser and LED PBM remains a controversial topic in PBM research.

1.5.4 Biphasic dose response

PBM has been observed to have a biphasic dose response whereby the magnitude of its positive effects increases in relation to the applied energy level until a particular dose is reached, after which effects are significantly less beneficial or even adverse. The biphasic dose response curve is consistent with "Arndt-Schulz law" which states that

weak stimuli slightly accelerates vital activity with stronger stimuli raising it further until a maximum response is reached. At this point, a stronger stimulus will cause suppression until a negative response is achieved. This phenomenon has been demonstrated on cortical neurons in vitro[177,185] where it was noted that at low energy levels, PBM increased mitochondrial membrane potential, but that at high energy there was an adverse effect on this parameter, causing it to decline to below that of untreated cells. In rat models of myocardial infarction, beneficial effects were observed at 5 mW/cm^2 whilst higher irradiances of 25 mW/cm^2 were associated with considerably less benefits.[186] In another study, only treatment with an irradiance of 8 mW/cm^2 out of a range of 0.7-40 mW/cm^2 improved wound ulcers in irradiated mice.[187] Chu-Tan et al.[188] further reported a biphasic dose response for PBM following low, medium or high light-induced retinal injury in rats. In low or medium light-induced retinal injury, lower fluences of 9 J/cm^2 and 18 J/cm^2 decreased photoreceptor apoptosis, however 36 J/cm^2 was ineffective and 90 J/cm^2 even increased photoreceptor death. With high intensity light-induced retinal injuries, only 90 J/cm^2 PBM significantly reduced photoreceptor apoptosis, suggesting the efficacy of PBM dosages are intrinsically linked to the severity of damage.

1.5.5 Photobiomodulation in degenerative retinal diseases

1.5.5.1 Laboratory studies of PBM

There have been numerous laboratory studies investigating the effect of PBM in rodent models of retinal degeneration.

1.5.5.1a Age-related retinal degeneration

In an aged mouse model of retinal degeneration, Kokkinopoulos[164] reported that PBM improved mitochondrial function in RPE cells and also reduced tissue inflammation. Following five treatments of NIR light exposure at 40 mW/cm^2 lasting 90 seconds, researchers detected a significantly increased mitochondrial membrane potential as well as reducing Complement Component C3d, pro-inflammatory cytokine TNF-α and total macrophage numbers. This was confirmed by Begum *et al.*.[137] who reported similar results in Complement Factor H (CFH) knockout mice. Mice exposed to R/NIR light at 20 mW/cm^2 for 6 minutes twice daily for 2 weeks had significantly increased COX expression, decreased Complement C3 deposition in the outer retina as well as reduced reactive gliosis markers vimentin and GFAP. There were also notable changes in the morphology of RPE cells, macrophages and dendritic cells however there was no significant change in numbers. It is important to note here that the relatively indirect delivery of PBM through supplemental environmental lighting in this study demonstrated the effectiveness of RR/NIR light in penetrating tissue to reach the target. Calaza *et al.*[189] reported improved retinal ATP levels in CFH knockout mice following R-NIR light exposure at 40 mW/cm^2 supporting evidence that PBM improves oxidative phosphorylation. In a separate experiment, Kokkinopoulos[190] reported that PBM can drastically ameliorate inflammation from innate immunity. CFH knockout mice exhibited decreased Complement C3b expression in the outer retina following exposure to regular 90 second doses of R/NIR light twice a day for two days at 40 mW/cm^2 over 8 weeks. Interestingly, Toll-like receptor 2 (TLR 2) 2 and Toll-like receptor 4 (TLR 4) expression decreased in the retinal inner nuclear layer but not in the RPE in these

animals showing differential effects on distinct cell types. Expression of the systemic inflammatory marker calcitonin was also significantly decreased in all layers.

1.5.5.1.b Retinal light toxicity

In a light induced model of atrophic AMD, 3 minutes of daily R/NIR light exposure at 9 J/cm^{2}over 5 days was reported to reduce complement propagation, C3 deposition, photoreceptor death and oxidative stress.[163] Abarracin et al.[191] also reported a significant decrease in photoreceptor apoptosis, mitigation of OS loss, preservation of the *opn1mw* cone opsin gene and improvement of cone ERG b-wave amplitudes in eyes treated with 3 minutes of PBM at 60 mW/cm^2 irradiance compared to untreated eyes in a light-induced AMD rodent model. In this light-induced AMD model, Natoli et al.[192] were able to show down-regulation of genes for the proinflammatory cytokine ccl2, and stress factors GFAP and fgf-2 in PBM treated eyes, further suggesting that PBM interacts with inflammatory and apoptotic pathways. In a retinopathy of prematurity rodent model, Natoli et al. [140] reported decreased vaso-obliteration, neovascularization and peripheral retinal vessel branching after PBM. Similarly, Di Marco et al.[193] described PBM preconditioning 2-10 days prior to light-induced retinal injury with reduced photoreceptor apoptosis, ameliorated ONL thinning and downregulated GFAP expression in Müller cells. In a non-human primate model of laser-induced retinal injury, Eells et al.[194] reported preservation of multifocal ERG amplitude and total retinal thickness following PBM treatment. Most remarkably, as the authors reported upregulation of COX expression in the lateral geniculate nucleus suggesting extension of PBM benefits beyond the treated retina.

1.5.5.1c Retinitis Pigmentosa

In P23H rats, Eells et al.[195] described decreased photoreceptor apoptosis and upregulation of COX, ciliary neurotrophic factor (CNTF) and mitochondrial superoxide dismutase (Mn-SOD) in PBM treated eyes.

1.5.5.1d Other retinal degenerative models

PBM has also been demonstrated to decrease oxidative stress and inflammatory markers, protect retinal ganglion cells as well as improve visual function in diabetic retinopathy [139,196] in addition to optic nerve injury[197,198] rodent and in-vitro models.

1.5.5.2 PBM clinical studies

There have been clinical studies that suggest PBM provides benefit for sufferers of degenerative retinal disease, however, they are largely limited and far from robust in design.

1.5.5.2a Retinitis Pigmentosa

A single case report of PBM on an RP patient noted improvements in both visual acuity and visual field following four treatments provided over two weeks.[146]The study involved irradiation of the whole retina with 780 nm light from a continuous wave laser diode, lasting 40s at a total of 0.4 J/cm^2 per treatment. Interestingly, the patient's visual acuity was maintained for a further five years before a visual decline to pre-treatment levels. Reportedly only another four treatments were required to restore vision gains. The evidence of general benefit in this case remains at best unsubstantiated given the

small sample size, subjective nature of visual acuity measurements and the unexplained mechanism of maintaining vision over years despite only four treatments.

1.5.5.2b Diabetic macular oedema

Tang et al.[144] reported significant reductions in non-central diabetic macular oedema and focal retinal thickness in four eyes of four patients following PBM. Eyes prior to treatment had perfect visual acuity which was generally preserved post-treatment. The efficacy of PBM is difficult to conclude in this case series given the non-randomized design, absence of placebo control, small sample size and no mechanistic explanation for the observed reduction of retinal oedema.

1.5.5.2c Age-related Macular Degeneration

There have also been several clinical studies investigating the effects of PBM on AMD patients including a prospective study by Ivandic and Ivandic[142] where 348 eyes of 203 patients with dry and wet type AMD were exposed to 40 seconds of 780 nm light from a semiconductor laser diode with 0.3 J/cm^2 delivered to the macula four times over 2 weeks. The treatment group included 146 eyes with cataracts and 182 without. The remaining 20 eyes of 10 patients received sham treatments and served as the control group. There was substantial improvement in both treated groups with 97% of patients with cataracts improving in visual acuity by a mean of 2 lines and 94.5% of the non-cataract patients by the same amount up to 36 months. The authors also reported reduced pigmentation and cystic drusen as well as improvement in metamorphopsia, dyschromatopsia and relative scotomas. Patients with wet AMD had reduced oedema and bleeding. No change was observed in the control group. The TORPA II study, which examined 42 eyes in 24 patients with dry AMD by Merry G *et al.*.[199] consisted of

delivering 88 seconds of 670 nm light at 4-7.7 J/cm^2 through LED-based devices as well as 590 and 790 nm for 35 seconds delivering 0.1 J/cm^2 in nine treatments over 3 weeks. Following PBM, there were positive functional changes indicated by improvement of contrast sensitivity and visual acuity at 3 weeks and 3 months as well as anatomical improvement exhibited by decrease in drusen volume and central drusen thickness. However, there were significant flaws in the methodologies of both studies: lack of a suitable control arm or significant number discrepancies between treatment groups, large ranges in total dosages delivered, as well as a broad patient demographic with varying stages of disease being noted and uncontrolled. Hence, it is difficult to conclude clinical efficacy of PBM in these studies.

1.5.6 Safety profile

PBM has an impressive safety profile likely due to the low-power and non-thermal nature of the administering devices (lasers and LEDs). Furthermore, R/NIR laser treatment is non-invasive compared to surgery or intravitreal injections, which are used, for example, in the treatment of wet AMD. The treatment regimens in previous studies have used mainly LED to deliver R-NIR light and have varying dosages, duration and frequency. Therefore, there is currently no consensus on treatment parameters in particular to the delivery of R-NIR light through laser.

1.6 Aims of the study

1.6.1 Rationale for the study

The overall rationale behind the study is the exploration of novel strategies to protect or prevent degeneration of photoreceptors in devastating retinal diseases such as RP[34,35], AMD[36,37], diabetic retinopathy[38] and central retinal artery/vein occlusion[39,40]. It is believed that one common component in the pathogenesis of these conditions is a degree of energy deficiency to part of the retina. Hence, it is hypothesized that one pertinent avenue of treatment would be based on the principle of augmenting the available retinal energy supply.

As stated, PBM has been found in previous studies to increase cellular metabolism, energy availability and metabolic repair processes. PBM is thus believed to provide a strong protective effect to cells that have been exposed to injury, particularly when the insult is based upon an energy deficit. The overall focus of this work, therefore, was to investigate whether PBM represents a valid neuroprotective strategy in the treatment of blinding eye diseases, especially involving degeneration of photoreceptors, and especially where an energy deficit is likely involved.

1.6.2 Specific aims of the study

(1) **To assess the safety profile of the R/NIR laser as our means of applying PBM to a rodent retina and to define suitable parameters for treatment with this laser.**

An important consideration in the development of a novel disease treatment is whether the intervention alone causes any detrimental effects. To this end, the first experiment

was designed to investigate the safety profile of PBM in rodent eyes. More specifically, R/NIR light was applied to rodent eyes, via laser treatment, to determine whether it caused any adverse or detrimental effects to the retina.

(2) **To determine whether PBM, as applied by R/NIR laser, could prevent secondary cone degeneration in the rd1 mouse model of inherited photoreceptor loss.**

Having established both a suitable safety profile and the operating parameters for the PBM treatment, our second experiment was to examine the neuroprotective efficacy of this treatment for the rd1 mouse model of autosomal recessive RP. We undertook this investigation by examining the effect of PBM in preserving cones and their function in this model.

2. Materials and Methods

2.1 Animals ethics and handling

Permission to use animals was obtained from the Central Adelaide Local Health Network Animal Ethics Committee. The work undertaken conforms with both the Australian Code of practice for the Care and Use of Animals for Scientific Purposes, 2013, and to the ARVO statement for the Use of Animals in Ophthalmic and Vision Research. Animals were obtained from the University of Adelaide, Adelaide, South Australia. They were housed in temperature- and humidity-regulated rooms with 12 hour light and 12 hour dark cycles. Food and water were provided ad libitum. Prior to procedures in the first experiment, animals underwent general anaesthesia with an intraperitoneal injection of a mixture of 100mg/kg ketamine (Sigma-Aldrich, Missouri, USA) and 10mg/kg xylazine (Sigma-Aldrich, Missouri, USA). In the second experiment, only isofluorane was required for anaesthesia throughout the laser procedure. At the conclusion of the experiment, animals were humanely killed with transcardial perfusion of physiological saline under general anaesthesia. Globes with optic nerve attached were then carefully dissected. The superior aspect of the conjunctiva was marked with a dye for the purpose of orientation.

2.2 Laser equipment

The system comprised a slit-lamp (Ellex Medical Lasers, Adelaide, South Australia, Australia) that emits a 670 nm laser (Figure 2.1). The beam was 4.5 mm in diameter with a flat-top profile. Depending on the treatment group, the power setting was

adjusted according to a reference table created by Ellex Medical Lasers that took into consideration the animal's maximum dilated pupil size to produce the intended irradiance at the retina.

Figure 2.1 Laser equipment set-up. The anaesthetised rat is placed onto a custom-designed platform attached to a slit lamp. The irradiance dose was produced by adjusting the power setting with reference to a setting conversion table.

2.3 Laser procedure

Once the animal was anaesthetised, a drop of 1% tropicamide (Bausch and Lomb, New York, USA) and a drop of 0.4 % oxybuprocaine (Bausch and Lomb, New York, USA) were sequentially applied to one eye, in order to dilate the pupil and provide local anaesthesia, respectively. The animal was placed on a specially designed platform attached to the slit lamp. The fundus was then visualized by holding a microscope

coverslip lubricated with methylcellulose against the cornea of the eye. The power setting was adjusted to reflect the intended irradiance (Figure 2.2). Focusing and centring on the optic nerve head, continuous 670 nm laser was applied for 90 seconds (Figure 2.3). The fellow eye served as a control. Following the procedure, the animal was placed back into its cage that was heated to 37˚C to maintain body warmth.

Power Setting on Remote (mW)	Power Delivery on Target (mW)	Intensity on Target (mW/cm2)
50	**5.0**	**31**
60	6.0	38
70	7.0	44
80	8.0	50
90	9.0	56
100	10.0	63
110	11.0	69
120	12.0	75
130	13.0	81
140	14.0	88
150	15.0	94
160	16.0	100
170	17.0	106
180	18.0	113
190	19.0	119
200	**20.0**	**125**
220	22.0	138
240	24.0	150
260	26.0	163
280	28.0	175
300	30.0	188
320	32.0	200
340	34.0	213
360	36.0	225
380	38.0	238
400	**40.0**	**250**
420	42.0	263
440	44.0	275
460	46.0	288
480	48.0	300
500	50.0	313
550	55.0	344
600	60.0	375
650	65.0	406
700	70.0	438
750	75.0	469
800	80.0	500
850	85.0	531
900	90.0	563
950	95.0	594
1000	100.0	625

Figure 2.2: Power calibration table provided by Ellex lasers for the PBM laser. The table applies to both rats and mice.

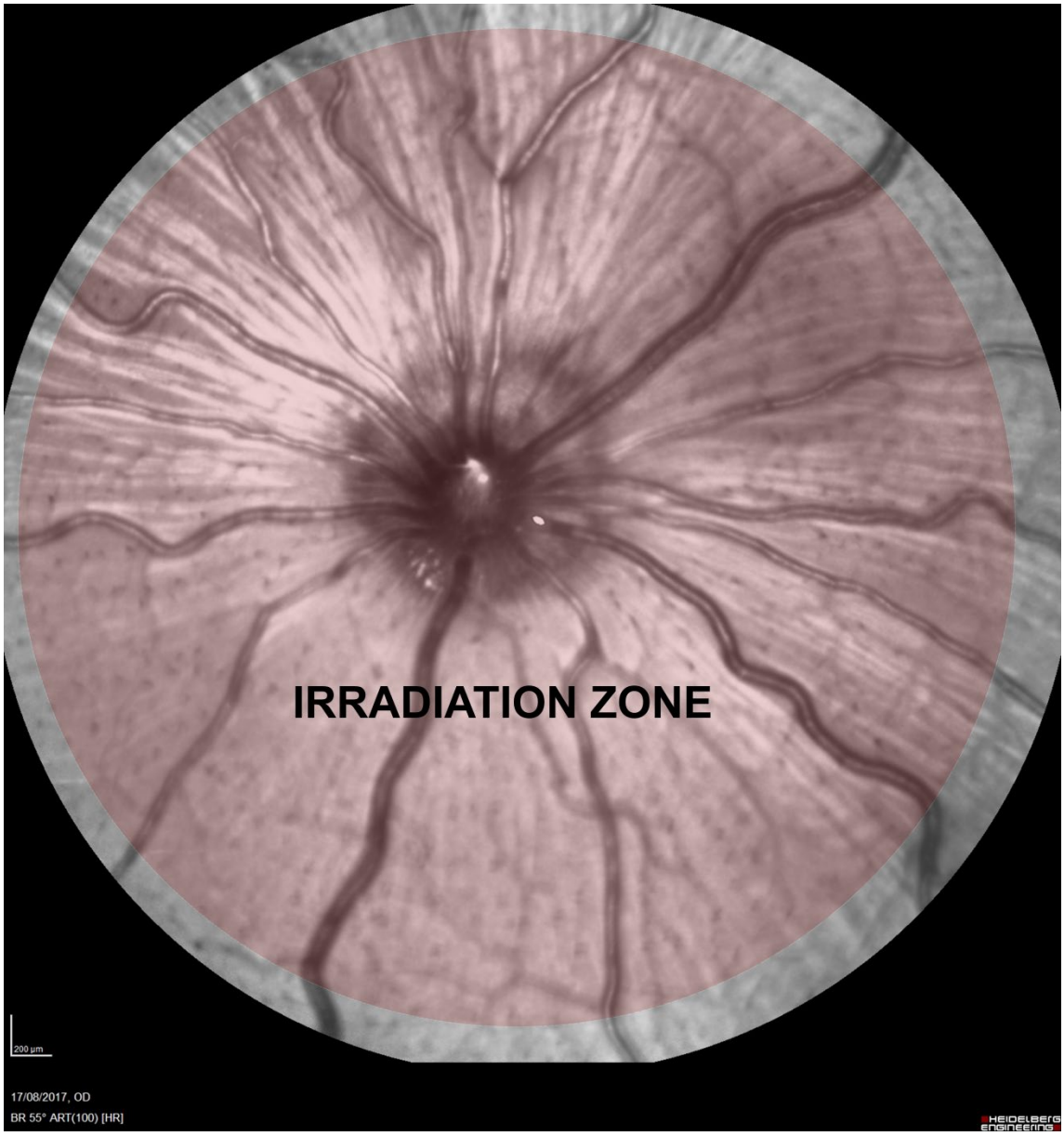

Figure 2.3: Confocal scanning laser ophthalmoscopy fundus photo with depicted irradiation zone. During the laser procedure, the fundus was visualized with a microscope coverslip lubricated with methylcellulose applied to the cornea.

2.4 Scotopic Electroretinography (ERG)

Animals were dark adapted overnight and prepared under dim red light in order to maintain adaptation.Animals were placed under intraperitoneal anaesthesia (ketamine 100 mg/kg and xylazine 10 mg/kg). Single drops of both anaesthetic (oxybuprocaine) and pupil dilator (tropicamide) was applied to each eye. The animal was placed on a heated platform to maintain body temperature throughout the procedure. Gold electrodes were used with the positive electrode placed on the central cornea, the reference electrode on the tongue and the ground electrode was attached to the scruff of the neck (Figure 2.4). Preservative-free lubricating eye drops (0.4% polyethylene glycol 400, 0.3% propylene glycole) were applied intermittently to prevent exposure keratopathy. A single bright light flash from a mini-ganzfeld photic stimulator (brightness of 20 cd·s/m^2, duration 10 ms, distance 10 cm) was directed at the animal's eye. The signals were amplified (gain set at 1000) and filtered (0.3 Hz high pass-300 Hz low pass) with a DC amplifier (ADI instruments, New South Wales, Australia). All recordings were performed under complete darkness. Ten responses were recorded and averaged with LabChart software (ADI instruments, New South Wales, Australia). The a-wave amplitude was measured from the pre-stimulus amplitude to the trough of the a-wave. The b-wave amplitude was measured from the trough of the a-wave to the peak of the b-wave (Figure 2.5). The negative a-wave reflects the reduction in the 'dark' currents from light absorption in the photoreceptor outer segments and closure of cGMP-gated cationic channels.[200] Hence, the a-wave is representative of photoreceptor function. The b-wave represents inner retinal function. It derives from changes in the membrane potential of Müller cells in response to light-induced increases in extracellular potassium

from depolarized bipolar cells.[201] The implicit time, which refers to the time from the start of stimulus to the peak of the wave, was also measured for the a- and b-wave.

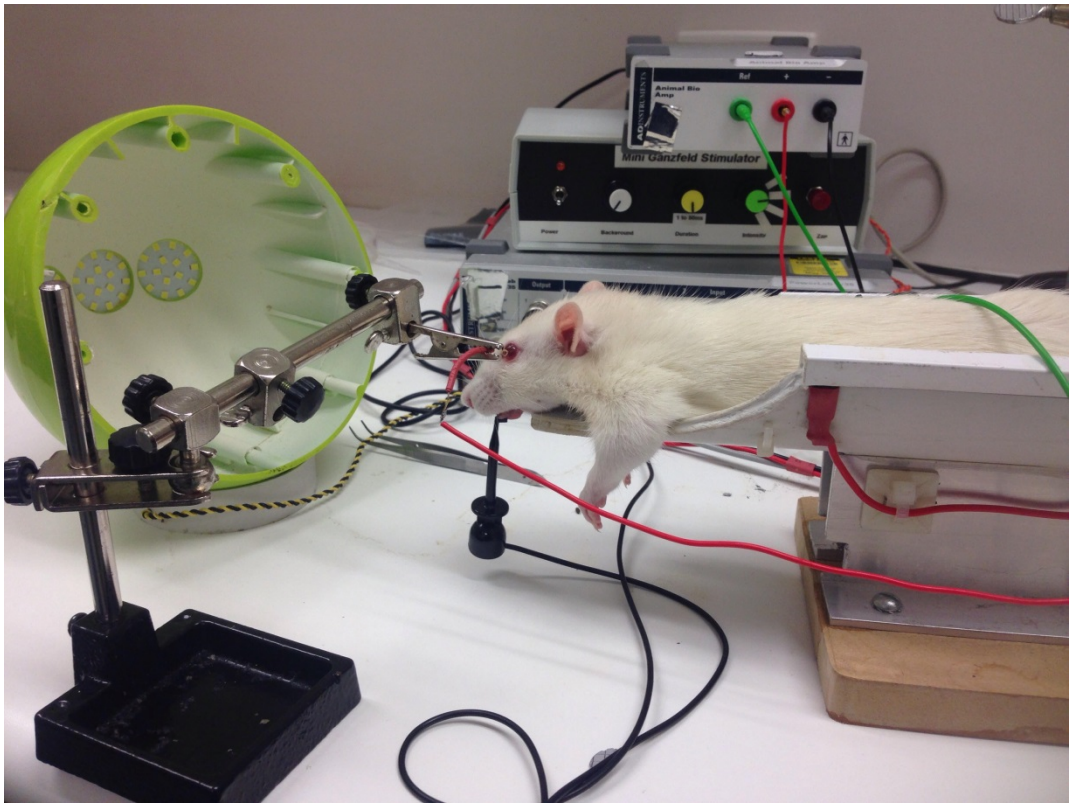

Figure 2.4 ERG set-up. The anaesthetized animal was placed onto a platform heated to 37˚ C. The positive electrode was placed lightly on the central cornea. The negative electrode and ground electrode were applied to the tongue and scruff of the neck, respectively. Recordings were performed in the dark with the animal dark-adapted overnight prior to readings being taken.

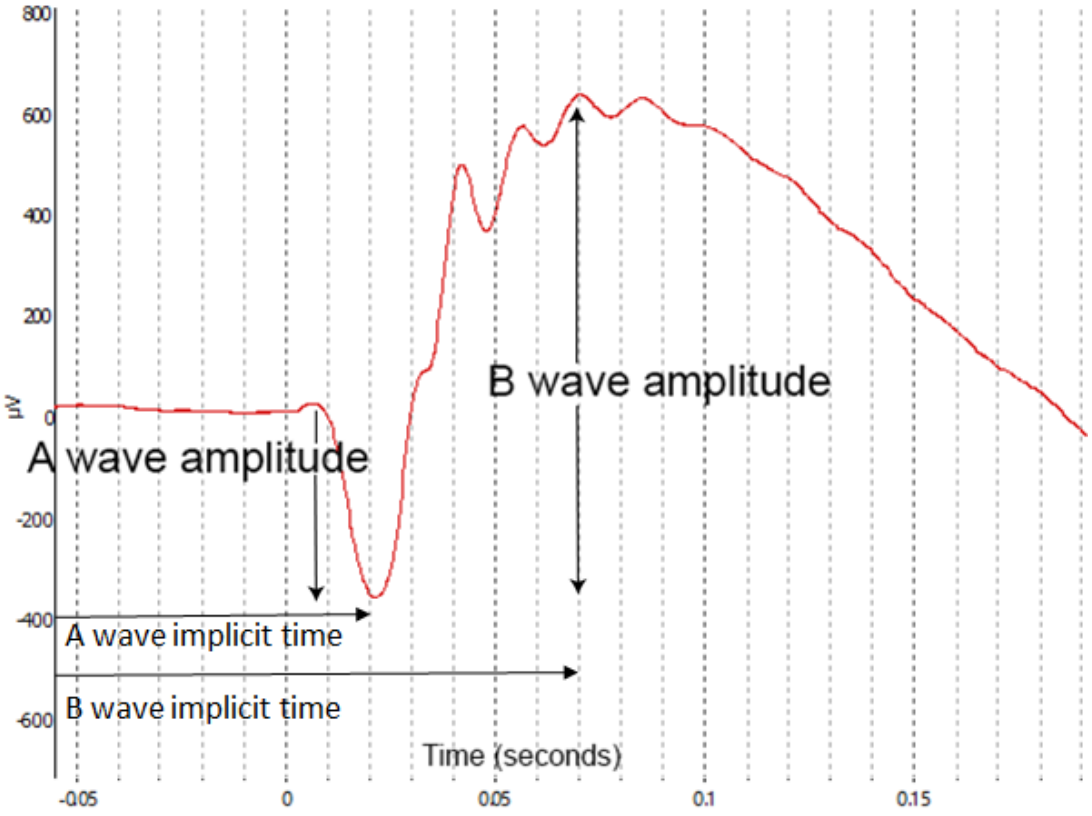

Figure 2.5 Representative ERG from a normal, untreated animal. Ten recordings were averaged and saved on Labchart. The a-wave amplitude, which represented photoreceptor function, was recorded as the pre-stimulus amplitude to the trough of the a-wave. The b-wave, which denotes inner retinal function, was measured from the trough of the a-wave to the peak of the b-wave. Implicit times for the a- and b-waves were measured from the start of the stimulus to the peak of the wave.

2.5 Spectral Domain Optical Coherence Tomography (SD-OCT)

Animals were anaesthetised with intraperitoneal ketamine/xylazine before receiving a drop of topical tropicamide to dilate the pupils, and then placed on a custom designed platform in a position so that the eye faced the camera. Capture of SD-OCT images was

performed using the Heidelberg Spectralis (Heidelberg Engineering, Heidelberg, Germany). A wide-field 55° lens was used to capture an overall view of the retina. A series of 97 B-scan SD-OCT images were captured at the optic nerve head, entirely contained within the lasered area and measuring 2.4 mm x 1.7 mm. The distance between each B-scan was 18 µm. A confocal scanning laser ophthalmoscopy image of the corresponding fundus was also taken. The corneal-curvature was adjusted to 3.0 mm, appropriate for rats, to allow accurate scaling for subsequent thickness measurements.[202] Throughout the procedure, preservative-free lubricant eye drops (0.4% polyethylene glycol 400, 0.3% propylene glycole) were administered to the eye to prevent corneal dryness and image artifacts. The total retinal thickness and outer nuclear layer (ONL) thickness were measured at specified points using the in-built Heidelberg Spectralis software (Figure 2.6). Thickness measurements were averaged for each eye.

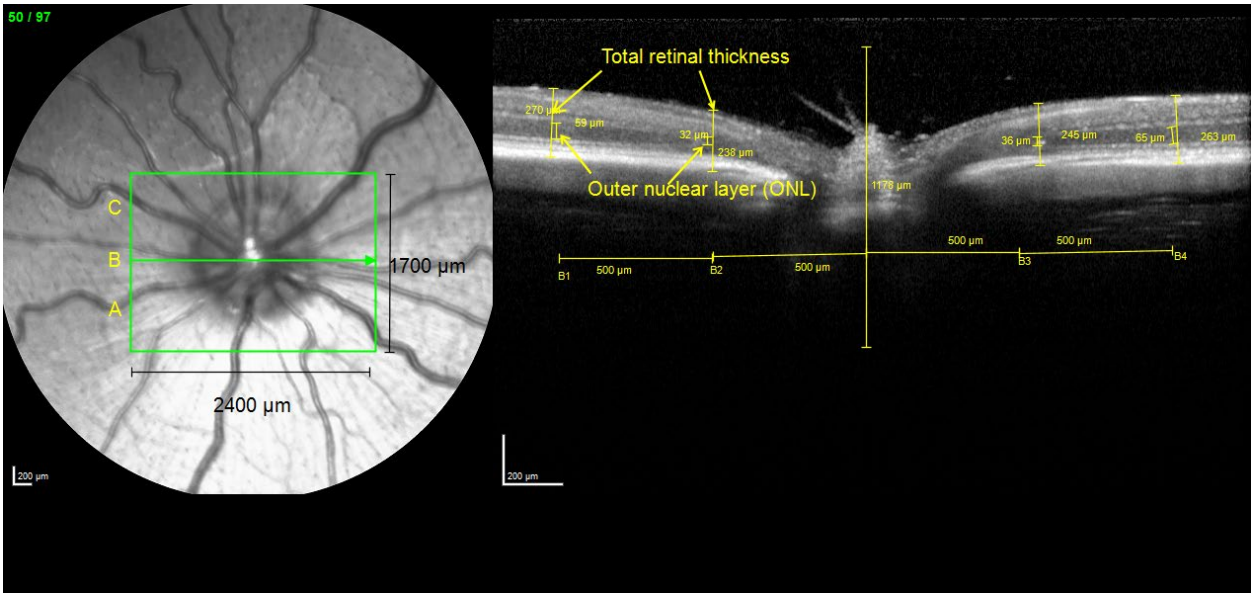

Figure 2.6 Representative SD-OCT image. Three SD-OCT slices (A, B and C) at 480 µm apart were used for each eye. The retinal cross-section of slice B is shown as an

example. Four measurements of total retinal thickness and ONL thickness were taken in each slice. Measurements were taken at a horizontal distance of 500 µm and 1000 µm from the centre of the optic nerve on each side. This produced 12 measurements for total retinal thickness and ONL thickness. Measurements were then averaged for each eye.

2.6 Fluorescein angiography (FA)

The animal was anaesthetized with intraperitoneal ketamine/xylazine, as described above, before a drop of the pupil dilator, tropicamide, was applied. Fluorescein (10%, w/v) 5 mL was injected intraperitoneally. The animal was then placed on the custom designed platform facing the camera. FA images were taken with the Heidelberg Spectralis in Angiography mode (Figure 2.7). FA images of the retinal vessels focusing on the area of the optic nerve head were captured at 0, 5, 10, 15 and 20 minutes after fluorescein injection. Preservative-free lubricant eye drops (0.4% polyethylene glycol 400, 0.3% propylene glycol) were administered to the eye to prevent corneal dryness and image artifacts throughout the scanning process. Images were analyzed for any leakage which was defined as any focal hyperfluorescence that increased in intensity and size over time.

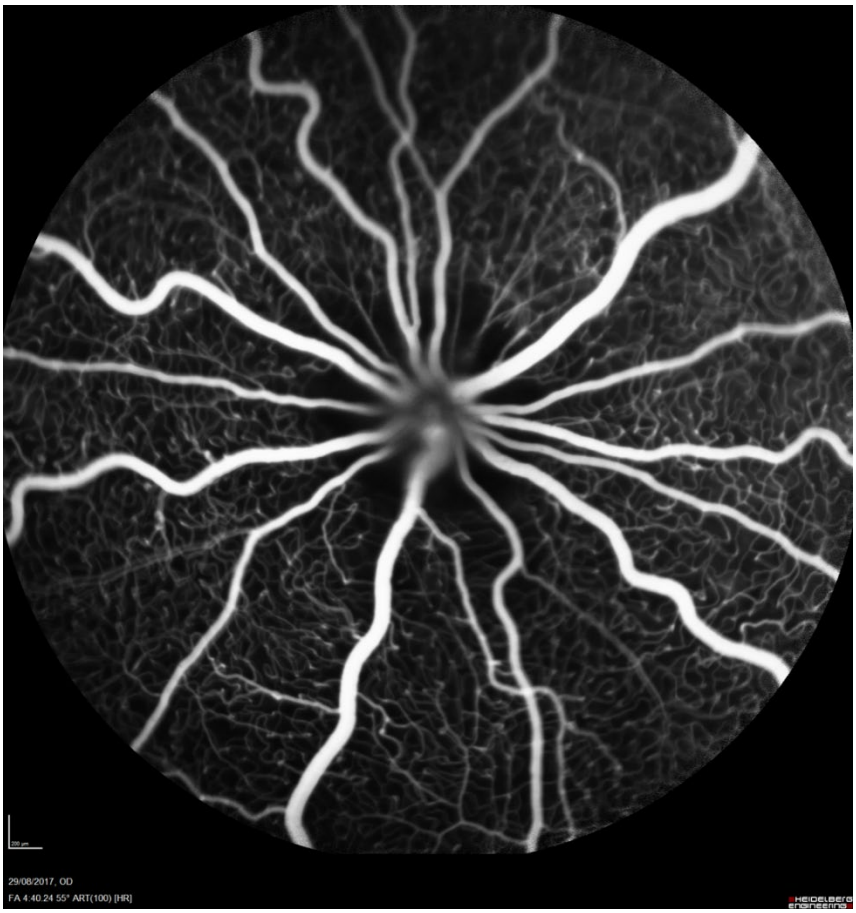

Figure 2.7 Representative FA image captured by confocal scanning laser ophthalmoscopy with the Heidelberg Spectralis in angiography mode.

2.7 Optokinetic Response

The optokinetic test is commonly used to measure the visual function of an animal by observing the maximum spatial frequency of a rotating visual stimulus for which the animal responds with a head reflex.[203] Animals were placed on a platform on a floor mirror surrounded by computer monitors that formed an enclosed area and allowed a continuous movement of the projected image. Vertical sine wave gratings (100% contrast) were projected on the computer monitors. The spatial frequencies tested were 0.05, 0.075, 0.1, 0.2, 0.3, 0.4, 0.5, and 0.6 cycles per degree (cpd). A camera was placed above

the platform to observe and record the animal's head movements. Mice were placed one at a time on the platform and allowed to acclimatize to their surroundings before starting the stimulus. The stimulus consisted of a grating perceptible to the mouse that was projected on the cylinder wall which rotated at a constant 12 degrees /second. Two independent experimenters blinded to the treatment groups monitored for a head reflex characterized by the animal displaying reflexive head movements corresponding to the direction and speed of the cylinder rotation that was not accompanied by any other body movements. A positive response was recorded only if the reflexive head movement occurred within the first 15 seconds of the stimulus and there was agreement between the experimenters. Assessment of the left or right eye was dependent on cylinder direction.[204] Clockwise direction of the cylinder corresponded to the left eye whilst counterclockwise direction was related to the right eye. The spatial frequency of the grating was progressively increased until the animal no longer responded. The maximum spatial frequency for a positive head reflex was recorded. This was repeated for each eye. Recorded videos of the test were reassessed by an independent observer for each mouse to avoid discrepancies in recorded results.

2.8 Retinal whole-mounts

2.8.1 Dissection

Eye globes were immersed in 10% (w/v) neutral buffered formalin for at least 24 hours before dissection. Dissection was performed under a high magnification operating microscope with the globe immersed in phosphate buffered saline (PBS) solution containing 137 mM NaCl, 2.7 mM KCl, 8 mM Na_2HPO_4, and 2 mM KH_2PO_4. An initial

cut was made below the ora serrata with a scalpel blade. With straight-blade spring scissors, the cut was extended circumferentially until separation between the anterior and posterior segments was achieved. At the point of the marked conjunctiva on the posterior eye cup, a small radial cut was made to signify the superior retina. Larger radial cuts were made to create the four "petal" quadrants of the retina whilst still attached to the RPE. Straight fine forceps were used to grasp the one side of the RPE petal behind the retina whilst angled forceps were applied on the other side. By pulling the forceps in opposite directions, the RPE petal was gently peeled away from retina. This was repeated for all remaining quadrants. Finally, blunt dissection was used to separate the retina from the RPE at the optic nerve head.

2.8.2 Immunohistochemistry

Initially, retinas were incubated in PBS containing 1% (v/v) Triton X-100 detergent (PBS-T) for 1 hour at room temperature. Next, retinas were incubated in PBS-T containing 3% (v/v) normal horse serum (NHS-T) for 1 hour at room temperature to block non-specific antibody binding. Retinas were then incubated overnight at 4°C with a combination of primary antibodies diluted in NHS-T. Anti-S-opsin antibody (see Table 2.1) was used to detect short-wave sensitive cones, whilst anti-M/L opsin antibody (see Table 2.1) was used to detect medium/long wave sensitive opsin cones. On day 2, retinas were washed for 1 hour at room temperature in PBS-T, then incubated overnight at 4°C with a combination of AlexaFluor-488 and -594 conjugated secondary antibodies (1:250; Invitrogen, Carlsbad, CA) diluted in NHS-T. Finally, retinas were

washed in PBS for 1 hour at room temperature prior to mounting with the photoreceptor side facing up, using anti-fade mounting medium (Dako, California, USA).

2.8.2 Quantification

All analyses were conducted in a blinded fashion. Photomicrographs of wholemounts were taken with an epifluorescent microscope with attached fluorescent optics (BX-61; Olympus, Mount Waverly, VIC, Australia). Rectangular areas of 350 x 250 µm were photographed adjacent to the optic disk and 2 mm away from the optic disk in each of the retinal quadrants (Figure 2.8). This yielded 8 photos per retina. Quantification of cone survival was performed using Image-J software (NIH, Bethesda, Maryland, USA). Initially, however, images were processed in Photoshop CS3 (Adobe). Images were corrected for uneven lighting using a flatten filter and where necessary linear gradient tool, then sharpened, levels enhanced, and finally converted to 8-bit mode.

Cone cell bodies were identified by both their wide ovoid morphology, segments by their narrow, bundle-like appearance. For determination of total S-cone and total M/L-cone labelling, images were manually thresholded until all cone cell bodies and segments were highlighted. The area in pixels was then calculated with the "analyze particles" function, using a minimum size of 5 square pixels. As shown in section 4.3.4 ML-opsin segments stained with greater fluorescent intensity then cell bodies. This permitted quantification of M/L-opsin-labelled cone segment survival (which necessarily comprises both genuine M/L-cones and dual cones). Quantification of segments was performed by adjusting the image threshold to isolate the more intensely stained M/L-

opsin segments. The area in pixels was then calculated with the "analyse particles" function, using a minimum size of 5 square pixels. In contrast to M/L-opsin, S-opsin cone cell bodies and segments stained with similar intensity. Hence, quantification of S-opsin cones included both cone cell bodies and segments.

For characterisation of the proportion of genuine M/L-cones, genuine S-cones, and dual cones in 60 day old rd1 mice, images captured from the superior, inferior, temporal and nasal quadrants of the peripheral retina of 24 animals were analysed. In Photoshop CS3, each pair of S-Opsin and M/L-opsin images were corrected for uneven lighting using a flatten filter, and where necessary linear gradient tool, and adjusted to be of approximately the same intensity. The images were then merged (M/L-opsin, green channel; S-Opsin, red channel), sharpened, levels enhanced, filtered for "noise/dust" and finally converted to 8-bit mode. In Image-J software, colour thresholding was performed on each merged image to determine the proportion of "red", "yellow" and "green" cones, which correspond to "genuine S-cones", "dual cones", and "genuine M/L-cones", respectively. To facilitate this goal, the total area of "all" cones within the image was first determined by manually thresholding using the "brightness" scale, with "saturation" and "Hue" set at the maximum range of 0-255. Next, to delineate the proportion of individual cone types, the "Hue scale was altered as follows: Hue 0-14 (red), Hue 14-50 (yellow), Hue 50-150 (green). For each "Hue" setting, the area in pixels was calculated using the "analyze particles" function, using a minimum size of 100 square pixels to remove background any debris or shards of staining. For each Hue setting, a mask of the labelled area was produced.

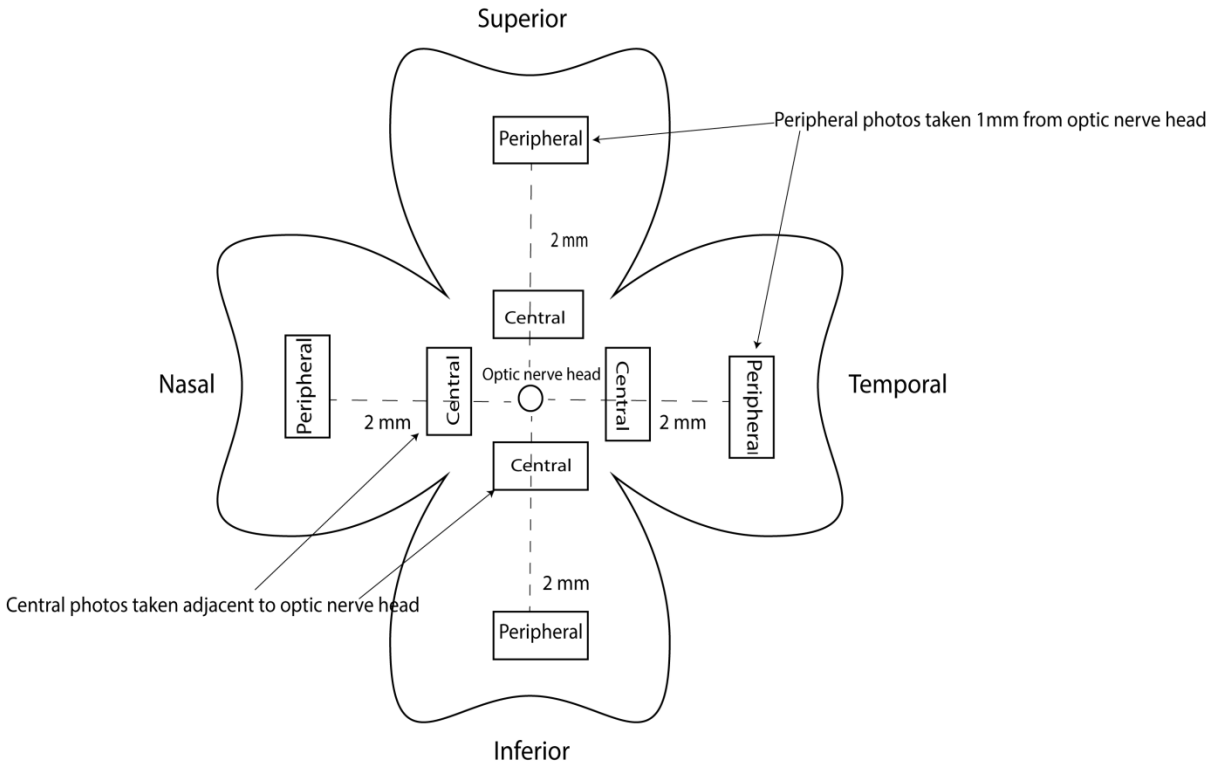

Figure 2.8 Schematic diagram of wholemount retina with photographic areas selected for quantification. Photographic dimensions were 350 µm x 250 µm. The central photographs were taken immediately adjacent to the optic nerve head whilst the peripheral photographs were captured 2 mm from the optic nerve head. Central and peripheral photos were taken for each region: superior, inferior, nasal and temporal.

2.9 Retinal transverse sections

2.9.1 Tissue preparation

Prior to enucleation, the superior aspect of each globe was marked using surgical ink. Eyes with globe attached were carefully removed and placed in 10% neutral buffered formalin for at least 24 hours. Tissues were processed by sequential immersion in 70% ethanol for 30 min, 3 × 100% ethanol for 30 min, 2 × xylene for 30 min, 50% xylene/50%

wax for 30 min at 62°C followed by 2 × wax for 30 min at 62°C. Eye globes were embedded sagittally in paraffin. Following the embedding process, 4 μm serial sections were cut with a microtome. Tissue sections were stained for hematoxylin and eosin using a standard methodology.

2.9.1 Immunohistochemistry

Tissue sections were deparaffinised, rinsed in 100% ethanol and treated for 20 min with hydrogen peroxide in absolute methanol to block endogenous peroxidase activity. Antigen retrieval was achieved by microwaving the sections in 1mM EDTA buffer (pH 8.0) for 10 min at 95 – 100°C. The microwave used, NEC N702EP, had been previously calibrated such that a stable temperature range of 95 – 100°C was achieved when two preheated plastic containers, each filled with 250 ml of retrieval solution, were microwaved on power setting 2. Tissue sections were blocked with PBS containing 3% normal horse serum and incubated overnight at room temperature in primary antibody containing 3% normal horse serum (Table 2.1). Subsequent to this, consecutive incubations were carried out with biotinylated secondary antibody (1:250; Vector, Burlingame, CA) and streptavidin–peroxidase conjugate (1:1000; Pierce, Rockford, IL). Color development was achieved using 3,3'-diaminobenzidine. Sections were counterstained with hematoxylin, dehydrated, cleared in histolene, and mounted in DPX.

2.9.2 Quantification

All analyses were conducted in a blinded fashion. Photomicrographs of stained transverse tissue sections were taken under a light microscope (BX-51; Olympus, Mount

Waverly, VIC, Australia). From each stained section, rectangular areas of 350 x 260 µm were photographed adjacent to the optic nerve head on each side, and 1 mm away from the optic nerve head on each side. For quantification of GFAP, iba1, FGF-2 and CNTF, the immunoreactive area in each photomicrograph was demarcated. Firstly, colour deconvolution was applied to extract the DAB staining. Any uneven illuminated background was removed using the "rolling ball" method. After manual thresholding, the area of positive staining was then measured. Evaluations were performed using the ImageJ 1.42q software package platform (http://rsb.info.nih.gov/ij/).

Table 2.1 Antibodies used in the study

Target	Host	Clone/#Cat No.	Dilution	Source
CNTF	goat	#AF 557-NA	1:1000	R&D Systems
cone arrestin	rabbit	#AB15282	1:5000	Merck-Millipore
FGF-2	mouse	clone bFM-2	1:500	Merck-Millipore
GFAP	rabbit	#Z0 334	1:40,000	Dako
iba1	rabbit	#019-19741	1:20,000	WAKO
M/L-opsin	rabbit	#AB5405	1:1000	Merck-Millipore
RPE65	goat	sc-53489	1:3000	Santa-Cruz
S-opsin	goat	sc-14363	1:1500	Santa-Cruz

2.10 Statistical analysis

Data are presented as mean ± SEM. In chapter 3, ERG and SD-OCT measurements at baseline and post-laser were analyzed with a paired t-test for each treatment group. Immunohistochemistry for GFAP, iba1, FGF-2 and CNT were analysed by ANOVA. In chapter 4, cone cell body, cone OS counts and optokinetic responses were analyzed between treatment groups with one-way ANOVA followed by post-hoc Tukey's test or a paired t-test for matched values. Statistical analysis and generation of graphs were performed with GraphPad Prism software (GraphPad Software V6, La Jolla, CA). P values less than 0.05 were considered statistically significant.

3. A safety study of photobiomodulation laser on the rat retina

3.1 Introduction

Chapter 3 represents the findings of the photobiomodulation (PBM) safety study. To date, the benefit of PBM in degenerative retinal disease has essentially been studied through LED delivery of R/NIR light. There is currently no consensus on whether coherent laser-delivered irradiation is superior to non-coherent LED sources; studies on wound healing have found no difference in effect;[205,206] however, coherent R/NIR light may be required for adequate exposure for the retina, which is housed within the enclosed structure of the eye. LED-delivered PBM leads to a theoretical random scattering of incoherent irradiation that may be variably filtered and absorbed by ocular structures. As a result, accurate treatment parameters for the retina are difficult to determine and present as a barrier to clinical translation. Herein, a custom-designed PBM laser attached to a slit lamp has been used to address this conundrum. Of importance, the safety threshold of laser-based PBM of the retina has not been investigated. Prior to assessing the neuroprotection efficacy of laser-delivered PBM, it is imperative to examine whether any adverse effects occur. Hence, the purpose of the experiments detailed in chapter 3 was to examine the safety of a range of irradiances of laser-delivered PBM in the normal rat retina.

3.2 Study design

3.2.1 Safety in pigmented – Dark Agouti (DA) – rats, analysed one week post-PBM

Experiment 3.1 comprised 10 DA rats (n=20 eyes) that received PBM laser at the following irradiance doses: control (n=4), sham (aiming beam only, n=4), 25 mW/cm^2 (low dose, n=4), 100 mW/cm^2 (medium dose, n=4), 500 mW/cm^2 (high dose, n=4). Owing to one of the high dose eyes displaying localised peripapillary changes, ie. changes around the optic disk, the study was extended by a further 7 rats as follows: control (n=2), sham (n=3), 100 mW/cm^2 (n=3) 500 mW/cm^2 (n=6). In total, therefore, the number of eyes analysed in each group was as follows: control (n=6), sham (n=7), 25 mW/cm^2 (n=4), 100 mW/cm^2 (n=7), 500 mW/cm^2 (n=10).

Rats received three PBM treatments aimed at the optic nerve (Figure 2.3) on non-consecutive days and were killed one week after the final laser session (see Figure 3.1). SD-OCTs were performed on all rats at baseline and prior to humane killing to assess for structural and functional changes. Total retinal thickness and outer nuclear layer (ONL) thickness were measured at preselected points (as detailed in Chapter 2). Concurrent with SD-OCT scans, fundus images were captured using a confocal scanning laser ophthalmoscope. ERGs were conducted at baseline and at 7 days post-laser. The amplitude and implicit times of the b- and a- wave were measured from the average of 10 ERG recordings for each eye. Whilst under terminal anaesthesia, each rat underwent a fluorescent angiogram (FA) for 20 minutes to assess vascular integrity. Rats were humanely killed by transcardial perfusion with physiological saline followed

by neutral buffered formalin, and the eyes were then dissected for histological analysis (see chapter 2).

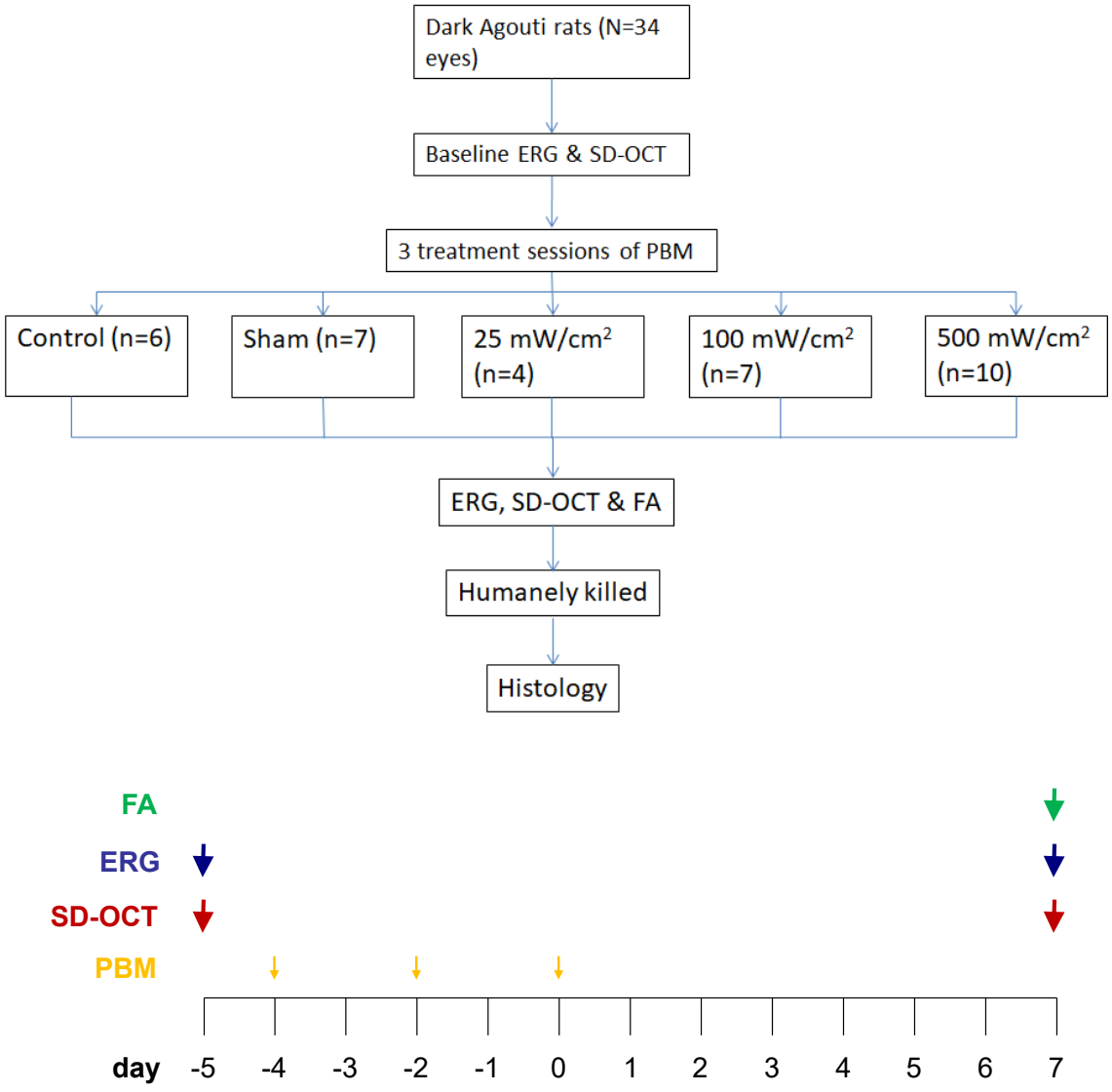

Figure 3.1 Experimental plan and timeline of experiment 3.1

3.2.2 Safety in pigmented – DA – rats, analysed three days post-PBM

A follow-up safety study (experiment 3.2) was performed in which rats were analysed at an earlier time point, 3 days compared to 7 days, in order to establish whether any overt

vascular leakage or retinal edema was evident in the first few days following multiple sessions of PBM. The experimental design (see Figure 3.2) was as follows: sham (n=3), 100 mW/cm^2 (n=3), 500 mW/cm^2 (n=6). SD-OCT and fundus images were taken pre- and post-PBM. FA was also performed. Eyes were then analyzed for histology.

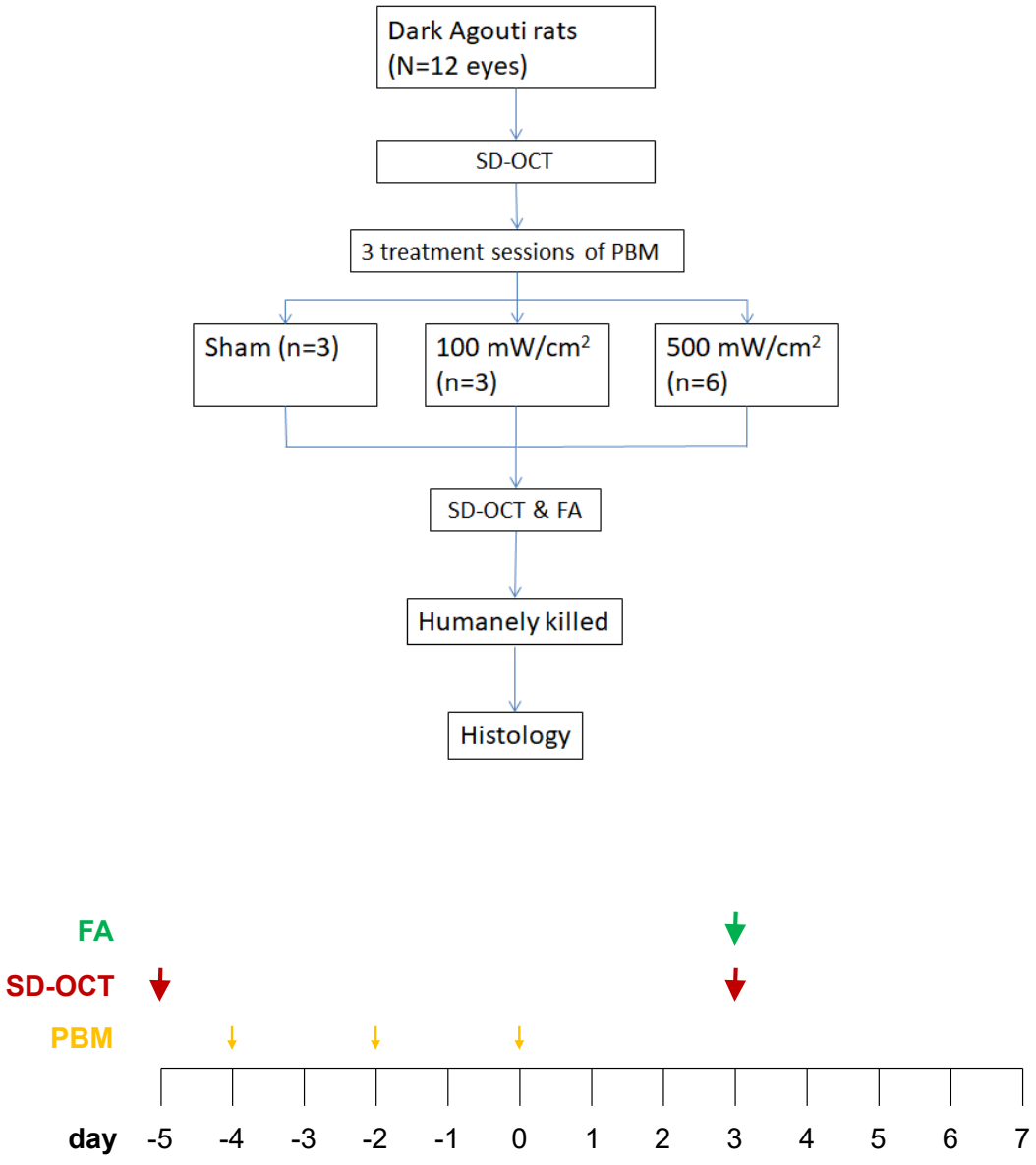

Figure 3.2 Experimental plan and timeline of experiment 3.2

3.2.3 Safety in albino – Sprague Dawley (SD) – rats, analysed one week post-PBM

A final safety study (experiment 3.3) was performed using a non-pigmented rat strain in order to reveal whether the peripapillary damage that was sometimes manifest at the high dose of PBM in DA rats was related to absorption by the heavily pigmented RPE/choroid. The experimental design (see Figure 3.3) was as follows: sham (n=3), 100 mW/cm^2 (n=3), 500 mW/cm^2 (n=6). SD-OCT and fundus images were taken pre- and post-PBM. FA was also performed. Eyes were then analyzed for histology.

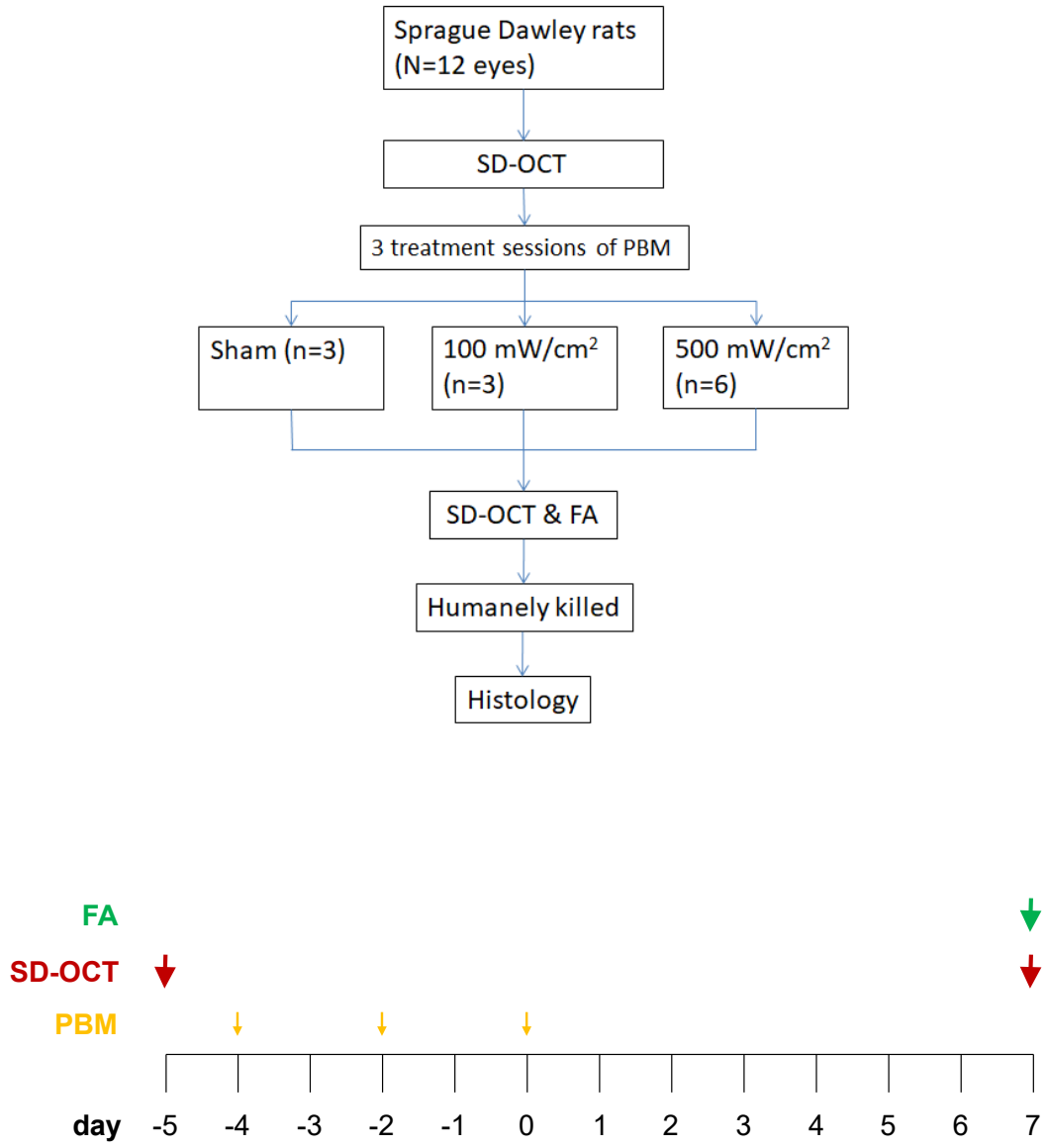

Figure 3.3 Experimental plan and timeline of experiment 3.3

3.3 Results

3.3.1 Experiment 3.1 – Safety study in pigmented DA rats, analysed one week post-PBM

3.3.1.1 ERG

Overall, ERG parameters were unaffected by PBM, irrespective of the energy setting (Figure 3.4). Summaries of the b-wave and a-wave amplitudes are shown in Tables 3.1 and 3.2, whilst the b-wave and a-wave implicit times are given in Tables 3.3 and 3.4. Paired Student's t-test analysis revealed no statistical difference in b-wave amplitude in any of the treatment groups (baseline versus post-PBM). Similarly, paired Student's t-test analysis revealed no statistical difference in a-wave amplitude in any of the treatment groups (baseline versus post-PBM). The b-wave and a-wave implicit times were also not statistically significant in any of the treatment groups (baseline versus post-PBM).

Table 3.1 Effect of PBM on b-wave amplitude

Treatment group	Baseline b-wave amplitude (μv)	Post-PBM b-wave amplitude (μv)	Difference b-wave amplitude (μv)	P value
Control	837.5 ± 185	868.9 ± 108.1	31.3 ± 44.9	0.54
Sham	907.1 ± 111.6	917.9 ± 78.7	10.7 ± 51.1	0.84
25 mW/cm^2	825.0 ± 147.9	823.8 ± 89.1	-1.2 ± 53.2	0.98
100 mW/cm^2	903.6 ± 80.7	900.0 ± 96.4	-3.6 ± 47.1	0.94
500 mW/cm^2	941.0 ± 124.2	935.0 ± 95.5	-6.0 ± 33.7	0.86

Data are expressed as mean ± SEM, where n=6 (control), n=7 (sham), n=4 (25 mW/cm^2), n=7 (100 mW/cm^2), n=10 (500 mW/cm^2).

Table 3.2 Effect of PBM on a-wave amplitude

Treatment group	Baseline a-wave amplitude (μv)	Post-PBM a-wave amplitude (μv)	Difference a-wave amplitude (μv)	P value
Control	200.0 ± 91.9	225.0 ± 55.9	25.0 ± 27	0.42
Sham	225.0 ± 55.9	203.6 ± 31.1	-21.4 ± 25.3	0.43
25 mW/cm^2	137.5 ± 41.5	156.3 ± 37	18.8 ± 31.3	0.59
100 mW/cm^2	196.4 ± 50.8	203.6 ± 38.8	7.1 ± 28.7	0.81
500 mW/cm^2	230.0 ± 72.3	207.5 ± 38.8	-23.0 ± 15	0.17

Data are expressed as mean ± SEM, where n=6 (control), n=7 (sham), n=4 (25 mW/cm^2), n=7 (100 mW/cm^2), n=10 (500 mW/cm^2).

Table 3.3 Effect of PBM on b-wave implicit time

Treatment group	Baseline b-wave implicit time (msec)	Post-PBM b-wave implicit time (msec)	Difference b-wave implicit time (msec)	P value
Control	73.3 ± 1.3	75.0 ± 0.8	1.7 ± 0.9	0.16
Sham	77.1 ± 2	78.0 ± 1.8	0.9 ± 0.8	0.21
25 mW/cm^2	76.5 ± 1.3	77.3 ± 2.5	0.8 ± 1	0.22

100 mW/cm^2	76.6 ± 3.3	77.9 ± 1.3	1.3 ± 1.2	0.33
500 mW/cm^2	76.7 ± 2.3	77.9 ± 1.2	1.2 ± 0.9	0.19

Data are expressed as mean ± SEM, where n=6 (control), n=7 (sham), n=4 (25 mW/cm^2), n=7 (100 mW/cm^2), n=10 (500 mW/cm^2).

Table 3.4 Effect of PBM on a-wave implicit time

Treatment group	Baseline b-wave implicit time (msec)	Post-PBM b-wave implicit time (msec)	Difference b-wave implicit time (msec)	P value
Control	20.3 ± 1.7	21.3 ± 1.7	1.0 ± 0.5	0.39
Sham	22.0 ± 0.8	21.7 ± 0.8	-0.3 ± 0.5	0.57
25 mW/cm^2	21.5 ± 1	22.0 ± 1.1	0.5 ± 0.5	0.39
100 mW/cm^2	21.9 ± 0.7	21.6 ± 1	-0.3 ± 0.5	0.57
500 mW/cm^2	21.2 ± 0.8	21.2 ± 0.8	0.0 ± 0.4	0.99

Data are expressed as mean ± SEM, where n=6 (control), n=7 (sham), n=4 (25 mW/cm^2), n=7 (100 mW/cm^2), n=10 (500 mW/cm^2).

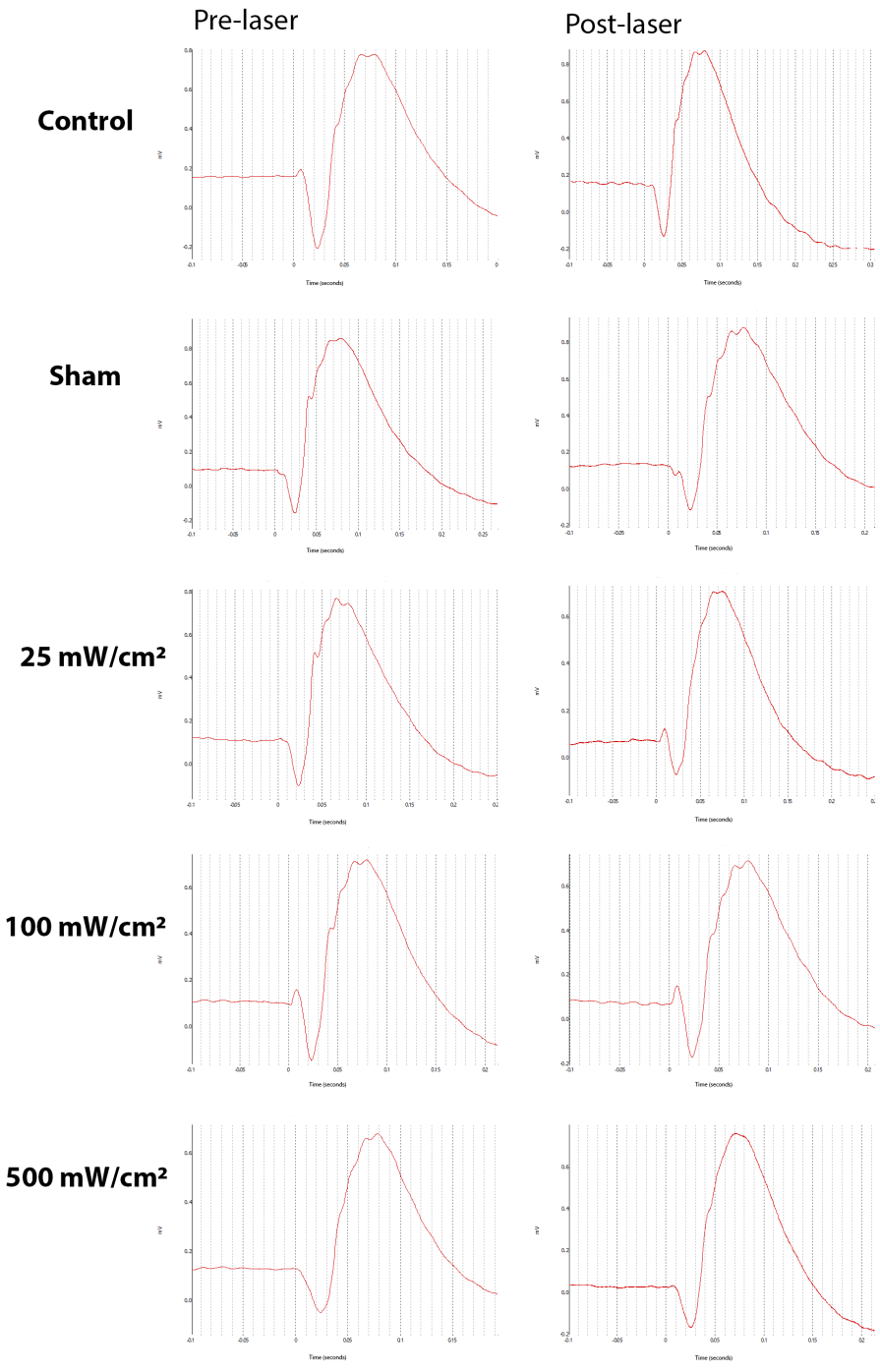

Figure 3.4 Representative baseline and post-PBM ERG traces in the different treatment groups.

3.3.1.2 SD-OCT

Paired Student's t-test analysis revealed no statistically significant difference between total retinal thickness at baseline versus 7 days post-PBM in any of the treatment groups (Table 3.5, Figure 3.5A); however, at the highest energy setting (500 mW/cm^2), the mean total retinal thickness was 15.6 ± 6.9 µm thinner than at baseline, a difference that almost reached significance (P=0.051). Analysis of ONL thickness showed no statistically significant differences between ONL thickness at baseline versus 7 days post-PBM in the control, sham, 25 mW/cm^2 and 100 mW/cm^2 groups (Table 3.6, Figure 3.5B). However, there was a statistically significant (P<0.05) difference in ONL thickness (-8.4 ± 3.7 µm; baseline versus 7 days post-PBM) in the 500 mW/cm^2 group (Table 3.6, Figure 3.5B). Further analysis of ONL thickness of each of the eyes in the 500 mW/cm^2 group revealed significant differences (Table 3.7, Figure 3.6) in Rat 8 RE, Rat 11 RE, Rat 14 RE and Rat 16 RE which were also accompanied by fundus changes (Figure 3.7). The remaining eyes in the 500 mW/cm^2 did not have any significant differences (Table 3.7) in ONL thickness before and 7 days after PBM laser.

Table 3.5 Effect of PBM on total retinal thickness in DA rats after 7 days

Treatment group	Baseline total retinal thickness (µm)	Post-PBM total retinal thickness (µm)	Difference total retinal thickness (µm)	P value	Fundus change (Yes/No)
Control	250.2 ± 12.3	249.3 ± 11.5	-0.9 ± 0.5	0.11	No
Sham	252.7 ± 8.6	252.2 ± 8.3	-0.5 ± 0.4	0.2	No

25 mW/cm^2	258.6 ± 1.9	259.9 ± 3.9	1.3 ± 1.9	0.53	No
100 mW/cm^2	254.4 ± 5.8	254.2 ± 5.3	-0.2 ± 0.5	0.67	No
500 mW/cm^2	251.1 ± 9.5	235.7 ± 27.9	-15.6 ± 6.9	0.051	Yes

Data are expressed as mean ± SEM, where n=6 (control), n=7 (sham), n=4 (25 mW/cm^2), n=7 (100 mW/cm^2), n=10 (500 mW/cm^2).

Table 3.6 Effect of PBM on ONL thickness in DA rats after 7 days

Treatment group	Baseline ONL thickness (μm)	Post-PBM ONL thickness (μm)	Difference ONL thickness (μm)	P value	Fundus change (Yes/No)
Control	51.4 ± 3.5	50.6 ± 2.4	-0.8 ± 0.6	0.21	No
Sham	52.9 ± 3.2	52.5 ± 3.1	-0.4 ± 0.3	0.24	No
25 mW/cm^2	55.7 ± 4.4	55.0 ± 4.5	-0.7 ± 0.5	0.31	No
100 mW/cm^2	52.6 ± 3.6	51.8 ± 4.3	-0.8 ± 0.5	0.12	No
500 mW/cm^2	52.7 ± 2.7	44.3 ± 11.8	-8.4 ± 3.7	0.049*	Yes

Data are expressed as mean ± SEM, where n=6 (control), n=7 (sham), n=4 (25 mW/cm^2), n=7 (100 mW/cm^2), n=10 (500 mW/cm^2). *P<0.05 by Student's paired t-test (baseline versus post-PBM).

Table 3.7 Effect of PBM on ONL thickness of each 500 mW/cm treated DA rat eye after 7 days

500 mW/cm^2 treatment group	Baseline ONL thickness (µm)	Post-PBM ONL thickness (µm)	Difference ONL thickness (µm)	P value	Fundus change (Yes/No)
Rat 3 RE	52.8 ± 4.2	53.4 ± 5.1	-0.67 ± 2	0.74	No
Rat 5 RE	57 ± 6.1	56.2 ± 6.1	-0.8 ± 2.6	0.77	No
Rat 8 RE	53.7 ± 8.3	17.9 ± 11.4	-35.8 ± 4.2	<0.001***	Yes
Rat 10 RE	45.4 ± 6.6	45.3 ± 5.6	-0.1 ± 2.6	0.97	No
Rat 11 RE	49.7 ± 5	39.6 ± 12.8	-10.1 ± 4	<0.01**	Yes
Rat 12 RE	53.6 ± 6.5	54.1 ± 5.6	0.5 ± 2.6	0.19	No
Rat 13 RE	53.7 ± 8.1	51.5 ± 6.9	-2.2 ± 3.2	0.5	No
Rat 14 RE	53.8 ± 5.1	35.8 ± 15.1	-18 ± 4.6	<0.001***	Yes
Rat 15 RE	52.9 ± 4.9	51.6 ± 4.7	-1.3 ± 2	0.52	No
Rat 16 RE	53.2 ± 5.4	37.7 ± 10.1	-15.5 ± 3.3	<0.001***	Yes

Data are expressed as mean ± SEM, **P<0.01,P<0.001 by Student's paired t test.***

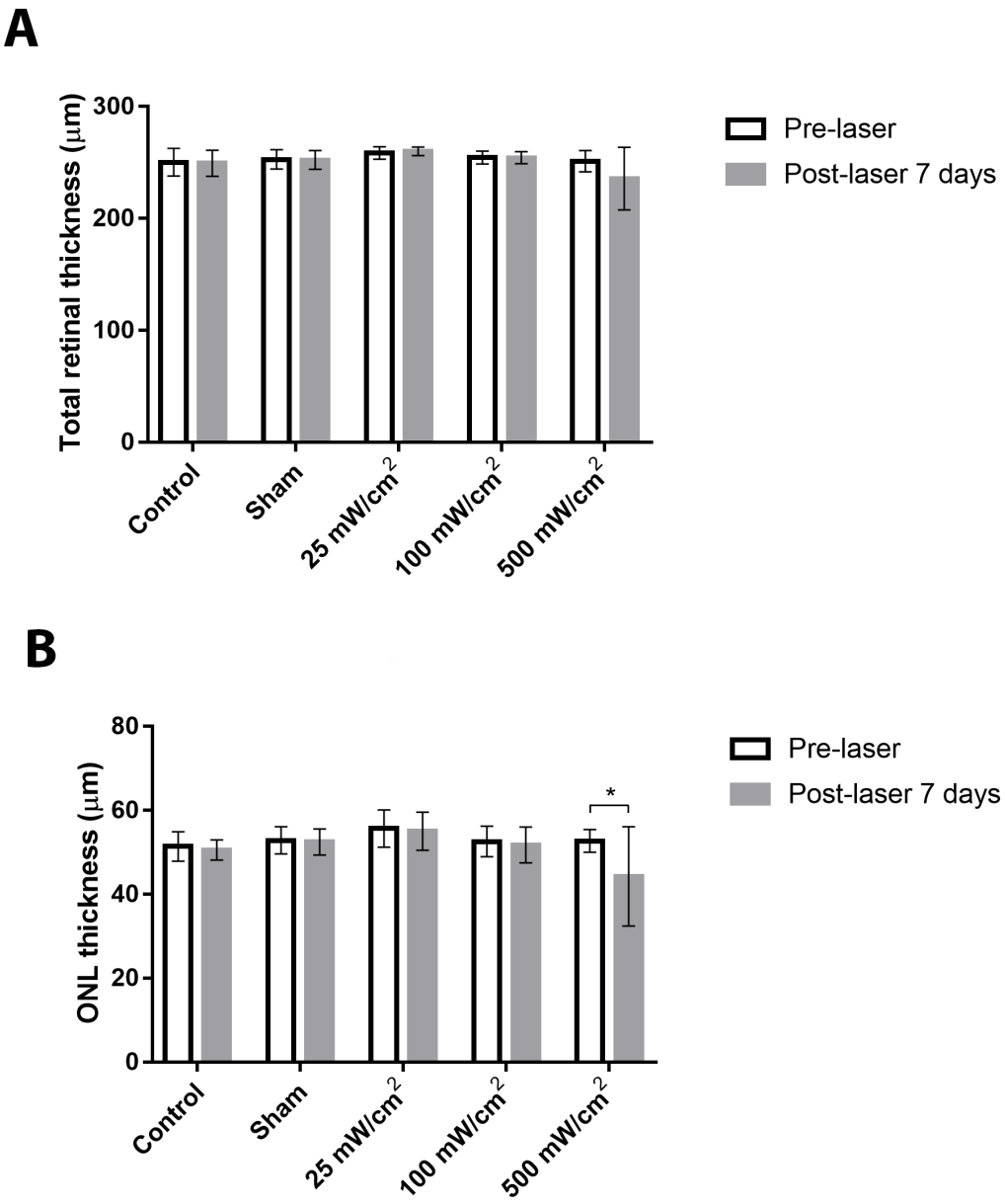

Figure 3.5 Effect of PBM on total retinal thickness (A) and ONL thickness (B) in DA rats after 7 days. Data are expressed as mean ± SEM. *P<0.05 by Student's paired t-test.

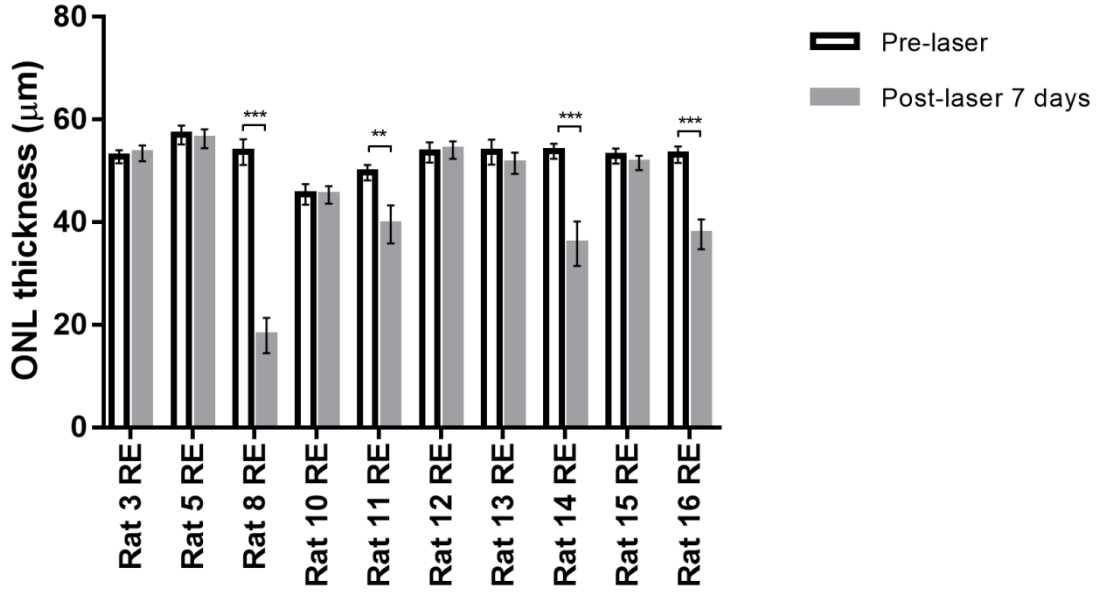

Figure 3.6 Effect of PBM on each 500 mW/cm^2 treated DA rat eye after 7 days. Data are expressed as mean ± SEM. **P<0.01, ***P<0.001 by Student's paired t-test.

Qualitative assessment of every sample revealed that none of the eyes from the control, sham, 25 mW/cm^2 or 100 mW/cm^2 groups displayed any abnormalities on SD-OCT or fundus imaging. This was not the case for the 500 mW/cm^2 group. Four out of ten eyes (40%) in the 500 mW/cm^2 group had noticeable fundus and SD-OCT changes at 7 days post-laser (see Figures 3.7-3.11, and Table 3.11). Evaluation of the fundus images of all four affected rats showed there to be marked pigment changes around the optic nerve head. The size of the affected area varied between rats, but it was always peripapillary and hence located within the centre of the irradiated area. On assessment of SD-OCT, there was localized damage mainly in the outer retina, specifically the ONL, which appeared thinned and disorganized. In the most severely affected eye (Figure 3.8), there was almost complete localised obliteration of the ONL and up to 40% reduction in total

retinal thickness compared to baseline. In contrast to the outer retina, the inner layers of each of the four affected eyes were morphologically normal. The slit lamp-delivered laser emits a collimated beam of 670 nm irradiation with a 4.5 mm diameter spot size on the retina. Hence, a substantial area of the entire rat retina receives irradiation. Excluding the peripapillary zone, no abnormalities were observed within the remainder of the irradiated zone in any of the affected rats.

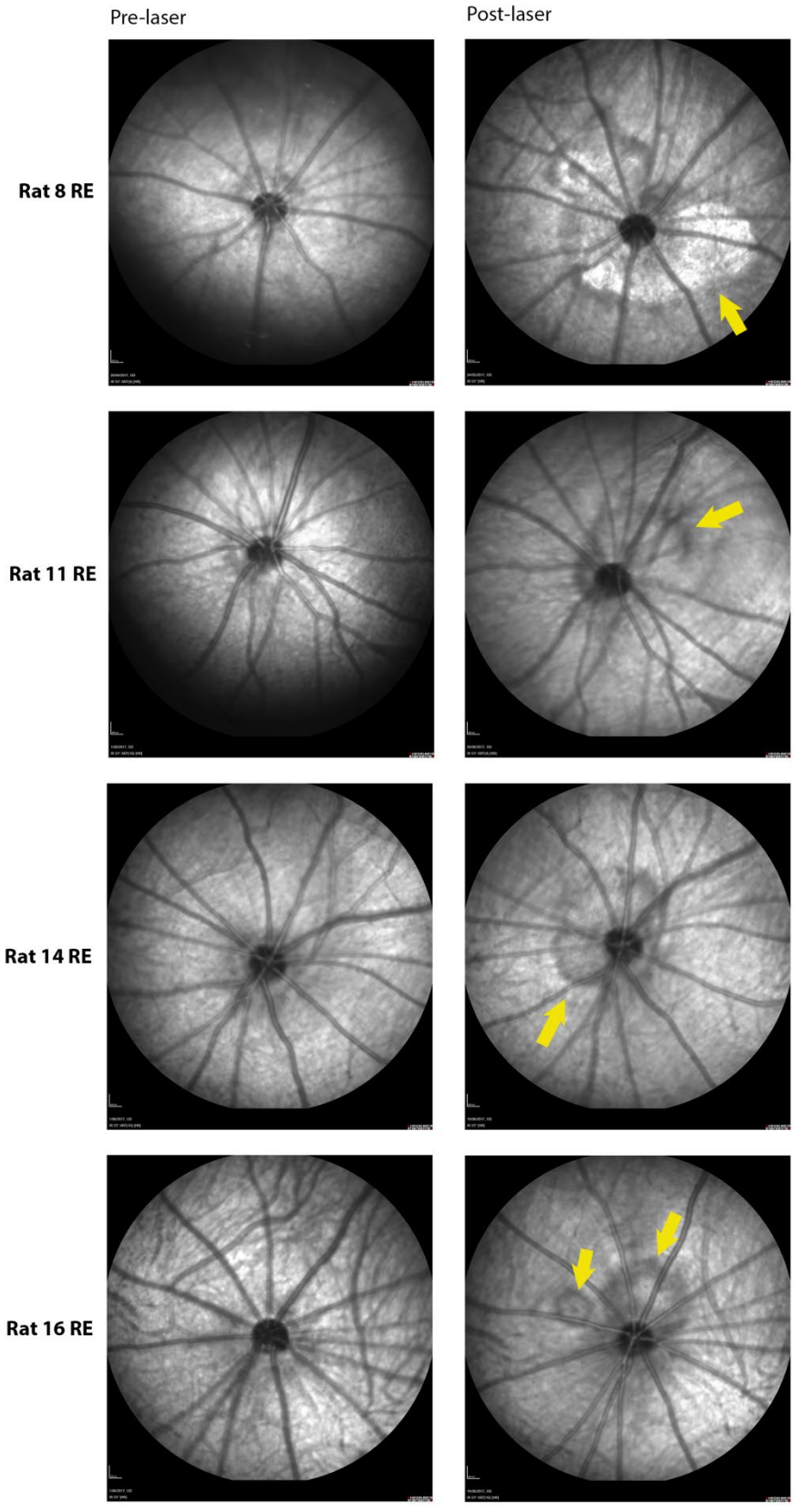
Pre-laser
Post-laser
Rat 8 RE
Rat 11 RE
Rat 14 RE
Rat 16 RE

Figure 3.7 Comparison of fundus photos taken at baseline and at 7 days post-PBM in four affected eyes that received 500 mW/cm^2 PBM. Yellow arrows indicate abnormalities post-laser.

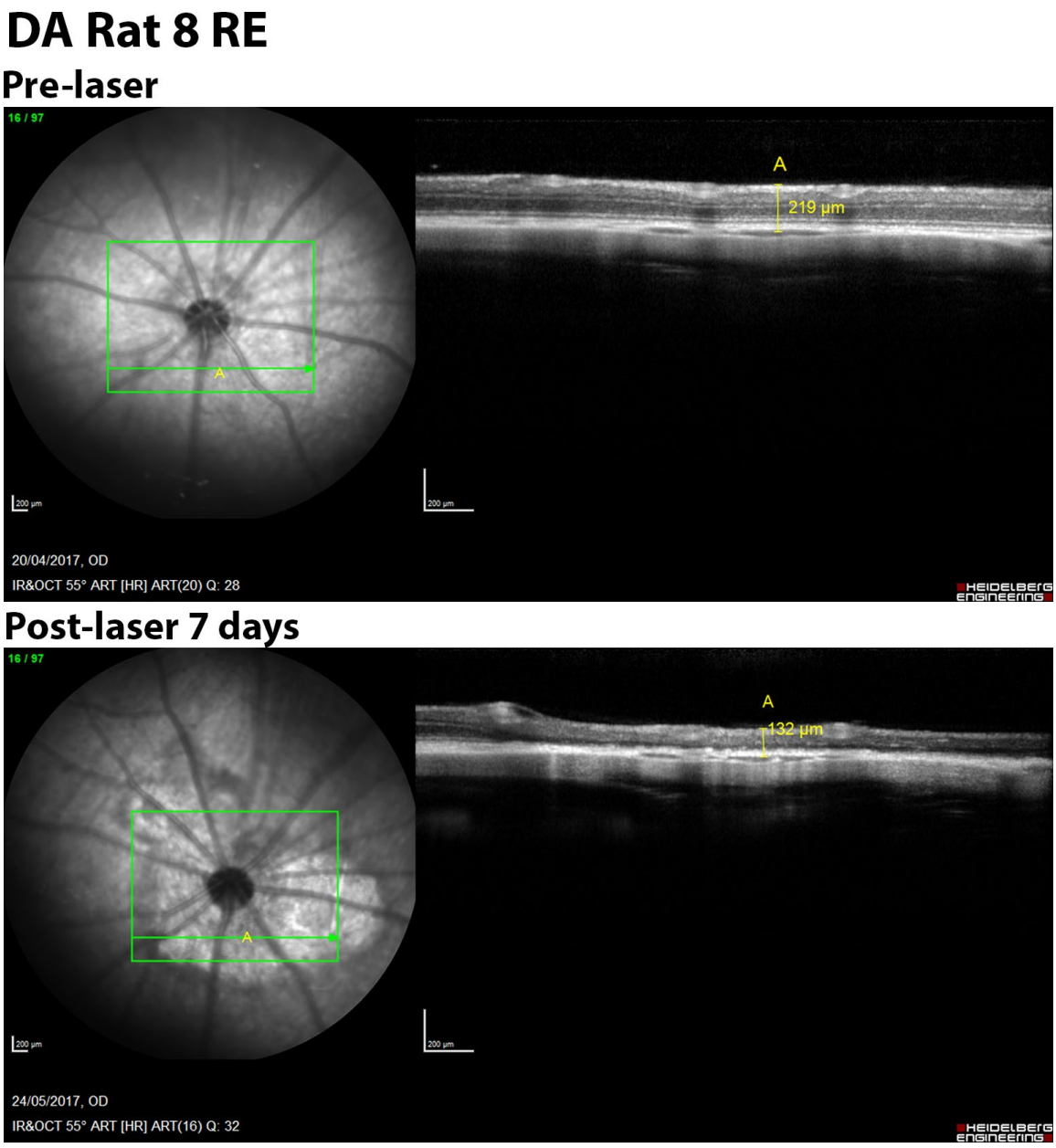

Figure 3.8 Upper panel represents SD-OCT at baseline in DA rat 8 right eye (500 mW/cm^2) with point A marking total retinal thickness of 219 µm. Lower panel shows SD- OCT of the same rat 7 days post-laser. There is notable atrophy and a decrease in

total retinal thickness at point A to 132 µm - a 40% reduction from baseline. The ONL appears obliterated and almost unmeasurable. The outer plexiform player is not readily distinguishable.

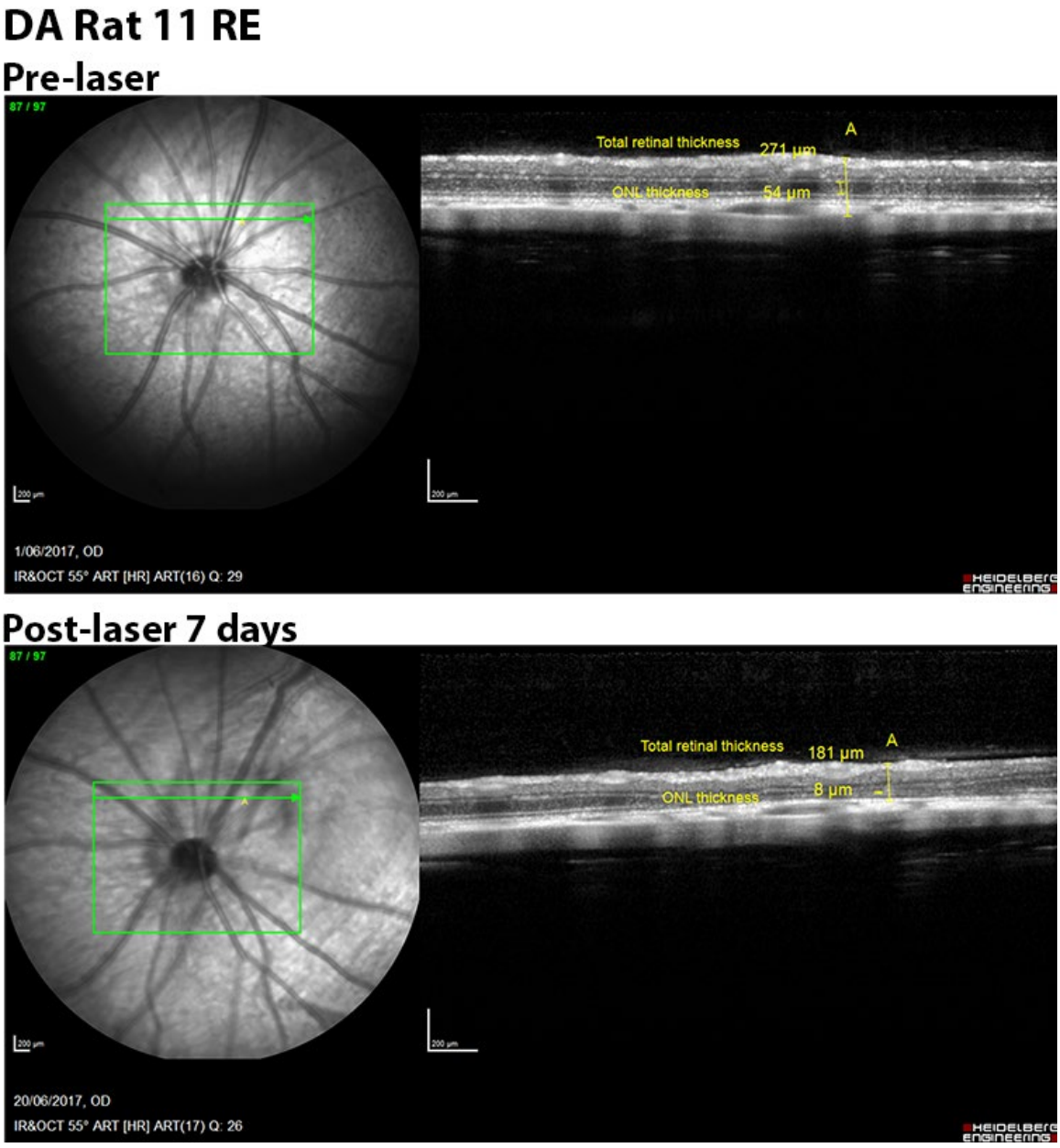

Figure 3.9 Upper panel represents SD-OCT at baseline in DA rat 11 right eye (500 mW/cm^2) with point A marking total retinal thickness of 271 µm and ONL thickness of 54 µm. Lower panel shows SD- OCT of the same rat 7 days post-laser. Total retinal

thickness and ONL thickness at point A are 181 µm (33% reduction) and 8 µm (85% reduction), respectively.

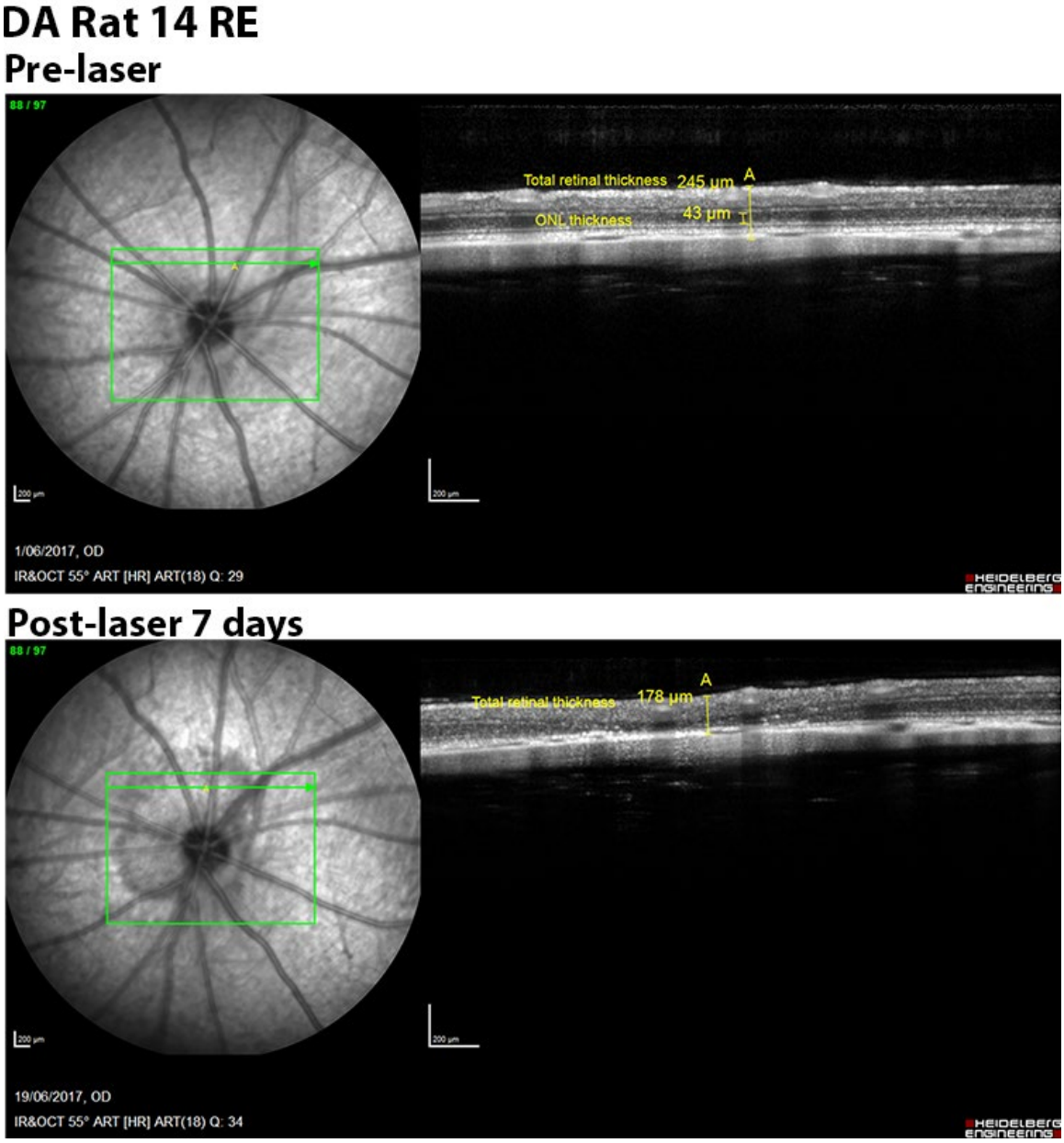

Figure 3.10 Upper panel represents SD-OCT at baseline in DA rat 14 right eye (500 mW/cm^2) with point A marking total retinal thickness of 245 µm. Lower panel shows SD- OCT of the same rat 7 days post-laser. Total retinal thickness at point A is 178

µm (27% reduction). The ONL has been severely damaged and is unmeasurable post-laser.

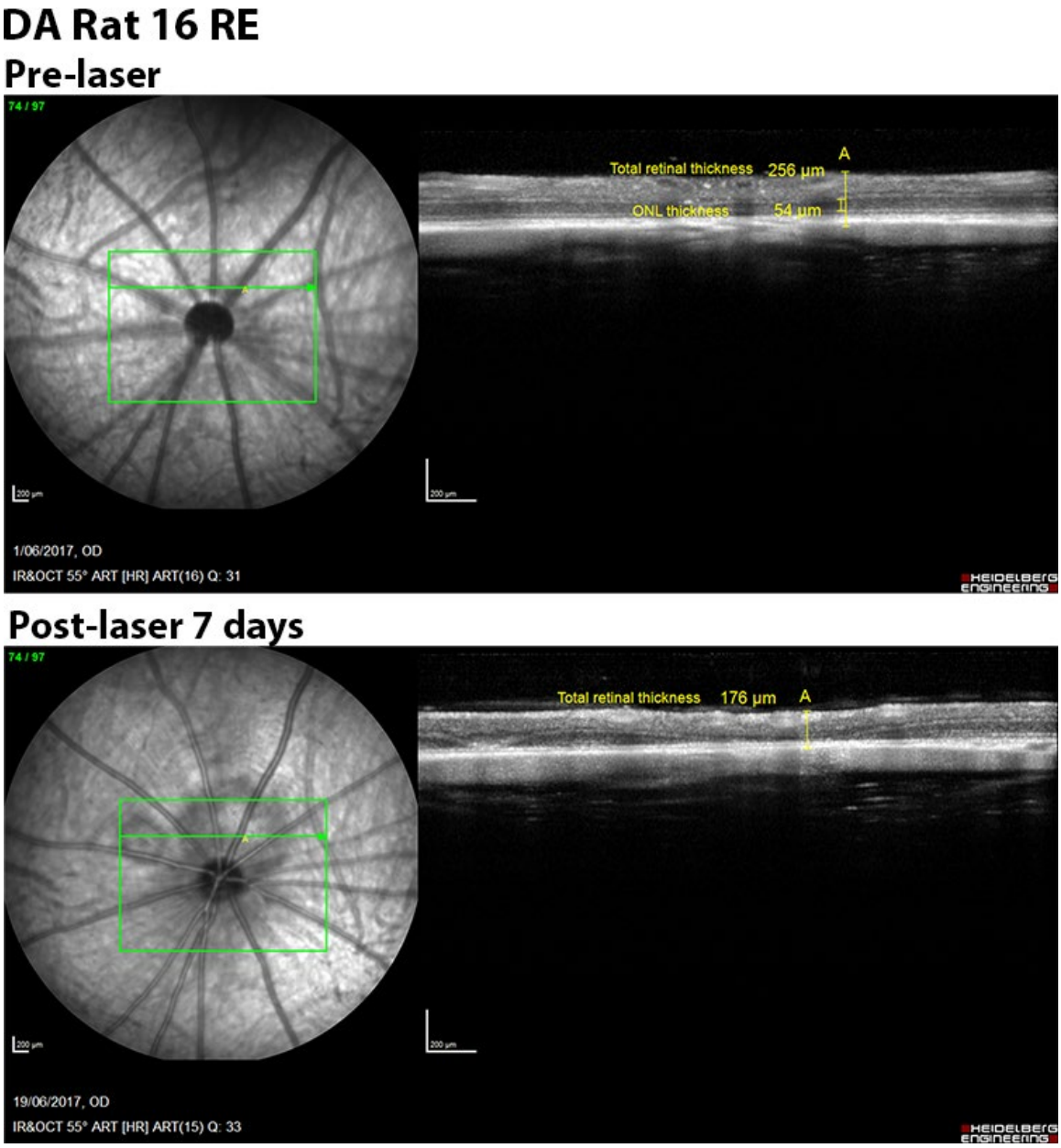

Figure 3.11 Upper panel represents SD-OCT at baseline in DA rat 16 right eye (500 mW/cm^2) with point A marking total retinal thickness of 256 µm. Lower panel shows SD- OCT of the same rat 7 days post-laser. Total retinal thickness at point A is 176

μm (31% reduction). Post-laser, the ONL is too severely damaged at this point to accurately measure.

3.3.1.3 FA

Fluorescein angiograms taken of every eye from the control, sham, 25 mW/cm^2, and 100 mW/cm^2 groups showed normal vasculature and no fluorescein leakage at 7 days post-laser; however, 3/10 eyes (30%) treated with 500 mW/cm^2 PBM displayed abnormal fluorescein leakage at 7 days post-laser (Figure 3.12, Table 3.8) that was present immediately upon injection of fluorescein, reached a peak after 15 minutes, plateaued until 20 minutes, before subsiding. The leakage is most likely to derive from deep within the retina, either at the deep capillary plexus or from the choroid. There were no other morphological vascular abnormalities.

Table 3.8 FA characteristics of affected eyes treated with 500 mW/cm^2 PBM

Rat ID	Days post-laser	FA description
DA rat 8 RE	7	Dense hyperfluorescence attributed to leakage noted inferior-nasally around the optic disc Dimensions: 2.6 x 0.9mm
DA rat 14 RE	7	Cloudy hyperfluorescence superior to the optic nerve head Dimensions: 0.63 x 0.31mm
DA rat 16 RE	7	Subtle leakage of fluorescein superior to the optic nerve head Dimensions: 0.2 x 0.2mm

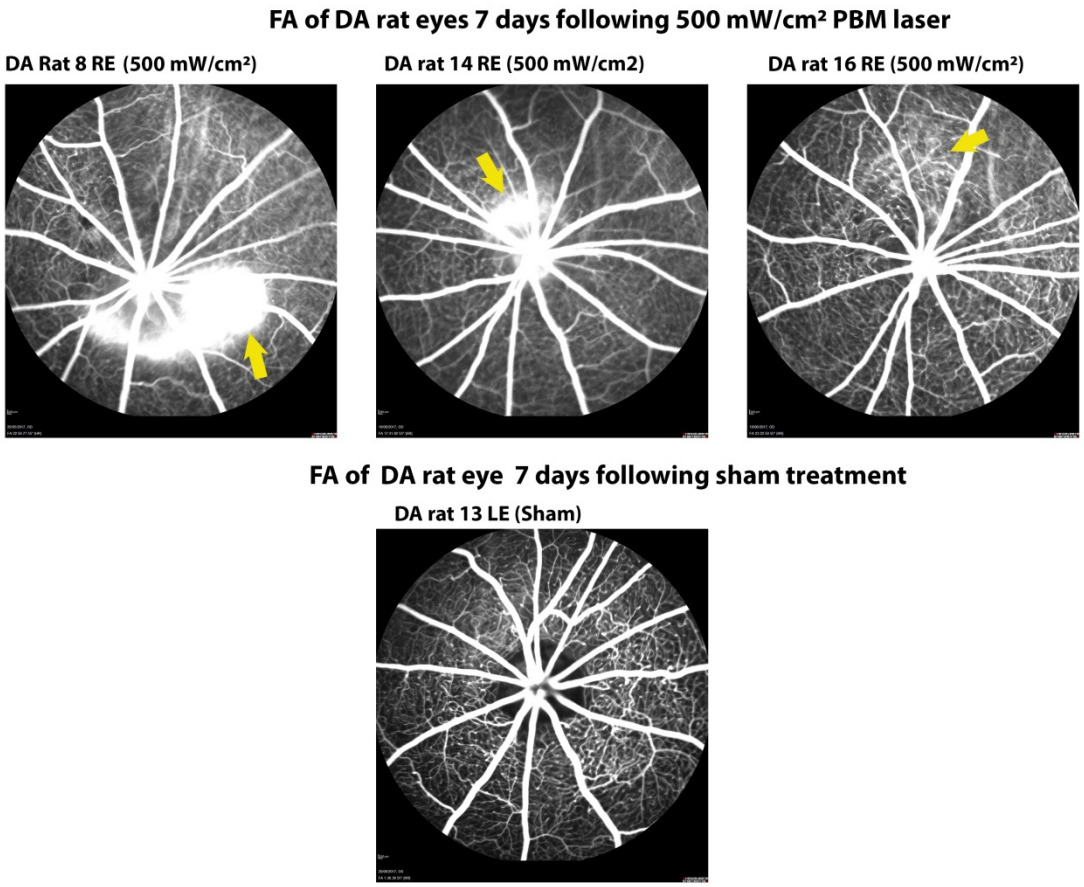

Figure 3.12 Top panel* shows *FA images of three affected eyes (500 mW/cm^2) taken at 7 days post-laser demonstrating varying levels of fluorescein leakage. Bottom panel represents FA images of sham treated eye that is normal. Images were captured between 15-23 minutes post-injection of sodium fluorescein. Yellow arrows indicate fluorescein leakage.

3.3.1.4 Histology

Gross examination of whole eye specimens analysed at 7 days post-PBM showed no evidence of retinal haemorrhages or cataracts in eyes from any of the treatment groups. Histological evaluation of retinas from control, sham, 25 mW/cm^2 (low dose), and 100 mW/cm^2 (medium dose) groups yielded results that were entirely consistent with those

obtained from SD-OCT and FA. Specifically, there was no evidence of photoreceptor destruction, disorganisation of photoreceptor segments, macro- or micro-gliosis, upregulation of stress proteins, or damage to the RPE, either within the peripapillary zone or throughout the remainder of the irradiated zone (see Figs. 3.14, 3.16, 3.17).

Histological examination of rats treated with 500 mW/cm^2 (high dose) confirmed the findings obtained from SD-OCT and FA. Thus, in a proportion of eyes (4/10; specifically DA 8R, DA 11R, DA 14R and DA 16R), localised peripapillary retinal damage was observed, but no obvious injury was manifest in the remainder of the irradiated zone (See Figs. 3.13-3.17). The affected rats (see Figs. 3.13 and 3.15 for representative images from DA rats 8R and 16R) featured very localised damage to the ONL with loss of photoreceptor nuclei as well as inner and outer segments. This was accompanied by localised upregulations of the stereotypical macroglial stress markers glial fibrillary acidic protein (GFAP) and ciliary neurotrophic factor (CNTF). Furthermore, an increased microglial presence was evident in the affected region, particularly in the degenerating outer nuclear layer. The RPE layer was mostly intact in the affected peripapillary zone, but individual areas of damage, or hypertrophy indicative of cell death and regeneration, could be discerned. The inner retina of affected rats remained structurally intact. Aside from the localised area of damage, minimal injury or glial responses could be observed in other areas around the ONH in four affected rats (see Figs. 3.16-3.17). Thus, in DA rat 16R for example, retinal injury is apparent immediately superior to the ONH, but not inferior to the ONH, nor at 1mm from the ONH in a superior or inferior direction. In the remaining 6/10 eyes, no

abnormalities were apparent either within the peripapillary zone or throughout the remainder of the irradiated zone.

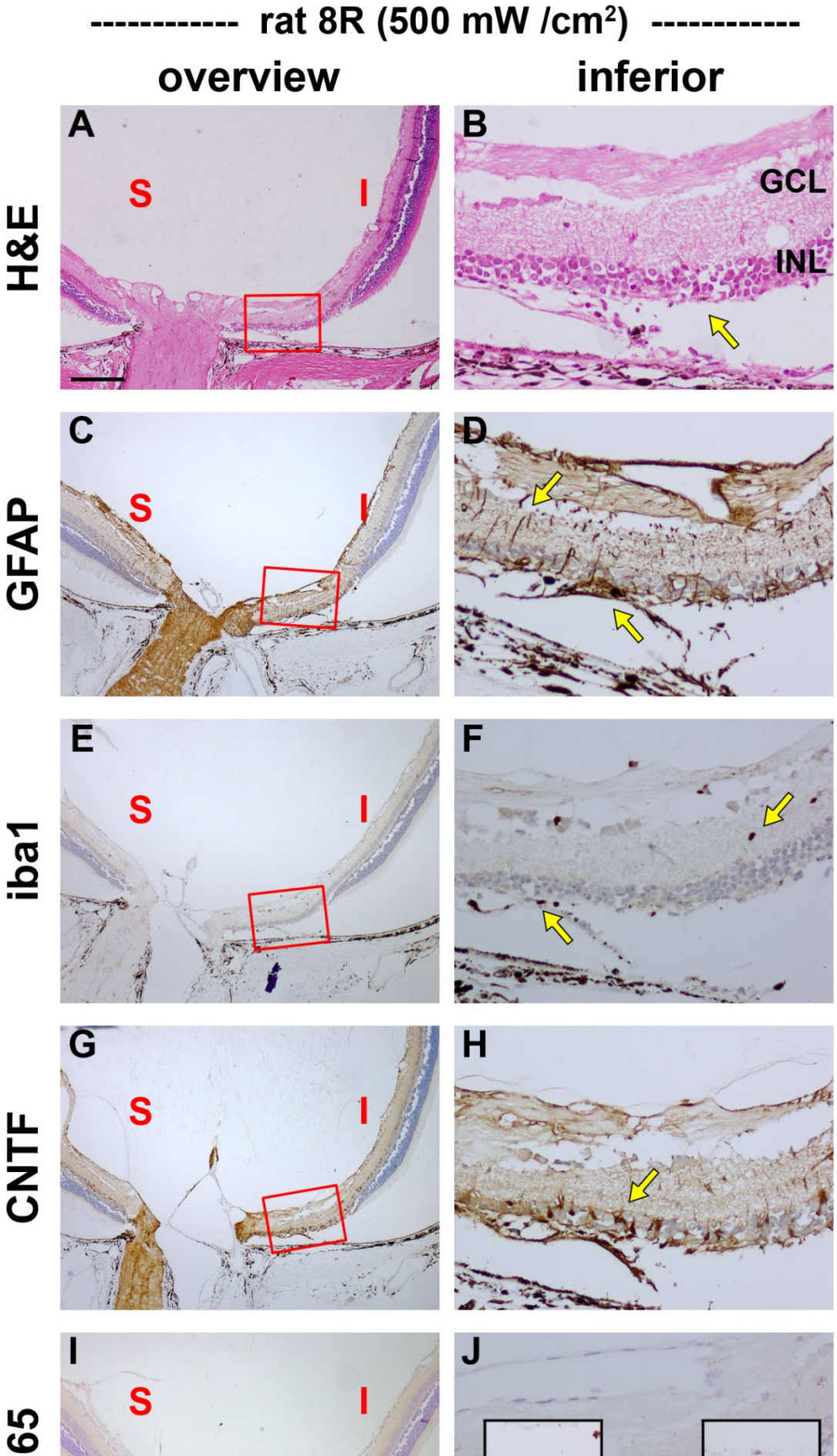
---------- rat 8R (500 mW /cm²) ----------
overview
inferior
H&E
GFAP
iba1
CNTF
65
A
B
C
D
E
F
G
H
I
J
S
I
GCL
INL

Figure 3.13 Histology of DA rat 8 right eye (500 mW/cm^2). Transverse sections at the level of the optic nerve head (ONH) were stained for haematoxylin and eosin (A-D), and immunolabelled for GFAP (E-H), iba1 (I-L), CNTF (M-P) and RPE65 (Q-T). There is localised destruction of photoreceptor nuclei, inner and outer segments immediately inferior to the ONH (A, B, arrow). This is accompanied by greatly increased expression of GFAP (E, F, arrows) and CNTF (M, N, arrows) by Müller cells and astrocytes overlying and immediately adjacent to the affected area. Iba1-positive activated microglia can be observed within the damaged area of the retina (I, J, arrows). The RPE layer appears relatively intact, but discrete areas of injury are apparent (Q, R, arrows, highlighted within insets). On the superior side of the ONH, there is no patent injury or upregulation of glial markers. Scale bar: A, C, E, G, I, K, M, O, Q, S = 250 μm; B, D, F, H, J, L, N, P, R, T = 50 μm. GCL, ganglion cell layer; INL, inner nuclear layer; ONL, outer nuclear layer; RPE, retinal pigment epithelium.

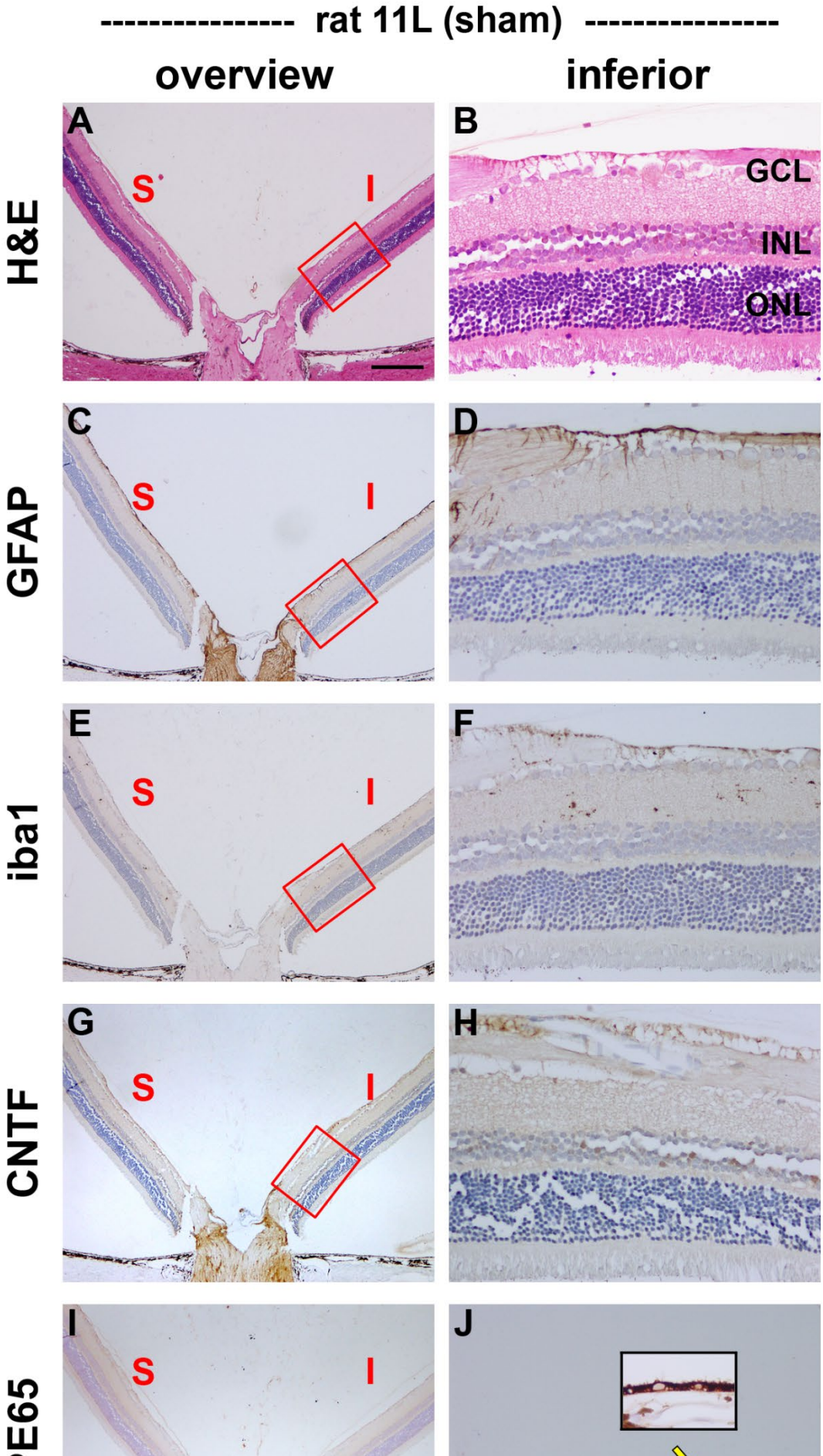
rat 11L (sham)
overview
inferior
H&E
GFAP
iba1
CNTF
RPE65
A
B
C
D
E
F
G
H
I
J
S
I
GCL
INL
ONL

Figure 3.14 Histology of DA rat 11 left eye (sham). Transverse sections at the level of the optic nerve head (ONH) were stained for haematoxylin and eosin (A-D), and immunolabelled for GFAP (E-H), iba1 (I-L), CNTF (M-P) and RPE65 (Q-T). There is no evidence of any abnormalities in any of the markers analysed. Scale bar: A, C, E, G, I, K, M, O, Q, S = 250 μm; B, D, F, H, J, L, N, P, R, T = 50 μm. GCL, ganglion cell layer; INL, inner nuclear layer; ONL, outer nuclear layer; RPE, retinal pigment epithelium.

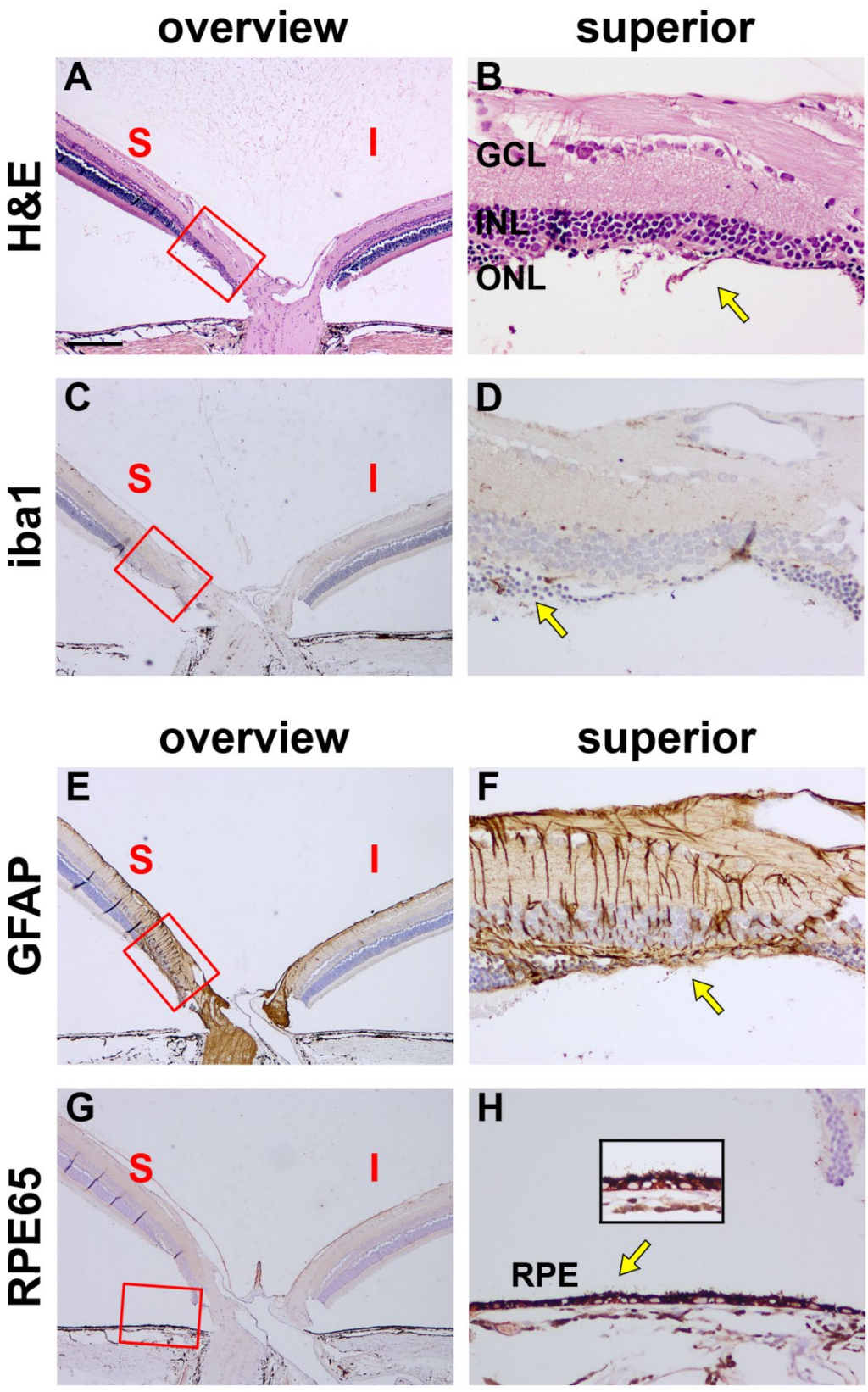
overview
superior
H&E
A
S
I
B
GCL
INL
ONL
iba1
C
S
I
D
overview
superior
GFAP
E
S
I
F
RPE65
G
S
I
H
RPE

Figure 3.15 Histology of DA rat 16 right eye (500 mW/cm^2). Transverse sections at the level of the optic nerve head (ONH) were stained for haematoxylin and eosin (A, B), and immunolabelled for iba1 (C, D), GFAP (E, F), and RPE65 (G, H). Localised destruction of photoreceptor nuclei, inner and outer segments immediately superior to the ONH is evident (A, B, arrow). This is accompanied by greatly increased expression of GFAP (E, F, arrow) by Müller cells and astrocytes overlying and immediately adjacent to the affected area. Iba1-positive activated microglia can be observed within the degenerating ONL (C, D, arrow). The RPE layer appears intact, but some hypertrophy/cell regeneration is apparent (G, H, arrow, highlighted within inset). On the inferior side of the ONH, there is no patent injury or upregulation of glial markers. Scale bar: A, C, E, G = 250 μm; B, D, F, H = 50 μm. GCL, ganglion cell layer; INL, inner nuclear layer; ONL, outer nuclear layer; RPE, retinal pigment epithelium.

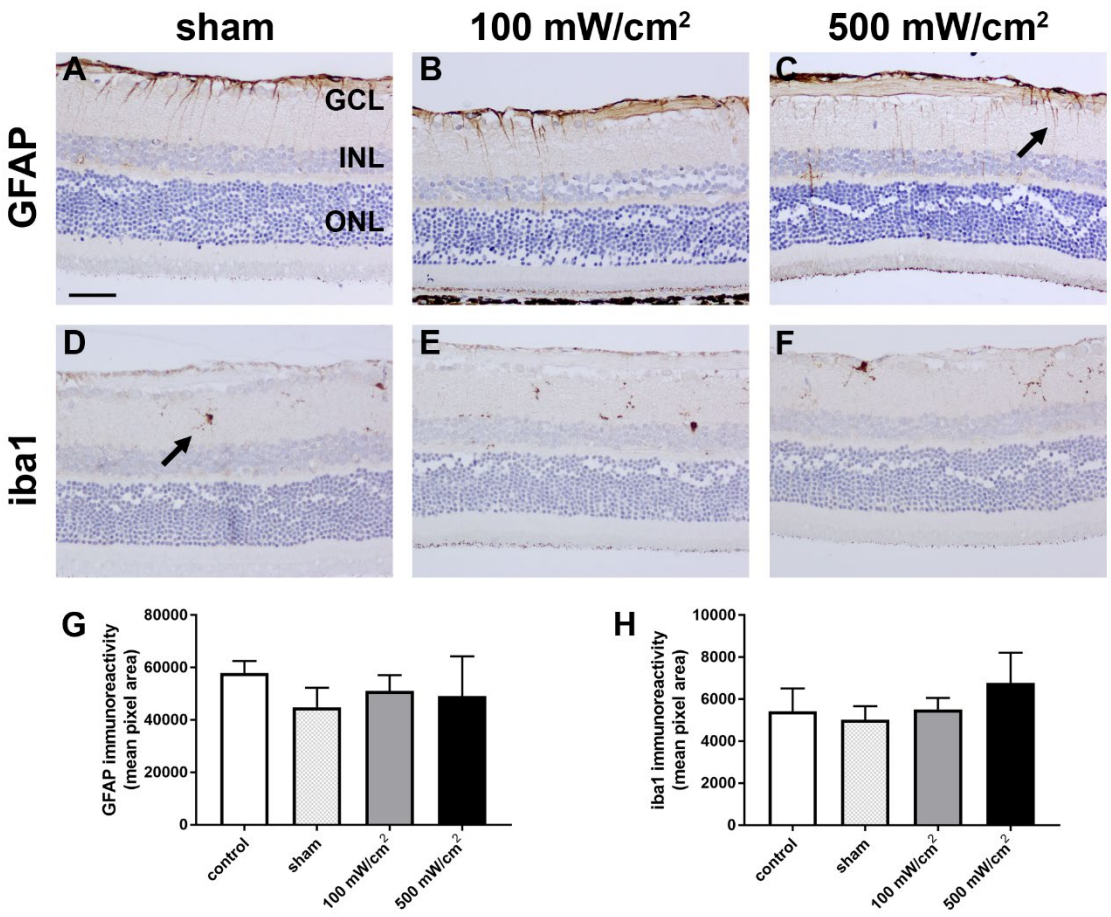

Figure 3.16 Effect of PBM on macroglia and microglia in DA rats at 7 days post-PBM. (A-F) Representative images of normal retinas from sham, 100 mW/cm^2 and damaged retina from the 500 mW/cm^2 group immunolabelled for GFAP and iba1 (arrows). Images were captured within the irradiated zone at approximately 1 mm from the optic nerve head. (G, H) Quantification of GFAP and iba1 abundances, as defined in the Materials and Methods. Data are expressed as the mean ± SEM, where n=6-10 for each group. ANOVA revealed no significant differences in GFAP or iba1 abundance between treatment groups. Scale bar = 50 μm. GCL, ganglion cell layer; INL, inner nuclear layer; ONL, outer nuclear layer.

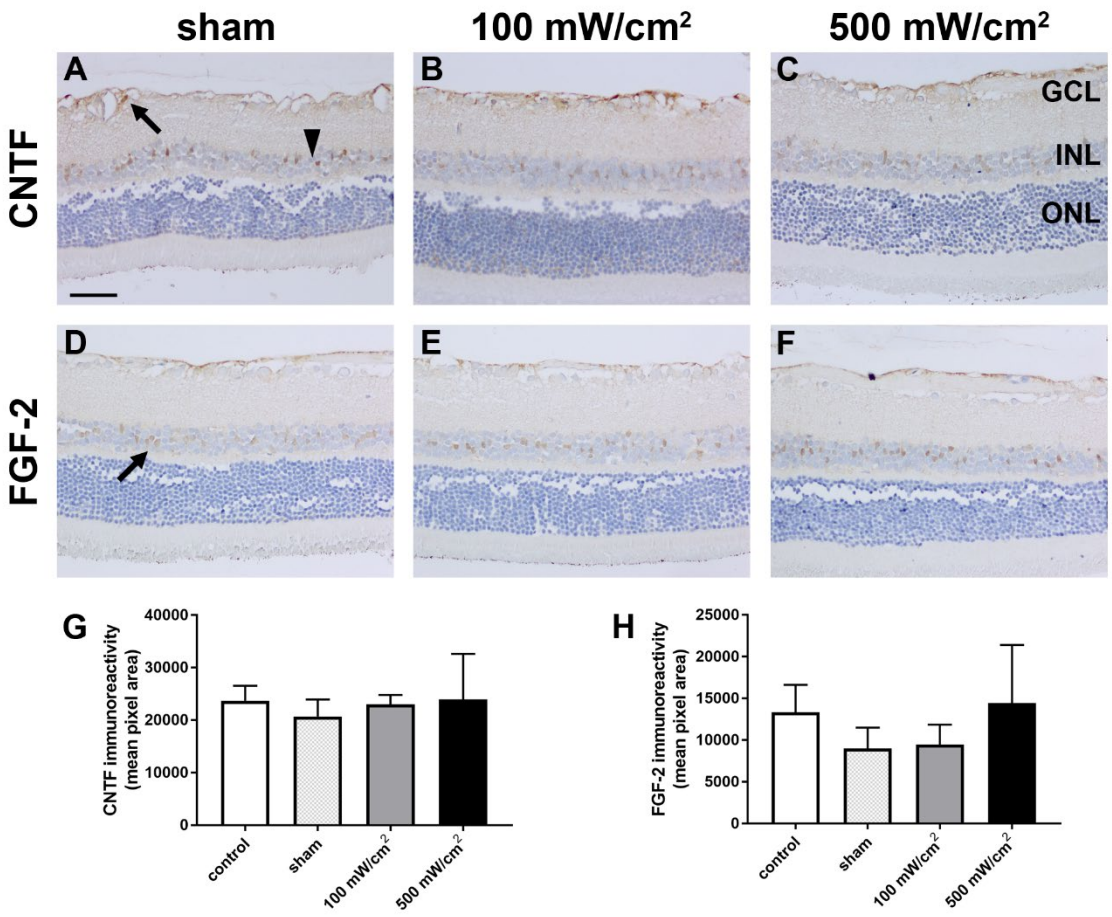

Figure 3.17 Effect of PBM on levels of stress proteins in DA rats at 7 days post-PBM. (A-F) Representative images of normal retinas from sham, 100 mW/cm^2 and damaged retina from the 500 mW/cm^2 group immunolabelled for CNTF and FGF-2 (arrows). Images were captured within the irradiated zone at approximately 1 mm from the optic nerve head. (G, H) Quantification of CNTF and FGF-2 abundances, as defined in the Materials and Methods. Data are expressed as the mean ± SEM, where n=6-10 for each group. ANOVA revealed no significant differences in CNTF and FGF-2 abundance between treatment groups. Scale bar = 50 μm. GCL, ganglion cell layer; INL, inner nuclear layer; ONL, outer nuclear layer.

3.3.2 Experiment 3.2 –Safety study in pigmented DA rats, analysed at three days post-PBM

3.3.2.1 SD-OCT

Paired Student's t-test analysis revealed no statistically significant difference between total retinal thickness or ONL thickness at baseline versus 3 days post-PBM in any of the treatment groups (Tables 3.9, 3.10; Figure 3.18). Nevertheless, 2/6 eyes (33%) at the highest energy setting (500 mW/cm^2) showed noticeable fundus and SD-OCT changes at the 3 day time point (Figures 3.19-3.21), which were similar to those documented at the 7 day endpoint.

Table 3.9 Effect of PBM on retinal thickness in DA rats after 3 days

Treatment group	Baseline total retinal thickness (µm)	Post-PBM total retinal thickness (µm)	Difference total retinal thickness (µm)	P value	Fundus change (Yes/No)
Sham	55.9 ± 1.9	55.3 ± 1.7	-0.6 ± 0.4	0.25	No
100 mW/cm^2	55.7 ± 3.9	56.4 ± 4.1	-0.7 ± 0.3	0.16	No
500 mW/cm^2	56.4 ± 2.3	52.6 ± 4.7	-3.9 ± 2.8	0.22	Yes

Data are expressed as mean ± SEM, where n=3 (sham), n=3 (100 mW/cm^2), n=6 (500 mW/cm^2).

Table 3.10 Effect of PBM on ONL thickness in DA rats after 3 days

Treatment group	Baseline ONL thickness (μm)	Post-PBM ONL thickness (μm)	Difference ONL thickness (μm)	P value	Fundus change (Yes/No)
Sham	55.9 ± 1.9	55.3 ± 1.7	-0.6 ± 0.4	0.25	No
100 mW/cm^2	55.7 ± 3.4	56.4 ± 4.1	0.7 ± 0.3	0.16	No
500 mW/cm^2	56.4 ± 2.3	52.6 ± 4.7	-3.8 ± 2.8	0.22	Yes

Data are expressed as mean ± SEM, where n=3 (sham), n=3 (100 mW/cm^2), n=6 (500 mW/cm^2).

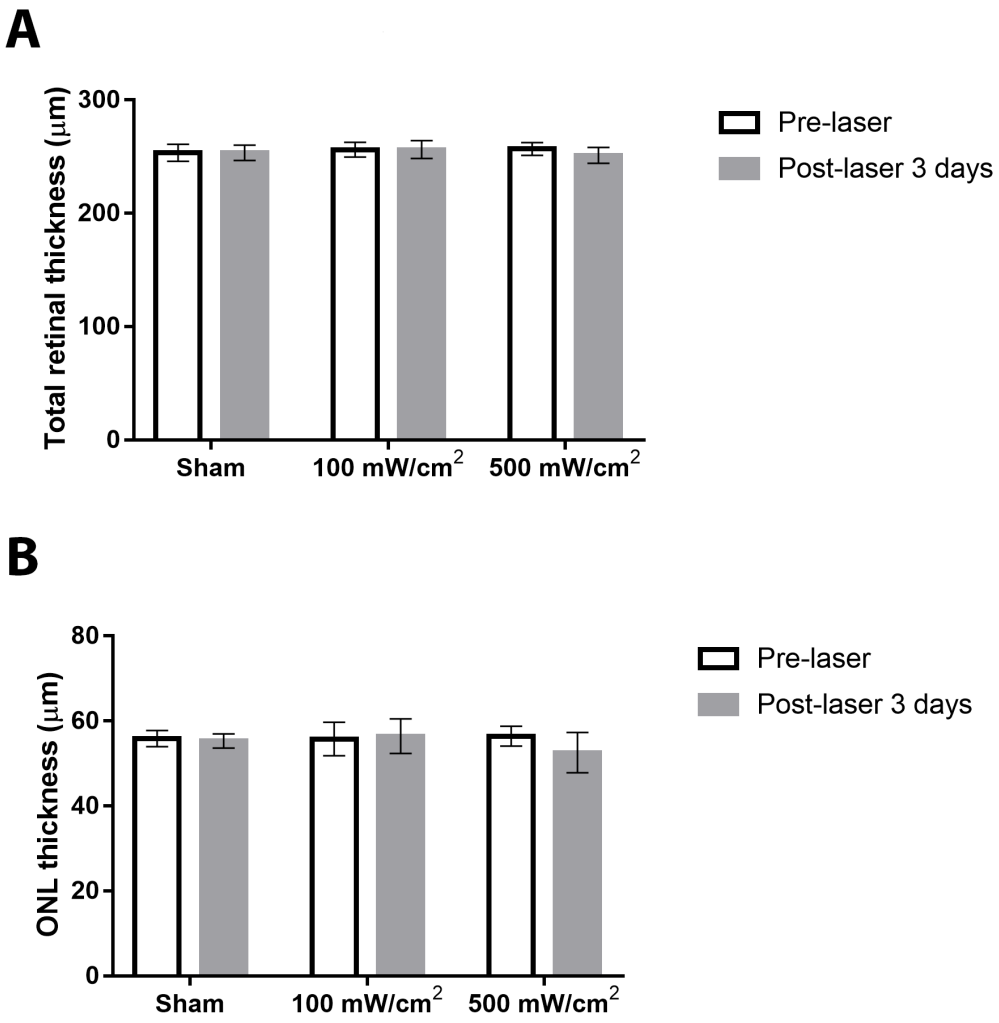

Figure 3.18 Effect of PBM on total retinal thickness (A) and ONL thickness (B) in DA rats after 3 days. Data are expressed as mean ± SEM.

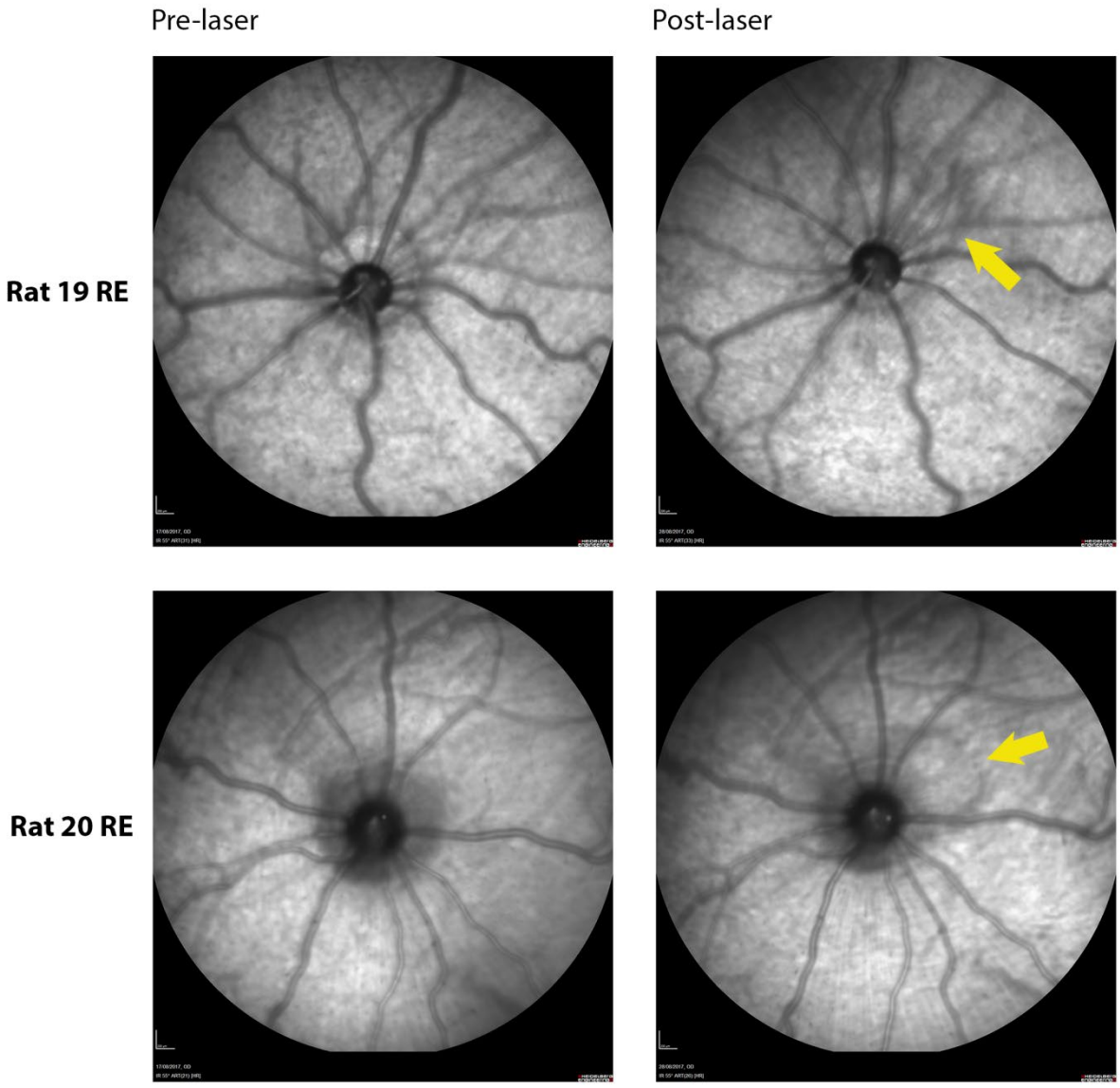

Figure 3.19 Comparison of fundus photos taken at baseline and at 3 days post-PBM in two eyes that received 500 mW/cm^2 PBM. Yellow arrows indicate abnormalities post-laser.

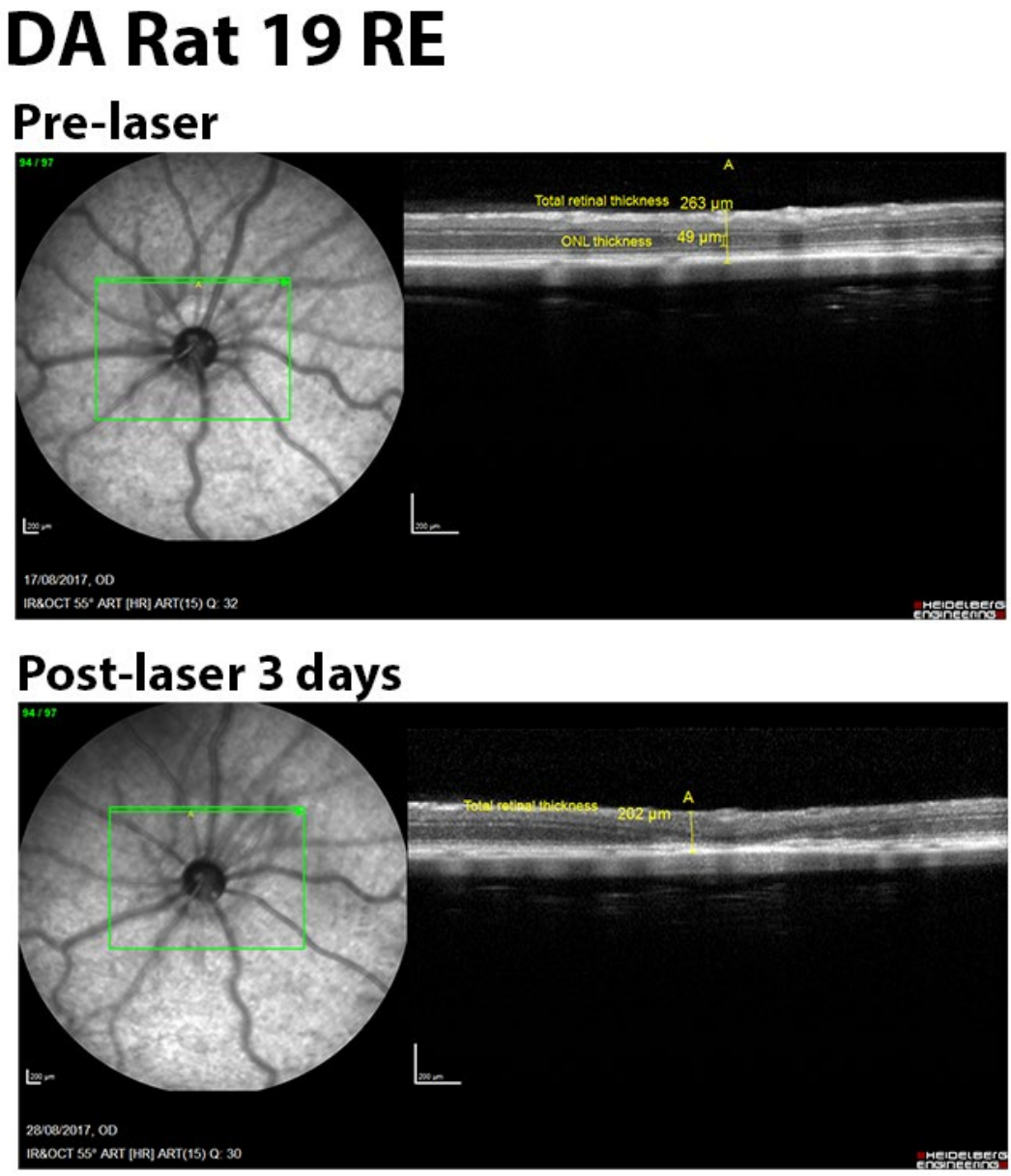

Figure 3.20 Upper panel represents SD-OCT at baseline in DA rat 19 right eye (500 mW/cm^2) with point A marking total retinal thickness of 263 µm. Lower panel shows SD- OCT of the same rat 3 days post-laser. Total retinal thickness at point A is 202 µm (23% reduction), while there is focal destruction of the ONL at point A.

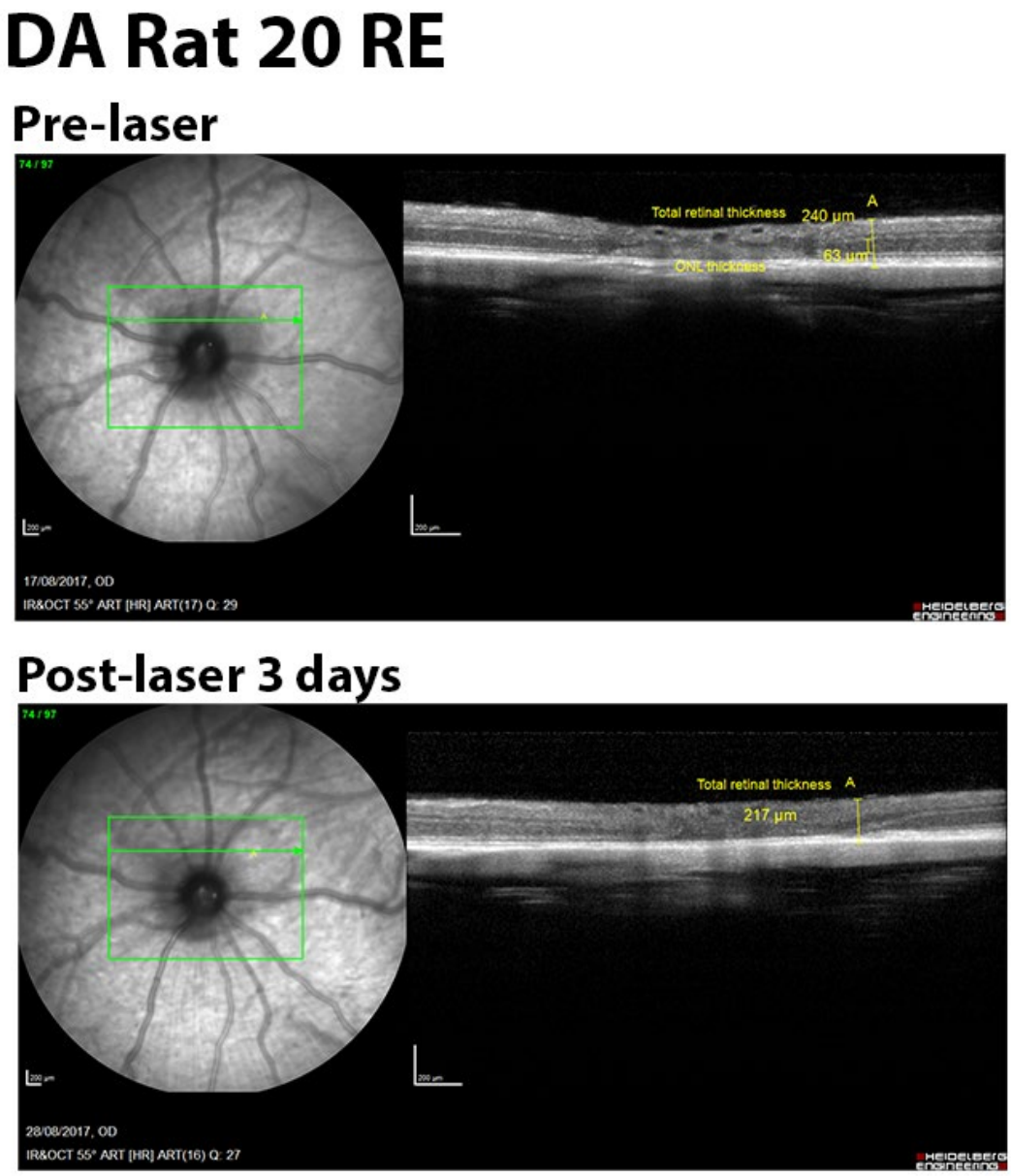

Figure 3.21 Upper panel represents SD-OCT at baseline in DA rat 20 right eye (500 mW/cm^2) with point A marking total retinal thickness of 240 µm. Lower panel shows SD- OCT of the same rat 3 days post-laser. Total retinal thickness at point A is 217 µm (10% reduction), while there is focal destruction of the ONL at point A.

3.3.2.2 FA

Fluorescein angiograms taken of every eye from the sham, 100 mW/cm^2 and 500 mW/cm^2 groups showed normal vasculature and no fluorescein leakage at 3 days post-laser, including the two eyes from the 500 mW/cm^2 group that had peripapillary abnormalities as evidence by SD-OCT and fundus photography (Figure 3.22).

Figure 3.22 FA images of the right eyes of DA rats 19 and 20 taken at 3 days post-laser, which appear normal despite having fundus and SD-OCT changes.

3.3.2.3 Histology

Gross examination of whole eye specimens analysed at 3 days post-PBM showed no evidence of retinal haemorrhages or cataracts in eyes from any of the treatment groups. Histological evaluation of retinas from sham and 100 mW/cm^2 groups yielded results that were entirely consistent with those obtained from SD-OCT and FA. Specifically,

there was no evidence of photoreceptor destruction, disorganisation of photoreceptor segments, macro- or micro-gliosis, upregulation of stress proteins, or damage to the RPE, either within the peripapillary zone or throughout the remainder of the irradiated zone (see Figs. 3.24-3.26).

Histological examination of rats treated with 500 mW/cm^2 (high dose) confirmed the findings obtained from SD-OCT and FA. Thus, in 2/6 eyes (DA 19R and DA 20R), localised peripapillary retinal damage was observed, but no neuronal injury was manifest in the remainder of the irradiated zone (See Figs. 3.23, 3.25, 3.26). The affected rats (see Figs. 3.23 for representative images from DA rat 19R) featured very localised damage to the ONL with loss of photoreceptor rod and cone nuclei, inner and outer segments. This was accompanied by localised upregulations of the stereotypical macroglial stress markers glial fibrillary acidic protein (GFAP) and ciliary neurotrophic factor (CNTF). Furthermore, a dramatically increased microglial presence was evident in the affected region, particularly in the degenerating outer nuclear layer. Overt damage to the RPE layer could be discerned. The inner retina of affected rats remained structurally intact. As for the 7d rats, the peripapillary damage was very localised (See Fig. 3.23). Unlike the 7d rats, subtle stress responses, such as GFAP and FGF-2 upregulations, could be observed 1 mm from the ONH on the affected side, a distance well within the irradiated zone (See Figs. 3.25, 3.26). In the remaining 4/6 eyes, no abnormalities were apparent either within the peripapillary zone or throughout the remainder of the irradiated zone.

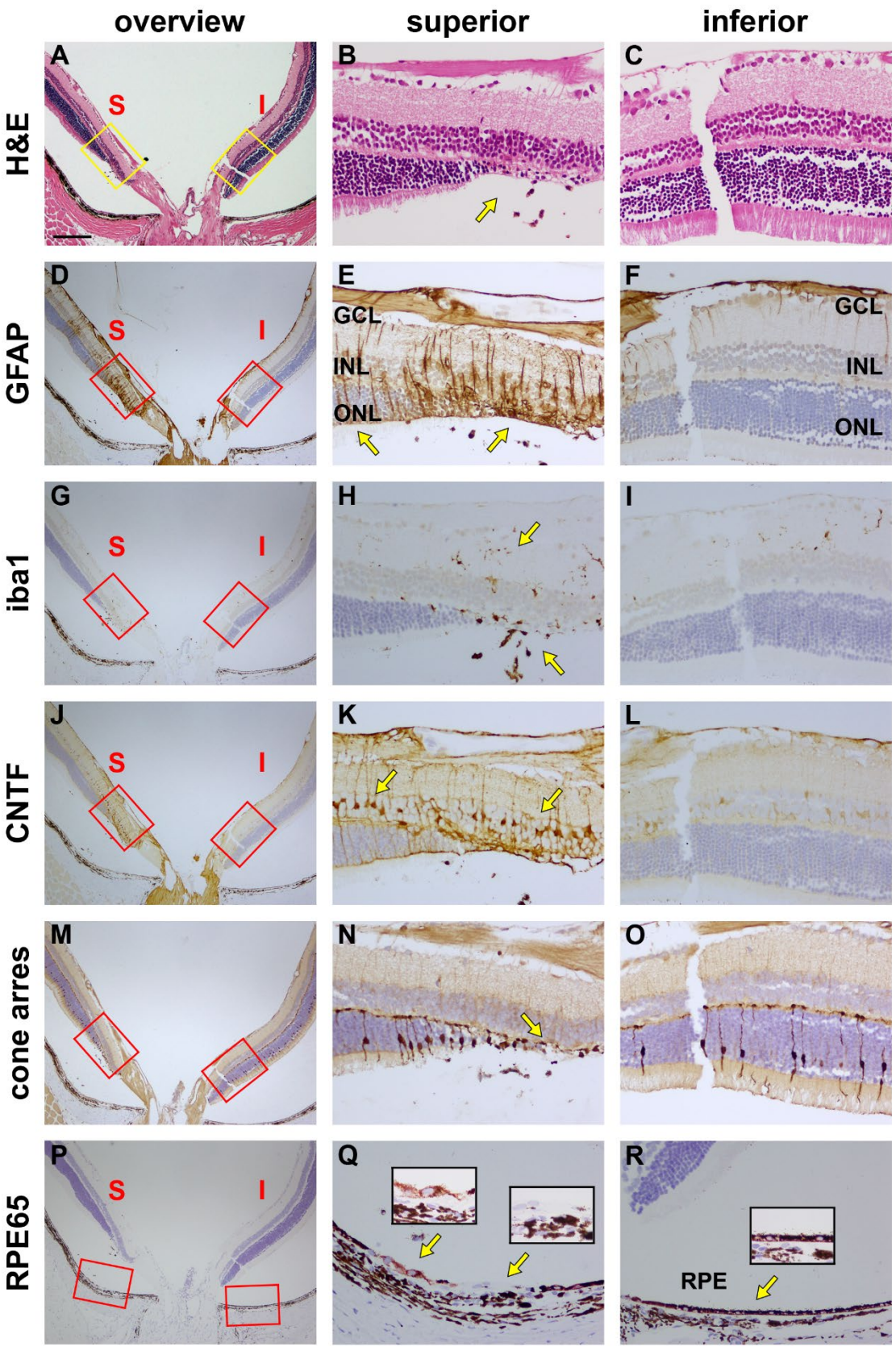
overview
superior
inferior
H&E
GFAP
iba1
CNTF
cone arres
RPE65
A
B
C
D
E
F
G
H
I
J
K
L
M
N
O
P
Q
R
S
I
GCL
INL
ONL
RPE

Figure 3.23 Histology of DA rat 19 right eye (500 mW/cm^2). Transverse sections at the level of the optic nerve head (ONH) were stained for haematoxylin and eosin (A-C), and immunolabelled for GFAP (D-F), iba1 (G-I), CNTF (J-L), cone arrestin (cone arres, M-O) and RPE65 (P-R). There is localised destruction of photoreceptor rod and cone nuclei, inner and outer segments immediately superior to the ONH (A, B, M, N arrows). This is accompanied by greatly increased expression of GFAP (D, E, arrows) and CNTF (J, K, arrows) by Müller cells and astrocytes overlying and immediately adjacent to the affected area. Numerous iba1-positive, activated microglia can be observed within the damaged area of the retina (G, H, arrows). The RPE layer shows loss of RPE65 immunolabelling at the lesion (Q, arrows, highlighted within insets). On the inferior side of the ONH, there is no patent injury or upregulation of glial markers (C, F, I, L, O, R). Scale bar: A, D, G, J, M, P = 250 μm; B, C, E, F, H, I, K, L, N, O, Q, R = 50 μm. GCL, ganglion cell layer; INL, inner nuclear layer; ONL, outer nuclear layer; RPE, retinal pigment epithelium.

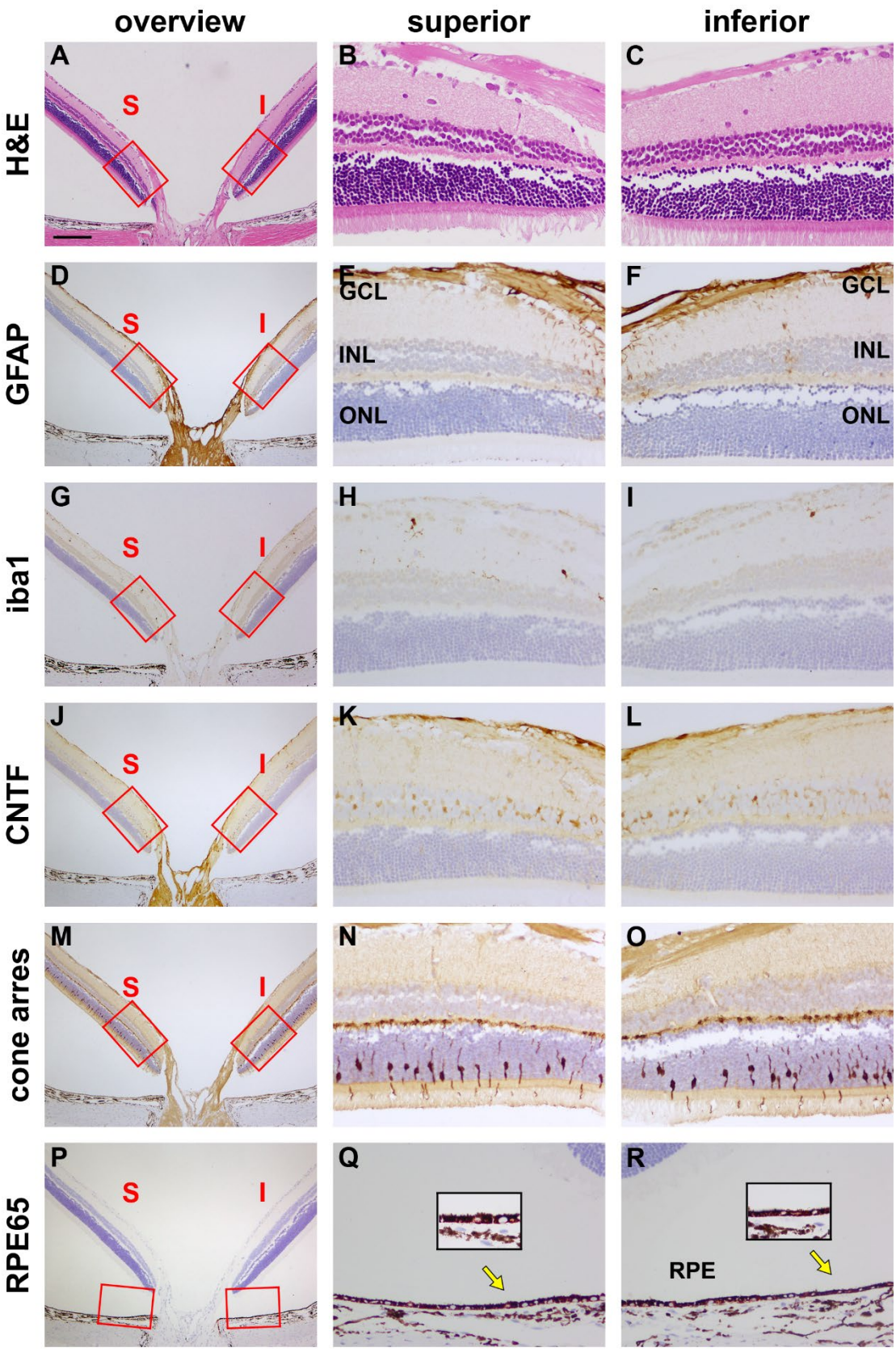
overview
superior
inferior
H&E
GFAP
iba1
CNTF
cone arres
RPE65
A
B
C
D
E
F
G
H
I
J
K
L
M
N
O
P
Q
R
S
I
GCL
INL
ONL
RPE

Figure 3.24 Histology of DA rat 21 left eye (100 mW/cm^2). Transverse sections at the level of the optic nerve head (ONH) were stained for haematoxylin and eosin (A-C), and immunolabelled for GFAP (D-F), iba1 (G-I), CNTF (J-L), cone arrestin (cone arres, M-O) and RPE65 (P-R). There is no discernible injury to rod or cone photoreceptor nuclei, nor to inner and outer segments either superior or inferior to the ONH (A-C, M-O). This is no upregulation of GFAP (D-F) or CNTF (J-L) by Müller cells or astrocytes. There is no obvious increase in the number of iba1-positive microglia nor do they display any morphological signs of activation (G, H, arrows). The RPE layer appears normal on both sides of the ONH (P-R arrows, highlighted within insets). Scale bar: A, D, G, J, M, P = 250 μm; B, C, E, F, H, I, K, L, N, O, Q, R = 50 μm. GCL, ganglion cell layer; INL, inner nuclear layer; ONL, outer nuclear layer; RPE, retinal pigment epithelium.

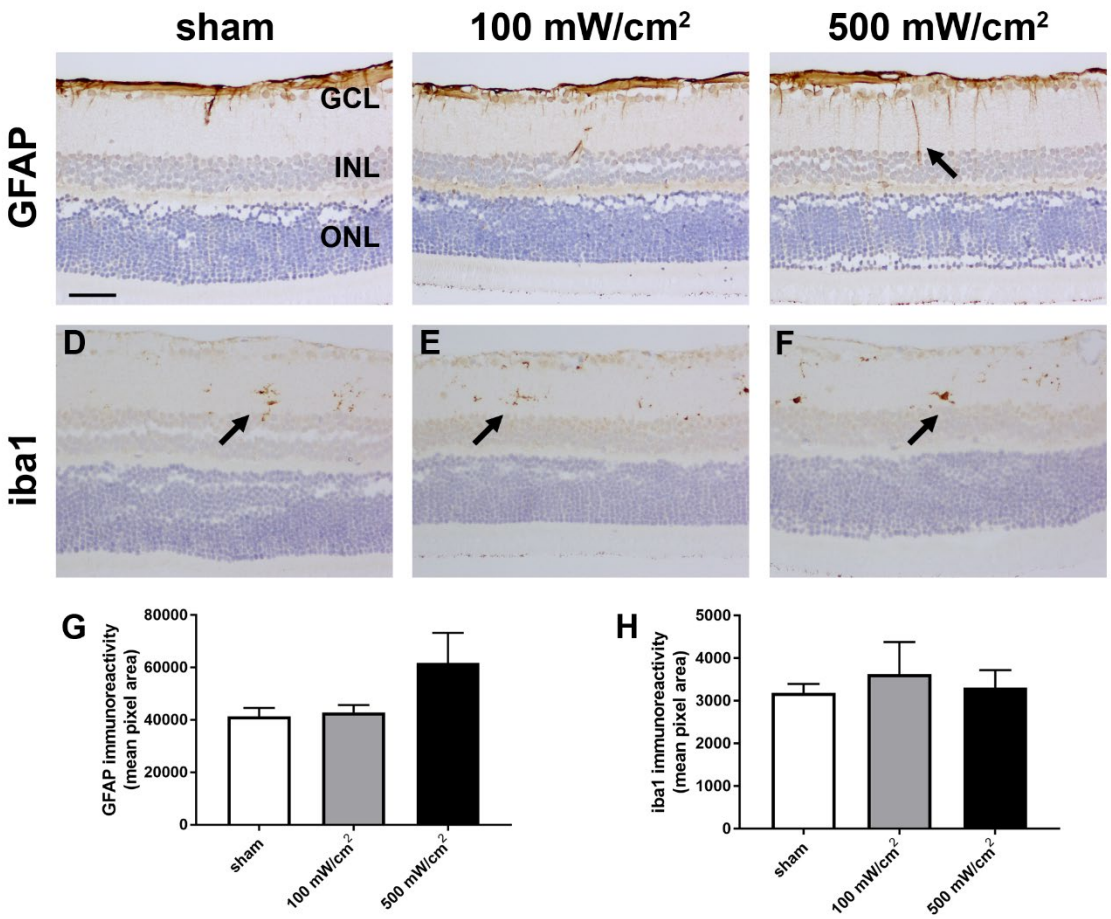

Figure 3.25 Effect of PBM on macroglia and microglia in DA rats at 3 days post-PBM. (A-F) Representative images of retinas from sham, 100 mW/cm^2 and 500 mW/cm^2 groups immunolabelled for GFAP and iba1 (arrows). Images were captured within the irradiated zone at approximately 1 mm from the optic nerve head. (G, H) Quantification of GFAP and iba1 abundances, as defined in the Materials and Methods. Data are expressed as the mean ± SEM, where n=3-6 for each group. ANOVA revealed no significant differences in GFAP or iba1 abundance between treatment groups. Nevertheless, there was a tendency for elevated GFAP abundance in the 500 mW/cm^2 group. Scale bar = 50 μm. GCL, ganglion cell layer; INL, inner nuclear layer; ONL, outer nuclear layer

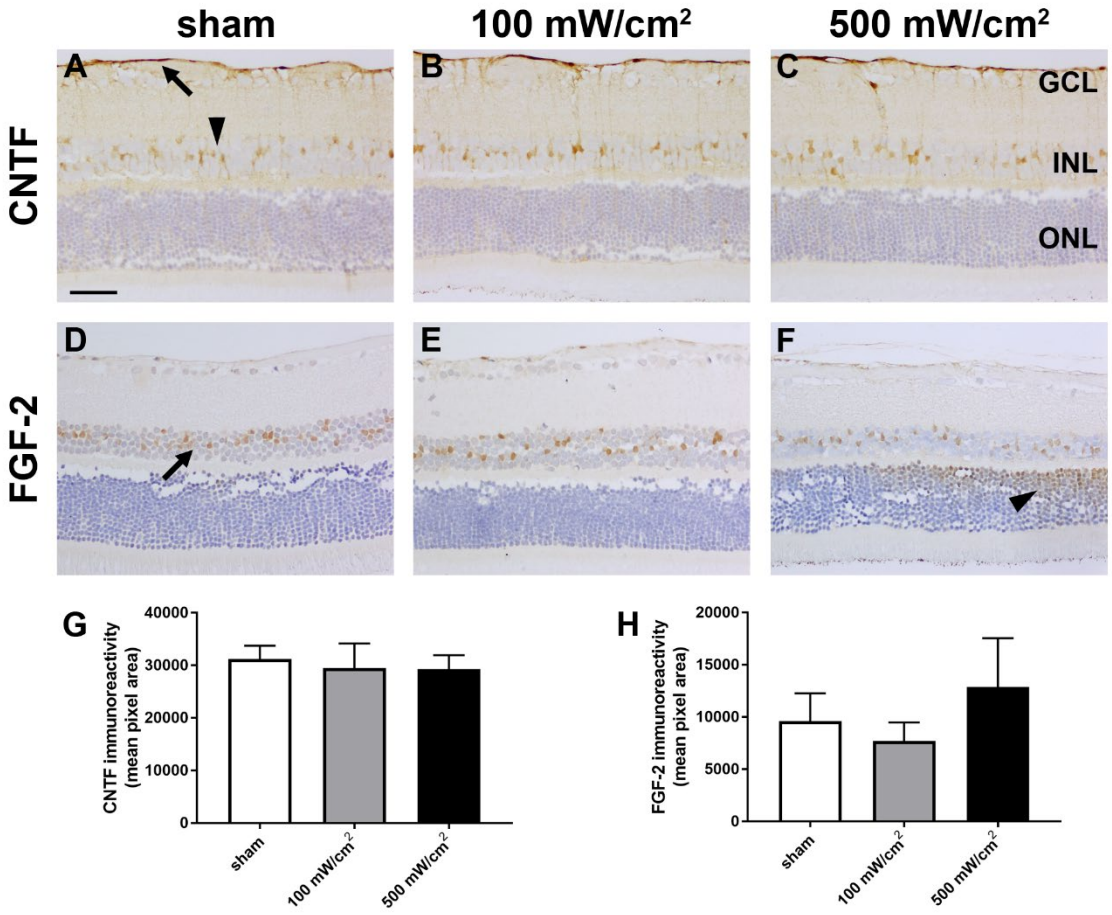

Figure 3.26 Effect of PBM on levels of stress proteins in DA rats at 3 days post-PBM. (A-F) Representative images of retinas from sham, 100 mW/cm² and 500 mW/cm² groups immunolabelled for CNTF and FGF-2 (arrows). Images were captured within the irradiated zone at approximately 1 mm from the optic nerve head. (G, H) Quantification of CNTF and FGF-2 abundances, as defined in the Materials and Methods. Data are expressed as the mean ± SEM, where n=3-6 for each group. ANOVA revealed no significant differences in CNTF and FGF-2 abundance between treatment groups. Nevertheless, there was de novo FGF-2 expression by

photoreceptors in rat 20R from the 500 mW/cm^2 group (see F). Scale bar = 50 μm. GCL, ganglion cell layer; INL, inner nuclear layer; ONL, outer nuclear layer.

Table 3.11 Summary of affected 500 mW/cm^2 treated DA rats with SD-OCT/fundus changes

Rat ID	Mean baseline total retinal thickness (μm)	Mean post-laser total retinal thickness (μm)	Mean baseline ONL thickness (μm)	Mean post-laser ONL thickness (μm)	Description of fundus and OCT changes
DA 8R (7d)	238.9 ± 7.8	175.9 ±19.4	53.7 ± 8.3	17.9 ± 11.4	Distinct retinal pigment changes around the optic disk, particularly inferior nasally on fundus imaging. On SD-OCT, there were points of severe damage with reduction of total retinal thickness by 40% and destruction of the ONL.
DA 11R (7d)	253.9 ± 7.2	223.9 ±10.2	49.7 ± 5.0	39.6 ± 12.8	Fundus imaging shows notable pigment changes from the adjacent temporal side of the optic disk extending superiorly. On SD-OCT, there is up to 33% and 85% reduction of total retinal thickness and ONL respectively in focal areas of severe damage.
DA 14R (7d)	249.7 ± 8	218 ± 14.3	53.8 ± 5.1	35.8 ± 15.1	There is marked pigment changes surrounding the temporal and superior side of the optic disk on fundus imaging. SD-OCT shows a decrease of up to 27% total retinal thickness as well as complete destruction of the ONL.

DA 16R (7d)	239 ± 5.9	212.4 ± 12.7	53.2 ± 5.5	37.7 ± 10.1	Fundus imaging reveals two confluent spots of pigment change- one larger area situated superiorly while a smaller area located superior-temporally relative to the optic disk. On SD-OCT, there is a reduction of total retinal thickness of 31% whilst the ONL is severely damaged and immeasurable.
DA 19R (3d)	266 ± 6.7	247.4 ± 18	59.4 ± 10.7	48.3 ± 16.6	There are subtle pigment changes superiorly to the optic disk. On SD-OCT, there is 23% reduction of total retinal thickness and deformation of the ONL.
DA 20R (3d)	252.9 ± 9.3	239.8 ± 16.7	59 ± 10.4	45.2 ± 19	Fundus imaging again subtle pigment changes superior-nasally to the optic disk. There is relatively minor thinning of the total retinal thickness (10%). However, the ONL thickness immeasurable in these damaged areas.

3.3.3 Experiment 3.3 – Safety study in non-pigmented rats analysed at one week post-PBM

3.3.3.1 SD-OCT

No qualitative changes were observed in the SD rat retina at 7 days post-laser. Neither the total retinal nor ONL thickness were significantly different between baseline and post-laser in any of the treatment groups (Tables 3.12 and 3.13, Fig. 3.27).

Table 3.12 Effect of PBM on retinal thickness in SD rats after 7 days

Treatment group	Baseline ONL thickness (µm)	Post-PBM ONL thickness (µm)	Difference ONL thickness (µm)	P value	Fundus change (Yes/No)
Sham	231.6 ± 2.8	232.5 ± 1.8	0.9 ± 0.7	0.33	No
100 mW/cm^2 dose	232.0 ± 3.6	232.4 ± 5.5	0.4 ± 1.4	0.83	No
500 mW/cm^2	236.3 ± 5.8	235.5 ± 4.4	-0.8 ± 0.7	0.60	No

Data are expressed as mean ± SEM, where n=3 (sham), n=3 (100 mW/cm^2), n=6 (500 mW/cm^2).

Table 3.13 Effect of PBM on ONL thickness in SD rats after 7 days

Treatment group	Baseline ONL thickness (µm)	Post-PBM ONL thickness (µm)	Difference ONL thickness (µm)	P value	Fundus change (Yes/No)
Sham	55.7 ± 3.9	54.9 ± 2	-0.7 ± 0.3	0.25	No
100 mW/cm^2	55.4 ± 0.6	56 ± 0.8	0.6 ± 1	0.66	No
500 mW/cm^2	53.1 ± 2	53.6 ± 1.8	0.5 ± 0.6	0.39	No

Data are expressed as mean ± SEM, where n=3 (sham), n=3 (100 mW/cm^2), n=6 (500 mW/cm^2).

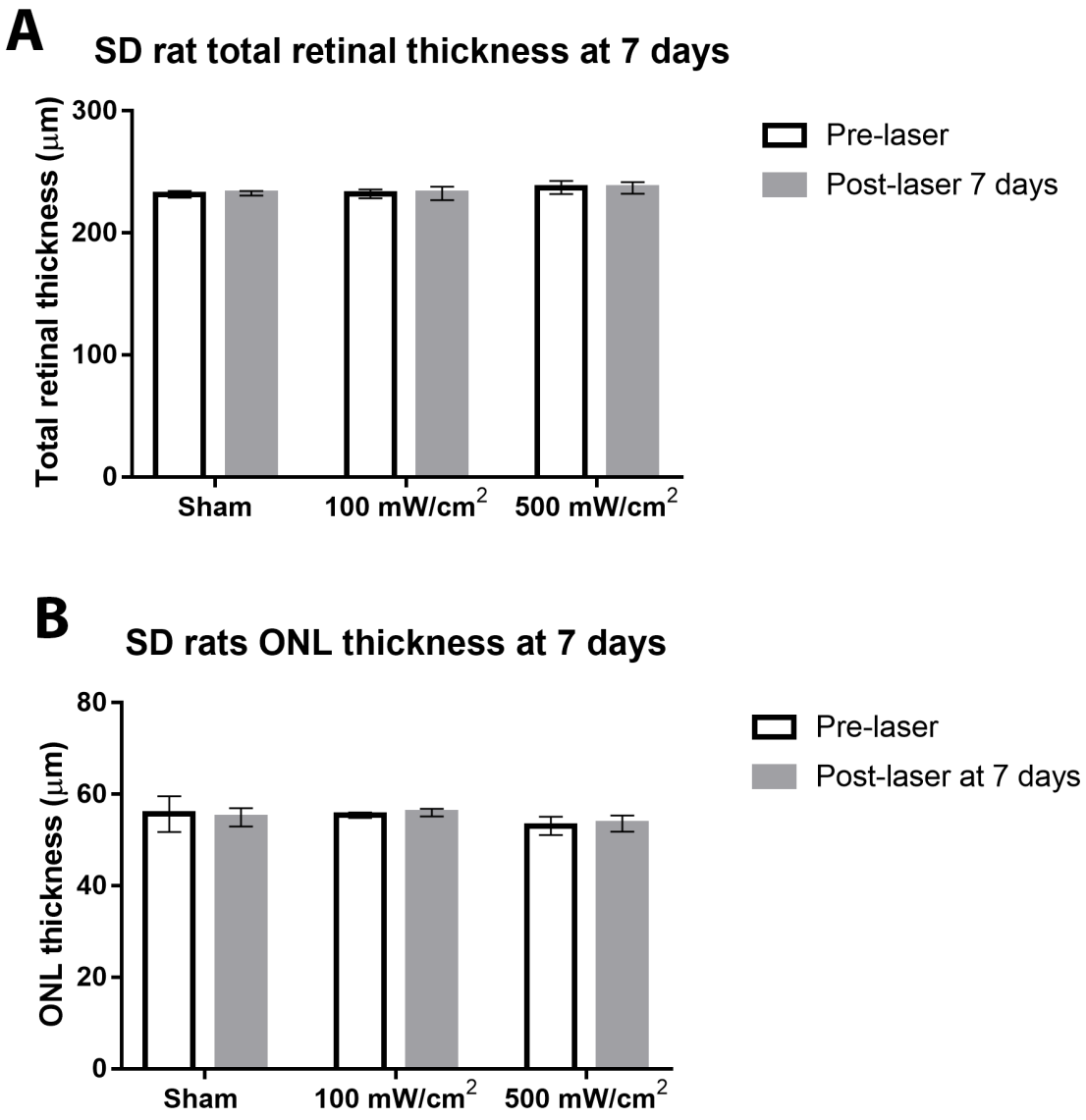

Figure 3.27 Effect of PBM on total retinal thickness (A) and ONL thickness (B) in SD rats after 7 days. Data are expressed as mean ± SEM.

3.3.3.2 FA

SD rat eyes showed normal FA with no evidence of fluorescein leakage in any of the treatment groups. There were no structural retinal vascular abnormalities.

3.3.3.3 Histology

Gross examination of whole eye specimens analysed at 7 days post-PBM showed no evidence of retinal haemorrhages or cataracts in eyes from any of the SD treatment groups.

Unlike DA rats, at the high energy setting (500 mW/cm^2), there was no focal damage noted within the peripapillary zone in any of the 6 rats analysed (Fig. 3.28). All retinal layers were intact. No injury to the ONL, inner or outer segments was discernible. There was no upregulation of glial stress markers or damage to the RPE. Similarly, at 1 mm from the ONH, within the irradiated zone, there were no differences in the abundances of GFAP, iba1 or stress proteins between the various treatment groups (Figs. 3.29, 3.30).

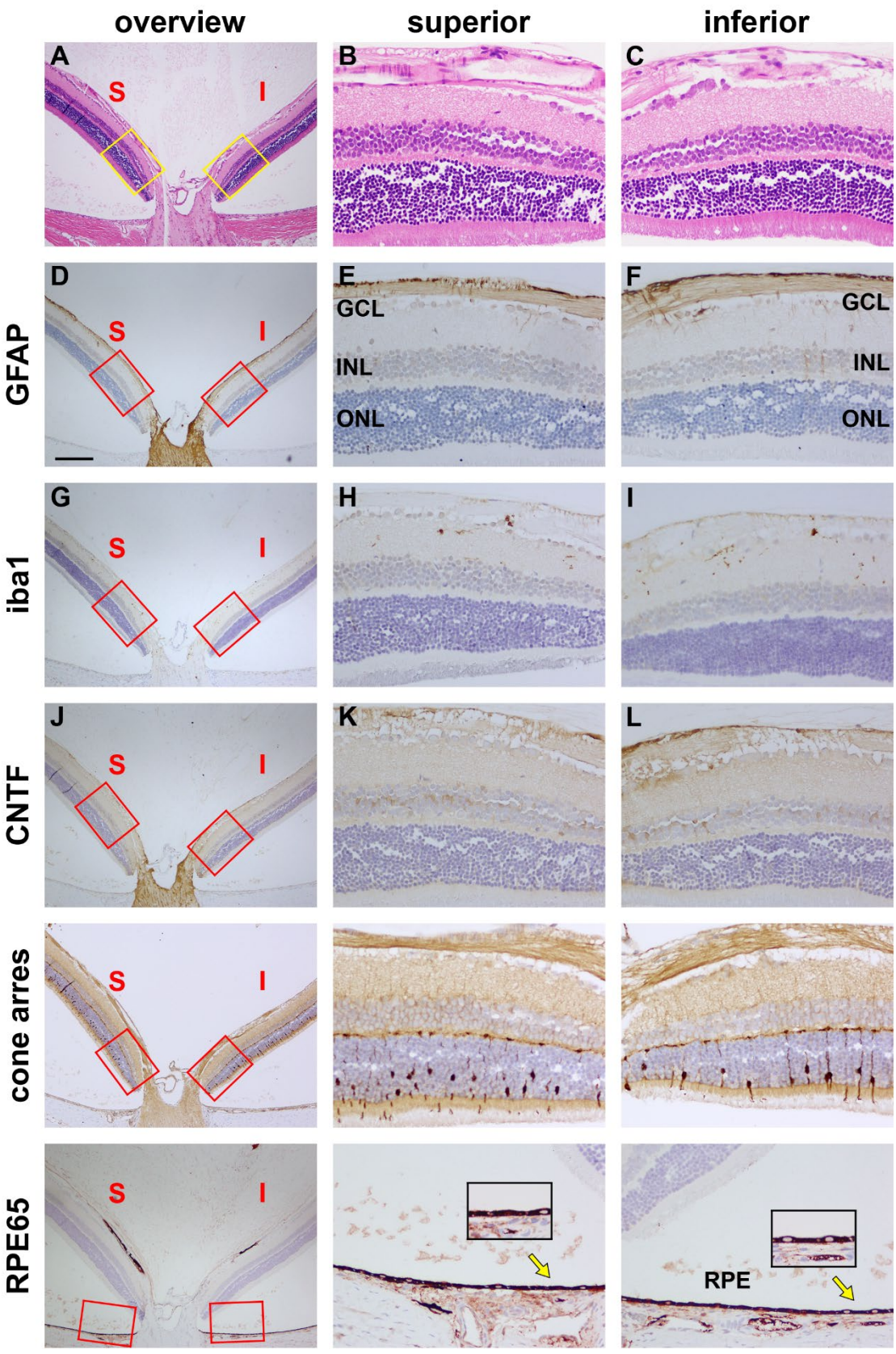
overview
superior
inferior
A
S
I
B
C
GFAP
D
E
GCL
INL
ONL
F
iba1
G
H
I
CNTF
J
K
L
cone arres
RPE65
RPE

Figure 3.28 Histology of SD rat 26 right eye (500 mW/cm^2). Transverse sections at the level of the optic nerve head (ONH) were stained for haematoxylin and eosin (A-C), and immunolabelled for GFAP (D-F), iba1 (G-I), CNTF (J-L), cone arrestin (cone arres, M-O) and RPE65 (P-R). There is no discernible injury to rod or cone photoreceptor nuclei, nor to inner and outer segments either superior or inferior to the ONH (A-C, M-O). This is no upregulation of GFAP (D-F) or CNTF (J-L) by Müller cells or astrocytes. There is no obvious increase in the number of iba1-positive microglia nor do they display any morphological signs of activation (G, H, arrows). The RPE layer appears normal on both sides of the ONH (P-R arrows, highlighted within insets). Scale bar: A, D, G, J, M, P = 250 μm; B, C, E, F, H, I, K, L, N, O, Q, R = 50 μm. GCL, ganglion cell layer; INL, inner nuclear layer; ONL, outer nuclear layer; RPE, retinal pigment epithelium.

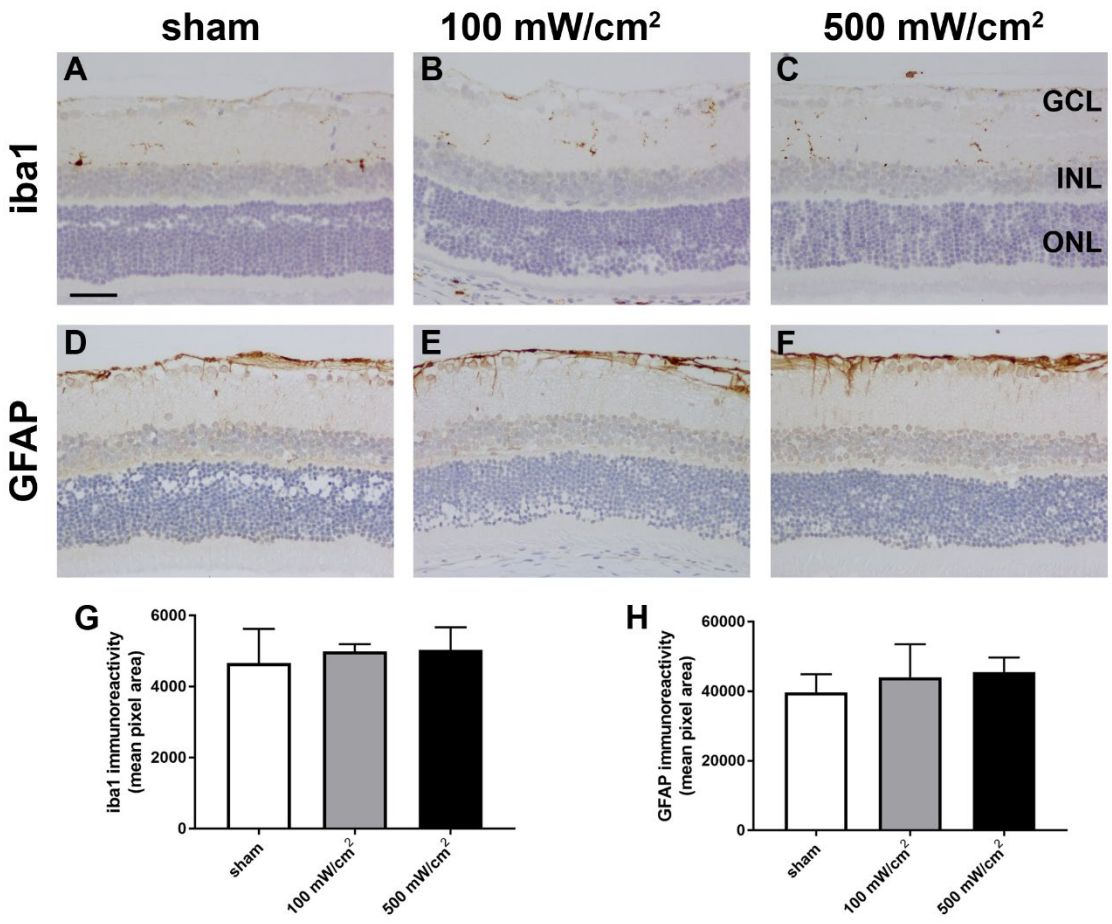

Figure 3.29 Effect of PBM on macroglia and microglia in SD rats at 7 days post-PBM. (A-F) Representative images of retinas from sham, 100 mW/cm^2 and 500 mW/cm^2 groups immunolabelled for iba1 and GFAP. Images were captured within the irradiated zone at approximately 1 mm from the optic nerve head. (G, H) Quantification of iba1 and GFAP abundances, as defined in the Materials and Methods. Data are expressed as the mean ± SEM, where n=3-6 for each group. ANOVA revealed no significant differences in GFAP or iba1 abundance between treatment groups. Scale bar = 50 μm. GCL, ganglion cell layer; INL, inner nuclear layer; ONL, outer nuclear layer.

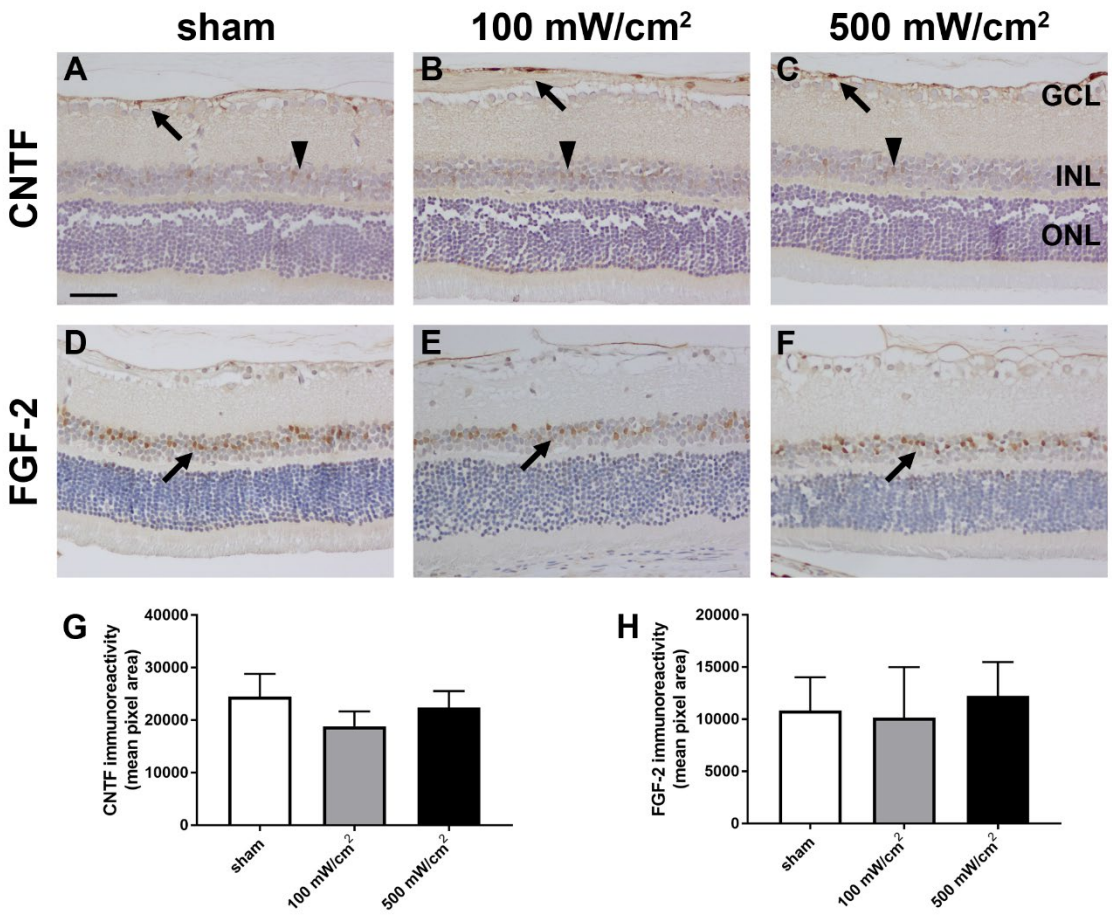

Figure 3.30 Effect of PBM on levels of stress proteins in SD rats at 7 days post-PBM. (A-F) Representative images of retinas from sham, 100 mW/cm^2 and 500 mW/cm^2 groups immunolabelled for CNTF and FGF-2 (arrows). Images were captured within the irradiated zone at approximately 1 mm from the optic nerve head. (G, H) Quantification of CNTF and FGF-2 abundances, as defined in the Materials and Methods. Data are expressed as the mean ± SEM, where n=6-10 for each group. ANOVA revealed no significant differences in CNTF and FGF-2 abundance between treatment groups. Scale bar = 50 μm. GCL, ganglion cell layer; INL, inner nuclear layer; ONL, outer nuclear layer.

3.4 Discussion

3.4.1 Laser-delivered PBM is safe in albino rats and at doses of 100 mW/cm^2 in pigmented rats

The results from this chapter reveal that there exists a safety threshold for laser-delivered PBM in pigmented rats, which could be identified as 500 mW/cm^2 irradiance or 45 J/cm^2 fluence (see section 3.4.2). However, at irradiance doses of up to 100 mW/cm^2, PBM caused no adverse changes to the pigmented retina, as determined by fundus photography, SD-OCT, FA, electroretinography, and immunohistochemical assessment of neuronal and glial markers. In albino rats, no adverse events were identified even at 500 mW/cm^2 irradiance; there were no structural changes identified post-laser using any of the methods identified above. Furthermore, there was no upregulation of GFAP within the irradiated zone. GFAP, a cytoskeletal protein produced by macroglial cells, is generally considered the most sensitive indicator of retinal stress.[207]

3.4.2 Laser-delivered PBM causes occasional localised damage at 500 mW/cm^2 in pigmented rats

At the highest irradiance dose (500 mW/cm^2), occasional localized damage was noted in pigmented rats within the peripapillary region. This was clearly identifiable by SD-OCT, FA and histological changes post-laser when compared to baseline. Changes were evident by 3 days following the last laser session and were still present at 7 days post-laser. Damage was confined to the outer retina, encompassing the ONL, inner and outer segments, and RPE. SD-OCT changes corresponded well with histological degenerative

changes found in photoreceptor nuclei, inner and outer segments. Moreover, in affected rats, there were marked increases of damage markers at the site of injury, including evidence of macro- (GFAP) and micro-gliosis (iba1 microglial cells), as well as glial-derived stress proteins (CNTF and FGF-2). These are common immunohistochemical markers for homeostatic dysfunction and are therefore sensitive markers for retina injury.[208] CNTF and FGF-2, in particular, are trophic factors upregulated as part of the retina's endogenous survival mechanism against injuries including light damage, trauma, ischemia, excitotoxicity and laser-induced damage.[208-212] Of importance, upregulation of these histological markers were confined to the peripalliary zone. Only very occasional effects were observed at distances of 1 mm from the ONH, which remains well within the zone of irradiation. At 1 mm from the ONH, there were no statistically significant increases in expression of GFAP, iba1, CNTF or FGF-2 between the sham and 500 mW/cm^2 groups, indicating the absence of any overt homeostatic disruption. It is important to emphasize that the quantification of immunohistochemistry was only performed away from the optic nerve head. As there was no difference between affected and unaffected rats in the 500 mW/cm^2 group away from the nerve head, there was no need to subdivide analysis.

On SD-OCT, retinal changes appeared more prominent at 7 days post-laser, which was manifest as greater total retinal thickness loss compared to 3 days post-laser. This suggests an evolving loss of photoreceptors in the affected area. Interestingly, the significant difference in ONL thickness before and 7 days-post laser in the 500 mW/cm^2 seems largely driven by very severe thinning in the affected animals- Rats 8 RE, Rat 11

RE, Rat 14 RE and Rat 16RE (Table 3.11), causing the mean post-PBM ONL thickness to be significantly lower. In contrast to affected rats at 7 days post-laser, affected rats analysed at 3 days post-laser did not demonstrate FA changes, despite having clear histological and SD-OCT evidence of focal damage. One explanation for this finding is that inflammatory changes post-laser cause a delayed effect upon the deep vessels of the retina or choroidal vessels, causing leakage that may not be visible initially. Due to the focal nature of damage, it is worthy to mention that changes in retinal thickness may be underestimated by the measurement of the pre-determined SD-OCT analysis points which may miss particular areas of focal thinning. In hindsight, these pre-determined analysis points were selected to reflect generalized changes within the irradiation zone rather than focal changes which were not anticipated. We acknowledge that there may be slight variations measurements on retinal thinning before and after treatment due to the slight differences in the angle of scans captured. This was minimized by corresponding measurement points to landmarks such as vessels to ensure the same point was measured before and after treatment. Despite SD-OCT, histology and FA showing damage in some pigmented rats treated with 500 mW/cm^2 PBM, no significant changes in b- or a-wave amplitude or implicit times were measurable on ERG. A likely reason for this finding is that ERG detects global visual changes reflecting pan-retinal damage. The focal damage observed in these rats may well have been detectable on multifocal ERG.[213] It is a limitation of the current study that multifocal ERG was not available. Another potential minor confounding factor is the presence of oscillatory potentials that may impact measurements of implicit time and b-wave amplitudes. The use of a low pass filter may address this. On another note, it is worthy to mention the

reason for the use of rats instead of mice in the current safety study was that dilated mice eyes could only sufficiently receive up to 100 mW/cm^2 hence rat eyes were required to examine the 500 mW/cm^2 irradiance dose.

The mechanism behind the localised damage seen following high dose, laser-delivered PBM is presently unknown. One putative explanation is that it may be a manifestation of PBM's biphasic dose response. This phenomenon is based on the premise that a dose too low will not produce benefit, however, too high a dose may suppress PBM's positive influence or even cause damage. Therefore, the efficacy of PBM relies on determining an optimal dose. The biphasic dose response nature of PBM is a well-documented phenomenon.[177] Indeed, Chu-Tan et al.[188] reported a biphasic dose response of 670 nm LED in a light-induced retinal degeneration rat model. The irradiance was fixed at 60 mW/cm^2 whilst a fluence range of 9-90 J/cm^2 was assessed on varying severities of light-induced retinal injuries. At low to medium damage setting, low dose PBM fluence provided neuroprotective benefit, whilst 90 J/cm^2 was ineffective and even increased photoreceptor apoptosis. Interestingly, in eyes with high damage, only 90 J/cm^2 was beneficial, suggesting higher doses may be required for more severe injuries. Most retinal degeneration animal studies have used an irradiance range of 20-60 mW/cm^2 or fluence range of 3.4-9 J/cm^2 and have not reported any adverse effects of PBM.[137,163,164,189-192] The high dose tested in our study is well above previous safe fluence ranges. PBM is known to upregulate ROS in normal tissues in a dose-dependent manner whilst reducing ROS during oxidative stress.[165,185] Conceivably, higher doses in

affected rats may lead to excess ROS that overwhelms the intrinsic cellular antioxidant system and result in oxidative damage.

An alternative explanation for the focal damage is that it may be laser-induced. The mechanisms underlying laser-induced damage are photochemical, photomechanical and photothermal.[214] Photochemical damage is caused by free radicals that are generated following interaction of high-energy, shorter wavelength visible light with chromophore molecules contained within the retina and RPE. The free radicals attack nearby cellular structures causing lipid and protein peroxidation particularly lipid rich POS and protein-rich neurosensory retina. Photochemical damage is associated with increased exposure duration, accumulative doses and progressive retinal degeneration.[215] Given the PBM laser emits a longer wavelength 670 nm light, a photochemical cause is unlikely. In addition, the neurosensory retina, which appeared unaffected in the study, would also have been expected to be damaged by protein oxidation. Varying the duration and the number of sessions in further studies may provide a clue as to whether a photochemical component is present.

Photomechanical damage results from mechanical compressive or tensile forces produced by the rapid introduction of energy into the RPE melanosomes.[216] In the present study, photomechanical damage is unlikely given that it requires both an enormous irradiance doses in the range of megawatts or terawatts per cm squared as well as an extremely brief exposure times in the range of nanoseconds to picoseconds.

Photothermal damage derives from photon absorption by tissue molecules causing increased mean kinetic energy which is dissipated by molecules colliding, resulting in a temperature rise.[214] Generally, the wavelength is inversely proportional to the potential increase of kinetic energy and subsequent temperature rise for a given exposure time. Photon absorption is facilitated by pigments, including melanin, which is most abundant in the RPE. Pigmented rats have higher melanin in their RPE and are thus much more susceptible to photothermal laser damage than albino rats. Photothermal damage is initially evident histologically in photoreceptors and the RPE which is consistent with the focal damage observed in the affected rats of this study.[215,217,218] Of the various theoretical possibilities, photothermal damage would seem to be the most likely mechanism of laser-induced injury, due to the distribution and scale of damage and the fact that only pigmented rats were affected. However, it is worth noting that the PBM laser has a flat-top beam profile and thus broader damage would have been expected within the irradiance zone with photothermal injury.

The results from the present study indicate that there exists a safety threshold for PBM laser which was identified as 500 mW/cm^2 irradiance or 45 J/cm^2 fluence for pigmented rats. The findings have some resemblance to those of a long-term safety study of transcranial laser-delivered 808 nm PBM on SD rat brain that reported photothermal damage with continuous wave laser at irradiances of 750 mW/cm^2 (90 J/cm^2 fluence).[219] Rats treated with PBM of up to 375 mW/cm^2 irradiance were unaffected. Histological analysis of affected brain tissue at the high setting revealed focal areas characterized by subdural necrosis, loss of neuronal tissue, infiltration of macrophages, foci of granular

mineralization and meningeal artery degeneration that were consistent with thermal damage. These rats displayed thermal-related skin reddening and blistering in irradiated areas in addition to neurological deficits.

Safe treatment parameters from preclinical studies are often difficult to extrapolate to the clinical setting due to variation of delivery methods, wavelength and physiological differences between targeted tissues. The rationale for the current study was to precisely examine safe PBM dosages for treatment of the retina with a novel laser prior to assessment of neuroprotection efficacy and eventual clinical translation. There have been clinical safety studies of PBM laser in stroke[220,221] and hair loss[222], but very few studies targeting application to the retina. The most notable exception is that study of Al Kent et al.[223], who performed a clinical study to examine the safety of PBM in neonates with retinopathy of prematurity using 670 nm light at 9 J/cm^2 for 15 minutes (10 mW/cm^2). There were no adverse effects reported, however, a non-confluent LED source was used and the primary outcomes were skin-related rather than eye-associated adverse effects. Thus, the results have little relevance to the current study.

There is little doubt that laser is a highly suitable delivery method for PBM as it allows for direct exposure of calculated irradiances to to the retina, avoiding random scattering of R/NIR light that comes from non-coherent LED-based PBM. In addition, the laser device, which is mounted on a slit-lamp, provides the advantage of immediate translation to the clinical setting, as the setup would be familiar to clinicians due to its similarity to other retinal laser procedures such as photocoagulation.

3.5 Conclusion

The PBM laser is safe at low and medium irradiation doses, however, in some pigmented rats, very localised damage were noted at the high irradiance dose setting (500 mw/cm^2). The study findings reflect a safety threshold for PBM, facilitating the use of a safe dose range when examining neuroprotection efficacy in Chapter 4.

4. Neuroprotection efficacy of laser-delivered photobiomodulation in a mouse model of retinitis pigmentosa

4.1 Aims

The aims of the experiments detailed in chapter 4 were as follows: 1) to characterize the populations of genuine short wavelength opsin sensitive (S-opsin$^+$) cones, genuine medium/long wavelength opsin sensitive (M/L-opsin$^+$) cones, and dual cones (cones that express both S-opsin and M/L-opsin) in the four retinal quadrants of 60 day old rd1 mice; 2) to investigate whether laser-directed PBM augments cone photoreceptor survival in rd1 mice using the safe irradiance settings identified from Chapter 3. The hypothesis to be tested was that laser-delivered PBM promotes survival of S-opsin$^+$ and M/L-opsin$^+$ cones in rd1 mice.

4.2 Design

4.2.1 Characterization study

The rd1 mice is a well-known rodent model for autosomal RP, characterized by rapid rod loss starting from P8-10 and finishing at P21.[76] However, to our knowledge there are no studies that have characterized the ratio of different cone types in this animal model. The rationale for this study was to characterize the cone population in the rd1 mice. Such information would provide important baseline data for the subsequent neuroprotection study. Rd1 eyes (N=24) at P60 from control animals were collected and dissected for immunohistochemical analysis (Figure 4.1). Whole-mount retinae were double labelled with OPN1SW and anti-R/G opsin. OPN1SW labels ultraviolet sensitive

opsin expressed by S-opsin^{+} cones. Anti-R/G opsin labels red and green sensitive M/L-opsin expressed by M/L-opsin^{+} cones. Dual cones express both S-opsin and M/L-opsin. Quantification was performed according to the Methods detailed in Chapter 2.

4.2.2 Neuroprotection study

Rd1 mice were divided into three treatment groups: sham, low dose PBM (25mW/cm^2) and high dose PBM (100mW/cm^2). In each animal, one eye received sham or PBM, while the fellow eye was untreated. Treatment began from P21 and occurred every twice weekly until euthanasia. Optokinetic (OKN) function was assessed at P35 by determining maximal spatial frequency for a positive head reflex. Animals were euthanized at P60 (experiment 4.2a- Figure 4.2) or P90 (experiment 4.2b- Figure 4.3) and the retinas dissected for determination of cone survival. The densities of S-opsin^{+} cones and M/L-opsin^{+} cones were determined following fluorescent double immunolabelling of retinal wholemounts (Figure 4.10, 4.14). In addition, cone segment density was separately determined. Cone segments were identified by their narrow bundle-like appearance and labelled with greater fluorescent intensity (Fig. 4.18). To assess the cone segment density, the threshold was adjusted so that only segments were highlighted. All quantifications were performed according to the Methods detailed in Chapter 2.

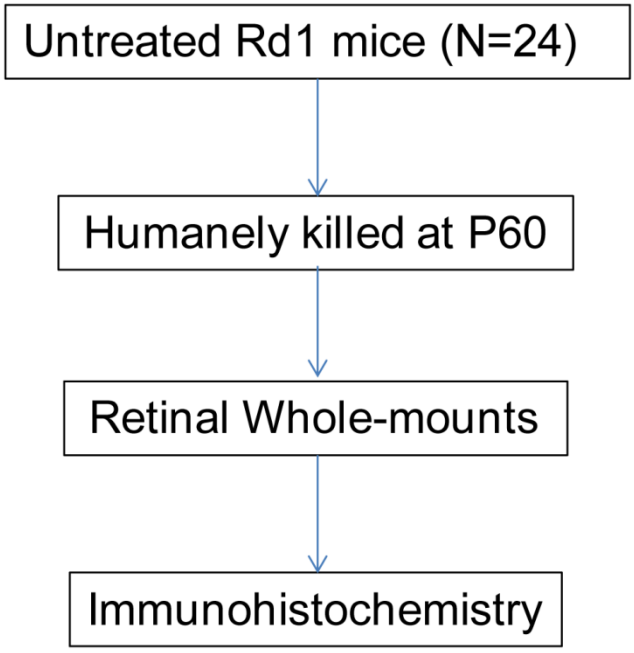

Figure 4.1: Flow chart of the experimental plan for experiment 4.1

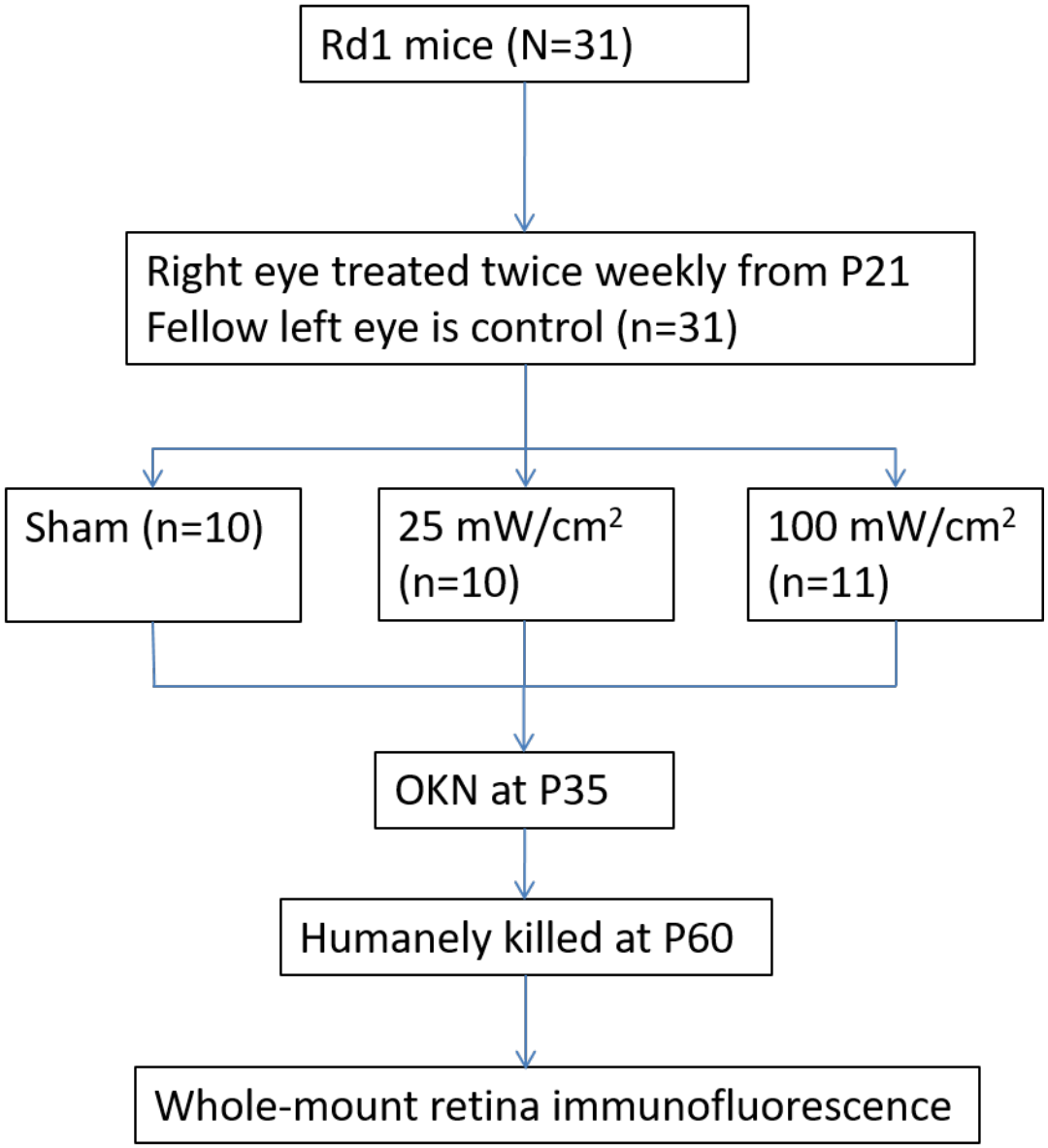

Figure 4.2: Flow chart of the experimental plan for experiment 4.2a

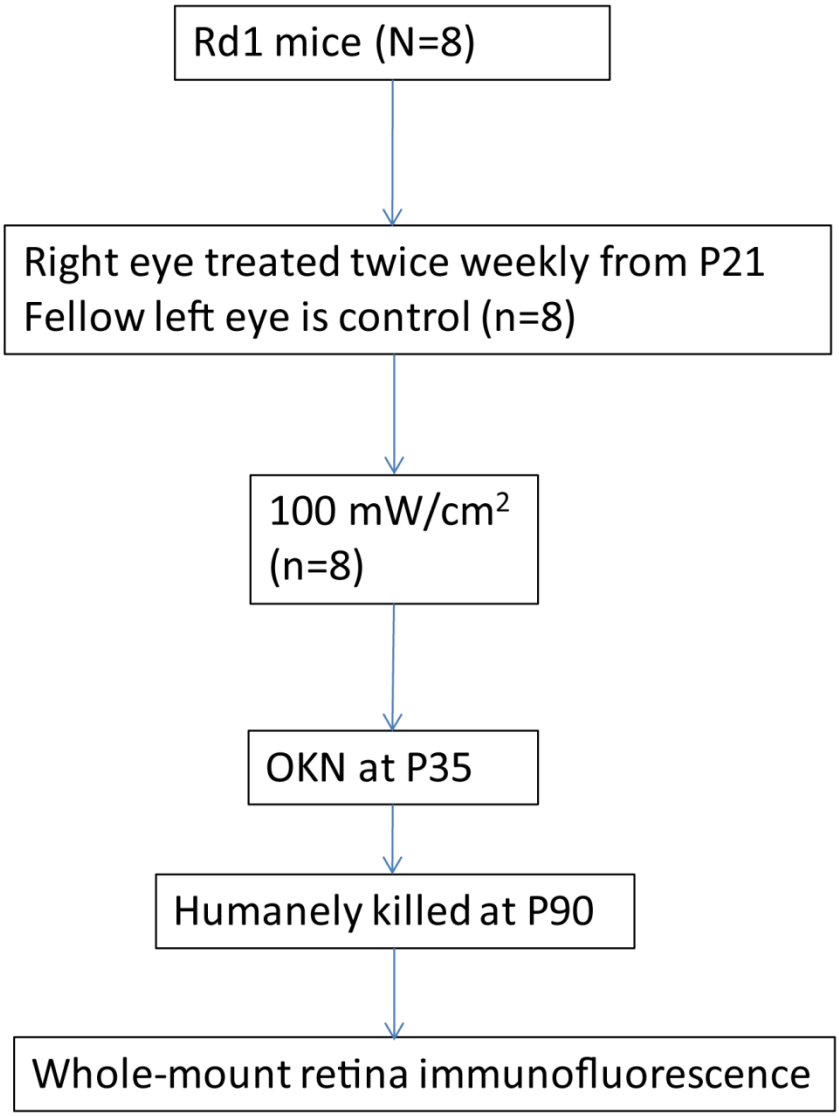

Figure 4.3: Flow chart of the experimental plan for experiment 4.2b

4.2.3 Laser procedure

Mice were sedated with isofluorane throughout the laser procedure. One drop of a local anaesthetic (oxybuprocaine 0.4%) and one drop of a pupil dilator (tropicamide 1%) to enable opening of the pupil and visualisation of the optimum area of retina through the eye. Mice were anaesthetised using isofluorane throughout the procedure. The mice was placed on a custom-designed rodent holder by the researcher at the slit lamp laser

delivery system. The laser was centred on the optic nerve and the retina was exposed to R/NIR irradiation for 90 seconds**.**

4.3 Results

4.3.1 Characterization of cone populations

The mean cone population of rd1 mice composed 59.07% S-opsin^{+} cones, 14.01 M/L-opsin^{+} cones and 26.92% dual cones (Figure 4.8). In the superior retina, the mean cone population comprised 8.23% S-opsin^{+} cones, 38.1% M/L-opsin^{+} cones and 53.67% dual cones (Figure 4.4, 4.9A). In the inferior retina, M/L-opsin^{+} cones were absent whilst S-opsin^{+} cones and dual cones accounted for 97.71% and 2.29% of the cone population, respectively (Figure 4.5, 4.9B). In the nasal retina (Figure 4.6, 4.9C), the mean cone population comprised 30.16% S-opsin^{+} cones, 23.59% M/L-opsin^{+} cones and 46.25% dual cones. The mean cone population in the temporal retina (Figure 4.7, 4.9D) consisted of 23.18% S-opsin^{+} cones, 18.69% M/L-opsin^{+} cones and 58.13% dual cones.

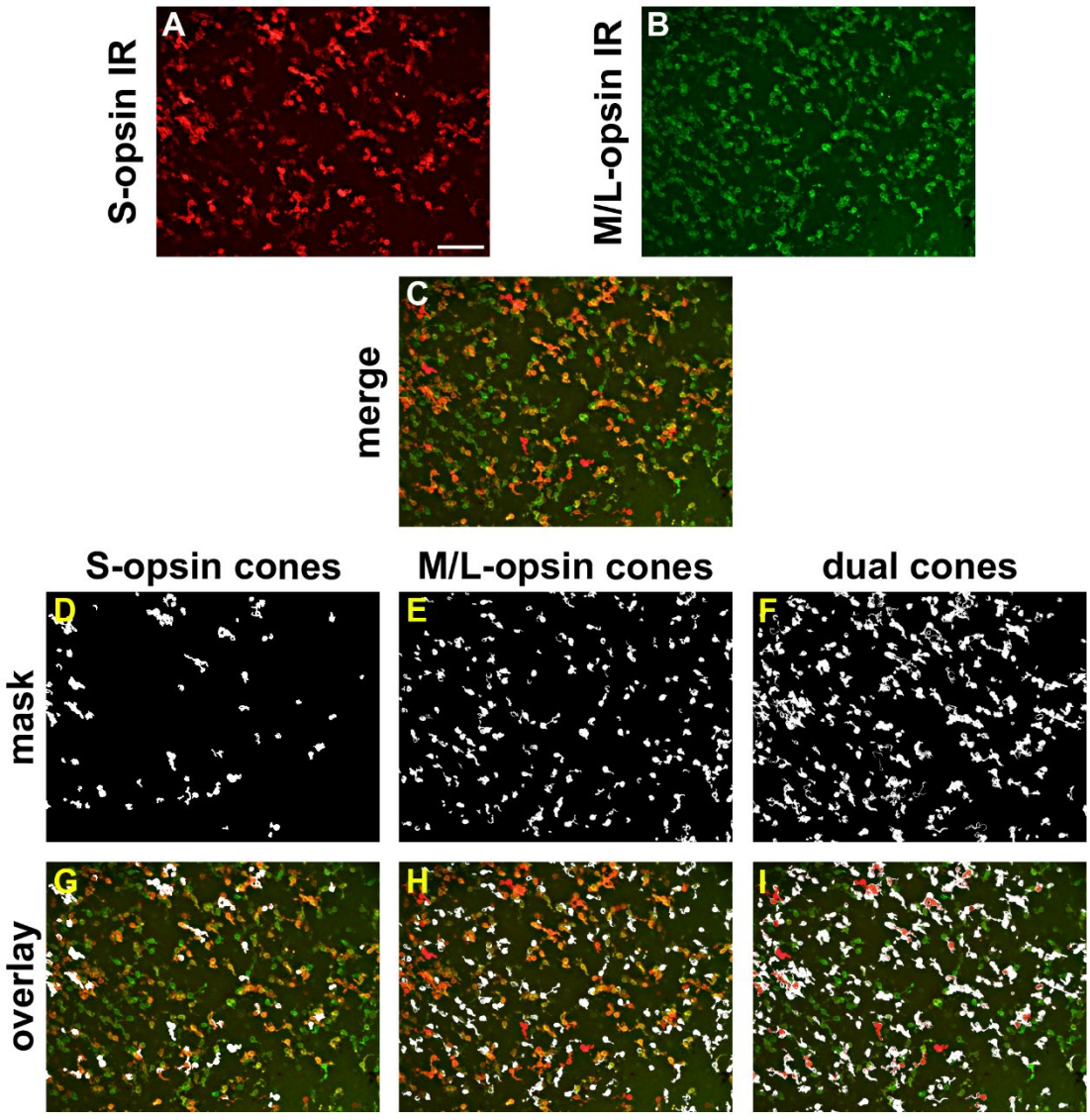

Figure. 4.4 Double-labelled immunofluorescence photomicrograph of rd1 superior retina. (A) shows OPNSW1 labelled S-opsin^{+} cones,(D) shows masked S-opsin^{+} cones and (G) represent overlay image. (B) shows anti-R/G opsin labelled M/L-opsin^{+} cones , (E) shows masked M/L-opsin^{+} cones and (H) represents overlay image. (C) shows dual cones from a composite merged image of S-opsin^{+} and M/L-opsin^{+} cones. (F) shows masked dual cones and (I) represents overlay image.

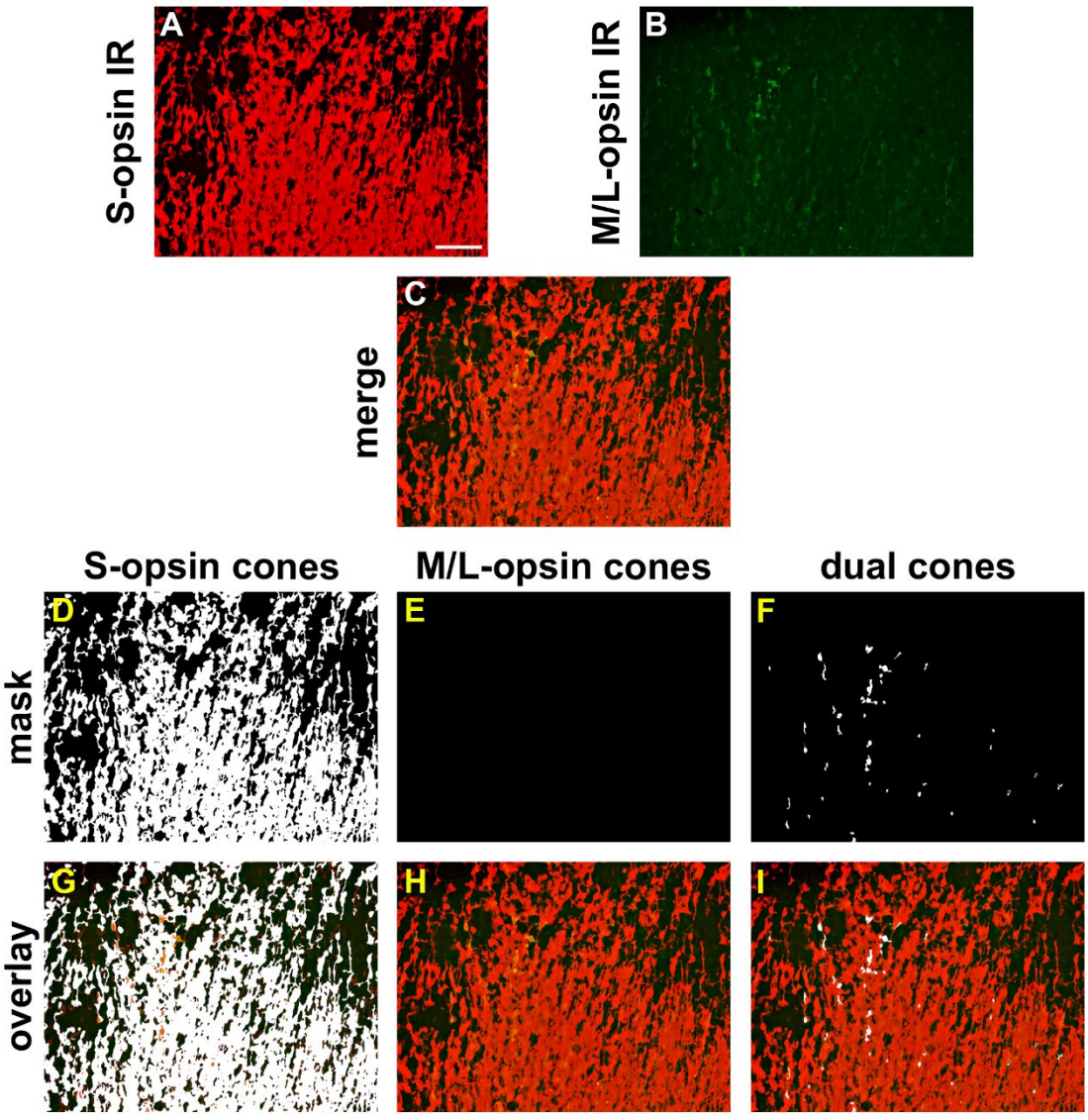

Figure 4.5 Double-labelled immunofluorescence photomicrograph of rd1 inferior retina. (A) shows OPNSW1 labelled S-opsin$^+$ cones,(D) shows masked S-opsin$^+$ cones and (G) represent overlay image. (B) shows anti-R/G opsin labelled M/L-opsin$^+$ cones , (E) shows masked M/L-opsin$^+$ cones and (H) represents overlay image. (C) shows dual cones from a composite merged image of S-opsin$^+$ and M/L-opsin$^+$ cones. (F) shows masked dual cones and (I) represents overlay image.

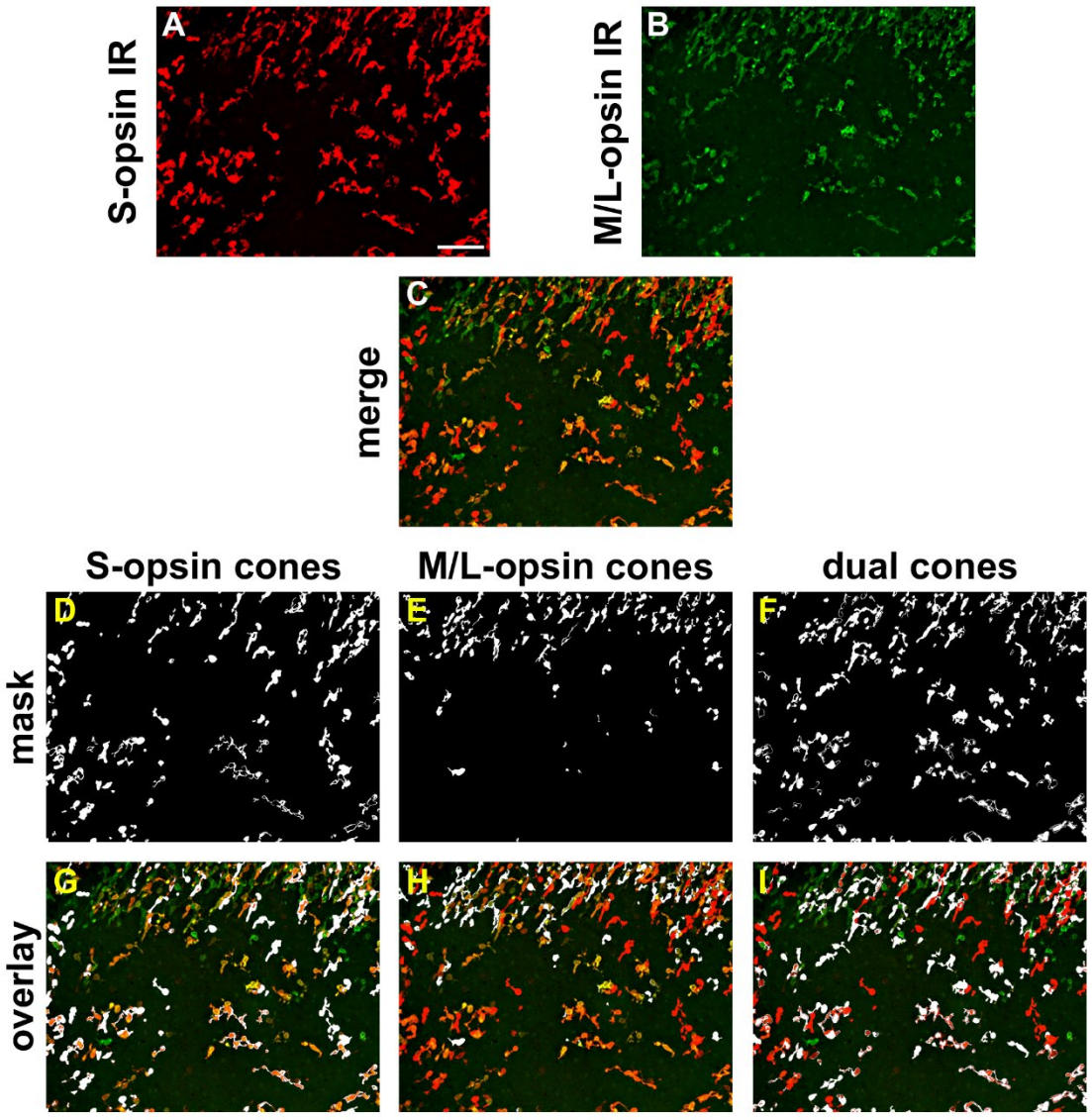

Figure 4.6 Double-labelled immunofluorescence photomicrograph of rd1 nasal retina. (A) shows OPNSW1 labelled S-opsin^{+} cones,(D) shows masked S-opsin^{+} cones and (G) represent overlay image. (B) shows anti-R/G opsin labelled M/L-opsin^{+} cones , (E) shows masked M/L-opsin^{+} cones and (H) represents overlay image. (C) shows dual cones from a composite merged image of S-opsin^{+} and M/L-opsin^{+} cones. (F) shows masked dual cones and (I) represents overlay image.

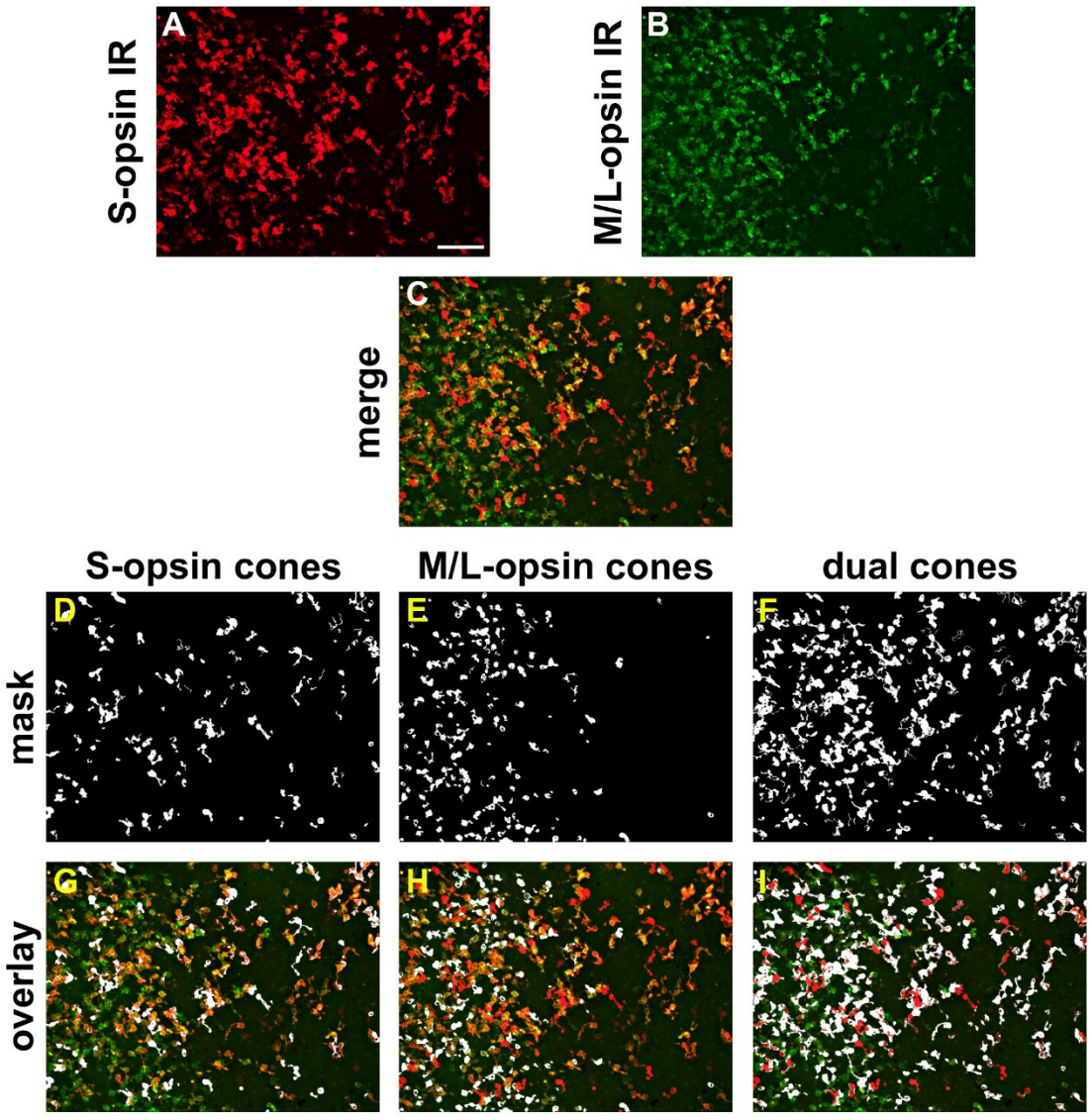

Figure 4.7 Double-labelled immunofluorescence photomicrograph of rd1 temporal retina. (A) shows OPNSW1 labelled S-opsin$^+$ cones,(D) shows masked S-opsin$^+$ cones and (G) represent overlay image. (B) shows anti-R/G opsin labelled M/L-opsin$^+$ cones , (E) shows masked M/L-opsin$^+$ cones and (H) represents overlay image. (C) shows dual cones from a composite merged image of S-opsin$^+$ and M/L-opsin$^+$ cones. (F) shows masked dual cones and (I) represents overlay image.

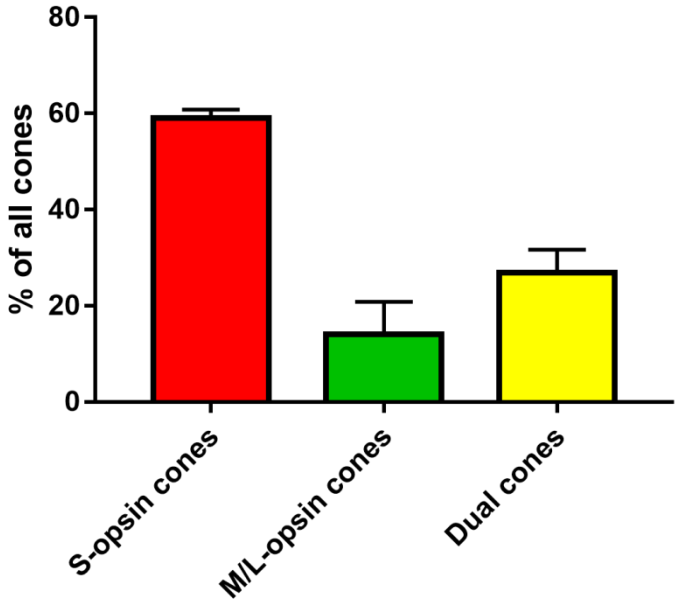

Figure 4.8 Bar graph displaying mean composition of cone population in rd1 mice retinae (N=24) at P60. Data represent mean±SEM.

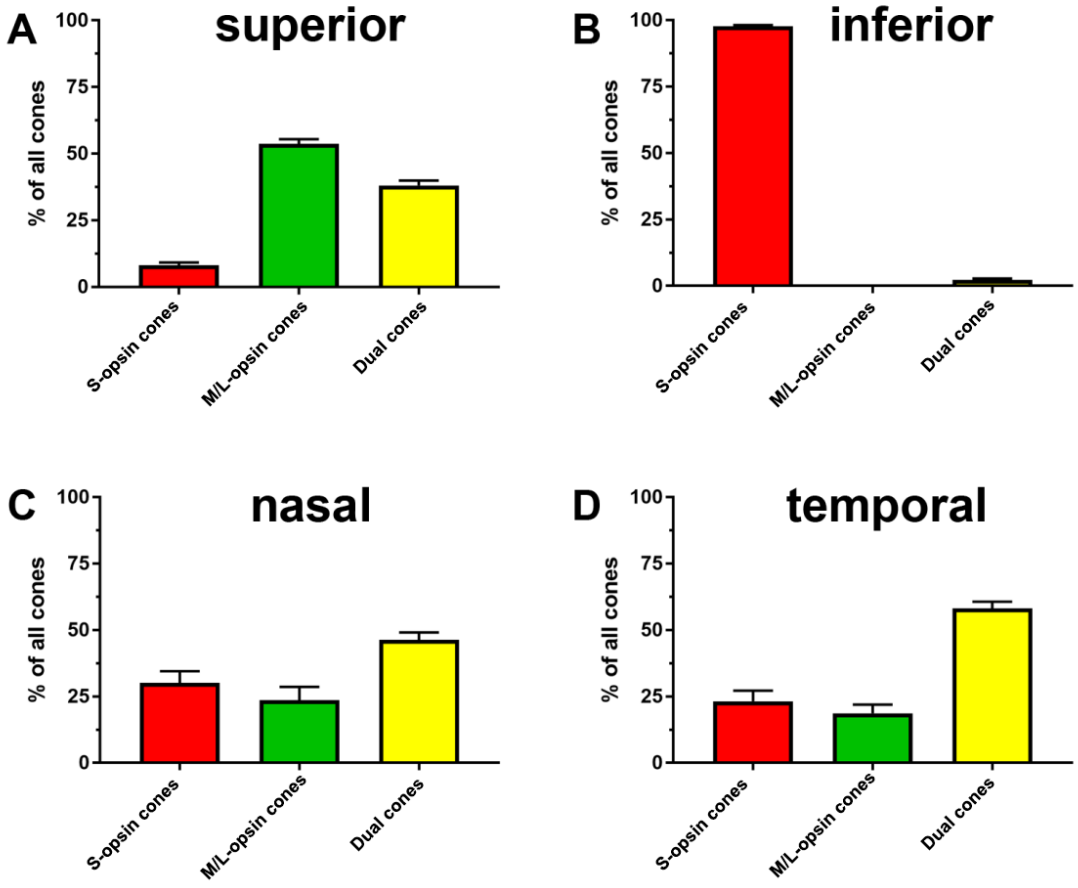

Figure. 4.9 Bar graphs displaying composition of the cone population in the superior (A), inferior (B), nasal (C) and temporal (D) quadrants of the rd1 retina at P60. Data represent mean±SEM.

4.3.2 Effect of photobiomodulation on survival of S-opsin$^+$ cones at P60

Compared to control (n=31) and sham (n=10) animals, the PBM-treated 25 mW/cm^2 (n=10) and 100 mW/cm^2 (n=11) groups had significantly greater (P<0.001) S-opsin$^+$ cone density at P60 (Figure 4.10, 4.11). There was no significant difference in cone density between 25 mW/cm^2 and 100 mW/cm^2 group (P=0.99).

Analysis of the distribution of S-opsin$^+$ cones at P60 revealed significantly (P<0.001) higher cone densities in both the inferior and superior quadrants of the retina in both PBM groups when compared to control or sham-treated mice (Figure 4.12A, B). Furthermore, there were significantly (P<0.001) higher cone densities in both the central and peripheral regions of the retina in both PBM groups when compared to control- or sham-treated mice (Figure 4.12C, D). When normalised (on a pairwise basis) to the control left eyes, S-opsin-$^+$ cones displayed a trend to greater protection in the superior retina versus the inferior retina in all treatment groups (25 mW/cm^2, 100 mW/cm^2); however this was not statistically significant (*P=0.79* for 25 mW/cm^2; *P=0.13* for 100 mW/cm^2) (Figure 4.13A). When normalised (on a pairwise basis) to the control left eyes, preservation of S-opsin-$^+$ cones was significantly greater in the peripheral retina versus the central retina in both the 25 mW/cm^2 (P<0.01) and 100 mW/cm^2 PBM (P<0.05) groups (Figure 4.13B).

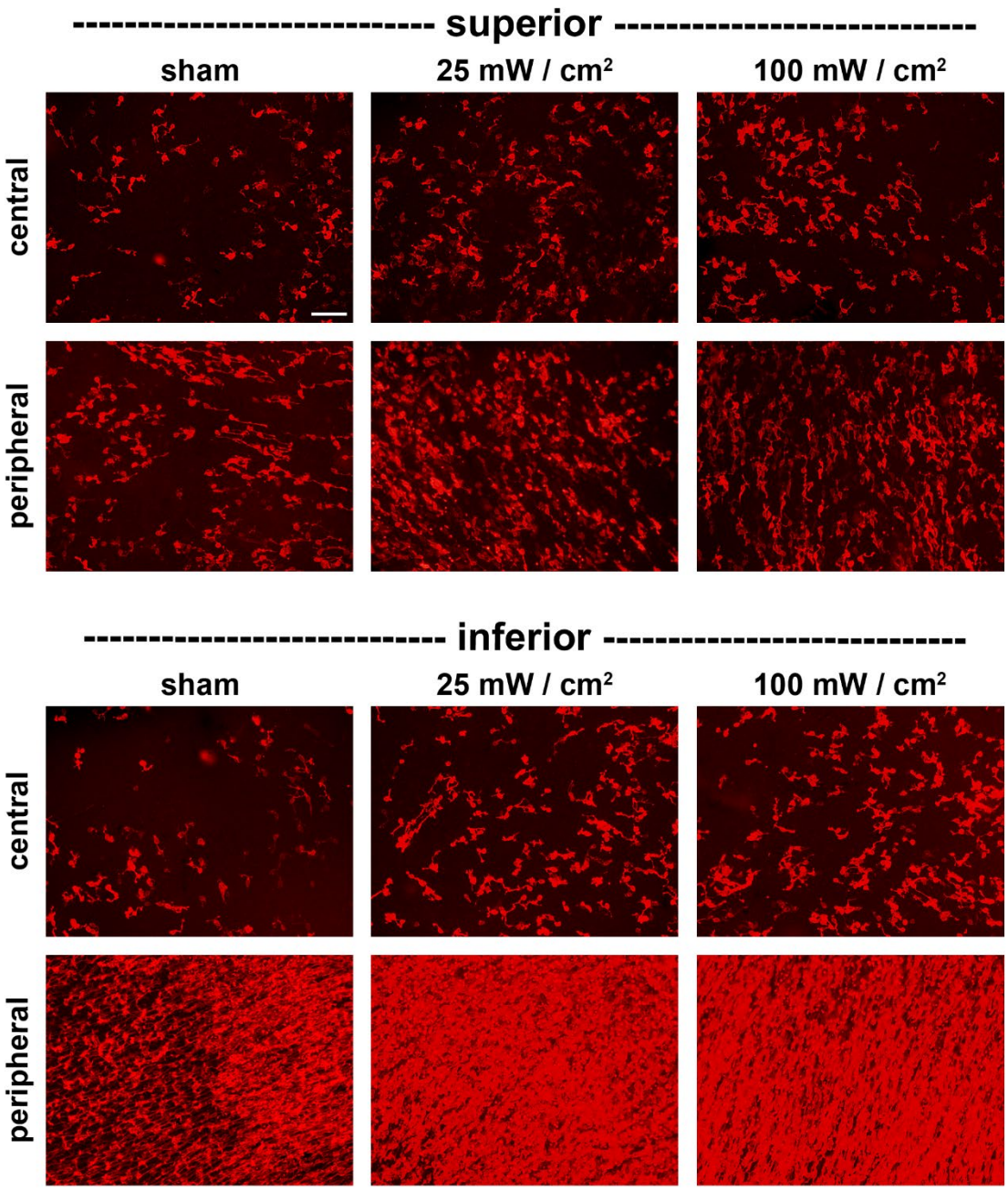

Figure 4.10 Representative immunofluorescent photomicrographs of rd1 (P60) retinal wholemounts labelled with OPNSW1 from the sham, 25 mW/cm^2 and 100 mW/cm^2 groups. Images shown are from the central and peripheral portions of the superior and inferior quadrants of the retina. Scale bar: 100 μm.

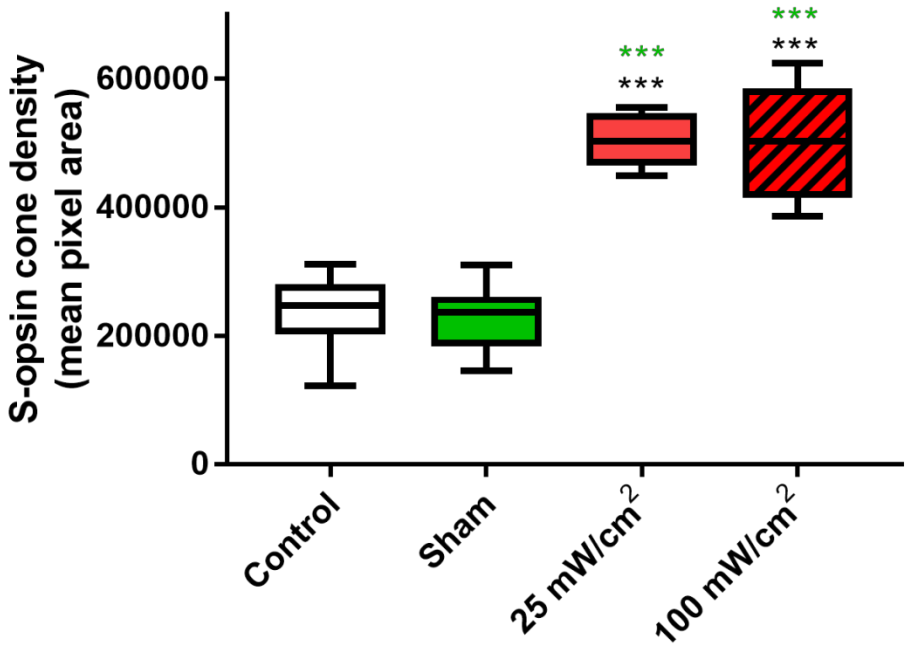

Figure 4.11 Boxplot representation of mean S-opsin^{+} cone density at P60 in the control, sham, 25 mW/cm^{2} and 100 mW/cm^{2} groups. Results were analyzed by ANOVA with Tukeys' multi-comparison test (P<0.001). Black stars against control, green stars against sham. Error bars represent 1.5 times the 1st and 3rd interquartile range.***

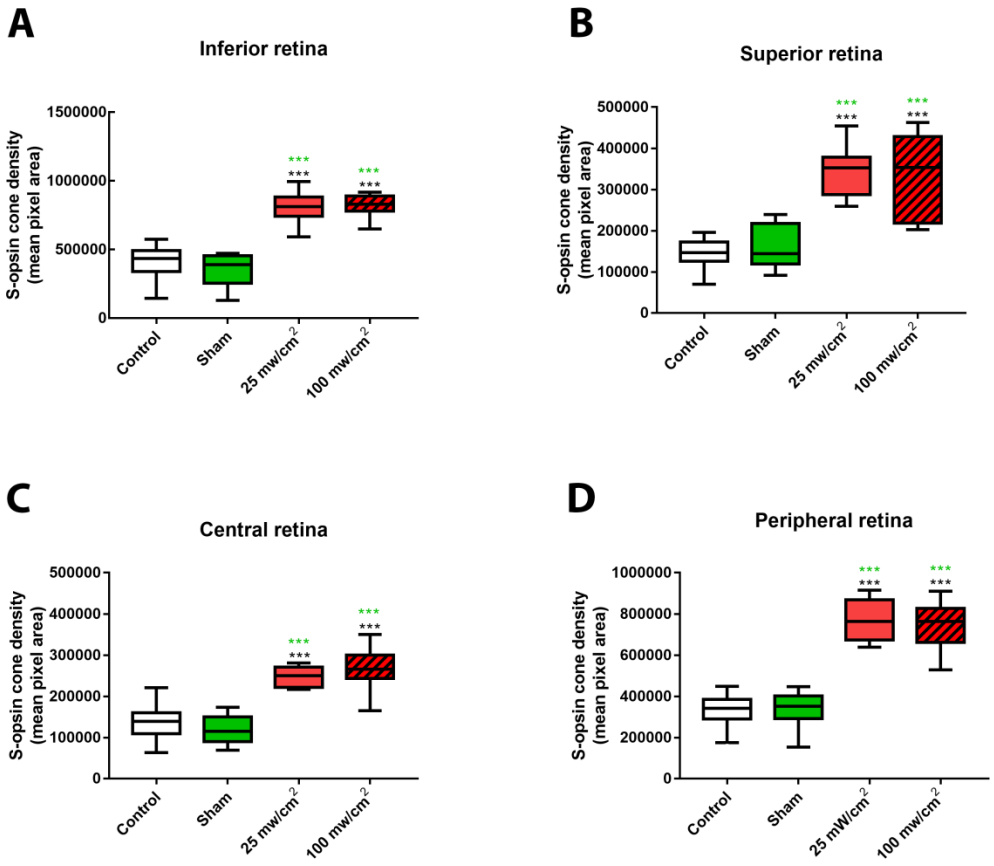

Figure 4.12 Boxplot representation of the spatial distribution of S-opsin^{+} cone density at P60 in the inferior retina (A), superior retina (B), central retina (C) and peripheral retina (D). Results were analyzed by ANOVA analysis with post-Tukey's comparison test (P=<0.001). Black stars against control, green stars against sham. Error bars represent 1.5 times the 1st and 3rd interquartile range.***

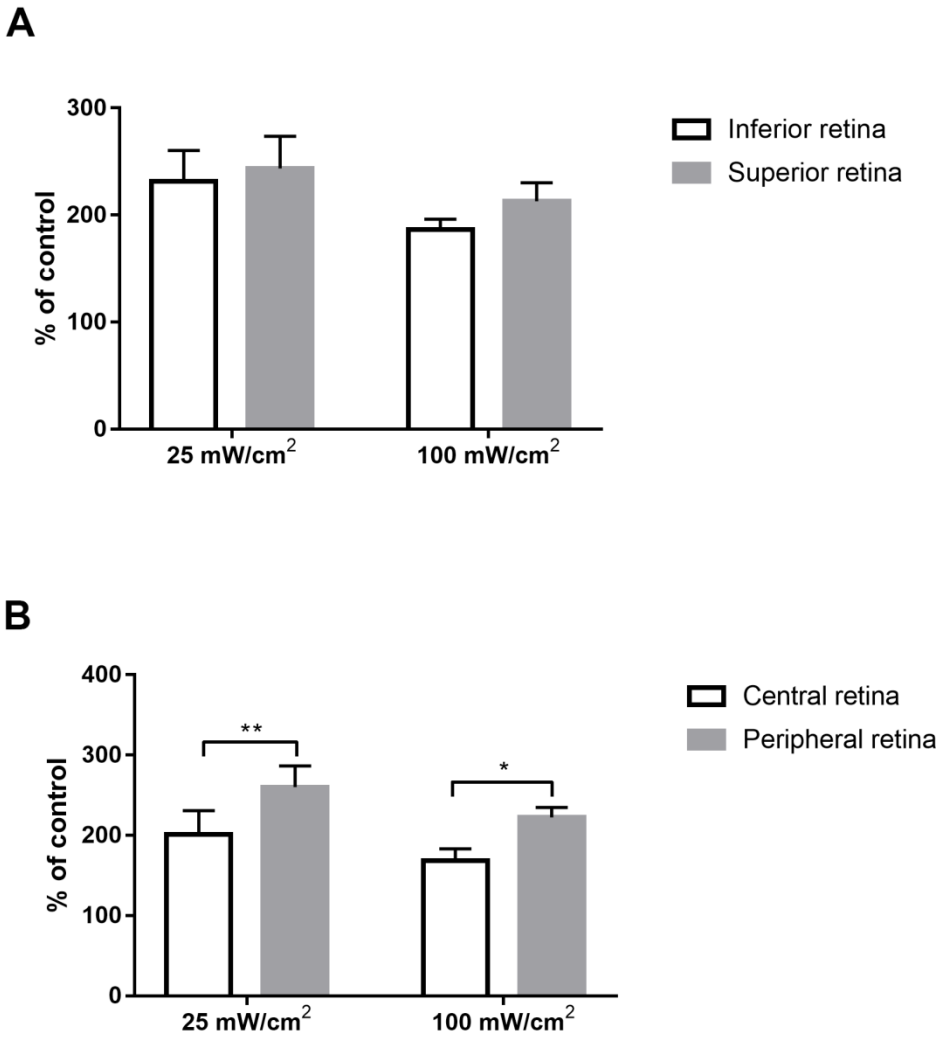

Figure 4.13 Bar graphs displaying comparative regional efficacy of neuroprotection of S-opsin^{+}-cones at P60 as a percentage of control for superior vs inferior retina (A) and peripheral vs central retina (B). Data represent mean±SEM. Results were analyzed by Student's paired t-test. *P=<0.05 **P<0.01

4.3.3 Effect of photobiomodulation on survival of M/L-opsin$^+$ cones at P60

The data produced in the characterization study of the distribution of different cone types at P60 in the rd1 strain (section 4.3.1) reveals that M/L-opsin$^+$ cone survival in the inferior retina was negligible. As such, throughout the neuroprotection experiments, M/L-opsin$^+$ cone survival was quantified in the superior, nasal and temporal quadrants of the retina, but not in the inferior retina. PBM treated 25 mW/cm^2 (P<0.001, n=8) and 100 mW/cm^2 groups (P<0.001, n=9) had significantly higher M/L-opsin$^+$ -cone density at P60 compared to the control (n=24) and sham (n=7) groups (Figures 4.14, 4.15). There was, however, no significant difference between the 25 mW/cm^2 and 100 mW/cm^2 group (P=0.33).

Analysis of the distribution of M/L-opsin$^+$ cones at P60 revealed that, when compared to controls, the 25 mW/cm^2 group had significantly (P<0.001) higher M/L-opsin$^+$ cone density in the superior (P<0.001), peripheral (P<0.001) and central (P<0.01) areas of the retina (Figure 4.16). When compared to shams, there was also a significantly higher M/L-opsin$^+$ cone density in the superior (P<0.001), peripheral (P<0.001) and central (P<0.01) areas of the retina in the 25 mW/cm^2 group (Figure 4.16). The 100 mW/cm^2 group had significantly higher M/L-opsin$^+$ cone densities compared to controls or shams in the periphery (P<0.001) and in the superior quadrant (P<0.001), but the protection in the centre did not reach significance (P=0.19, 100mW vs sham; P=0.31, 100mW vs controls) (Figure 4.16). When normalised (on a pairwise basis) to the control left eyes ice, the relative protection of M/L-opsin$^+$ cones by 25 mW/cm^2 PBM was greater in the centre and periphery but was not significant (P=0.79; Figure 4.17). When normalised

(on a pairwise basis) to the control left eyes, the relative protection of M/L-opsin^{+} cones by 100 mW/cm^{2} PBM was greater in the periphery than the centre, but the difference did reach significance (P=0.79; Figure 4.17).

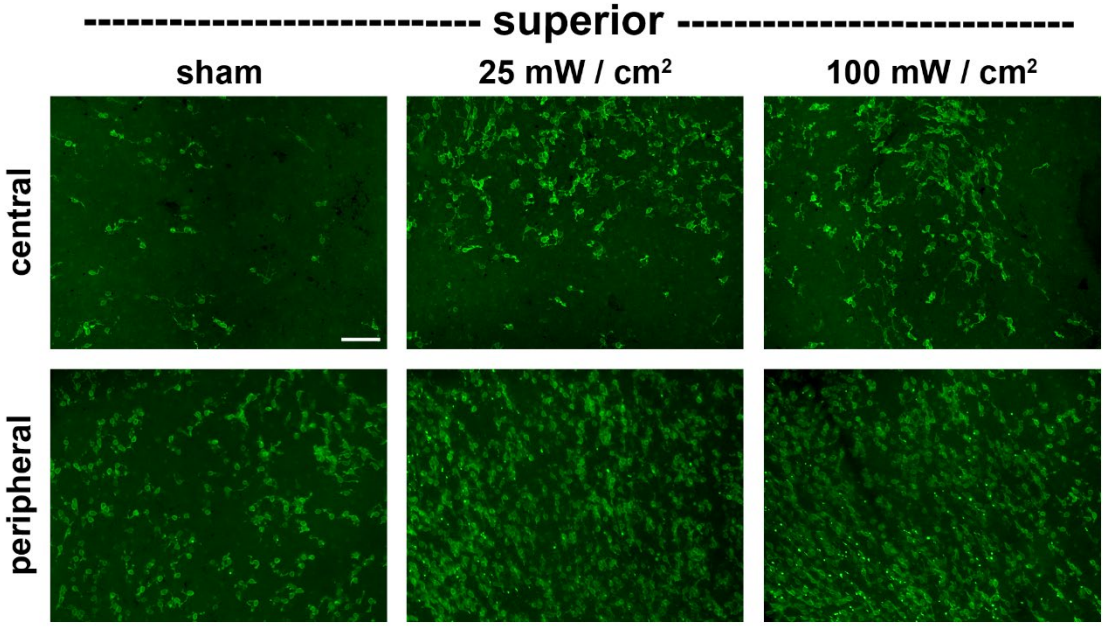

Figure 4.14 Representative immunofluorescent photomicrographs of rd1 (P60) retinal wholemounts labelled with Anti-R/G opsin from the sham, 25 mW/cm^{2} and 100 mW/cm^{2} groups. Images shown are from the central and peripheral portions of the superior quadrant of the retina. Scale bar: 100 μm.

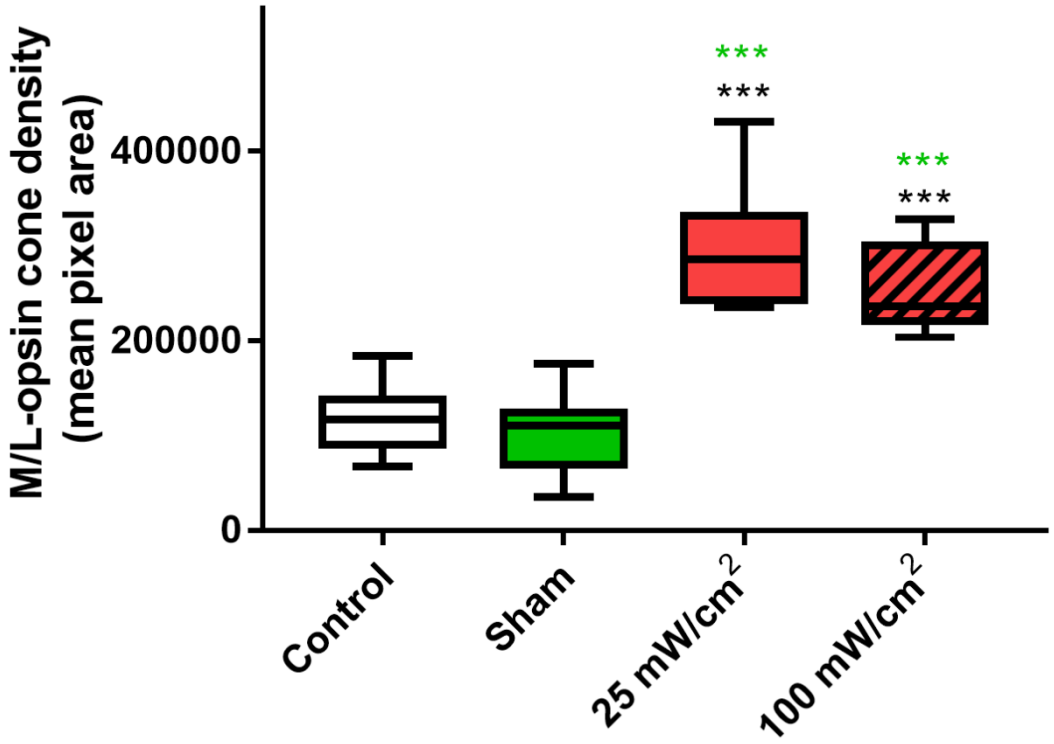

Figure 4.15 Boxplot representation of mean M/L-opsin^{+} cone density at P60 for treatment groups: control, sham, 25 mW/cm^2 and 100 mW/cm^2. Results were analyzed with ANOVA with Tukeys' multi-comparison test. ***P<0.001. Black stars against control, green stars against sham. Error bars represent 1.5 times the 1st and 3rd interquartile range.

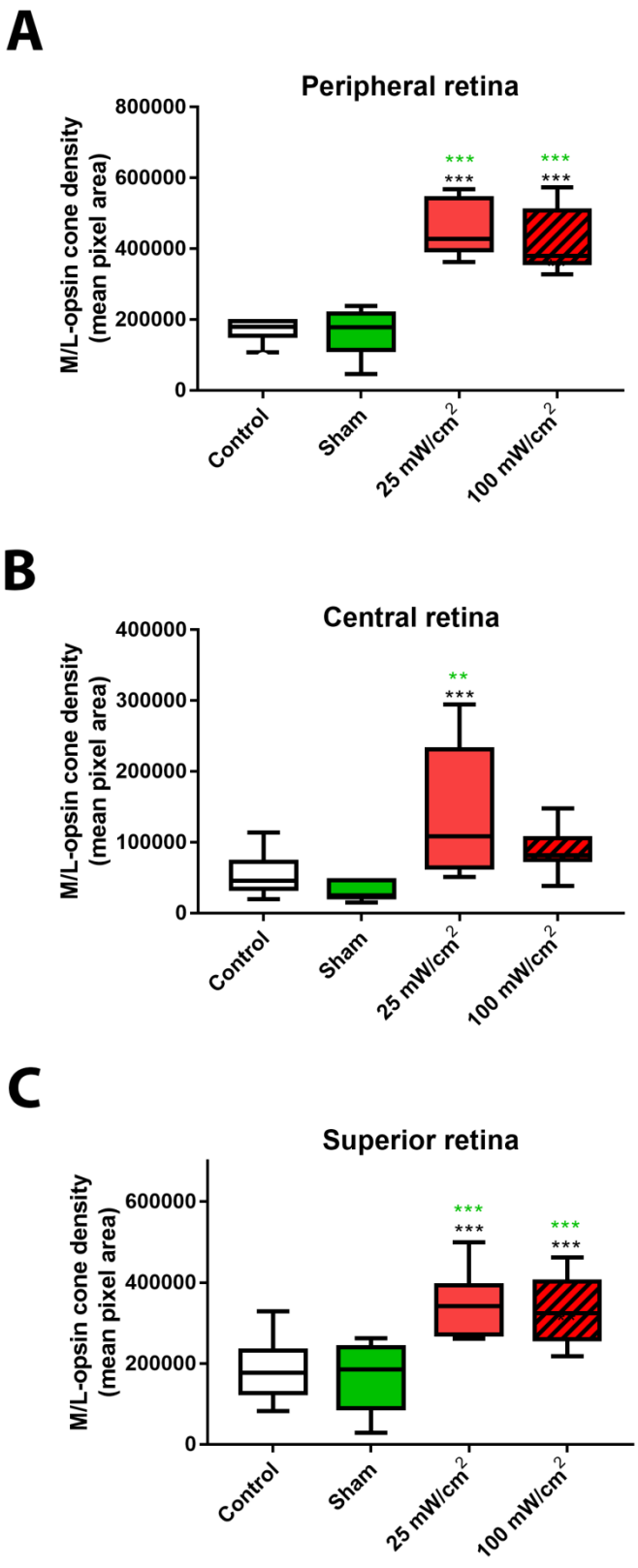
A
Peripheral retina
M/L-opsin cone density (mean pixel area)
800000
600000
400000
200000
0
***
***
***
***
Control
Sham
25 mW/cm2
100 mW/cm2
B
Central retina
M/L-opsin cone density (mean pixel area)
400000
300000
200000
100000
0
**
***
Control
Sham
25 mW/cm2
100 mW/cm2
C
Superior retina
M/L-opsin cone density (mean pixel area)
600000
400000
200000
0
***
***
***
***
Control
Sham
25 mW/cm2
100 mW/cm2

Figure 4.16 Boxplot representation of the spatial distribution of M/L-opsin^{+} cone density at P60 in the peripheral retina (A), central retina (B) and superior retina (C). Results were analyzed with ANOVA and post-Tukey's comparison test. **P<0.01 ***P<0.001 Black stars against control, green stars against sham. Error bars represent 1.5 times the 1st and 3rd interquartile range.

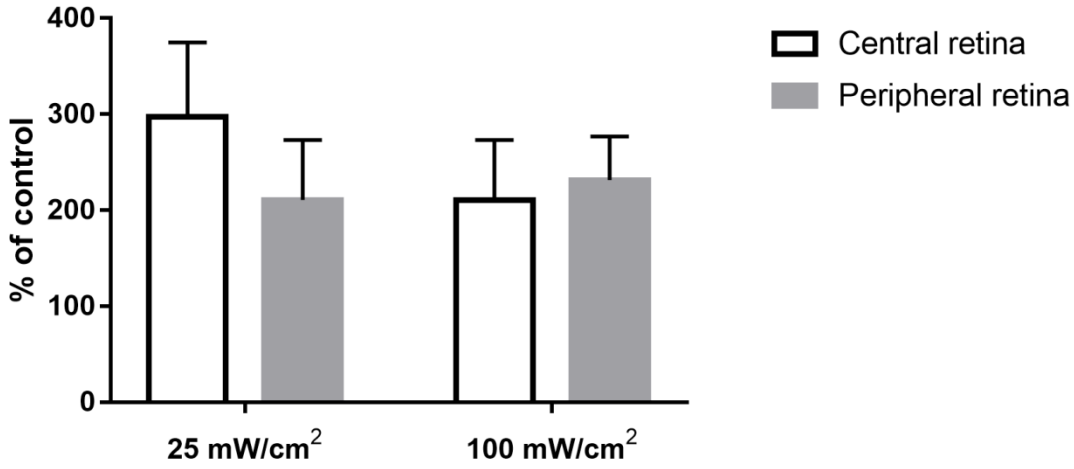

Figure 4.17 Column bar graph displaying comparative regional efficacy of M/L-opsin^{+} cone neuroprotection at P60 as a percentage of control for central vs peripheral. Results were analyzed with paired t-test. Data represent mean±SEM.

4.3.4 Effect of photobiomodulation on survival of cone segments at P60

ML-opsin$^+$ segments stained with greater fluorescent intensity than cell bodies (Figure 4.18A). This permitted separate quantification of segments, which was achieved by adjusting the image threshold to isolate M/L-opsin$^+$ segments. In contrast, S-opsin$^+$ cone cell bodies and segments stained with approximately equal intensity (Figure 4.18B). Separate quantification of S-opsin$^+$ segments from cone cell bodies could not be accurately attained using image thresholding. Hence, for quantification of separate cone segment densities only M/L-opsin$^+$ segments were used, which necessarily represent both genuine ML-opsin$^+$ cones and dual cones.

At P60, the mean cone segment density was significantly higher in the 25 mW/cm^2 (P<0.001, n=8) and 100 mW/cm^2 PBM-treated groups (P<0.01, n=9) when compared to controls (n=24) (Figure 4.19). When compared to shams (n=7), there was significantly higher neuroprotection in eyes treated with 25 mW/cm^2 PBM (P<0.001), but not 100 mW/cm^2 PBM (P=0.17). There was, however, no statistical significance between the 25 mW/cm^2 and 100 mW/cm^2 groups (P=0.14).

Analysis of the distribution of M/L-opsin$^+$ segments showed that there was a significantly higher density in the 25 mW/cm^2 group compared to controls in the superior retina (P<0.01), central retina (P<0.05) and peripheral retina (P<0.05) (Figure 4.20). The 25 mW/cm^2 PBM group also showed significantly higher numbers of M/L-opsin$^+$ segments than shams in all three regions analysed (P<0.05 - P<0.01). When normalised (on a pairwise basis) to the control left eyes, the 100 mW/cm^2 PBM group

had significantly higher cone segment density in the superior (P<0.01), central (P<0.05) and peripheral (P<0.05) regions of the retina. Relative to the sham group, however, segment density did not reach significance in the superior (P=0.067), central (P=0.3) or peripheral regions (P=0.24). When normalised (on a pairwise basis) to the control left eyes, the relative preservation of segment density afforded by 25 mW/cm^2 PBM (P=0.82) and 100 mW/cm^2 PBM (P=0.74) was of a similar magnitude in the central and peripheral regions of the retina (Figure 4.21).

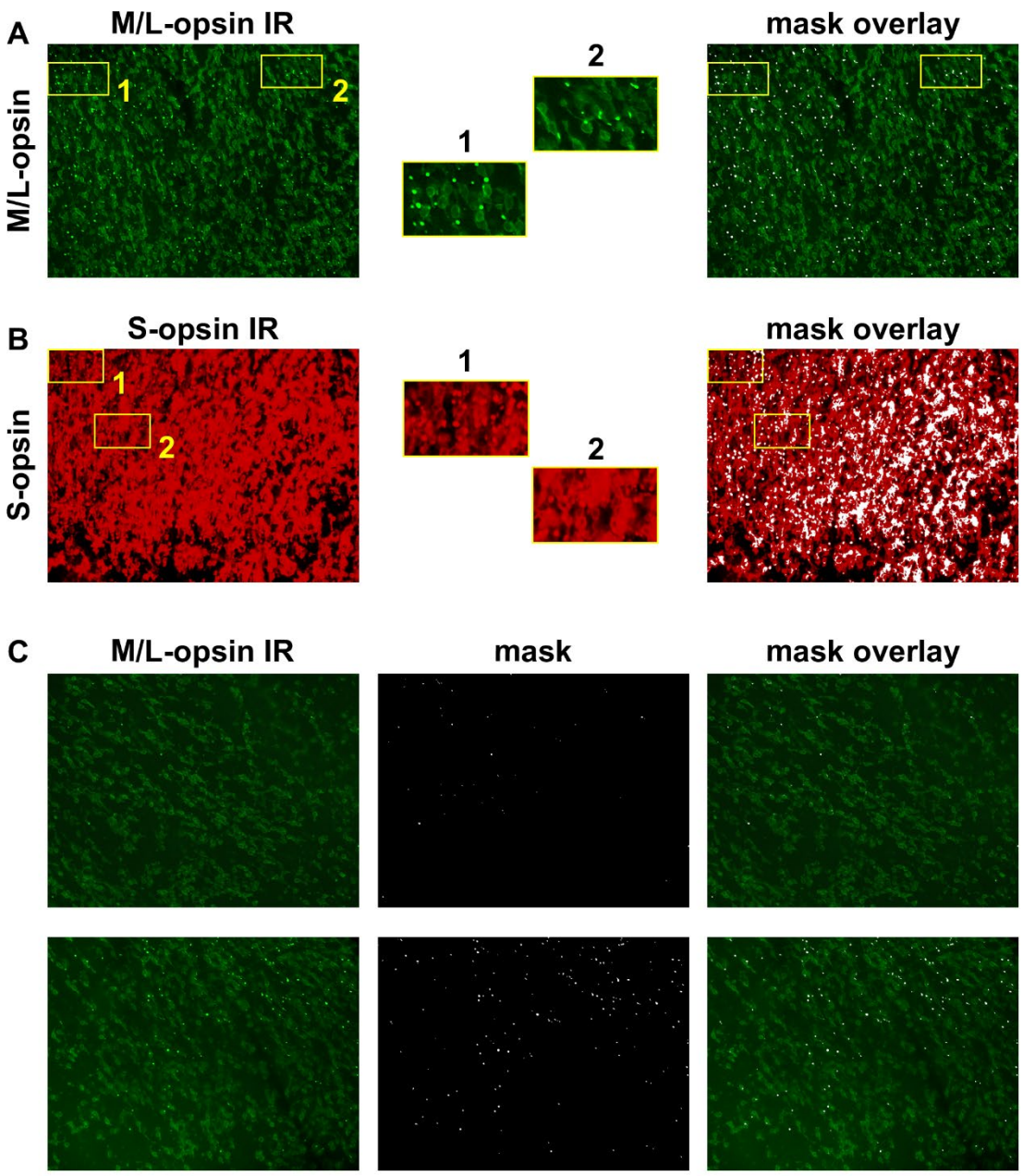

Figure 4.18 Representative images of M/L-opsin$^+$ (A) and S-opsin$^+$ (B) immunoreactivities (IR). Insets 1 and 2 are magnified views of two regions from each photomicrograph. (A) For M/L-opsin$^+$, cell bodies stain lightly, but segments stain intensely (see insets). Thus, segments can be differentiated from cell bodies using image thresholding. The right panel shows the ML-opsin$^+$ IR overlaid with the mask

derived from image thresholding (white represents areas to be quantified). It can be seen that the mask recapitulates the distribution of immunolabelled segments. (B) For S-opsin^{+}, cell bodies and segments both stain intensely (see insets). Thus, segments cannot be routinely differentiated from cell bodies using image thresholding, as illustrated by the S-opsin^{+} IR overlaid with the mask derived from image thresholding. The mask does not recapitulate the distribution of immunolabelled segments. (C) Representative M/L-opsin^{+} IR photomicrographs (left), masks derived from image thresholding (centre), and M/L-opsin^{+} IRs overlaid with the mask (right), from the superior peripheral quadrants of two retinas, both of which feature substantial M/L-opsin^{+} cone survival. It can be seen that the retina in the lower panel has much greater segment survival than the retina in the upper panel, as illustrated by the respective masks.

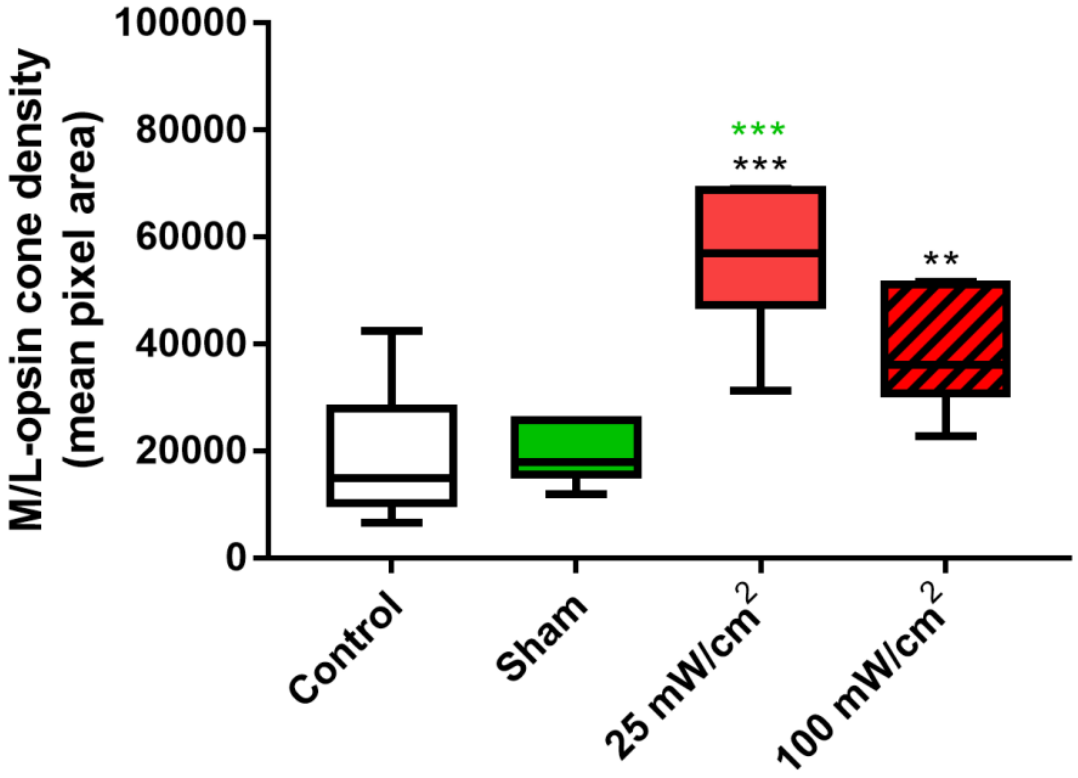

Figure 4.19 Boxplot representation of mean cone segment density at P60 for treatment groups: control, sham, 25 mW/cm^2 and 100 mW/cm^2. Results were analyzed with ANOVA with Tukey's multi-comparison test. **P<0.01 ***P<0.001 Black stars against control, green stars against sham. Error bars represent 1.5 times the 1st and 3rd interquartile range.

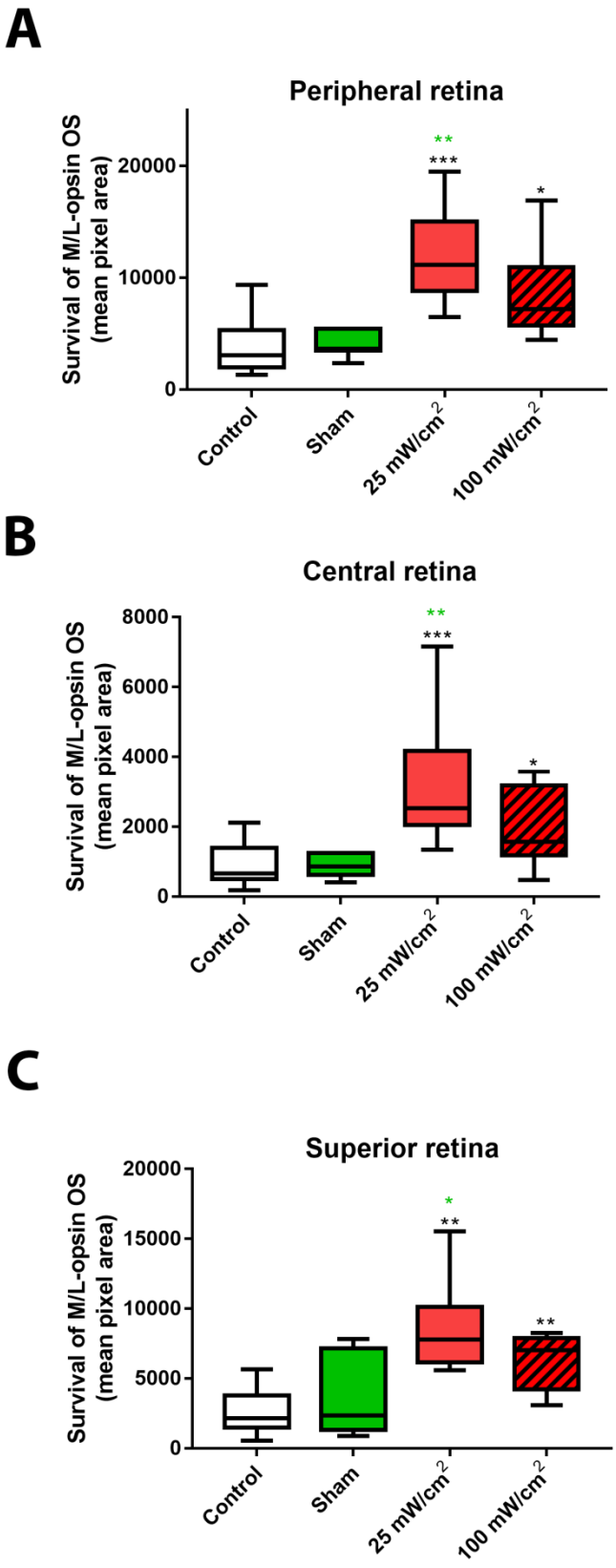
A
Peripheral retina
Survival of M/L-opsin OS (mean pixel area)
20000
10000
0
**
***
*
Control
Sham
25 mW/cm2
100 mW/cm2
B
Central retina
Survival of M/L-opsin OS (mean pixel area)
8000
6000
4000
2000
0
**
***
*
Control
Sham
25 mW/cm2
100 mW/cm2
C
Superior retina
Survival of M/L-opsin OS (mean pixel area)
20000
15000
10000
5000
0
*
**
**
Control
Sham
25 mW/cm2
100 mW/cm2

Figure 4.20 Boxplot representation of the spatial distribution of cone segments at P60 in the peripheral retina (A), central retina (B) and superior retina (C). Results were analyzed with ANOVA and post-Tukey's comparison test. Error bars represent 1.5 times the 1st and 3rd interquartile range. *P<0.05 **P<0.01 ***P<0.001

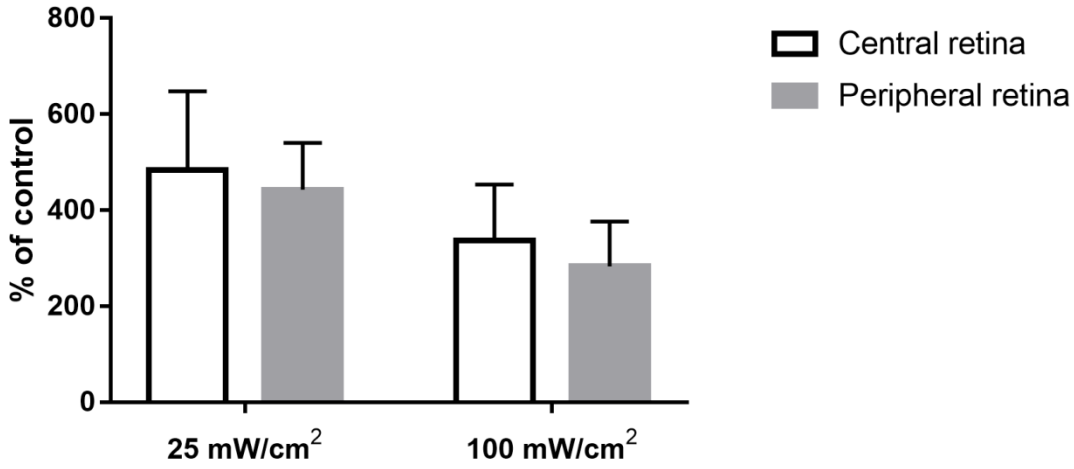

Figure 4.21 Column bar graph displaying comparative regional efficacy of cone segment neuroprotection at P60 as a percentage of controls for central vs peripheral. Results were analyzed with paired t-test. Data represent mean±SEM.

4.3.5 Effect of photobiomodulation on survival of S-opsin^{+} cones at P90

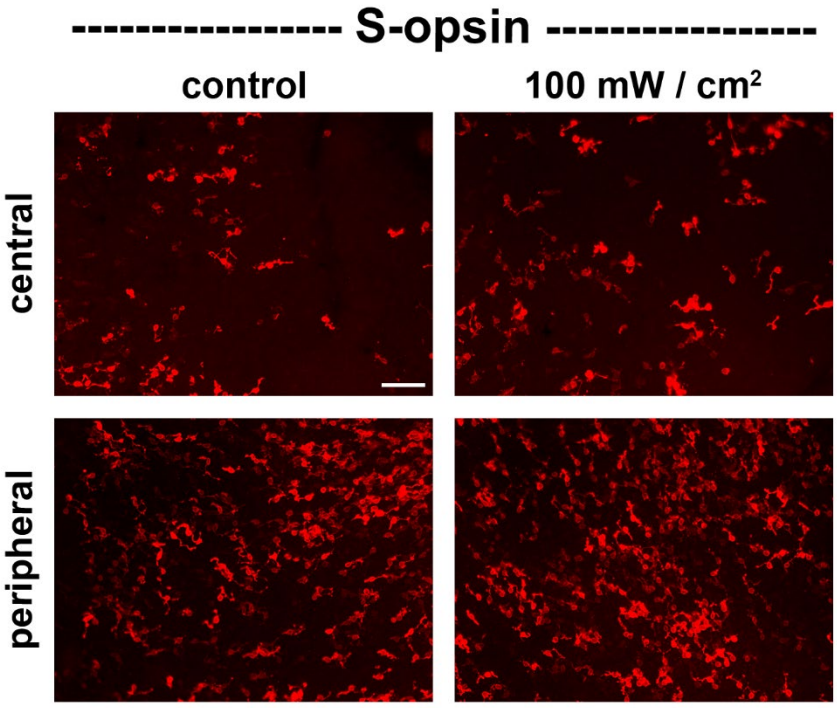

Figure 4.22 Representative immunofluorescent photomicrographs of rd1 (P90) retinal wholemounts labelled with OPNSW1 from the sham, 25 mW/cm^2 and 100 mW/cm^2 groups. Images shown are from the central and peripheral quadrants of the retina. Scale bar: 100 μm.

In order to ascertain whether the neuroprotective influence of PBM extended to longer durations, a small study was conducted in which PBM was administered until P90. This study featured only 8 mice, to which the left eye was left untreated, while the right eye received twice weekly PBM (100 mW/cm^2) until P90. Compared to controls (n=8), there was significantly (P<0.001) higher mean survival of S-opsin^{+} cones in the PBM-treated group (n=8) at P90 (Figure 4.22, 4.23). When analysed by distribution, the

neuroprotective effect of PBM was significant in the superior (P<0.05), inferior (P<0.01), and peripheral (P<0.001) regions of the retina, but the effect did not reach significance in the central (P=0.11) region (Figure 4.24). When normalised (on a pairwise basis) to the control left eyes, the extent of neuroprotection by PBM was greater in the superior compared to the inferior regions of the retina but was not statistically significant (P=0.20). When normalised (on a pairwise basis) to the control left eyes, PBM neuroprotection was similar in the central and peripheral (P=0.62) retina (Figure 4.25).

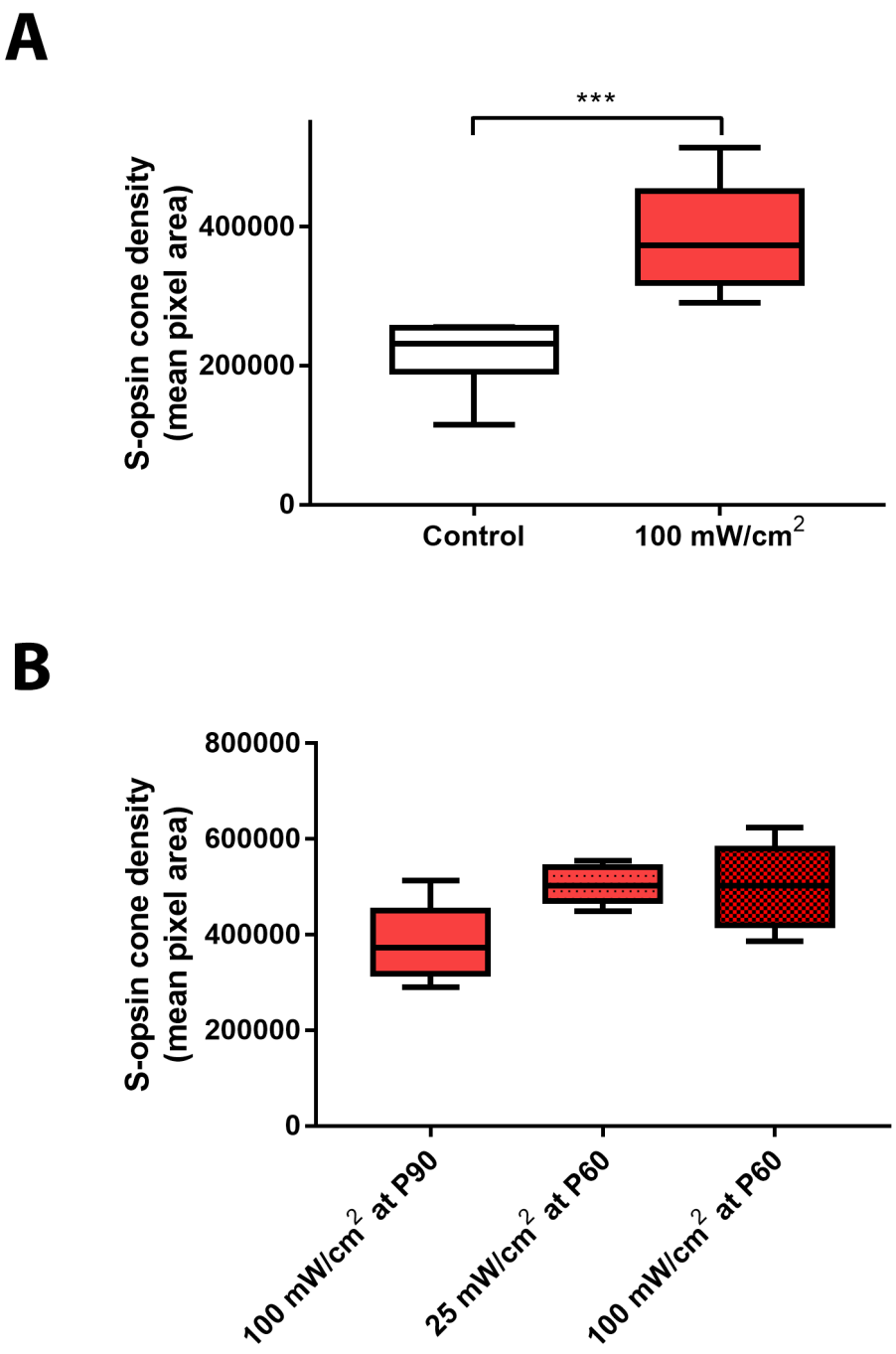

Figure 4.23 Boxplot representation of mean S-opsin$^+$ cone density at P90. (A) mean S-opsin$^+$ cone density following 100 mW/cm^2 PBM at P90 compared to control and (B)

*25 mW/cm^2 PBM and 100 mW/cm^2 PBM at P60._ Data of 100 mW/cm^2 PBM and control at P90 were analyzed with paired t-test. Whiskers represent 1.5 times the 1st and 3rd interquartile range. ***P<0.001*

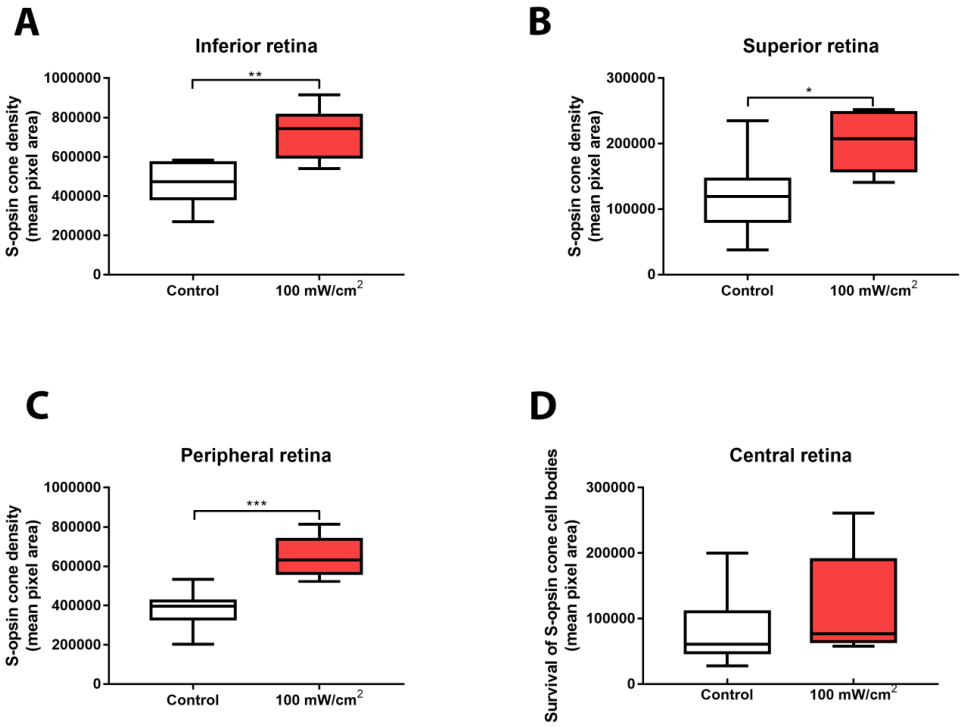

*Figure 4.24 Boxplot representation of the spatial distribution of S-opsin$^+$ cone density at P90 in the inferior (A), superior (B), peripheral (C) and central (D) regions. Results were analyzed with paired t-test. Whiskers represent 1.5 times the 1st and 3rd interquartile range. *P<0.05 **P<0.01 ***P<0.001*

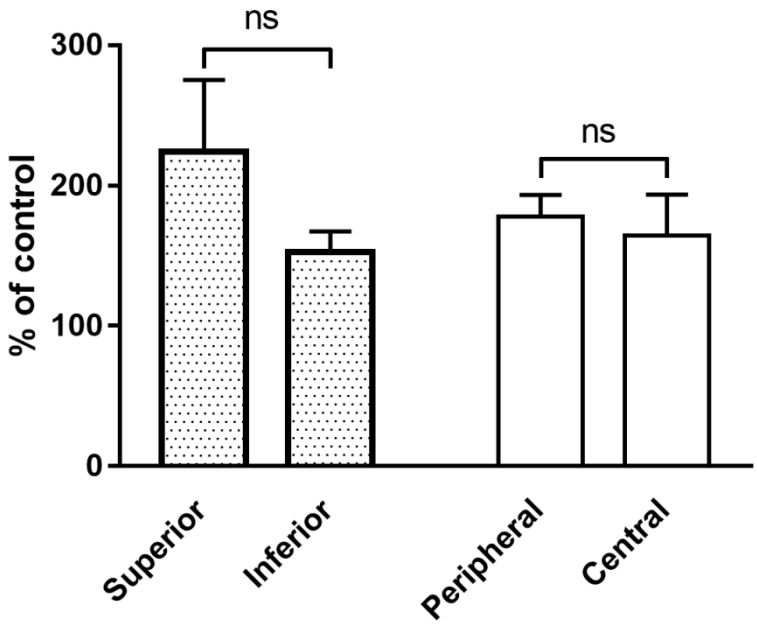

Figure 4.25 Column bar graph showing comparative regional efficacy of S-opsin^{+} neuroprotection with 100 mW/cm^{2} PBM expressed as percentage of control. Results were analyzed with a paired t-test. Data represent mean±SEM. ns=Not statistically significant

4.3.6 Effect of photobiomodulation on survival of M/L-opsin$^+$ cones at P90

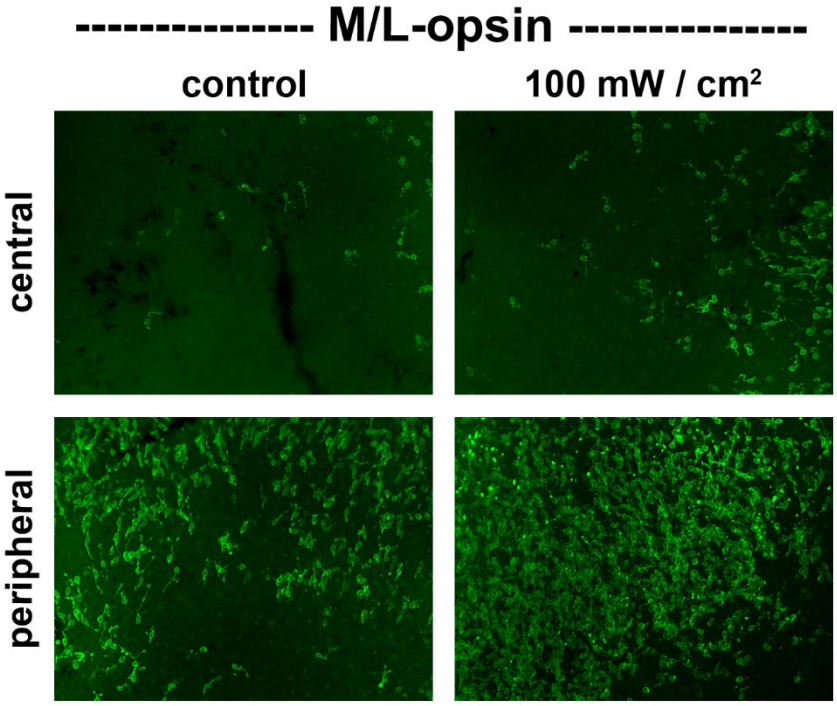

Figure 4.26 Representative immunofluorescent photomicrographs of rd1 (P90) retinal wholemounts labelled with Anti-R/G opsin from the sham, 25 mW/cm^2 and 100 mW/cm^2 groups. Images shown are from the central and peripheral quadrants of the retina. Scale bar: 100 μm.

Overall, there was significantly (P<0.001) greater M/L-opsin$^+$ cone density in the PBM group compared to the control group (Figure 4.26, 4.27). When subdivided by area, M/L-opsin$^+$ cone density in the PBM treated group was significantly greater in the periphery (P<0.01), the centre (P<0.05) and the superior quadrant of the retina (P<0.01) compared to controls (Figure 4.28). When normalised (on a pairwise basis) to the control left eyes, the relative preservation of M/L-opsin$^+$ cone density by PBM was

greater in peripheral compared central regions magnitude but did not reach statistical significance (*P*=0.52; Figure 4.29).

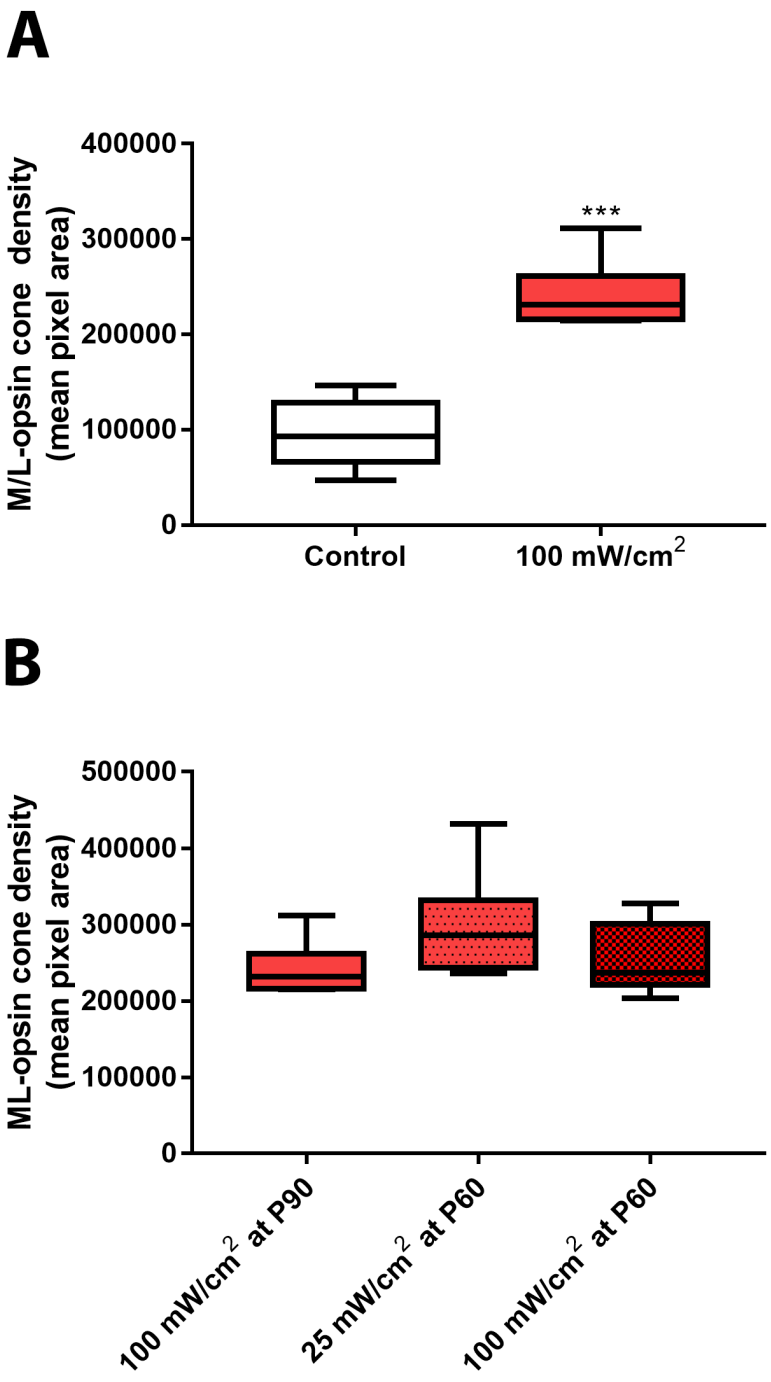

Figure 4.27 Boxplot representation of mean M/L-opsin^{+} cone density at P90. (A) mean ML-opsin^{+} cone density following 100 mW/cm^2 PBM at P90 compared to control and (B) 25 mW/cm^2 PBM and 100 mW/cm^2 PBM at P60._ Data of 100 mW/cm^2 and control at P90 were analyzed with paired t-test. Error bars represent 1.5 times the 1st and 3rd interquartile range. ***P<0.001

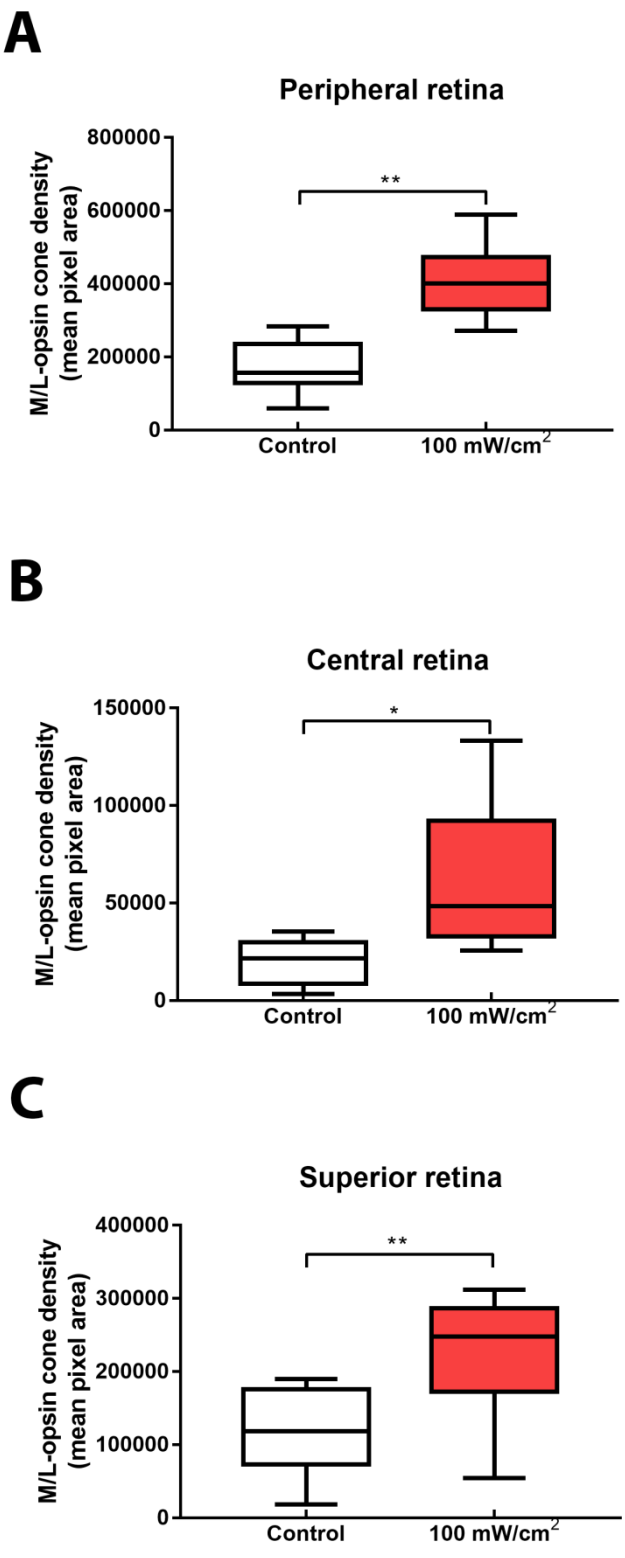
A
Peripheral retina
M/L-opsin cone density (mean pixel area)
800000
600000
400000
200000
0
**
Control
100 mW/cm2
B
Central retina
M/L-opsin cone density (mean pixel area)
150000
100000
50000
0
*
Control
100 mW/cm2
C
Superior retina
M/L-opsin cone density (mean pixel area)
400000
300000
200000
100000
0
**
Control
100 mW/cm2

Figure 4.28 Boxplot representation of the spatial distribution of M/L-opsin^{+} cone density at P90 in the peripheral retina (A), central retina (B) and superior retina (C). Results were analyzed with ANOVA and post-Tukey's comparison test. Whiskers represent 1.5 times the 1st and 3rd interquartile range. *P<0.05 **P<0.01

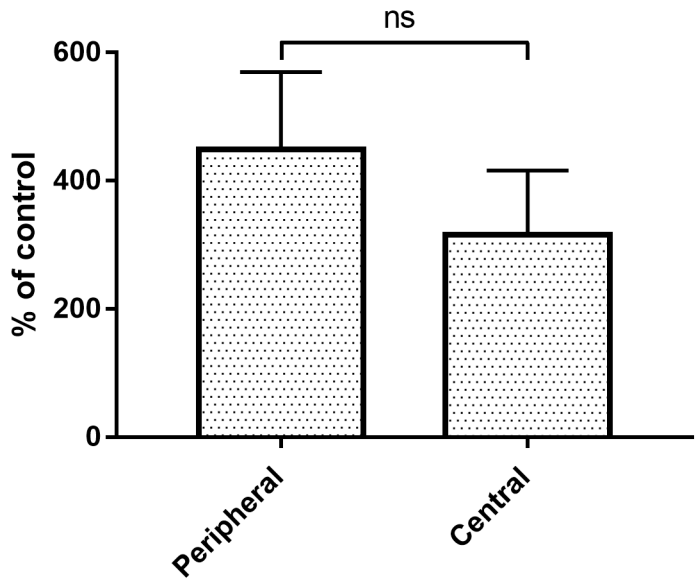

Figure 4.29 Column bar graph showing comparative regional efficacy of M/L-opsin^{+} cone neuroprotection with 100 mW/cm^{2} PBM at P90 expressed as percentage of control. Results were analyzed with a paired t-test. Data represent mean±SEM. ns=Not statistically significant

4.3.7 Effect of photobiomodulation on survival of cone segments at P90

There was significantly (P<0.01) greater cone segment density in eyes treated with 100 mW/cm^2 PBM (n=8) compared to controls (n=8) at P90 (Figure 4.30). When analysed by distribution, cone segment density in PBM-treated eyes was greater in the peripheral (P<0.05) and central (P<0.01) retina (Figure 4.31). The difference did not quite reach significant in the superior retina when analysed in isolation (P=0.093). When normalised (on a pairwise basis) to the control left eyes, the relative protection of cone segment density by PBM was similar (P=0.55) in the peripheral versus the central retina (Figure 4.32).

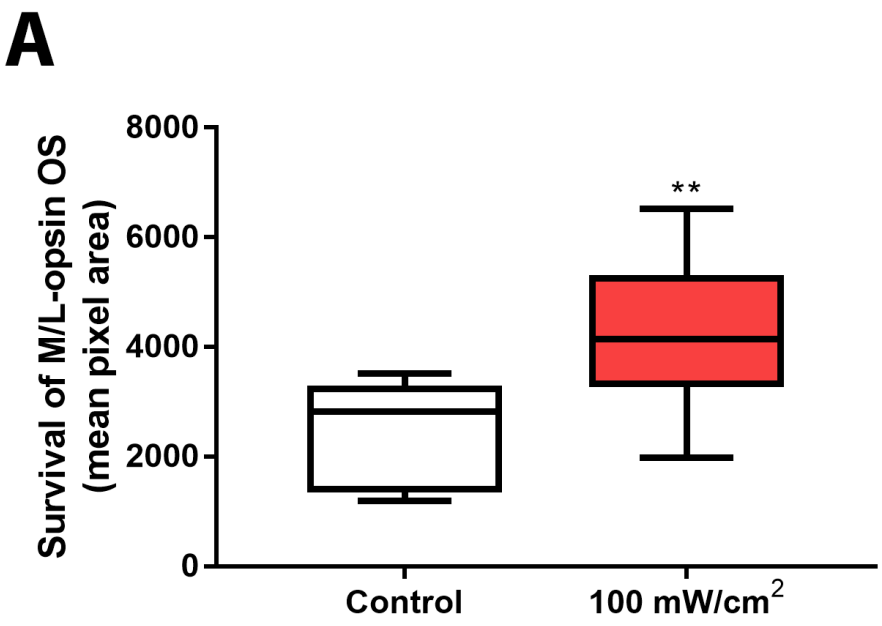
A
Survival of M/L-opsin OS
(mean pixel area)
8000
6000
4000
2000
0
**
Control
100 mW/cm2

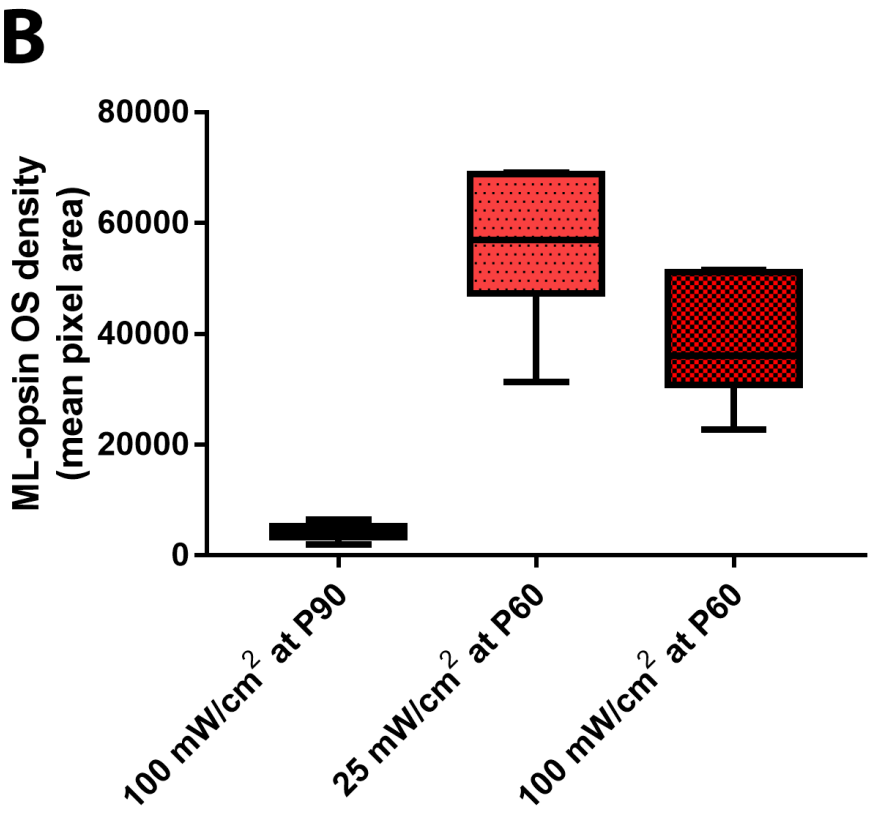
B
ML-opsin OS density
(mean pixel area)
80000
60000
40000
20000
0
100 mW/cm2 at P90
25 mW/cm2 at P60
100 mW/cm2 at P60

Figure 4.30 Boxplot representation of mean cone segment density at P90. (A) mean ML-opsin^{+} OS density following 100 mW/cm^{2}PBM at P90 compared to control and (B) 25 mW/cm^2 PBM and 100 mW/cm^2 PBM at P60._ Data of 100 mW/cm^2 and control at P90 were analyzed with paired t-test. Error bars represent 1.5 times the 1st and 3rd interquartile range. **P<0.01

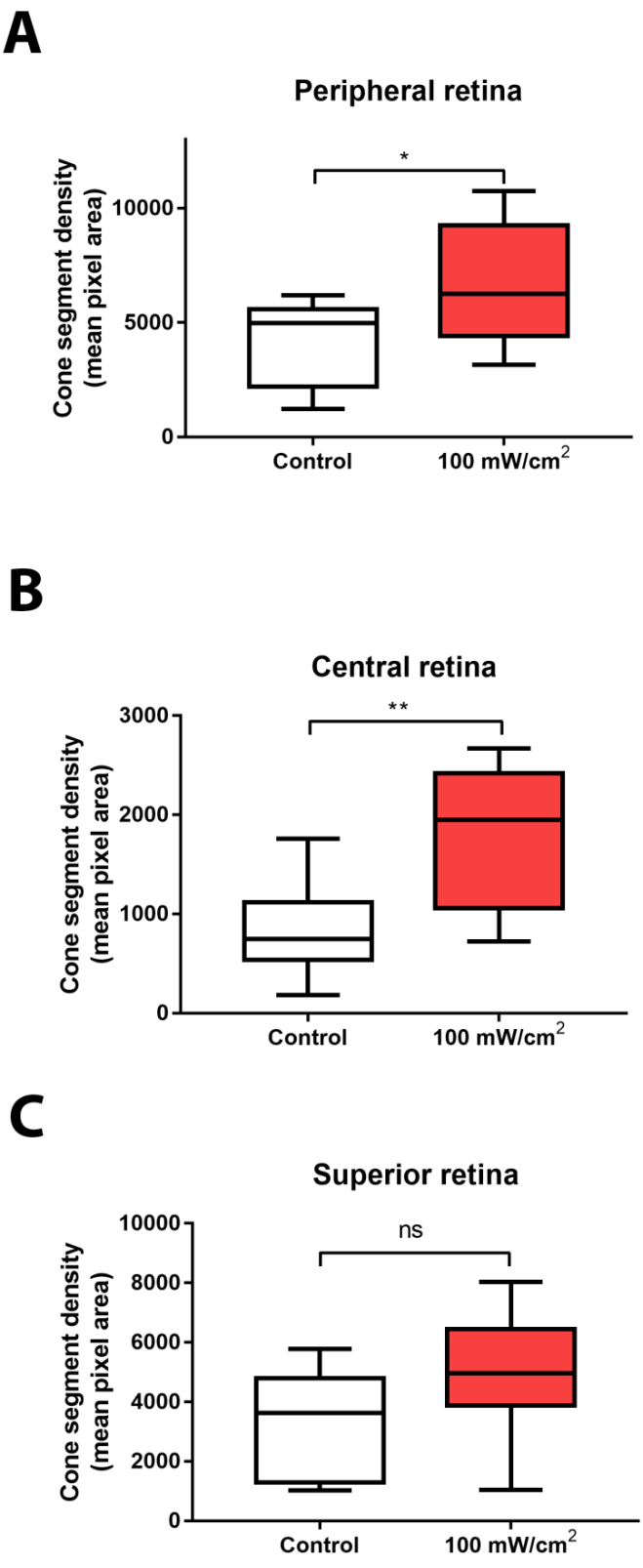
A
Peripheral retina
Cone segment density (mean pixel area)
10000
5000
0
*
Control
100 mW/cm2
B
Central retina
3000
2000
1000
0
**
Control
100 mW/cm2
C
Superior retina
10000
8000
6000
4000
2000
0
ns
Control
100 mW/cm2

Figure 4.31 Boxplot representation of the spatial distribution of cone segment density at P90 in the peripheral (A), central (B) and superior (C) regions. Results were analyzed with paired t-test. Error bars represent 1.5 times the 1st and 3rd interquartile range. *P<0.05 **P<0.01

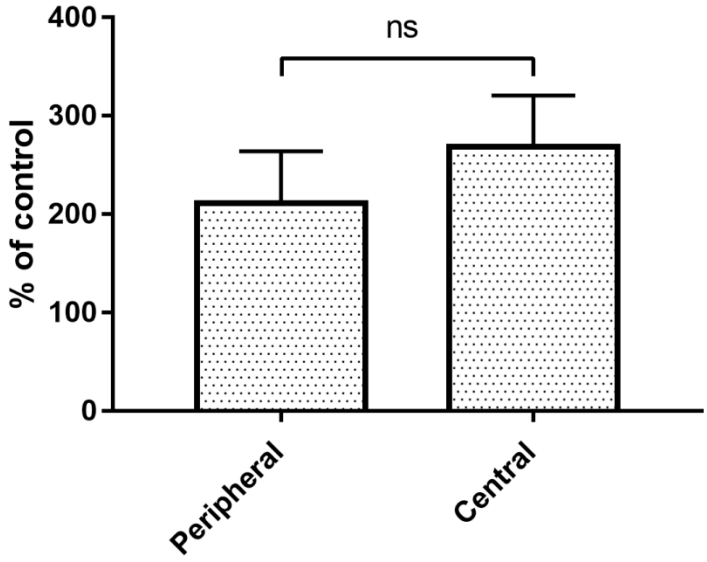

Figure 4.32 Column bar graph showing comparative regional efficacy of cone segment neuroprotection with 100 mW/cm^2 PBM at P90 expressed as percentage of control. Results were analyzed with a paired t-test. Data represent mean±SEM. ns=Not statistically significant

4.3.8 Effect of photobiomodulation on optomotor performance at P35

PBM significantly improved optomotor tracking performance, measured at P35, in eyes treated with 25 mW/cm^2 (P<0.001, n=4) or 100 mW/cm^2 (P<0.001, n=14) when compared to controls (n=21) (Figure 4.33). Similarly, there were significantly higher optomotor functions for the 25 mW/cm^2 (P<0.01) and 100 mW/cm^2 (P<0.05) groups when compared to shams (n=4). There was no significant difference between the 25 mW/cm^2 and 100 mW/cm^2 groups (P=0.52).

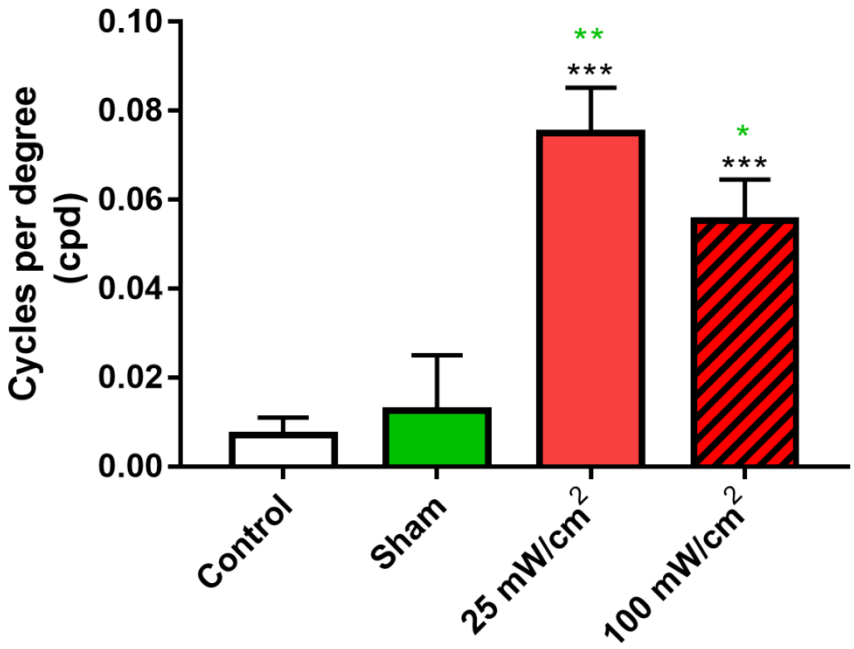

Figure 4.33 Column bar graph showing optokinetic (OKN) function of treatment groups at P35. Results were analyzed with ANOVA and Tukey's multi-comparison test. Data represent mean±SEM.*P<0.05 **P<0.01 ***P<0.001 Black stars against control, green stars against sham.

4.4 Discussion

The cause of secondary cone degeneration in RP is poorly understood. Several hypotheses including energy failure, oxidative stress, cone starvation and microglial activation have attempted to explain this phenomenon.[224] PBM is known to increase mitochondrial membrane potential via COX as well as reduce oxidative stress and inflammation through retrograde signaling pathways. [137,147,148,163,164,190] Hence, PBM may be a novel therapy to prevent secondary cone degeneration in RP.

The first part of the study was to characterize the cone population in the rd1 mouse retina at P60. While detailed information is available on the spatial distribution of genuine S-opsin cones, genuine M/L-opsin cones, and dual cones in the retinas of albino and pigmented mouse strains[225], as well as albino and pigmented rat strains[226], hitherto, relatively little has been published about the survival of the different cones types in the degenerating rd1 retina. Whilst there have been previous studies[34,227,228] examining patterns of cone degeneration in the rd1 mouse, none of them have examined dual cones which comprises a significant portion of cone subtypes in our study. Such data would not only augment knowledge of the patterns of loss of the different cone types, but would provide valuable baseline data for the PBM neuroprotection study. To achieve this goal, retinal whole-mounts from untreated rd1 eyes were immunolabelled with antibodies to S- and M/L-opsins. The cone densities of genuine S-opsin cones, genuine M/L-opsin cones, and dual cones were then quantified in each of the four retinal quadrants. Overall, the mean cone population at P60 comprised 59.1% genuine S-opsin cones, 26.9% dual cones, and 14.0% M/L-opsin cones. There was a marked divergence

in cone composition between the superior and inferior retina. The superior retina at P60 consisted of a majority of dual cones (53.67%), followed by genuine M/L-opsin cones (38.1%) and a sparse population of genuine S-opsin cones (8.23%). In contrast, the inferior retina at P60 contained almost exclusively genuine S- opsin cones (97.71%) with a small minority of dual cones (2.29%), and no identifiable genuine M/L-opsin cones. Nasal and temporal regions had similar compositions of genuine S-opsin cones (30.16%, 23.18%), genuine M/L-opsin cones (23.59%, 18.69%) and dual cones (46.25%, 58.13%).

The patterns of regional cone distribution found in the current study were similar, although not identical, to the distributions described in earlier characterization studies using normal pigmented and albino rodents.[225,226] Thus, S-opsin$^+$ cones tended to be more densely populated in the inferior-nasal regions and became sparser superiorly. Dual cones tended to be more densely populated in the superior nasal regions and became scarcer in the inferior regions. These were in agreement with our data. The results obtained herein showed S-opsin$^+$ cones formed the majority of the cone population at P60 pan-retinally, which can be explained by the comparatively slower degeneration of S-opsin$^+$ cones relative to M/L$^+$ cones in rd1 mice.[34] We did, however, find a greater number of S-opsin$^+$ cones in the superior retina of P60 rd1 mice compared to those identified by Lin et al.[227] The explanation underlying this difference is not immediately obvious, but may conceivably be related to the fact that different S-opsin antibodies were used in the two studies. Alternatively, it could simply represent a difference between the population of rd1 mice used in the present study to those used by

Lin et al. a decade ago. Nevertheless, our finding that an overwhelming proportion of cones in the inferior retina at P60 were S-opsin^{+} cones, and hence that there were correspondingly very few M/L-opsin^{+} cones, is consistent with the results of both Lavail et al[228] and Lin et al.[227]

In wild type pigmented and albino rats, M/L-opsin^{+} cones have a central-peripheral gradient with density greatest around the optic nerve,[225,226] a pattern that differs from the superior-inferior gradient displayed in our rd1 mice. The simplest explanation for this apparent discrepancy is that M/L-opsin^{+} cones degenerate more rapidly in the inferior than the superior retina, and in the central compared to peripheral retina. This deduction is supported by the results of previous rd1 mouse characterization studies.[34,227] Moreover, the data presented here represent a characterization of rd1 cone population at only one timepoint, P60, which will have evolved from earlier time points and will continue to evolve as cones continue to degenerate. We do have preliminary data characterizing the spatio-temporal distribution of S-opsin^{+} and M/L-opsin^{+} cone degeneration in the rd1 mouse at time-points up to P300 that augment the current data.[229] At P7, S-opsin^{+} cones have the highest density in the inferior region and the lowest in the superior region. In contrast, M/L-opsin^{+} cones are uniformly distributed. S-opsin^{+} and M/L-opsin^{+} cones degenerate in a hemispheric asymmetric fashion; S-opsin^{+} cone loss occurs faster in the superior regions, whilst M/L-opsin^{+} degenerates quicker in the inferior retina. At P300, only a sparse population of M/L-opsin^{+} cones remain in the peripheral inferior and nasal regions, whilst a limited number of S-opsin^{+} cones remain in the peripheral superior and nasal regions. Overall, the data from this characterization

study are particularly informative in terms of the neuroprotection study. In terms of characterizing the distribution of genuine S-opsin, genuine M/L-opsin cones and dual cones in the rd1 retina, it will be important in the future to examine earlier time points, for example, P14 prior to commencement of cone degeneration, and P30, a time point relatively early in cone degeneration. Such data will inform about the relative survival of different cone populations in this animal model of RP and will prove useful in future studies that use the rd1 mouse model to examine cone loss and neuroprotection strategies.

The second part of the present study assessed the neuroprotection efficacy of laser-directed PBM on cone degeneration in the rd1 mouse. The primary outcomes were S-opsin^{+} and M/L-opsin^{+} cone densities in whole-mount retinae. The secondary outcome was functional measurement of OKN. The results showed significant neuroprotection of S-opsin^{+} and M/L-opsin^{+} cone cell bodies, as well as segments, at P60 in groups treated with 25 mW/cm^2 or 100 mW/cm^2 PBM, when compared to shams and untreated controls. In addition, PBM at 100mW/cm^2 provided significant neuroprotection of S-opsin^{+} and M/L-opsin^{+} cones compared to control eyes at P90. The histological protection of cones likely explains the finding that eyes treated with PBM at both irradiances also had significantly better OKN function when compared to control and sham eyes.

The overall findings augment the published body of data showing the benefit of 670nm PBM in preclinical studies of photoreceptor protection in retinal degeneration

models.[134,147,180,191-193] Eells et al.[147] were the first to describe in-vivo photoreceptor protection by PBM. They used a rodent model of retinal methanol toxicity and showed that PBM preserved photoreceptor morphology on histopathology and significantly recovered rod- and cone-mediated ERG amplitudes. Abarracin et al. in several studies[134,141,191] reported that PBM protected photoreceptors and visual function in light-induced retinal injury and oxygen-induced degeneration. PBM treated retinal sections had significantly lower photoreceptor apoptosis marked by reduced TUNEL (dUTP nick end labelling) staining in the ONL, preserved retinal structures histologically, reduced stress markers and reduced oxidative stress. PBM prior to, or during, light-induced retinal injury resulted in preserved rod and M/L-opsin^{+} cone OS structures, as well as preserved cone opsin gene opn1mw. Moreover, eyes treated with PBM before and during light-induced retinal injury had higher photopic b-wave amplitude compared to untreated eyes, suggesting preservation of cone function. Subsequent studies of PBM in light-induced retinal injury have similarly described decreased photoreceptor apoptosis, ONL preservation, reduced oxidative stress and inflammatory markers.[180,193]. Whilst these studies utilized 670 nm LED with irradiances ranging from 18 mW/cm^2 to 60 mW/cm^2, we report significant neuroprotection of cones and preservation of visual function with a 670nm laser with irradiances up to 100 mW/cm^2 or 9 J/cm^2 fluence which is within range of previous PBM studies.[230,231]

The present study is the first to examine the neuroprotection efficacy of PBM on the rd1 mouse. This strain is a well-defined autosomal recessive model of RP that is characterized by a PDE6B gene mutation resulting in rapid degeneration of rods by P8-

10 and thinning of the ONL which is complete by P21. Progressive cone loss occurs subsequently with almost complete depletion by P300. Hence, there is a narrow therapeutic window in this rapidly progressive RP model. ERG was not deemed useful as the ERG signal in the rd1 mouse becomes absent at P21[232], coinciding with initiation of PBM treatment. Similarly, SD-OCT was not considered valuable as most of the retinal thickness reduction had occurred by the initiation of treatment. OKN function is still measurable despite an absent ERG as remaining opsins in the inner segments can facilitate photopic vision.[76]

The neuroprotective benefits of PBM are observable in rd1 mice as early as P35 following 2 weeks of PBM, exhibited by OKN improvement, and persists to at least P90 where there was still significant cone and segment survival. The mean cone survival in PBM treated eyes was generally lower at P90 compared to P60, suggesting PBM did not completely halt cone loss, rather significantly delaying it. Our results support findings from Eells et al.[195] which examined PBM on the P23H-3 rat, a comparative RP rodent model that possesses a rhodopsin mutation similar to an autosomal dominant form of human RP. Daily delivery of 670 nm LED with 50 mW/cm^2 irradiance or 4 J/cm^2 fluence was administered to P23H-3 pups during the critical period of photoreceptor development P16-20. Following treatment there was decreased photoreceptor apoptosis, increased retinal COX particularly in the photoreceptor inner segments, upregulation of antioxidant enzyme Mn-SOD and increased neurotropin CNTF.[195]It must be kept in mind that photoreceptor loss is considerably slower in P23H rats[233] and at their

timepoints, no cone loss would have occurred. Hence, comparisons of neuroprotective efficacy against secondary cone loss is impossible to draw from Eells et al. [195]

Unlike previous PBM studies[180,188,191] which examined photoreceptor protection predominantly with TUNEL staining of retinal sections, the use of double labelling immunofluorescence on wholemount retinae in our study allowed us to examine the efficacy of PBM on survival of cone subtypes throughout the retina. The use of OPN1SW and RG-opsin antibodies, which demarcate both cone cell bodies and segments, is preferable to peanut agglutinin, as the latter stains only cone outer/inner segments and hence is unable to stain surviving cone cell bodies, which persist long after segments have degenerated.[227]

Our data suggest PBM confers protection to both cone subtypes up to P90. There was significantly greater neuroprotection efficacy at P60 in peripheral regions compared to central regions for both the 25 mW/cm^2 and 100 mW/cm^2 groups. One explanation for this finding is that cone degeneration occurs at a slower rate in the periphery than in central regions, hence there is greater scope for cone survival in the central retina.[234]. At P90, the peripheral versus central divergence was no longer observed for S-opsin, although a caveat is that "N" numbers were lower than at P60. Up to P90, both 25 mW/cm^2 and 100 mW/cm^2 PBM conferred significant M/L-$opsin^+$ cones in all regions. There was no significance regional difference in neuroprotective efficacy between PBM treated peripheral and central regions.

Whilst there was significant neuroprotection with both irradiation doses, there was a trend for greater protection of cones and their segments with 25 mW/cm^2 PBM; although no significant differences in neuroprotective efficacy between the two irradiation doses was found on Tukey's post-hoc test- a relatively conservative test. A statistical significance may be anticipated with a higher "N" number. With hindsight, therefore greater neuroprotective efficacy might have been expected with 25 mW/cm^2 PBM at P90. Nonetheless, the data highlights a useful irradiance range of 25-100 mW/cm^2 PBM laser for future photoreceptor neuroprotection studies. Further work is needed particularly on the rd1 mice and other models of RP to identify an "ideal" PBM irradiance dose.

The observed significant neuroprotection in the treated eyes compared to the fellow control eye suggests PBM produces a localized effect, differing from other studies[196,235,236] that suggest systemic benefits. On the other hand, Tang et al.[144] reported localized improvement of non-central diabetic macular oedema in PBM treated eyes compared to the fellow control eyes of patients. We suspect this mechanism is dependent on the biomechanics of the targeted tissue and the delivery modality which impacts penetrance and any subsequent systemic effects.

The neuroprotective mechanisms of PBM on rd1 mice were not explored in this study. Further elucidation will be needed in future studies. We have preliminary data demonstrating PBM pretreatment of mixed retinal cultures with 670nm PBM laser up to 500 mW/cm^2 irradiance protects against sodium azide induced mitochondrial inhibition,

highlighting potential mitochondrial protection and anti-oxidative mechanisms.[237] Investigating PBM's impact on oxidative stress, mitochondrial function and microglial activation in rd1 mice would be an important step in addressing theories of secondary cone degeneration and validating PBM as a novel therapy for RP.

Another limitation is that our study lacked quantitative analysis of outer segments. We used cone arrestin to qualitatively assess outer segments. We did not find any discernable differences in cone arrestin labelling away from the optic nerve between any of the treatment groups even in the affected 500 mW/cm^2 however we do acknowledge quantitative analysis may provide a clearer insight on the effect of PBM on outer segments.

4.5 Conclusion

In conclusion, PBM significantly augmented S-opsin$^+$ and ML-opsin$^+$ cone survival in rd1 mice up to P90 and improved visual function as determined by OKN. Further studies are needed to elucidate the mechanisms to explain the observed PBM neuroprotection in this study.

5. General discussion and conclusions

5.1 Introduction

Outer retinal degenerative diseases including RP or AMD are characterized by photoreceptor degeneration. It is believed that a deficiency in the supply of energy to the outer retina plays a crucial part in these conditions. It therefore seems logical to attempt therapeutic intervention in each case by utilising a bio-energetic approach.

RP is an inherited retinal degenerative condition, but due to the quantity and heterogeneity of causative gene mutations, an effective treatment remains elusive. These gene defects initially cause the death of rod cells, but secondary cone death inevitably follows. Since abrogation of rod loss in RP is unlikely to be achieved in a clinical scenario without genetic intervention, then the understanding and prevention of cone degeneration represents the most clinically significant therapeutic target. Furthermore, prevention of cone loss would essentially prevent blindness in afflicted patients. The quest for an understanding of secondary cone loss in RP has received much attention. Mechanistic explanations include oxidative stress, microglial activation, loss of rod-derived survival factors and an increase in toxins derived from dying rods.[224] More recently, the role of an energy deficiency in cones as a result of rod cell loss has also been implicated.[34,35,119] If this were verified, it would suggest that a bio-energetic-based strategy may prevent or reduce cone loss in RP.

PBM is a potential therapy in which red/near infrared light is applied non-invasively with the aim of protecting a tissue or alleviating the negative effects of a disease or toxic treatment. Mechanistically PBM has been proven to enhance mitochondrial functioning,

and thus, could represent an ideal candidate bioenergetics-based strategy for applying to cone preservation in RP. PBM has previously been shown to have some positive effects in different models of retinal degeneration or damage[134,141,191] when applied via LED delivery. However when applied in this way there is necessarily an associated random scattering and filtering of light by the eye, thus, determining safe, acceptable dosages is practically difficult. With this in mind, the present body of work aimed to assess the safety of applying PBM directly to the retina via laser and, having established this, to determine its efficacy at providing protection to this t in a well-characterised model of degeneration. The model selected against which to test the neuroprotective efficacy of the PBM laser was the rd1 mouse, a rapidly progressive autosomal recessive RP model.

5.2 Summary of findings

The findings from the safety study in Chapter 3 reflect that PBM, as applied by laser, has a safety threshold of below 500 mW/cm^2 irradiance or 45 J/cm^2 fluence in pigmented rats. In rats exposed to PBM at an irradiance of 500 mW/cm^2 but not 100 mW/cm^2, histological damage was observed to both the ONL and the RPE which was consistent with SD-OCT findings. These changes were obvious as early as 3 days following laser with more severe damage noted at 7 days post-laser by SD-OCT analysis. In agreement with this, on FA, fluorescein leakage was present in pigmented rats at 7 days but not 3 days after PBM treatment with an irradiance of 500 mW/cm^2. The presence of fluorescein leakage suggests vessel damage and the appearance of this leakage between 3 and 7 days post-treatment is reflective of evolving retinal degeneration. It is suspected that the damage is a reflection of photothermal laser injury or an oxidative damage corresponding to PBM's biphasic dose response. There was no

functional retinal change in any of the rats, as reflected by scotopic ERG assessment, however, a multifocal ERG analysis would have been more sensitive than the system employed and therefore may have detected damage. As a comparison, albino rats were not adversely affected even at 500 mW/cm^2 irradiance, again, suggesting a photothermal mechanism for damage in the pigmented animals, where melanin may have acted as an additional photoacceptor for the laser light. Overall, these results provided guidance for the appropriate irradiance levels of the PBM laser for the subsequent neuroprotection study.

The second study, as described in Chapter 4, demonstrated that PBM, as applied by laser at irradiances of both 25 mW/cm^2 and 100 mW/cm^2 has a strong neuroprotective effect against cone degeneration in the rd1 mouse. This was observed as a significantly increased cone survival level at P60 and P90 as compared with both non-lasered or sham-lasered controls. The PBM laser treatment significantly protected ML-opsin and S-opsin cones throughout all regions of the rd1 retina at P60 but was less pronounced in certain regions at P90. Moreover, there was significant preservation of visual function in eyes treated with PBM as assessed by OKN analysis at P35. The significant neuroprotection in treated eyes compared to fellow control eyes also suggested that PBM provides a localized rather systemic effect. These findings form a strong foundation for future neuroprotective studies in other retinal degenerative models as well as in the clinical setting.

5.3 Overall significance

The safety study, described in Chapter 3, is the first to specifically define safe and optimal PBM treatment parameters on retinal tissue with use of a specially designed 670

nm laser. Although there have been previous safety studies applying PBM via laser to brain[219] and hair[222] to define treatment parameters, all tissues have a unique physiology and so such data are not necessarily appropriate for retinal treatment. Hence, the elucidation of the therapeutic limits for PBM laser in this study are extremely important for any future treatment of this tissue with a similar system. The presence of focal damage at high irradiance doses of 500 mW/cm^2 in some pigmented rat retinae supports the existence of a definite safety threshold and an optimal effective irradiance, likely corresponding to the biphasic dose phenomenon observed and described in previous PBM studies[186-188]. Thus, when applied to the variably pigmented eyes of patients in the clinic, although the potential therapeutic range for the laser may be large, there are definite limits to treatment doses, above which retinal damage may be induced.

The impressive findings from the neuroprotective study support previous studies of PBM as a viable therapy for retinal degenerative disease. Furthermore, this is the first study to demonstrate the capacity of PBM to protect cones in the genetic rd1 mouse which is typically considered a severe RP model with a narrow therapeutic window. The preservation of OKN function in PBM-treated eyes suggests preservation of functional OS which means that the treatment has significant benefits. A strategy to prevent cone degeneration in RP patients would essentially prevent blindness and would represent a major medical breakthrough. Hence, the present results provide a significant impetus for further studies assessing laser-delivered PBM in both laboratory-based and clinical investigations of RP.

5.4 Limitations

There are several limitations to the safety study (Chapter 3). The first limitation is the limited time-points for assessment of changes. Additional assessments between day 3 and 7 may allow closer observation of SD-OCT/histological changes and provide a clue to the evolution of detrimental effects. Furthermore, time-points beyond 7 days would offer a better longitudinal perspective on the safety of PBM. Another limitation is the use of only three irradiance doses: 25 mW/cm^2 (2.25 J/cm^2 fluence), 100 mW/cm^2 (9 J/cm^2 fluence) and 500 mW/cm^2 (45 J/cm^2 fluence), with a large range between them. Assessment of additional doses between 100 and 500 mW/cm^2 may be helpful in narrowing the boundary between safe and destructive irradiances. In addition, when examining post-mortem tissue, histological examination of oxidative stress markers may have helped reveal the mechanisms of dose-related damage and defining, for example, whether tissue lesions were oxidative or photochemical in nature. As mentioned previously, a multifocal ERG would also have provided a greater measure of functional changes given the focal degree of damage observed in affected rats.

The main limitation in the rd1 mouse study was that the mechanism of neuroprotection for PBM was not explored. It is believed that PBM provides its neuroprotective benefit through increasing mitochondrial function, reduction of oxidative stress and suppression of inflammation. Additionally, only the 100 mW/cm^2 irradiance dose was examined at P90. Hence, comparisons of efficacy between 25 and 100 mW/cm^2 at P90 cannot be made.

5.5 Future directions

Subsequent experiments should highlight the mechanisms of PBM-derived neuroprotection observed within this body of work. Either purified cone cultures or mixed retinal cultures with a cone population can provide a useful in-vitro platform to examine neuroprotection efficacy of PBM against oxidative and metabolic insults. At an in-vivo level, measurement of oxidative stress markers (acrolein, haemoxygenase-1, NADPH oxidase and 8-Hydroxy-2'- deoxyguanosine), COX expression, inflammatory markers (GFAP, C3, TNF-α), microglial activation (iba1, CD68), via techniques such as immunohistochemistry or Western blot would shed light on the mechanisms behind the significant cone neuroprotection observed in this study.

The use of alternative RP rodent models with slower photoreceptor degeneration including S334ter-3 rats and rd10 mice would allow longer therapeutic windows to observe cone neuroprotection. This would permit the use of ERG and SD-OCT as useful adjunctive in-vivo measurements of cone function and structure.

Further experiments examining the variation of dose frequency and duration of effect may also provide useful data for clinical translation. Given the fact that the laser device is mounted on a slit-lamp with a similar arrangement to current lasers in the ophthalmic clinic, it means that a PBM laser such as the one used in the present study requires minimal training for clinicians. This therefore potentially allows for immediate clinical translation. Finally, the results from this present work have created an incentive for a phase 1 clinical trial of PBM on RP patients. Such a pilot study will examine the safety and efficacy of PBM laser in the clinical setting, providing a foundation for more robust clinical studies.

6. References

1. Sand A, Schmidt TM, Kofuji P. Diverse types of ganglion cell photoreceptors in the mammalian retina. *Progress in retinal and eye research* 2012; **31**: 287-302.
2. Nickell S, Park PS-H, Baumeister W, Palczewski K. Three-dimensional architecture of murine rod outer segments determined by cryoelectron tomography. *J Cell Biol* 2007; **177**: 917-25.
3. Gilliam JC, Chang JT, Sandoval IM, Zhang Y, Li T, Pittler SJ, Chiu W, Wensel TG. Three-dimensional architecture of the rod sensory cilium and its disruption in retinal neurodegeneration. *Cell* 2012; **151**: 1029-41.
4. Carterer.wson LD, Lavail MM. Rods and cones in the mouse retina. I. Structural analysis using light and electron microscopy. *Journal of Comparative Neurology* 1979; **188**: 245-62.
5. Price BA, Sandoval IM, Chan F, Nichols R, Roman-Sanchez R, Wensel TG, Wilson JH. Rhodopsin gene expression determines rod outer segment size and rod cell resistance to a dominant-negative neurodegeneration mutant. *PLoS One* 2012; **7**: e49889.
6. Nemet I, Tian G, Imanishi Y. Organization of cGMP sensing structures on the rod photoreceptor outer segment plasma membrane. *Channels* 2014; **8**: 528-35.
7. Molday RS, Moritz OL. Photoreceptors at a glance. *J Cell Sci* 2015; **128**: 4039-45.
8. Mustafi D, Engel AH, Palczewski K. Structure of cone photoreceptors. *Progress in retinal and eye research* 2009; **28**: 289-302.
9. Gegenfurtner KR, Sharpe LT. *Color vision: From genes to perception*: Cambridge University Press, 2001.
10. Kawamura S, Tachibanaki S. Phototransduction in Rods and Cones. In: Furukawa T, Hurley JB, Kawamura S, eds.*Phototransduction in Rods and Cones*, Tokyo: Springer Japan, 2014; 23-45.
11. Peng C, Rich ED, Varnum MD. Subunit configuration of heteromeric cone cyclic nucleotide-gated channels. *Neuron* 2004; **42**: 401-10.
12. Chen C-K, Woodruff ML, Chen FS, Chen Y, Cilluffo MC, Tranchina D, Fain GL. Modulation of mouse rod response decay by rhodopsin kinase and recoverin. *Journal of Neuroscience* 2012; **32**: 15998-6006.
13. Baehr W, Palczewski K. Guanylate cyclase-activating proteins and retina disease. In.*Guanylate cyclase-activating proteins and retina disease*: Springer, 2007; 71-91.
14. Barrett DJ, Redmond TM, Wiggert B, Oprian DD, Chader GJ, Nickerson JM. cDNA clones encoding bovine interphotoreceptor retinoid binding protein. *Biochemical and biophysical research communications* 1985; **131**: 1086-93.
15. Fong S-L, Liou GI, Landers R, Alvarez R, Bridges C. Purification and characterization of a retinol-binding glycoprotein synthesized and secreted by bovine neural retina. *Journal of Biological Chemistry* 1984; **259**: 6534-42.
16. Gudas L, Sporn M, Roberts A, Sporn M, Roberts A, Goodman D. The Retinoids: Biology. *Chemistry and Medicine (Sporn, MB, Roberts, AB, and Goodman, DS, eds) Raven Press, New York* 1994.
17. Sun H, Kawaguchi R. The membrane receptor for plasma retinol-binding protein, a new type of cell-surface receptor. *International review of cell and molecular biology* 2011; **288**: 1-41.
18. Baehr W, Wu SM, Bird AC, Palczewski K. The retinoid cycle and retina disease. In.*The retinoid cycle and retina disease*: Pergamon, 2003.
19. Wang J-S, Kefalov VJ. The cone-specific visual cycle. *Progress in retinal and eye research* 2011; **30**: 115-28.

20. Das SR, Bhardwaj N, Kjeldbye H, Gouras P. Muller cells of chicken retina synthesize 11-cis-retinol. *Biochemical Journal* 1992; **285**: 907-13.
21. Mata NL, Radu RA, Clemmons RS, Travis GH. Isomerization and oxidation of vitamin a in cone-dominant retinas: a novel pathway for visual-pigment regeneration in daylight. *Neuron* 2002; **36**: 69-80.
22. Winkler BS, Pourcho RG, Starnes C, Slocum J, Slocum N. Metabolic mapping in mammalian retina: a biochemical and 3H-2-deoxyglucose autoradiographic study. *Exp Eye Res* 2003; **77**: 327-37.
23. Chih CP, Lipton P, Roberts EL, Jr. Do active cerebral neurons really use lactate rather than glucose? *Trends Neurosci* 2001; **24**: 573-8.
24. Narayan DS, Chidlow G, Wood JP, Casson RJ. Glucose metabolism in mammalian photoreceptor inner and outer segments. *Clinical & Experimental Ophthalmology* 2017.
25. Warburg O, Dickens F. Kaiser Wilhelm-Institut für Biologie, B.(1930). *The metabolism of tumours: Investigations from the Kaiser-Wilhelm Institute for Biology, Berlin-Dahlem London: Constable*.
26. Vander Heiden MG, Cantley LC, Thompson CB. Understanding the Warburg effect: the metabolic requirements of cell proliferation. *science* 2009; **324**: 1029-33.
27. Ng SK, Wood JP, Chidlow G, Han G, Kittipassorn T, Peet DJ, Casson RJ. Cancercere metabolic requirements of cell prolif*Clinical & experimental ophthalmology* 2015; **43**: 367-76.
28. Noell WK. The effect of iodoacetate on the vertebrate retina. *Journal of Cellular and Comparative Physiology* 1951; **37**: 283-307.
29. Graymore C. Metabolism of the Developing Retina: III. Respiration in the Developing Normal Rat Retina and the Effect of an Inherited Degeneration of the Retinal Neuro-Epithelium. *The British journal of ophthalmology* 1960; **44**: 363.
30. Graymore C. METABOLISM OF THE DEVELOPING RETINA: I. AEROBIC AND ANAEROBIC GLYCOLYSIS IN THE DEVELOPING RAT RETINA. *The British journal of ophthalmology* 1959; **43**: 34.
31. Chertov AO, Holzhausen L, Kuok IT, Couron D, Parker E, Linton JD, Sadilek M, Sweet IR, Hurley JB. Roles of glucose in photoreceptor survival. *Journal of Biological Chemistry* 2011; **286**: 34700-11.
32. Okawa H, Sampath AP, Laughlin SB, Fain GL. ATP consumption by mammalian rod photoreceptors in darkness and in light. *Current Biology* 2008; **18**: 1917-21.
33. Wang L, Tornquist P, Bill A. Glucose metabolism of the inner retina in pigs in darkness and light. *Acta physiologica Scandinavica* 1997; **160**: 71-4.
34. Punzo C, Kornacker K, Cepko CL. Stimulation of the insulin/mTOR pathway delays cone death in a mouse model of retinitis pigmentosa. *Nature neuroscience* 2009; **12**: 44.
35. Ait-Ali N, Fridlich R, Millet-Puel G, Clerin E, Delalande F, Jaillard C, Blond F, Perrocheau L, Reichman S, Byrne LC, Olivier-Bandini A, Bellalou J, Moyse E, Bouillaud F, Nicol X, Dalkara D, van Dorsselaer A, Sahel JA, Leveillard T. Rod-derived cone viability factor promotes cone survival by stimulating aerobic glycolysis. *Cell* 2015; **161**: 817-32.
36. Karunadharma PP, Nordgaard CL, Olsen TW, Ferrington DA. Mitochondrial DNA damage as a potential mechanism for age-related macular degeneration. *Investigative ophthalmology & visual science* 2010; **51**: 5470.
37. Nordgaard CL, Karunadharma PP, Feng X, Olsen TW, Ferrington DA. Mitochondrial proteomics of the retinal pigment epithelium at progressive stages of age-related macular degeneration. *Investigative ophthalmology & visual science* 2008; **49**: 2848-55.
38. Kowluru RA. Diabetic retinopathy: mitochondrial dysfunction and retinal capillary cell death. *Antioxidants & redox signaling* 2005; **7**: 1581.

39. Zhang Y, Cho C-H, Atchaneeyasakul L-o, McFarland T, Appukuttan B, Stout JT. Activation of the mitochondrial apoptotic pathway in a rat model of central retinal artery occlusion. *Investigative ophthalmology & visual science* 2005; **46**: 2133-9.
40. Sun C, Li X-x, He X-j, Zhang Q, Tao Y. Neuroprotective effect of minocycline in a rat model of branch retinal vein occlusion. *Experimental eye research* 2013; **113**: 105-16.
41. Schober MS, Chidlow G, Wood JP, Casson RJ. Bioenergetic‐based neuroprotection and glaucoma. *Clinical & experimental ophthalmology* 2008; **36**: 377-85.
42. Matthews RT, Ferrante RJ, Klivenyi P, Yang L, Klein AM, Mueller G, Kaddurah-Daouk R, Beal MF. Creatine and cyclocreatine attenuate MPTP neurotoxicity. *Experimental neurology* 1999; **157**: 142-9.
43. Dedeoglu A, Kubilus JK, Yang L, Ferrante KL, Hersch SM, Beal MF. Creatine therapy provides neuroprotection after onset of clinical symptoms in Huntington's disease transgenic mice. *Journal of neurochemistry* 2003; **85**: 1359-67.
44. Matthews RT, Yang L, Jenkins BG, Ferrante RJ, Rosen BR, Kaddurah-Daouk R, Beal MF. Neuroprotective effects of creatine and cyclocreatine in animal models of Huntington's disease. *Journal of Neuroscience* 1998; **18**: 156-63.
45. Ryu H, Rosas HD, Hersch SM, Ferrante RJ. The therapeutic role of creatine in Huntington's disease. *Pharmacology & therapeutics* 2005; **108**: 193-207.
46. Klivenyi P, Ferrante RJ, Matthews RT, Bogdanov MB, Klein AM, Andreassen OA, Mueller G, Wermer M, Kaddurah-Daouk R, Beal MF. Neuroprotective effects of creatine in a transgenic animal model of amyotrophic lateral sclerosis. *Nature medicine* 1999; **5**: 347-50.
47. Zhu S, Li M, Figueroa BE, Liu A, Stavrovskaya IG, Pasinelli P, Beal MF, Brown RH, Kristal BS, Ferrante RJ. Prophylactic creatine administration mediates neuroprotection in cerebral ischemia in mice. *Journal of Neuroscience* 2004; **24**: 5909-12.
48. Scheff SW, Dhillon HS. Creatine-enhanced diet alters levels of lactate and free fatty acids after experimental brain injury. *Neurochemical research* 2004; **29**: 469-79.
49. Ji D, Li G-Y, Osborne NN. Nicotinamide attenuates retinal ischemia and light insults to neurones. *Neurochemistry international* 2008; **52**: 786-98.
50. Lam TT. The effect of 3-aminobenzamide, an inhibitor of poly-ADP-ribose polymerase, on ischemia/reperfusion damage in rat retina. *Research communications in molecular pathology and pharmacology* 1997; **95**: 241-52.
51. Malcon C, Kaddurah-Daouk R, Beal MF. Neuroprotective effects of creatine administration against NMDA and malonate toxicity. *Brain research* 2000; **860**: 195-8.
52. Beal MF. Bioenergetic approaches for neuroprotection in Parkinson's disease. *Annals of neurology* 2003; **53**.
53. Matthews RT, Yang L, Browne S, Baik M, Beal MF. Coenzyme Q10 administration increases brain mitochondrial concentrations and exerts neuroprotective effects. *Proceedings of the National Academy of Sciences* 1998; **95**: 8892-7.
54. Beal MF, Matthews RT, Tieleman A, Shults CW. Coenzyme Q 10 attenuates the 1-methyl-4-phenyl-1, 2, 3, 6-tetrahydropyridine (MPTP) induced loss of striatal dopamine and dopaminergic axons in aged mice. *Brain research* 1998; **783**: 109-14.
55. Lee D, Shim MS, Kim KY, Noh YH, Kim H, Kim SY, Weinreb RN, Ju WK. Coenzyme Q10 inhibits glutamate excitotoxicity and oxidative stress-mediated mitochondrial alteration in a mouse model of glaucoma. *Investigative ophthalmology & visual science* 2014; **55**: 993-1005.
56. Casson RJ, Chidlow G, Wood JP, Osborne NN. The effect of hyperglycemia on experimental retinal ischemia. *Arch Ophthalmol* 2004; **122**: 361-6.
57. Holman MC, Chidlow G, Wood JP, Casson RJ. The effect of hyperglycemia on hypoperfusion-induced injury. *Investigative ophthalmology & visual science* 2010; **51**: 2197-207.

58. Ebneter A, Chidlow G, Wood JP, Casson RJ. Protection of retinal ganglion cells and the optic nerve during short-term hyperglycemia in experimental glaucoma. *Archives of ophthalmology* 2011; **129**: 1337-44.
59. Casson RJ, Han G, Ebneter A, Chidlow G, Glihotra J, Newland H, Wood JP. Glucose-induced temporary visual recovery in primary open-angle glaucoma: a double-blind, randomized study. *Ophthalmology* 2014; **121**: 1203-11.
60. Shibeeb OS, Chidlow G, Han G, Wood JP, Casson RJ. Effect of subconjunctival glucose on retinal ganglion cell survival in experimental retinal ischaemia and contrast sensitivity in human glaucoma. *Clinical & experimental ophthalmology* 2016; **44**: 24-32.
61. Patel SP, Sullivan PG, Pandya JD, Goldstein GA, VanRooyen JL, Yonutas HM, Eldahan KC, Morehouse J, Magnuson DS, Rabchevsky AG. N-acetylcysteine amide preserves mitochondrial bioenergetics and improves functional recovery following spinal trauma. *Exp Neurol* 2014; **257**: 95-105.
62. Pandya JD, Readnower RD, Patel SP, Yonutas HM, Pauly JR, Goldstein GA, Rabchevsky AG, Sullivan PG. N-acetylcysteine amide confers neuroprotection, improves bioenergetics and behavioral outcome following TBI. *Exp Neurol* 2014; **257**: 106-13.
63. Storch A. [Coenzyme Q10 in Parkinson's disease. Symptomatic or neuroprotective effects?]. *Der Nervenarzt* 2007; **78**: 1378-82.
64. Wang J, Xiao Y, Chen S, Zhong C, Luo M, Luo H. Creatine for Parkinson's disease. *Cochrane Database Syst Rev* 2012.
65. Verbessem P, Lemiere J, Eijnde B, Swinnen S, Vanhees L, Van Leemputte M, Hespel P, Dom R. Creatine supplementation in Huntington's disease A placebo-controlled pilot trial. *Neurology* 2003; **61**: 925-30.
66. Grant CA, Berson EL. Treatable forms of retinitis pigmentosa associated with systemic neurological disorders. *International ophthalmology clinics* 2001; **41**: 103-10.
67. Berson EL. Retinitis pigmentosa. The Friedenwald Lecture. *Investigative ophthalmology & visual science* 1993; **34**: 1659-76.
68. Daiger S, Sullivan L, Bowne S. Genes and mutations causing retinitis pigmentosa. *Clinical genetics* 2013; **84**.
69. Hartong DT, Berson EL, Dryja TP. Retinitis pigmentosa. *The Lancet* 2006; **368**: 1795-809.
70. Geller AM, Sieving PA. Assessment of foveal cone photoreceptors in Stargardt's macular dystrophy using a small dot detection task. *Vision research* 1993; **33**: 1509-24.
71. Gränse L, Ponjavic V, Andréasson S. Full‐field ERG, multifocal ERG and multifocal VEP in patients with retinitis pigmentosa and residual central visual fields. *Acta ophthalmologica Scandinavica* 2004; **82**: 701-6.
72. Lewin AS, Drenser KA, Hauswirth WW, Nishikawa S, Yasumura D, Flannery JG, LaVail MM. Ribozyme rescue of photoreceptor cells in a transgenic rat model of autosomal dominant retinitis pigmentosa. *Nature medicine* 1998; **4**: 967-71.
73. Illing ME, Rajan RS, Bence NF, Kopito RR. A rhodopsin mutant linked to autosomal dominant retinitis pigmentosa is prone to aggregate and interacts with the ubiquitin proteasome system. *Journal of Biological Chemistry* 2002; **277**: 34150-60.
74. Böhm S, Riedmayr LM, Nguyen OP, Gießl A, Liebscher T, Butz ES, Schön C, Michalakis S, Wahl-Schott C, Biel M. Peripherin-2 and Rom-1 have opposing effects on rod outer segment targeting of retinitis pigmentosa-linked peripherin-2 mutants. *Scientific Reports* 2017; **7**.
75. McLaughlin ME, Ehrhart TL, Berson EL, Dryja TP. Mutation spectrum of the gene encoding the beta subunit of rod phosphodiesterase among patients with autosomal recessive retinitis pigmentosa. *Proceedings of the National Academy of Sciences* 1995; **92**: 3249-53.

76. Farber DB, Flannery JG, Bowes-Rickman C. The rd mouse story: seventy years of research on an animal model of inherited retinal degeneration. *Progress in retinal and eye research* 1994; **13**: 31-64.
77. Lolley RN, Farber DB, Rayborn ME, Hollyfield JG. Cyclic GMP accumulation causes degeneration of photoreceptor cells: simulation of an inherited disease. *Science* 1977; **196**: 664-6.
78. FARBER DB, SHUSTER TA. Cyclic necleotides in retinal function and degeneration. *The Retina A Model for Cell Biology Studies Part_1* 2012: 239.
79. Ulshafer R, Garcia C, Hollyfield J. Sensitivity of photoreceptors to elevated levels of cGMP in the human retina. *Investigative ophthalmology & visual science* 1980; **19**: 1236-41.
80. Farber D, Souza DW, Chase DG. Cone visual cell degeneration in ground squirrel retina: disruption of morphology and cyclic nucleotide metabolism by lodoacetic acid. *Investigative ophthalmology & visual science* 1983; **24**: 1236-49.
81. Cideciyan AV, Hood DC, Huang Y, Banin E, Li Z-Y, Stone EM, Milam AH, Jacobson SG. Disease sequence from mutant rhodopsin allele to rod and cone photoreceptor degeneration in man. *Proceedings of the National Academy of Sciences* 1998; **95**: 7103-8.
82. Kranz K, Paquet-Durand F, Weiler R, Janssen-Bienhold U, Dedek K. Testing for a gap junction-mediated bystander effect in retinitis pigmentosa: secondary cone death is not altered by deletion of connexin36 from cones. *PloS one* 2013; **8**: e57163.
83. Ripps H. Cell death in retinitis pigmentosa: gap junctions and the 'bystander' effect. *Exp Eye Res* 2002; **74**: 327-36.
84. Mesnil M, Piccoli C, Tiraby G, Willecke K, Yamasaki H. Bystander killing of cancer cells by herpes simplex virus thymidine kinase gene is mediated by connexins. *Proceedings of the National Academy of Sciences* 1996; **93**: 1831-5.
85. Freeman SM, Abboud CN, Whartenby KA, Packman CH, Koeplin DS, Moolten FL, Abraham GN. The “bystander effect”: tumor regression when a fraction of the tumor mass is genetically modified. *Cancer research* 1993; **53**: 5274-83.
86. Cotrina ML, Kang J, Lin JH, Bueno E, Hansen TW, He L, Liu Y, Nedergaard M. Astrocytic gap junctions remain open during ischemic conditions. *Journal of Neuroscience* 1998; **18**: 2520-37.
87. Rami A, Volkmann T, Winckler J. Effective reduction of neuronal death by inhibiting gap junctional intercellular communication in a rodent model of global transient cerebral ischemia. *Experimental neurology* 2001; **170**: 297-304.
88. Kedzierski W, Bok D, Travis GH. Non-cell-autonomous photoreceptor degeneration in rds mutant mice mosaic for expression of a rescue transgene. *The Journal of neuroscience : the official journal of the Society for Neuroscience* 1998; **18**: 4076-82.
89. Hicks D, Sahel J. The implications of rod-dependent cone survival for basic and clinical research. *Investigative ophthalmology & visual science* 1999; **40**: 3071-4.
90. Thanos S, Kacza J, Seeger J, Mey J. Old dyes for new scopes: the phagocytosis-dependent long-term fluorescence labelling of microglial cells in vivo. *Trends in neurosciences* 1994; **17**: 177-82.
91. Roque RS, Imperial CJ, Caldwell RB. Microglial cells invade the outer retina as photoreceptors degenerate in Royal College of Surgeons rats. *Investigative ophthalmology & visual science* 1996; **37**: 196-203.
92. Gupta N, Brown KE, Milam AH. Activated microglia in human retinitis pigmentosa, late-onset retinal degeneration, and age-related macular degeneration. *Exp Eye Res* 2003; **76**: 463-71.
93. Zeng HY, Zhu XA, Zhang C, Yang LP, Wu LM, Tso MO. Identification of sequential events and factors associated with microglial activation, migration, and cytotoxicity in

retinal degeneration in rd mice. *Investigative ophthalmology & visual science* 2005; **46**: 2992-9.
94. Kohno H, Chen Y, Kevany BM, Pearlman E, Miyagi M, Maeda T, Palczewski K, Maeda A. Photoreceptor Proteins Initiate Microglial Activation via Toll-like Receptor 4 in Retinal Degeneration Mediated by All-trans-retinal. *The Journal of Biological Chemistry* 2013; **288**: 15326-41.
95. Guo C, Otani A, Oishi A, Kojima H, Makiyama Y, Nakagawa S, Yoshimura N. Knockout of ccr2 alleviates photoreceptor cell death in a model of retinitis pigmentosa. *Exp Eye Res* 2012; **104**: 39-47.
96. Zabel MK, Zhao L, Zhang Y, Gonzalez SR, Ma W, Wang X, Fariss RN, Wong WT. Microglial phagocytosis and activation underlying photoreceptor degeneration is regulated by CX3CL1-CX3CR1 signaling in a mouse model of retinitis pigmentosa. *Glia* 2016; **64**: 1479-91.
97. Peng B, Xiao J, Wang K, So KF, Tipoe GL, Lin B. Suppression of microglial activation is neuroprotective in a mouse model of human retinitis pigmentosa. *The Journal of neuroscience : the official journal of the Society for Neuroscience* 2014; **34**: 8139-50.
98. Roque RS, Rosales AA, Jingjing L, Agarwal N, Al-Ubaidi MR. Retina-derived microglial cells induce photoreceptor cell death in vitro. *Brain research* 1999; **836**: 110-9.
99. Nita M, Grzybowski A. The role of the reactive oxygen species and oxidative stress in the pathomechanism of the age-related ocular diseases and other pathologies of the anterior and posterior eye segments in adults. *Oxidative medicine and cellular longevity* 2016; **2016**.
100. Yu D-Y, Cringle S, Valter K, Walsh N, Lee D, Stone J. Photoreceptor death, trophic factor expression, retinal oxygen status, and photoreceptor function in the P23H rat. *Investigative ophthalmology & visual science* 2004; **45**: 2013-9.
101. Campochiaro PA, Mir TA. The mechanism of cone cell death in Retinitis Pigmentosa. *Progress in retinal and eye research* 2017.
102. Shen J, Yang X, Dong A, Petters RM, Peng YW, Wong F, Campochiaro PA. Oxidative damage is a potential cause of cone cell death in retinitis pigmentosa. *Journal of cellular physiology* 2005; **203**: 457-64.
103. Komeima K, Rogers BS, Lu L, Campochiaro PA. Antioxidants reduce cone cell death in a model of retinitis pigmentosa. *Proceedings of the National Academy of Sciences* 2006; **103**: 11300-5.
104. Usui S, Oveson BC, Lee SY, Jo YJ, Yoshida T, Miki A, Miki K, Iwase T, Lu L, Campochiaro PA. NADPH Oxidase Plays a Central Role in Cone Cell Death in Retinitis Pigmentosa. *J Neurochem* 2009; **110**: 1028-37.
105. Martínez-Fernández de la Cámara C, Salom D, Sequedo MD, Hervás D, Marín-Lambíes C, Aller E, Jaijo T, Díaz LM, Millán JM, Rodrigo R. Altered Antioxidant-Oxidant Status in the Aqueous Humor and Peripheral Blood of Patients with Retinitis Pigmentosa. *PLoS One* 2013; **8**.
106. Campochiaro PA, Strauss RW, Lu L, Hafiz G, Wolfson Y, Shah SM, Sophie R, Mir TA, Scholl HP. Is there excess oxidative stress and damage in eyes of patients with retinitis pigmentosa? In.*Is there excess oxidative stress and damage in eyes of patients with retinitis pigmentosa?*: Mary Ann Liebert, Inc. 140 Huguenot Street, 3rd Floor New Rochelle, NY 10801 USA, 2015.
107. Komeima K, Rogers BS, Campochiaro PA. Antioxidants slow photoreceptor cell death in mouse models of retinitis pigmentosa. *J Cell Physiol* 2007; **213**: 809-15.
108. Dilger R, Baker D. Oral-acetyl--cysteine is a safe and effective precursor of cysteine. *Journal of animal science* 2007; **85**: 1712-8.

109. Lee SY, Usui S, Zafar AB, Oveson BC, Jo YJ, Lu L, Masoudi S, Campochiaro PA. N-Acetylcysteine promotes long-term survival of cones in a model of retinitis pigmentosa. *J Cell Physiol* 2011; **226**: 1843-9.
110. Usui S, Komeima K, Lee SY, Jo Y-J, Ueno S, Rogers BS, Wu Z, Shen J, Lu L, Oveson BC. Increased expression of catalase and superoxide dismutase 2 reduces cone cell death in retinitis pigmentosa. *Molecular Therapy* 2009; **17**: 778-86.
111. Usui S, Oveson BC, Iwase T, Lu L, Lee SY, Jo Y-J, Wu Z, Choi E-Y, Samulski RJ, Campochiaro PA. Overexpression of SOD in retina: need for increase in H 2 O 2-detoxifying enzyme in same cellular compartment. *Free Radical Biology and Medicine* 2011; **51**: 1347-54.
112. Mohand-Said S, Deudon-Combe A, Hicks D, Simonutti M, Forster V, Fintz A-C, Léveillard T, Dreyfus H, Sahel J-A. Normal retina releases a diffusible factor stimulating cone survival in the retinal degeneration mouse. *Proceedings of the National Academy of Sciences* 1998; **95**: 8357-62.
113. Léveillard T, Mohand-Saïd S, Lorentz O, Hicks D, Fintz A-C, Clérin E, Simonutti M, Forster V, Cavusoglu N, Chalmel F. Identification and characterization of rod-derived cone viability factor. *Nature genetics* 2004; **36**: 755-9.
114. Yang Y, Mohand-Said S, Danan A, Simonutti M, Fontaine V, Clerin E, Picaud S, Leveillard T, Sahel JA. Functional cone rescue by RdCVF protein in a dominant model of retinitis pigmentosa. *Molecular therapy : the journal of the American Society of Gene Therapy* 2009; **17**: 787-95.
115. Byrne LC, Dalkara D, Luna G, Fisher SK, Clérin E, Sahel J-A, Léveillard T, Flannery JG. Viral-mediated RdCVF and RdCVFL expression protects cone and rod photoreceptors in retinal degeneration. *The Journal of clinical investigation* 2015; **125**: 105.
116. Cronin T, Raffelsberger W, Lee-Rivera I, Jaillard C, Niepon M-L, Kinzel B, Clérin E, Petrosian A, Picaud S, Poch O. The disruption of the rod-derived cone viability gene leads to photoreceptor dysfunction and susceptibility to oxidative stress. *Cell Death & Differentiation* 2010; **17**: 1199-210.
117. Chalmel F, Leveillard T, Jaillard C, Lardenois A, Berdugo N, Morel E, Koehl P, Lambrou G, Holmgren A, Sahel JA, Poch O. Rod-derived Cone Viability Factor-2 is a novel bifunctional-thioredoxin-like protein with therapeutic potential. *BMC molecular biology* 2007; **8**: 74.
118. Lambard S, Reichman S, Berlinicke C, Niepon M-L, Goureau O, Sahel J-A, Léveillard T, Zack DJ. Expression of rod-derived cone viability factor: dual role of CRX in regulating promoter activity and cell-type specificity. *PloS one* 2010; **5**: e13075.
119. Venkatesh A, Ma S, Le YZ, Hall MN, Rüegg MA, Punzo C. Activated mTORC1 promotes long-term cone survival in retinitis pigmentosa mice. *The Journal of clinical investigation* 2015; **125**: 1446-58.
120. Laplante M, Sabatini DM. mTOR signaling at a glance. *Journal of cell science* 2009; **122**: 3589-94.
121. Berson EL, Rosner B, Sandberg MA, Hayes K, Nicholson BW, Weigel-DiFranco C, Willett W. A randomized trial of vitamin A and vitamin E supplementation for retinitis pigmentosa. *Archives of ophthalmology* 1993; **111**: 761-72.
122. Bennett J, Tanabe T, Sun D, Zeng Y, Kjeldbye H, Gouras P, Maguire AM. Photoreceptor cell rescue in retinal degeneration (rd) mice by in vivo gene therapy. *Nature medicine* 1996; **2**: 649-54.
123. Ali RR, Sarra GM, Stephens C, Alwis MD, Bainbridge JW, Munro PM, Fauser S, Reichel MB, Kinnon C, Hunt DM, Bhattacharya SS, Thrasher AJ. Restoration of photoreceptor ultrastructure and function in retinal degeneration slow mice by gene therapy. *Nat Genet* 2000; **25**: 306-10.

124. Kaplan HJ, Tezel TH, Berger AS, Wolf ML, Del Priore LV. Human photoreceptor transplantation in retinitis pigmentosa: a safety study. *Archives of Ophthalmology* 1997; **115**: 1168-72.
125. Mohand-Said S, Hicks D, Dreyfus H, Sahel JA. Selective transplantation of rods delays cone loss in a retinitis pigmentosa model. *Archives of ophthalmology* 2000; **118**: 807-11.
126. N Sahni J, Angi M, Irigoyen C, Semeraro F, R Romano M, Parmeggiani F. Therapeutic challenges to retinitis pigmentosa: from neuroprotection to gene therapy. *Current genomics* 2011; **12**: 276-84.
127. Dryja TP, McGee TL, Reichel E, Hahn LB, Cowley GS, Yandell DW, Sandberg MA, Berson EL. A point mutation of the rhodopsin gene in one form of retinitis pigmentosa. *Nature* 1990; **343**: 364-6.
128. García-Ayuso D, Ortín-Martínez A, Jiménez-López M, Galindo-Romero C, Cuenca N, Pinilla I, Vidal-Sanz M, Agudo-Barriuso M, Villegas-Pérez MP. Changes in the Photoreceptor Mosaic of P23H-1 Rats During Retinal Degeneration: Implications for Rod-Cone Dependent Survival. *Investigative ophthalmology & visual science* 2013; **54**: 5888-900.
129. Chang B, Hawes N, Hurd R, Davisson M, Nusinowitz S, Heckenlively J. Retinal degeneration mutants in the mouse. *Vision research* 2002; **42**: 517-25.
130. Gargini C, Terzibasi E, Mazzoni F, Strettoi E. Retinal organization in the retinal degeneration 10 (rd10) mutant mouse: a morphological and ERG study. *The Journal of comparative neurology* 2007; **500**: 222-38.
131. Pittler SJ, Baehr W. Identification of a nonsense mutation in the rod photoreceptor cGMP phosphodiesterase beta-subunit gene of the rd mouse. *Proc Natl Acad Sci U S A* 1991; **88**: 8322-6.
132. Carter-Dawson LD, LaVail MM, Sidman RL. Differential effect of the rd mutation on rods and cones in the mouse retina. *Investigative ophthalmology & visual science* 1978; **17**: 489-98.
133. Geneva II. Photobiomodulation for the treatment of retinal diseases: a review. *International Journal of Ophthalmology* 2016; **9**: 145.
134. Albarracin R, Eells J, Valter K. Photobiomodulation protects the retina from light-induced photoreceptor degeneration. *Investigative ophthalmology & visual science* 2011; **52**: 3582-92.
135. Qu C, Cao W, Fan Y, Lin Y. Near-infrared light protect the photoreceptor from light-induced damage in rats. In.*Near-infrared light protect the photoreceptor from light-induced damage in rats*: Springer, 2010; 365-74.
136. Lu Y-Z, Fernando N, Natoli R, Madigan M, Valter K. 670nm light treatment following retinal injury modulates Müller cell gliosis: Evidence from in vivo and in vitro stress models. *Experimental eye research* 2018; **169**: 1-12.
137. Begum R, Powner MB, Hudson N, Hogg C, Jeffery G. Treatment with 670 nm light up regulates cytochrome C oxidase expression and reduces inflammation in an age-related macular degeneration model. *PloS one* 2013; **8**: e57828.
138. Kirk DK, Gopalakrishnan S, Schmitt H, Abroe B, Stoehr M, Dubis A, Carroll J, Stone J, Valter K, Eells J. Photobiomodulation reduces photoreceptor death and regulates cytoprotection in early states of P23H retinal dystrophy. In.*Photobiomodulation reduces photoreceptor death and regulates cytoprotection in early states of P23H retinal dystrophy*: International Society for Optics and Photonics, 2013; 85690F-F-10.
139. Tang J, Du Y, Lee CA, Talahalli R, Eells JT, Kern TS. Low-intensity far-red light inhibits early lesions that contribute to diabetic retinopathy: in vivo and in vitro. *Investigative ophthalmology & visual science* 2013; **54**: 3681-90.

140. Natoli R, Valter K, Barbosa M, Dahlstrom J, Rutar M, Kent A, Provis J. 670nm photobiomodulation as a novel protection against retinopathy of prematurity: evidence from oxygen induced retinopathy models. *PloS one* 2013; **8**: e72135.
141. Albarracin R, Natoli R, Rutar M, Valter K, Provis J. 670 nm light mitigates oxygen-induced degeneration in C57BL/6J mouse retina. *BMC neuroscience* 2013; **14**: 125.
142. Ivandic BT, Ivandic T. Low-level laser therapy improves vision in patients with age-related macular degeneration. *Photomedicine and laser surgery* 2008; **26**: 241-5.
143. Merry G, Dotson R, Devenyi R, Markowitz S, Reyes S. Photobiomodulation as a new treatment for dry age related macular degeneration. results from the toronto and Oak ridge photobimodulation study in AMD (TORPA). *Investigative ophthalmology & visual science* 2012; **53**: 2049-.
144. Tang J, Herda AA, Kern TS. Photobiomodulation in the treatment of patients with non-center-involving diabetic macular oedema. *Br J Ophthalmol* 2014; **98**: 1013-5.
145. Ivandic BT, Ivandic T. Low-level laser therapy improves visual acuity in adolescent and adult patients with amblyopia. *Photomedicine and laser surgery* 2012; **30**: 167-71.
146. Ivandic BT, Ivandic T. Low-level laser therapy improves vision in a patient with retinitis pigmentosa. *Photomedicine and laser surgery* 2014; **32**: 181-4.
147. Eells J, Henry M, Summerfelt P, Wong-Riley M, Buchmann E, Kane M, Whelan N, Whelan H. Therapeutic photobiomodulation for methanol-induced retinal toxicity. *Proceedings of the National Academy of Sciences* 2003; **100**: 3439-44.
148. Wong-Riley MT, Liang HL, Eells JT, Chance B, Henry MM, Buchmann E, Kane M, Whelan HT. Photobiomodulation directly benefits primary neurons functionally inactivated by toxins: role of cytochrome c oxidase. *The Journal of Biological Chemistry* 2005; **280**: 4761-71.
149. Desmettre T, Maurage CA, Mordon S. Transpupillary thermotherapy (TTT) with short duration laser exposures induce heat shock protein (HSP) hyperexpression on choroidoretinal layers. *Lasers in surgery and medicine* 2003; **33**: 102-7.
150. Karu TI, Pyatibrat LV, Kolyakov SF, Afanasyeva NI. Absorption measurements of a cell monolayer relevant to phototherapy: reduction of cytochrome c oxidase under near IR radiation. *Journal of Photochemistry and Photobiology B: Biology* 2005; **81**: 98-106.
151. Chung H, Dai T, Sharma SK, Huang Y-Y, Carroll JD, Hamblin MR. The nuts and bolts of low-level laser (light) therapy. *Annals of biomedical engineering* 2012; **40**: 516-33.
152. de Freitas LF, Hamblin MR. Proposed mechanisms of photobiomodulation or low-level light therapy. *IEEE Journal of selected topics in quantum electronics* 2016; **22**: 348-64.
153. Sperandio FF, Simões A, Corrêa L, Aranha ACC, Giudice FS, Hamblin MR, Sousa SC. Low‐level laser irradiation promotes the proliferation and maturation of keratinocytes during epithelial wound repair. *Journal of biophotonics* 2015; **8**: 795-803.
154. Frozanfar A, Ramezani M, Rahpeyma A, Khajehahmadi S, Arbab HR. The effects of low level laser therapy on the expression of collagen type I gene and proliferation of human gingival fibroblasts (Hgf3-Pi 53): in vitro study. *Iranian journal of basic medical sciences* 2013; **16**: 1071.
155. Hamajima S, Hiratsuka K, Kiyama-Kishikawa M, Tagawa T, Kawahara M, Ohta M, Sasahara H, Abiko Y. Effect of low-level laser irradiation on osteoglycin gene expression in osteoblasts. *Lasers in medical science* 2003; **18**: 78-82.
156. Lim W, Kim J, Kim S, Karna S, Won J, Jeon SM, Kim SY, Choi Y, Choi H, Kim O. Modulation of Lipopolysaccharide‐Induced NF‐κB Signaling Pathway by 635 nm Irradiation via Heat Shock Protein 27 in Human Gingival Fibroblast Cells. *Photochemistry and photobiology* 2013; **89**: 199-207.

157. Yamaura M, Yao M, Yaroslavsky I, Cohen R, Smotrich M, Kochevar IE. Low level light effects on inflammatory cytokine production by rheumatoid arthritis synoviocytes. *Lasers in surgery and medicine* 2009; **41**: 282-90.
158. Hwang MH, Shin JH, Kim KS, Yoo CM, Jo GE, Kim JH, Choi H. Low level light therapy modulates inflammatory mediators secreted by human annulus fibrosus cells during intervertebral disc degeneration in vitro. *Photochem Photobiol* 2015; **91**: 403-10.
159. Gupta A, Keshri GK, Yadav A, Gola S, Chauhan S, Salhan AK, Bala Singh S. Superpulsed (Ga‐As, 904 nm) low‐level laser therapy (LLLT) attenuates inflammatory response and enhances healing of burn wounds. *Journal of biophotonics* 2015; **8**: 489-501.
160. Moriyama Y, Moriyama EH, Blackmore K, Akens MK, Lilge L. In Vivo Study of the Inflammatory Modulating Effects of Low‐level Laser Therapy on iNOS Expression Using Bioluminescence Imaging. *Photochemistry and photobiology* 2005; **81**: 1351-5.
161. de Lima FM, Vitoretti L, Coelho F, Albertini R, Breithaupt-Faloppa AC, de Lima WT, Aimbire F. Suppressive effect of low-level laser therapy on tracheal hyperresponsiveness and lung inflammation in rat subjected to intestinal ischemia and reperfusion. *Lasers in medical science* 2013; **28**: 551-64.
162. Muili KA, Gopalakrishnan S, Eells JT, Lyons J-A. Photobiomodulation induced by 670 nm light ameliorates MOG35-55 induced EAE in female C57BL/6 mice: a role for remediation of nitrosative stress. *PloS one* 2013; **8**: e67358.
163. Rutar M, Natoli R, Albarracin R, Valter K, Provis J. 670-nm light treatment reduces complement propagation following retinal degeneration. *Journal of neuroinflammation* 2012; **9**: 257.
164. Kokkinopoulos I, Colman A, Hogg C, Heckenlively J, Jeffery G. Age-related retinal inflammation is reduced by 670 nm light via increased mitochondrial membrane potential. *Neurobiology of aging* 2013; **34**: 602-9.
165. Huang YY, Nagata K, Tedford CE, McCarthy T, Hamblin MR. Low‐level laser therapy (LLLT) reduces oxidative stress in primary cortical neurons in vitro. *Journal of biophotonics* 2013; **6**: 829-38.
166. Giuliani A, Lorenzini L, Gallamini M, Massella A, Giardino L, Calzà L. Low infra red laser light irradiation on cultured neural cells: effects on mitochondria and cell viability after oxidative stress. *BMC complementary and alternative medicine* 2009; **9**: 8.
167. Martins D, Turnes B, Cidral-Filho F, Bobinski F, Rosas R, Danielski L, Petronilho F, Santos A. Light-emitting diode therapy reduces persistent inflammatory pain: role of interleukin 10 and antioxidant enzymes. *Neuroscience* 2016; **324**: 485-95.
168. Assis L, Moretti AI, Abrahao TB, Cury V, Souza HP, Hamblin MR, Parizotto NA. Low‐level laser therapy (808 nm) reduces inflammatory response and oxidative stress in rat tibialis anterior muscle after cryolesion. *Lasers in surgery and medicine* 2012; **44**: 726-35.
169. Tatmatsu-Rocha JC, Ferraresi C, Hamblin MR, Maia FD, do Nascimento NRF, Driusso P, Parizotto NA. Low-level laser therapy (904nm) can increase collagen and reduce oxidative and nitrosative stress in diabetic wounded mouse skin. *Journal of Photochemistry and Photobiology B: Biology* 2016; **164**: 96-102.
170. Liang H, Whelan H, Eells J, Meng H, Buchmann E, Lerch-Gaggl A, Wong-Riley M. Photobiomodulation partially rescues visual cortical neurons from cyanide-induced apoptosis. *Neuroscience* 2006; **139**: 639-49.
171. Li F-H, Liu Y-Y, Qin F, Luo Q, Yang H-P, Zhang Q-G, Liu TC-Y. Photobiomodulation on Bax and Bcl-2 Proteins and SIRT1/PGC-1α Axis mRNA Expression Levels of Aging Rat Skeletal Muscle. *International Journal of Photoenergy* 2014; **2014**.

172. Quirk BJ, Torbey M, Buchmann E, Verma S, Whelan HT. Near-infrared photobiomodulation in an animal model of traumatic brain injury: improvements at the behavioral and biochemical levels. *Photomedicine and laser surgery* 2012; **30**: 523-9.
173. Jere SW, Houreld NN, Abrahamse H. Photobiomodulation at 660nm stimulates proliferation and migration of diabetic wounded cells via the expression of epidermal growth factor and the JAK/STAT pathway. *Journal of Photochemistry and Photobiology B: Biology* 2018.
174. Wang Y, Huang Y-Y, Wang Y, Lyu P, Hamblin MR. Red (660 nm) or near-infrared (810 nm) photobiomodulation stimulates, while blue (415 nm), green (540 nm) light inhibits proliferation in human adipose-derived stem cells. *Scientific reports* 2017; **7**: 7781.
175. Fekrazad R, Asefi S, Allahdadi M, Kalhori KA. Effect of photobiomodulation on mesenchymal stem cells. *Photomedicine and laser surgery* 2016; **34**: 533-42.
176. Emelyanov AN, Kiryanova VV. Photomodulation of proliferation and differentiation of stem cells by the visible and infrared light. *Photomedicine and laser surgery* 2015; **33**: 164-74.
177. Huang Y-Y, Sharma SK, Carroll J, Hamblin MR. Biphasic dose response in low level light therapy–an update. *Dose-Response* 2011; **9**: dose-response. 11-009. Hamblin.
178. Enwemeka CS. Intricacies of dose in laser phototherapy for tissue repair and pain relief. *Photomedicine and laser surgery* 2009; **27**: 387-93.
179. Hamblin MR, Demidova TN. Mechanisms of low level light therapy. In.*Mechanisms of low level light therapy*, Vol. 6140: International Society for Optics and Photonics, 2006; 614001.
180. Giacci MK, Wheeler L, Lovett S, Dishington E, Majda B, Bartlett CA, Thornton E, Harford-Wright E, Leonard A, Vink R, Harvey AR, Provis J, Dunlop SA, Hart NS, Hodgetts S, Natoli R, Van Den Heuvel C, Fitzgerald M. Differential effects of 670 and 830 nm red near infrared irradiation therapy: a comparative study of optic nerve injury, retinal degeneration, traumatic brain and spinal cord injury. *PLoS One* 2014; **9**: e104565.
181. Heiskanen V, Hamblin MR. Photobiomodulation: lasers vs. light emitting diodes? *Photochemical & photobiological sciences : Official journal of the European Photochemistry Association and the European Society for Photobiology* 2018; **17**: 1003-17.
182. Dall Agnol MA, Nicolau RA, de Lima CJ, Munin E. Comparative analysis of coherent light action (laser) versus non-coherent light (light-emitting diode) for tissue repair in diabetic rats. *Lasers in medical science* 2009; **24**: 909-16.
183. Bastos JLN, Lizarelli RFZ, Parizotto NA. Comparative study of laser and LED systems of low intensity applied to tendon healing. *Laser Physics* 2009; **19**: 1925-31.
184. Corazza AV, Jorge J, Kurachi C, Bagnato VS. Photobiomodulation on the angiogenesis of skin wounds in rats using different light sources. *Photomedicine and laser surgery* 2007; **25**: 102-6.
185. Sharma SK, Kharkwal GB, Sajo M, Huang YY, De Taboada L, McCarthy T, Hamblin MR. Dose response effects of 810 nm laser light on mouse primary cortical neurons. *Lasers in surgery and medicine* 2011; **43**: 851-9.
186. Oron U, Yaakobi T, Oron A, Hayam G, Gepstein L, Rubin O, Wolf T, Haim SB. Attenuation of infarct size in rats and dogs after myocardial infarction by low-energy laser irradiation. *Lasers in surgery and medicine* 2001; **28**: 204-11.
187. Lanzafame RJ, Stadler I, Kurtz AF, Connelly R, Brondon P, Olson D. Reciprocity of exposure time and irradiance on energy density during photoradiation on wound healing in a murine pressure ulcer model. *Lasers in Surgery and Medicine: The Official Journal of the American Society for Laser Medicine and Surgery* 2007; **39**: 534-42.

188. Chu-Tan JA, Rutar M, Saxena K, Wu Y, Howitt L, Valter K, Provis J, Natoli R. Efficacy of 670 nm light therapy to protect against photoreceptor cell death is dependent on the severity of damage. *International Journal of Photoenergy* 2016; **2016**.
189. Calaza KC, Kam JH, Hogg C, Jeffery G. Mitochondrial decline precedes phenotype development in the complement factor H mouse model of retinal degeneration but can be corrected by near infrared light. *Neurobiology of aging* 2015; **36**: 2869-76.
190. Kokkinopoulos I. 670nm LED ameliorates inflammation in the CFH−/− mouse neural retina. *Journal of Photochemistry and Photobiology B: Biology* 2013; **122**: 24-31.
191. Albarracin RS, Valter K. Treatment with 670-nm Light Protects the Cone Photoreceptors from White Light-Induced Degeneration. *Retinal Degenerative Diseases Advances in Experimental Medicine and Biology* 2012; **723**: 121-8.
192. Natoli R, Zhu Y, Valter K, Bisti S, Eells J, Stone J. Gene and noncoding RNA regulation underlying photoreceptor protection: microarray study of dietary antioxidant saffron and photobiomodulation in rat retina. *Molecular vision* 2010; **16**: 1801.
193. Marco FD, Romeo S, Nandasena C, Purushothuman S, Adams C, Bisti S, Stone J. The time course of action of two neuroprotectants, dietary saffron and photobiomodulation, assessed in the rat retina. *American Journal of Neurodegenerative Disease* 2013; **2**: 208-20.
194. Eells JT, DeSmet KD, Kirk DK, Wong-Riley M, Whelan HT, Hoeve JV, Nork TM, Stone J, Valter K. Photobiomodulation for the Treatment of Retinal Injury and Retinal Degenerative Diseases. In.*Photobiomodulation for the Treatment of Retinal Injury and Retinal Degenerative Diseases*, Boston, MA: Springer US, 2008; 39-51.
195. Eells JT, Gopalakrishnan S, Valter K. Near-Infrared Photobiomodulation in Retinal Injury and Disease. *Advances in experimental medicine and biology* 2016; **854**: 437-41.
196. Saliba A, Du Y, Liu H, Patel S, Roberts R, Berkowitz BA, Kern TS. Photobiomodulation Mitigates Diabetes-Induced Retinopathy by Direct and Indirect Mechanisms: Evidence from Intervention Studies in Pigmented Mice. *PLoS One* 2015; **10**: e0139003.
197. Cummins N, Bartlett CA, Archer M, Bartlett E, Hemmi JM, Harvey AR, Dunlop SA, Fitzgerald M. Changes to mitochondrial ultrastructure in optic nerve vulnerable to secondary degeneration in vivo are limited by irradiation at 670 nm. *BMC neuroscience* 2013; **14**: 98.
198. Giacci MK, Wheeler L, Lovett S, Dishington E, Majda B, Bartlett CA, Thornton E, Harford-Wright E, Leonard A, Vink R. Differential effects of 670 and 830 nm red near infrared irradiation therapy: a comparative study of optic nerve injury, retinal degeneration, traumatic brain and spinal cord injury. *PloS one* 2014; **9**: e104565.
199. Merry GF, Munk MR, Dotson RS, Walker MG, Devenyi RG. Photobiomodulation reduces drusen volume and improves visual acuity and contrast sensitivity in dry age‐related macular degeneration. *Acta ophthalmologica* 2017; **95**.
200. Penn R, Hagins W. Signal transmission along retinal rods and the origin of the electroretinographic a-wave. *Nature* 1969; **223**: 201.
201. Dick E, Miller RF, Bloomfield S. Extracellular K+ activity changes related to electroretinogram components. II. Rabbit (E-type) retinas. *The Journal of general physiology* 1985; **85**: 911-31.
202. Bawa G, Tkatchenko TV, Avrutsky I, Tkatchenko AV. Variational analysis of the mouse and rat eye optical parameters. *Biomed Opt Express* 2013; **4**: 2585-95.
203. Prusky GT, Alam NM, Beekman S, Douglas RM. Rapid quantification of adult and developing mouse spatial vision using a virtual optomotor system. *Investigative ophthalmology & visual science* 2004; **45**: 4611-6.

204. Douglas R, Alam N, Silver B, McGill T, Tschetter W, Prusky G. Independent visual threshold measurements in the two eyes of freely moving rats and mice using a virtual-reality optokinetic system. *Visual neuroscience* 2005; **22**: 677-84.
205. Corazza AV, Jorge DJ, Kurachi C, Bagnato VS. Photobiomodulation on the Angiogenesis of Skin Wounds in Rats Using Different Light Sources. *Photomedicine and laser surgery* 2007; **25**: 102-6.
206. Chaves MEdA, Araújo ARd, Piancastelli ACC, Pinotti M. Effects of low-power light therapy on wound healing: LASER x LED. *Anais brasileiros de dermatologia* 2014; **89**: 616-23.
207. Bringmann A, Pannicke T, Grosche J, Francke M, Wiedemann P, Skatchkov SN, Osborne NN, Reichenbach A. Müller cells in the healthy and diseased retina. *Progress in retinal and eye research* 2006; **25**: 397-424.
208. Chidlow G, Daymon M, Wood JP, Casson RJ. Localization of a wide-ranging panel of antigens in the rat retina by immunohistochemistry: comparison of Davidson's solution and formalin as fixatives. *Journal of Histochemistry & Cytochemistry* 2011; **59**: 884-98.
209. Wen R, Cheng T, Song Y, Matthes MT, Yasumura D, LaVail MM, Steinberg RH. Continuous exposure to bright light upregulates bFGF and CNTF expression in the rat retina. *Curr Eye Res* 1998; **17**: 494-500.
210. Wen R, Song Y, Cheng T, Matthes MT, Yasumura D, LaVail MM, Steinberg RH. Injury-induced upregulation of bFGF and CNTF mRNAS in the rat retina. *The Journal of neuroscience : the official journal of the Society for Neuroscience* 1995; **15**: 7377-85.
211. Ju W-K, Lee M-Y, Hofmann H-D, Kirsch M, Chun M-H. Expression of CNTF in Müller cells of the rat retina after pressure-induced ischemia. *Neuroreport* 1999; **10**: 419-22.
212. Honjo M, Tanihara H, Kido N, Inatani M, Okazaki K, Honda Y. Expression of ciliary neurotrophic factor activated by retinal Muller cells in eyes with NMDA-and kainic acid–induced neuronal death. *Investigative ophthalmology & visual science* 2000; **41**: 552-60.
213. Azarmina M. Full-Field versus Multifocal Electroretinography. *Journal of ophthalmic & vision research* 2013; **8**: 191-2.
214. Youssef PN, Sheibani N, Albert DM. Retinal light toxicity. *Eye (London, England)* 2011; **25**: 1-14.
215. Youssef P, Sheibani N, Albert D. Retinal light toxicity. *Eye* 2011; **25**: 1.
216. Jacques SL. Laser-tissue interactions. Photochemical, photothermal, and photomechanical. *The Surgical clinics of North America* 1992; **72**: 531-58.
217. Brancato R, Pratesi R, Leoni G, Trabucchi G, Vanni U. Histopathology of diode and argon laser lesions in rabbit retina. A comparative study. *Investigative ophthalmology & visual science* 1989; **30**: 1504-10.
218. Green WR, Robertson DM. Pathologic findings of photic retinopathy in the human eye. *American journal of ophthalmology* 1991; **112**: 520-7.
219. Ilic S, Leichliter S, Streeter J, Oron A, DeTaboada L, Oron U. Effects of power densities, continuous and pulse frequencies, and number of sessions of low-level laser therapy on intact rat brain. *Photomedicine and laser surgery* 2006; **24**: 458-66.
220. Lampl Y, Zivin JA, Fisher M, Lew R, Welin L, Dahlof B, Borenstein P, Andersson B, Perez J, Caparo C, Ilic S, Oron U. Infrared laser therapy for ischemic stroke: a new treatment strategy: results of the NeuroThera Effectiveness and Safety Trial-1 (NEST-1). *Stroke* 2007; **38**: 1843-9.
221. Zivin JA, Albers GW, Bornstein N, Chippendale T, Dahlof B, Devlin T, Fisher M, Hacke W, Holt W, Ilic S, Kasner S, Lew R, Nash M, Perez J, Rymer M, Schellinger P, Schneider D, Schwab S, Veltkamp R, Walker M, Streeter J. Effectiveness and safety of transcranial laser therapy for acute ischemic stroke. *Stroke* 2009; **40**: 1359-64.

222. Jimenez JJ, Wikramanayake TC, Bergfeld W, Hordinsky M, Hickman JG, Hamblin MR, Schachner LA. Efficacy and safety of a low-level laser device in the treatment of male and female pattern hair loss: a multicenter, randomized, sham device-controlled, double-blind study. *American journal of clinical dermatology* 2014; **15**: 115-27.
223. Kent AL, Broom M, Parr V, Essex RW, Abdel-Latif ME, Dahlstrom JE, Valter K, Provis J, Natoli R. A safety and feasibility study of the use of 670 nm red light in premature neonates. *Journal of perinatology : official journal of the California Perinatal Association* 2015; **35**: 493-6.
224. Narayan DS, Wood JP, Chidlow G, Casson RJ. A review of the mechanisms of cone degeneration in retinitis pigmentosa. *Acta ophthalmologica* 2016; **94**: 748-54.
225. Ortín-Martínez A, Nadal-Nicolás FM, Jiménez-López M, Alburquerque-Béjar JJ, Nieto-López L, García-Ayuso D, Villegas-Pérez MP, Vidal-Sanz M, Agudo-Barriuso M. Number and distribution of mouse retinal cone photoreceptors: differences between an albino (Swiss) and a pigmented (C57/BL6) strain. *PLoS One* 2014; **9**: e102392.
226. Ortín-Martínez A, Jiménez-López M, Nadal-Nicolás FM, Salinas-Navarro M, Alarcón-Martínez L, Sauvé Y, Villegas-Pérez MP, Vidal-Sanz M, Agudo-Barriuso M. Automated quantification and topographical distribution of the whole population of S- and L-cones in adult albino and pigmented rats. *Investigative ophthalmology & visual science* 2010; **51**: 3171-83.
227. Lin B, Masland RH, Strettoi E. Remodeling of cone photoreceptor cells after rod degeneration in rd mice. *Experimental eye research* 2009; **88**: 589-99.
228. LAVAIL MM, T MATTHES M, YASUMURA D, STEINBERG RH. Variability in rate of cone degeneration in the retinal degeneration (rd/rd) mouse. *Experimental eye research* 1997; **65**: 45-50.
229. Narayan DS. Manipulation of Photoreceptor Energy Metabolism for Clinical Advantage. In.*Manipulation of Photoreceptor Energy Metabolism for Clinical Advantage*, Vol. MPhil: University of Adelaide, 2017.
230. Anders JJ, Romanczyk TB, Ilev IK, Moges H, Longo L, Wu X, Waynant RW. Light supports neurite outgrowth of human neural progenitor cells in vitro: the role of P2Y receptors. *IEEE Journal of Selected Topics in Quantum Electronics* 2008; **14**: 118-25.
231. Holanda VM, Chavantes MC, Wu X, Anders JJ. The mechanistic basis for photobiomodulation therapy of neuropathic pain by near infrared laser light. *Lasers in surgery and medicine* 2017; **49**: 516-24.
232. van Wyk M, Schneider S, Kleinlogel S. Variable phenotypic expressivity in inbred retinal degeneration mouse lines: A comparative study of C3H/HeOu and FVB/N rd1 mice. *Mol Vis* 2015; **21**: 811-27.
233. LaVail MM, Nishikawa S, Steinberg RH, Naash MI, Duncan JL, Trautmann N, Matthes MT, Yasumura D, Lau-Villacorta C, Chen J. Phenotypic characterization of P23H and S334ter rhodopsin transgenic rat models of inherited retinal degeneration. *Experimental eye research* 2018; **167**: 56-90.
234. Jimenez AJ, Garcia-Fernandez JM, Gonzalez B, Foster RG. The spatio-temporal pattern of photoreceptor degeneration in the aged rd/rd mouse retina. *Cell and tissue research* 1996; **284**: 193-202.
235. Rodrigo SM, Cunha A, Pozza DH, Blaya DS, Moraes JF, Weber JBB, Oliveira MGd. Analysis of the Systemic Effect of Red and Infrared Laser Therapy on Wound Repair. *Photomedicine and laser surgery* 2009; **27**: 929-35.
236. Johnstone DM, el Massri N, Moro C, Spana S, Wang XS, Torres N, Chabrol C, De Jaeger X, Reinhart F, Purushothuman S, Benabid AL, Stone J, Mitrofanis J. Indirect application of near infrared light induces neuroprotection in a mouse model of parkinsonism - an abscopal neuroprotective effect. *Neuroscience* 2014; **274**: 93-101.

237. Harpas Y, Wood JP, Chidlow G, Casson RJ. Red/Near-infrared irradiation therapy (R/NIR IT) LASER pretreatment promotes neuroprotection of retinal neurons in a model of retinal metabolic dysfunction in vitro. *Investigative ophthalmology & visual science* 2016; **57**: 4403-.